“The reconstruction of paleoclimate variability in Northern Germany, during Marine Isotope Stage 5”

Dissertation
zur Erlangung des Grades
„Doktor der Naturwissenschaften“

im Promotionsfach Geologie/Paläontologie

am Fachbereich Chemie, Pharmazie und Geowissenschaften
der Johannes Gutenberg-Universität Mainz

von

Jan Tolzmann

geb. in Leverkusen

Mainz, 2013

“Logic will get you from A to B,
imagination takes you
everywhere!”

(Albert Einstein)

„Wir müssen das, was wir denken, auch sagen.
Wir müssen, das was wir sagen auch tun.
Und wir müssen, das was wir tun, dann auch sein.”

(Alfred Herrhausen)

Abstract

Abstract

In order to obtain a better understanding about the influence of post-depositional diagenesis on speleothem ^{230}Th/U-ages and paleoclimate variability during Marine Isotope Stage (MIS) 5 in northern Germany, four stalagmites from the Riesenberghöhle (RBH) were investigated by thin section analysis, ^{230}Th/U-dating as well as stable oxygen and carbon isotope and laser ablation inductively coupled mass spectrometry (LA-ICPMS) trace element analysis. The RBH is located in the Weser Hills and is one of the northernmost limestone caves in Germany.

Multi collector (MC) ICPMS ^{230}Th/U-ages and thin section analysis of the RBH stalagmites shows that some growth phases of the stalagmites were diagenetically altered after their deposition. The impact of post-depositional diagenesis (PDD) on the ^{230}Th/U-ages is modeled, and potential processes leading to PDD are discussed. In this context, it is suggested that PDD may be induced by rapid climate change at the inception of the GIS.

Despite of the dating uncertainties resulting from PDD, ^{230}Th/U-dating shows that the RBH stalagmites grew during the Eemian and most of the Greenland Interstadials (GIS) during MIS 5. Thus, the growth phases of the RBH stalagmites might be related to a reorganization of the Atlantic Meridional Overturning Circulation (AMOC). The stable isotope (δ^{13}C and δ^{18}O) and the trace element variability of the stalagmites reflects rapid changes of past temperature and precipitation on millennial and sub-millennial timescales. These past climate changes can be amplified by orbitally forced variations of the July solar insolation at 65°N.

Zusammenfassung

Um ein besseres Verständnis über den nachträglichen Einfluss von Diagenese auf Speleothem ^{230}Th/U-Alter und die paläoklimatische Variabilität während des Marinen Isotopen Stadium 5 (MIS 5) in Norddeutschland zu gewinnen, wurden vier Stalagmiten aus der Riesenberghöhle (RBH). Sie wurden hinsichtlich, der ^{230}Th/U Datierung, sowie ihrer stabilen Sauerstoff- und Kohlenstoffisotope und mit ablation inducively coupled mass spectrometry (LA-ICPMS) ihrer Spurenelemente untersucht. Die RBH ist eine der nördlichsten Tropfsteinhöhlen Deutschlands und liegt im Weserbergland.

Multi collector (MC) ICPMS ^{230}Th/U Alter und Dünnschliffanalysen zeigen, dass nachträglich einige Wachstumsphasen der Stalagmiten diagenetisch verändert worden sind. In dieser Arbeit, wird die Auswirkung von Diagenese nach Ablagerung (PDD) auf die ^{230}Th/U-Alter modelliert, und potenzielle Prozesse, die zur PDD führen, diskutiert. In diesem Kontext, wird auch nahegelegt, dass PDD durch schnelle klimatische Veränderungen zu Beginn der GIS (Grönland Interstadiale) eingeleitet werden könnte.

Trotz der Datierungsunsicherheiten, welche aus der PDD resultieren, zeigt die ^{230}Th/U Datierung, dass die RBH Stalagmiten während des Eems und in den meisten der GIS des MIS 5 gewachsen sind. Deswegen könnte das Wachstum in RBH Stalagmiten mit einer Reorganisation der „Atlantic Meridional Overturning Circulation“ (AMOC) zusammenhängen. Die Variabilität der stabilen Isotope und der Spurenelemente (δ^{13}C und δ^{18}O) spiegeln eine schnelle Veränderung der Temperatur und des Niederschlags auf tausendjährigen und hundertjährigen Zeitskalen wieder. Diese schnellen Klimaveränderungen können durch die orbital erzwungenen Variationen der solaren Juli Einstrahlung bei 65°N verstärkt werden.

Table of contents

1. Introduction

There is an ongoing discussion about the human impact on recent and future climate change. In order to understand potential future climate change, it is important to understand the triggers and mechanisms that drive the climate system on orbital, millennial and centennial time scales. Various paleoclimate archives, such as ice cores, marine and lake sediments, tree rings, or corals and mollusks, provide this information (EPICA community members, 2004; Felis et al., 2004; Sirocko et al., 2005; Trouet et al., 2009).

Most climate archives are difficult to date beyond the limit of the ^{14}C dating method, and a potential way to constrain the chronology of such records is to line up events with those in another record (Henderson et al., 2006). A more elegant approach to establish longer and more reliable chronologies, however, is to use speleothems, such as stalagmites and flowstones, as paleoclimate archives. Their largest advantage is that they can be precisely and accurately dated in the range of the last 500ka by U-series disequilibrium methods (Richards and Dorale, 2003; Scholz and Hoffmann, 2008; Cheng et al., 2009). State-of-the-art analytical methods, such as the MC-ICPMS method, enable obtaining precise ages even for very small sample sizes (Hoffmann et al., 2007). In addition, different approaches to calculate age models for speleothems have been developed in recent years (Scholz and Hoffmann, 2011; Hercman and Pawlak, 2012; Scholz et al., 2012).

In this thesis, petrological and geochemical investigations of stalagmites from the Riesenberghöhle (RBH) in Northern Germany have been performed in order to obtain a better understanding of the U-Th system as well as on rapid climate shifts during Marine Isotope Stage (MIS) 5. Thus, one focus of this thesis is the understanding of potential changes of the U-Th system as a consequence of open system conditions. The other focus is the determination of the timing and duration of stalagmite growth phases during MIS 5 as a consequence of rapid climate change.

One principal requirement for $^{230}Th/U$-dating is, that the U-Th-system remains closed after deposition. Open system conditions, however, violates this principal requirement

and may lead to ^{230}Th/U-age inversions. Post depositional diagenesis (PDD) is a consequence of open system conditions in the U-Th system, which leads to ^{230}Th/U-age inversions. Stalagmite sections, which experienced PDD, can be observed with thin section analysis. In some sections of the RBH stalagmites, evidence for PDD has been observed. Here, different potential mechanisms that lead to PDD and, thus, to altered ^{230}Th/U-ages are discussed. Furthermore, particular sections influenced by PDD were selected to estimate and to model the impact of open system conditions on ^{230}Th/U-ages.

RBH stalagmites also contain paleoclimate information about rapid climate shifts during MIS 5. These rapid climate shifts are also called Greenland Interstadials (GIS) and are characterized by a fast switch from relatively cold to relatively warm climate conditions followed by a subsequent gradual cooling phase. The common explanation for the occurrence of the GIS is a reorganization of the Atlantic Meridional Overturning Circulation (AMOC), which in turn is a function of sea ice extent, seawater temperature and salinity as well as summer insolation at 65 N. Twenty-five of these rapid climate shifts have been observed throughout the Northern Hemisphere (e.g., NGRIP community members, 2004; Genty et al., 2003; Spötl et al., 2006; Fleitmann et al., 2009; Boch et al. 2011). MIS 5, which includes the Last Interglacial (MIS 5e) and the Early Glacial (MIS 5d-a), was associated with seven GIS (25-19). In terms of future climate change, it is important to understand the process of rapid climate change.

In chapter 2, the basics of this PhD thesis are shortly introduced. Chapter 2 is subdivided into three parts: Part one shortly explains the basic mechanisms of speleothem growth. Part two illustrates the fundamentals of U-series geochemistry, stable isotopes and trace elements, whereas part three gives an introduction to paleoclimate variability on orbital and millennial time scales. Chapter 3 presents the cave location and the RBH stalagmites that have been studied in this PhD thesis. Furthermore, it gives an overview of the methods, which have been applied. In chapter 4, all results are presented. This includes sedimentological as well as petrological observations, the ^{230}Th/U-ages as well as all results of stable isotope and trace element measurements. In chapter 5 is the discussion part and therefore the main part of this thesis. Thus, it is subdivided in chapter 5.1, which deals with the impact of PDD on speleothem ^{230}Th/U-ages is modeled and discussed. Chapter 5.2 discusses the conduction of the RBH age-models and compares the growth phases of the individual

stalagmites. Chapter 5.3 concentrates on the mechanisms of past climate variability reflected in the trace element and stable isotope variations of the RBH stalagmites during MIS 5. In chapter 5.4, the millennial scale variations observed in RBH stalagmites during MIS 5 are discussed, while in chapter 6, a conclusion as well as an outlook is given.

2. Basics

2.1 Speleothem growth

Speleothems, such as stalagmites, stalactites or flowstones are secondary calcite cave deposits. Calcite and aragonite are the main speleothem-forming minerals. Aragonite is meta-stable and usually has a higher U content comparison to calcite (Ivanovich and Harmon, 1992). However, calcite is the predominant mineral in speleothems. Three basic requirements have to be met for speleothem formation:

1. The host rock must contain $CaCO_3$.
2. The area must have an adequate water supply.
3. In the soil zone there has to be a sufficient amount of CO_2.

The process of speleothem formation is displayed in Fig. 2.1. Generally, root respiration or decay of organic material in the soil zone above the cave is the most common source for pCO_{2soil}. In the atmosphere, the CO_2 concentration is ≈ 350ppmV but can reach maximum values of 100000ppmV in the soil zone (McDermott, 2004).

Precipitation percolates through the soil above the cave. The percolating water equilibrates with the high soil pCO_2 producing carbonic acid (Fairchild et al. 2006):

$$H_2O + CO_{2(aq)} \Leftrightarrow H_2CO_3 \tag{2.1}$$

Carbonic acid dissolves according to:

$$H_2CO_3 \Leftrightarrow H^+ + HCO_3^- \Leftrightarrow 2H^+ + CO_3^{2-} \tag{2.2}$$

In turn, the acidic solution subsequently dissolves the carbonate host rock, which is expressed by the following formula:

$$CO_2 + H_2O + CaCO_3 \Leftrightarrow Ca^{2+} + 2HCO_3^- \tag{2.3}$$

The concentration of Ca^{2+} and HCO_3^- of the drip water entering the cave strongly depends on several parameters such as temperature, pCO_2 and whether dissolution takes places under open or closed system conditions (Kaufmann 2003, McDermott 2004).
When the drip water reaches the cave, it is usually saturated with respect to calcite. The cave air normally has a lower pCO_2 than the soil zone, leading to degassing of CO_2 from the drip water, which in turn leads to the establishment of supersaturation with respect to calcite and, finally, precipitation of speleothem calcite (Fairchild and Baker, 2012). According to Fairchild et al. (2006) this region can be called "precipitation region".

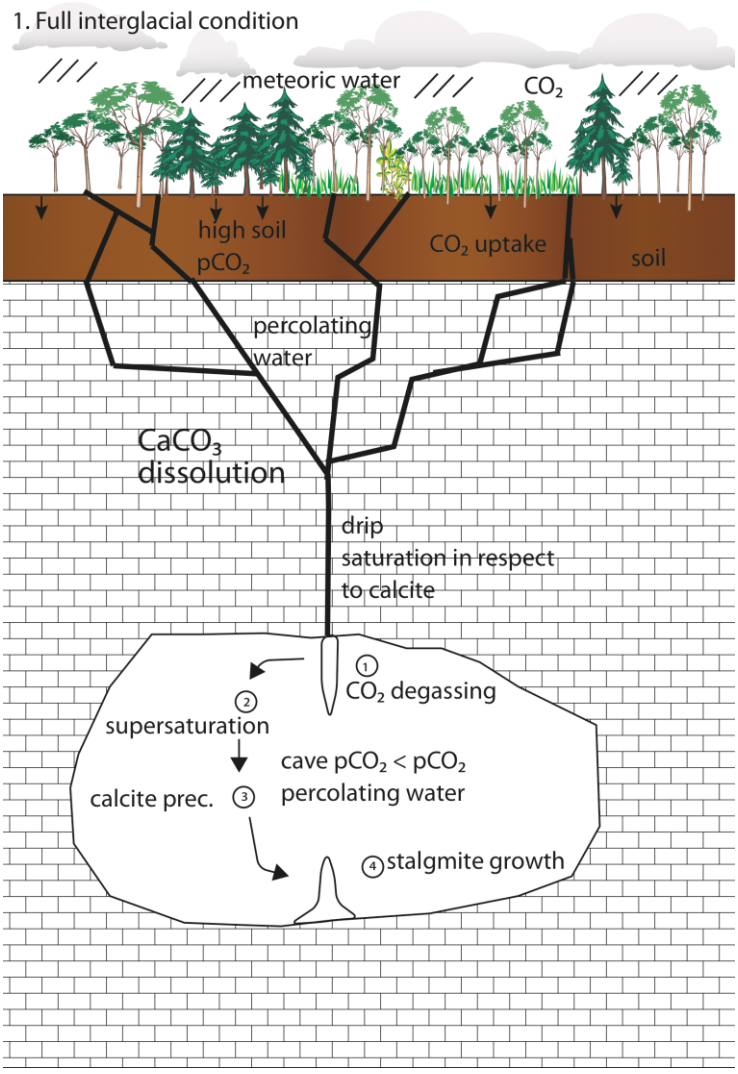

Figure 2.1: Schematic overview of speleothem formation during full interglacial conditions.

2.2 U-series geochemistry, stable isotopes and trace elements

For paleoclimate investigation, stalagmites have several advantages in comparison to other climate archives (e.g. Richards and Dorale, 2003; Scholz and Hoffmann 2008):

- They provide an excellent chronology due to a highly precise and accurate dating method (U-series dating).
- Stalagmites can be found almost all around the world e.g. in the tropics (e.g. Meckler et al. 2012; Fensterer et al. 2012, 2013), in the subtropics (e.g. Bardertscher et al. 2010; Burns et al. 2003), in temperate regions (e.g. Riechelmann et al. 2011) and high northern latitudes (e.g. Lauritzen and Lundberg 1999).
- Several proxies can be measured at high resolution, such as stable isotopes and trace elements.

U-series geochemistry:

The U-series dating method is a highly precise and accurate method for dating speleothems and corals younger than 500ka (Richards and Dorale, 2003; Scholz and Hoffmann, 2008). The method, also known as the U-series disequilibrium method, is based on the disequilibrium between the actinide ^{238}U and its short-lived daughter isotope ^{230}Th. In nature, three decay chains for the U-series exist starting with the long-living actinide nuclides, which expose different half-lives ($T_{1/2}$) ^{238}U ($T_{1/2}$ = 4.58 Ga), ^{235}U ($T_{1/2}$ = 0.7 ka) or ^{232}Th ($T_{1/2}$ = 14 Ga) (Jaffey, 1971). All actinides occur with their daughter nuclides, which have shorter half-lives. The ^{238}U decay chain is most important for the Th/U-dating method and is shown in Fig. 2.2. In this decay chain, the daughter nuclides ^{234}U occur with $T_{1/2}$ = 245.25 ± 490a, and $T_{1/2}$ = 75.69 ± 230a (Cheng et al., 2000). The limestone above the cave has normally reached a state of secular equilibrium after deposition occurred several million years ago, which is the basic requirement for U-series dating methods. When water percolates through the limestone, geochemical processes fractionate the nuclides and establish disequilibrium. Due to the return of equilibrium in time after secondary deposition, the quantification of this time is possible (Bourdon et al, 2003).

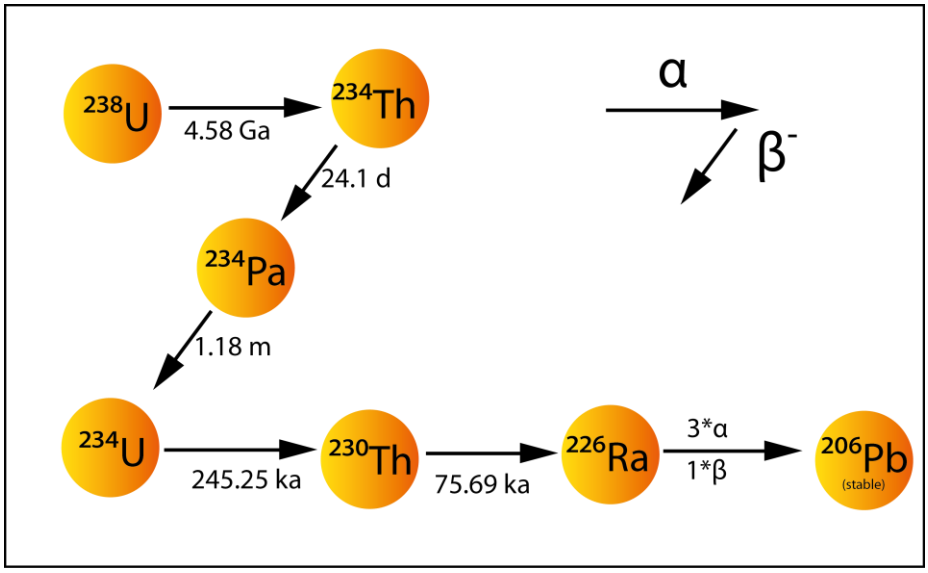

Figure 2.2: Schematic diagram of the ^{238}U decay chain and their corresponding half lives. The errors indicate α or β decay. Figure modified after Neff (2001).

2.2.1 U and Th geochemistry

The U concentrations of the continental crust commonly range from 0.1µg/g (basalt) to 6µg/g (granite), whereas limestones incorporate approximately 0 to 2µg/g U and typically reveal a Th concentration of 0 to 2.4µg/g (Ivanovich and Harmon, 1992). However extremely high U concentrations > 100µg/g have been reported by Cliff et al. (2010) from stalagmites in the Austrian Alps. The method itself benefits from the fact that several natural processes can disrupt the state of equilibrium between parent and daughter isotopes:

1. *The α-recoil effect.* During the decay of ^{238}U to ^{234}U, the crystal structure of calcite is damaged by the α particle, and the atom is displaced from its original position (Ivanovich and Harmon, 1992); (Bourdon et al, 2003). As a result the daughter nuclide ^{234}U can be more easily remobilized than its parent during weathering processes.
2. *The different geochemical behaviour of U and Th.* In an aquaeous solution U is soluble and mobile. In nature, U exists in two oxidation states (U^{4+} and U^{6+}) and occurs at the surface mainly in form of an uranyl complex $(UO_2)^{2+}$ as U^{6+}, while U^{4+}, which occurs mainly in reducing environments, and is insoluble and less mobile. In contrast, Th (Th^{4+}) is highly particle reactive, is therefore is not soluble in aquaeous solutions, and primarily transported adsorbed to particles or in minerals. Thus, Th cannot be incorporated during precipitation of secondary

carbonates such as corals, speleothems and travertins (Bourdon et al, 2003; Ivanovich and Harmon, 1992).

2.2.2 The Th/U-age equation

The Th/U-age is based on the decay law. The activity (A) of a number of atoms of a nuclide is the number of decay events per unit of time. In this thesis, all activities and activity ratios are indicated by parentheses (e.g. (^{238}U)). The equation of decay for a given numbers of atoms, N, of a nuclide is expressed as follows:

$$A = \frac{dN}{dt} = -\lambda N \tag{2.4}$$

Integration of eq. (2.4) gives:

$$N(t) = N_0 \cdot e^{-\lambda t} \tag{2.5}$$

N(t): Number of atoms at the time t

N_0: Number of atoms at the time = 0

λ: decay constant [a^{-1}]

λ is related to the half life,$T_{1/2}$, by:

$$\lambda = \frac{\ln 2}{T_{1/2}} \tag{2.6}$$

The equation of decay for the daughter atoms can be defined as:

$$\frac{dN_2}{dt} = -\lambda_2 N_2 + \lambda_1 N_1 \tag{2.7}$$

The first term describes the decay of the daughter nuclide, whereas the 2nd term describes the production of the daughter nuclide due to the decay of the mother.

For Th/U-dating, the following requirements have to be given:

1. (^{230}Th)$_{initial}$ must be zero. This is usually the case because the isotope cannot be incoorporated during the precipitation of secondary carbonate due to its insolubility and is only produced by the decay of ^{238}U.
2. The system remains closed after deposition and, thus, U and Th are not remobilized after deposition.

When these requirements are met, the age, t, of a stalagmite sample can be calculated iteratively using ($^{234}U/^{238}U$) and ($^{230}Th/^{238}U$) and the following equation (see Ivanovich and Harmon, 1992 for derivation):

$$\left(\frac{^{234}U}{^{238}U}\right)(t) = \left(\left(\frac{^{234}U}{^{238}U}\right)_{init.} - 1\right)e^{-\lambda_{234}t} + 1 \qquad (2.8)$$

$$\left(\frac{^{230}Th}{^{238}U}\right)(t) = \left(1 - e^{-\lambda_{234}t}\right) + \left(\left(\frac{234U}{238U}\right)(t) - 1\right)\frac{\lambda_{230}}{\lambda_{230} - \lambda_{234}}\left(1 - e^{-(\lambda_{230} - \lambda_{234})t}\right) \qquad (2.9)$$

Both equations can be illustrated graphically as shown in Figure 2.3.

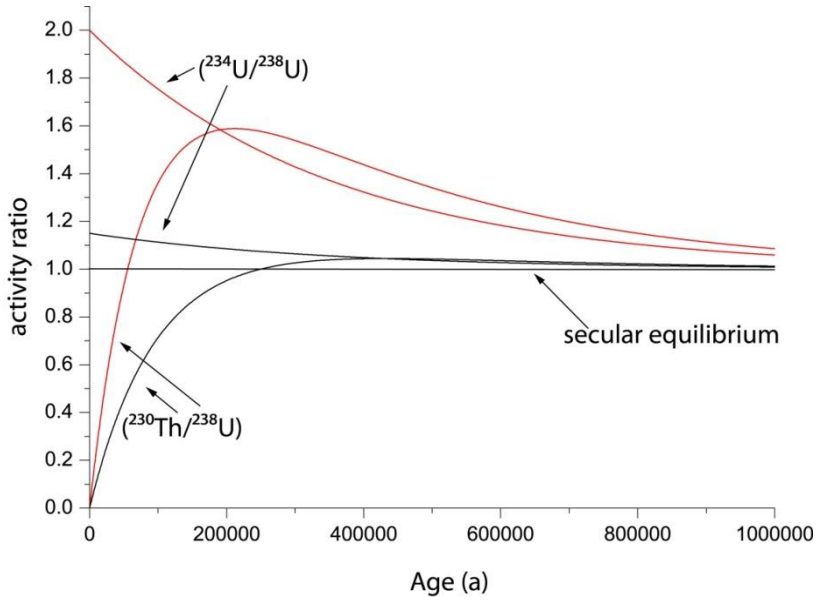

Figure 2.3: Figure adopted from Scholz and Hoffmann (2008). Temporal development of ($^{234}U/^{238}U$) and ($^{230}Th/^{238}U$) with no initial Th. Two different scenarios are shown: Marine samples usually have a $(^{234}U/^{238}U)_{init.}$ = 1.15 (black line), whereas other samples such as speleothems have a higher $(^{234}U/^{238}U)_{init.}$ for example 2 (red line). The dating limit is accomplished, when the secular equilibrium is reached.

2.2.3 Utilized standards and spikes

Sample preparation was similar to that described in Hoffmann et al. (2007). Dating was performed by MC-ICPMS at the Max-Planck-Institute for Chemistry (MPIC), Mainz, Germany, and at CENIEH, Burgos, Spain. Calibration of the U-Th spike used at CENIEH is described in (Hoffmann et al., 2007). The mixed ^{233}U-^{236}U-^{229}Th spike used

at MPIC was calibrated against a gravimetric U standard solution and a secular equilibrium standard solution. The gravimetric U standard solution was prepared from an NBL-112a metal bar and also used to calibrate the U-Th spike used at the Heidelberg Academy of Sciences (Hoffmann et al., 2007). The ^{229}Th concentration of the spike was calibrated against a secular equilibrium standard solution prepared from a 2Ma old speleothem sample from Wilder Mann Cave, Austria (Meyer et al., 2009; Meyer et al., 2011), which has been shown to be in secular equilibrium (Hoffmann et al., 2007). The calibration was checked using another secular equilibrium solution (Harwell Uraninite, HU) that was used to calibrate the U-Th spike used at the Heidelberg Academy of Sciences (Hoffmann et al., 2007).

2.2.4 Correction for detrital contamination

As shown in this chapter, one basic requirement for U-series dating is that all ^{230}Th present in a stalagmite sample is formed in situ by the radioactive decay of U under closed system conditions (Ivanovich and Harmon 1992). Unfortunately, in nature this basic requirement is not generally fulfilled. Instead, it is common that small quantities of initial ^{230}Th are incorporated during precipitation of speleothem $CaCO_3$ due to detrital contamination by clay minerals or biogenous material. In this case, a correction for initial (or non-radiogenic) ^{230}Th is necessary. To estimate the degree of contamination, the isotope ^{232}Th can be used, because it has the same chemical properties as ^{230}Th (Ludwig and Titterington, 1994). Thus, the (^{230}Th/^{232}Th) activity ratio indicates weather a correction needs to be applied. Thresholds for mass spectrometric analysis of activity ratios between 100-300 have been suggested by (Li et al. 1989 and Richards and Dorale, 2003).

To estimate the degree of contamination with initial ^{230}Th, an a-priori estimate for the isotopic composition of the contaminating phase (Ivonovich and Harmon 1992, Dorale et al. 1998, Hellstrom 2006) such as, the bulk earth ^{232}Th/^{238}U concentration ratio of the upper crust of 3.8 (Wedepohl 1995) and the secular equilibrium for all isotopes of the ^{238}U decay chain is assumed. Using the mean ratio of ^{232}Th/^{238}U $\approx$ 3.8±1.9 for the Earth's upper crust given by (Wedepohl 1995), the concentration for non-authogenic ^{238}U, ^{234}U and ^{230}Th can be calculated and corrected, applying the following equations:

$$c\left(^{238}U_{detr}\right) = \frac{c\left(^{232}Th_{meas}\right)}{c\left(^{232}Th_{detr}/^{238}U_{detr}\right)} = \frac{c\left(^{232}Th_{meas}\right)}{3.8} \tag{2.10}$$

The activity (^{238}U) of the detrital ^{238}U concentration c($^{238}U_{detr}$) can then be calculated by:

$$\left(^{238}U\right)_{detr} = -N\lambda = \frac{N_A \cdot c\left(^{238}U_{detr}\right)}{238} \cdot \lambda_{238} \tag{2.11}$$

$$\Rightarrow \left(^{238}U\right)_{detr} = c\left(^{238}U_{detr}\right) 0.7478 \tag{2.12}$$

The factor 0.7478 is used to derive the specific activity of (^{238}U) in dpm/g from a concentration in µg/g, whereas N_A is the Avogadro constant. Since the detritus is part of the host rock, which is in secular equilibrium, the activities of the isotopes in the ^{238}U decay chain are equal ($^{238}U)_{detr}$ = ($^{234}U)_{detr}$ = ($^{230}Th)_{detr}$. Thus, the detrital contribution can be substracted from the measured activities of the isotopes ^{238}U, ^{234}U an ^{230}Th and the activities of the pure carbonate can be estimated.

$$\left(^{238}U\right)_{carb} = \left(^{238}U\right)_{meas} - \left(^{238}U\right)_{detr} \tag{2.13}$$

$$\left(^{234}U\right)_{carb} = \left(^{234}U\right)_{meas} - \left(^{234}U\right)_{detr} \tag{2.14}$$

$$\left(^{230}Th\right)_{carb} = (^{230}Th)_{meas} - (^{230}Th)_{detr} \tag{2.15}$$

Depending on (^{230}Th/^{232}Th) of the sample and the correction factor, the correction may have a considerable effect on the ^{230}Th-, ^{234}U-, ^{238}U activity ratio. Thus, using an a-priori approximation, the effect of propagating the assumed uncertainty of the isotopic composition of the contaminating phase through the age calculation may be problematic (Hellstrom, 2006). Therefore, in case of detrital correction, precise and direct measurement of the isotopic composition of the contaminating phase is needed. Thus the composition of the detrital phases can differ substantially from the a-priori assumed bulk earth value, e.g., due to partial leaching effects, Th adsorption, alpha recoil or a non-silicate origin of the detrital phase prior to deposition (Hellstrom, 2006).

Stable isotopes:

Stable isotopes, specifically δ^{13}C and δ^{18}O, are commonly used as proxies for paleclimate reconstruction in speleothems (e.g., Boch et al. 2011; Wainer et al 2011; Couchoud et al. 2009; Spötl et al., 2006; Cruz Jr. et al. 2005a, 2005b). Moreover, they are also used as paleoclimate proxies in other paleoclimate archives.

The ^{18}O/^{16}O and ^{13}C/^{12}C isotope ratios (*R*) are usually given in the δ notation, which is

expressed by the deviation of the isotope ratio of the sample from that of a standard:

$$\delta = \frac{R_{sample} - R_{standard}}{R_{standard}}$$

(2.16)

The $\delta^{18}O$ and $\delta^{13}C$ values are usually given in per mil (‰) versus Vienna Standard Mean Ocean Water (VSMOW, mainly used for meteoric water) or Vienna Pee Dee Belemnite (VPDB, mainly used for carbonates).

Mass-dependent stable isotope fractionation allows the application of speleothem stable isotope ratios for paleoclimate reconstruction. In nature, the stable isotope ratios are not constant and vary with climate variability. This climate variability can be driven by climate cycles on teconical, orbital, millennial, sub-millennial and centennial time scales and is observed in various paleoclimate archives. Therefore, it is important to distinguish between different isotope fractionation types and processes.

According to Mook (2000), equilibrium isotope fractionation implies the establishment of constant isotope ratios between two phases. This, in turn, may imply that the relative isotope abundances are controlled by temperature. Thus, it was believed that only stable isotope ratios of spleoethems precipitated under equilibrium conditions would contain paleoclimate information (Hendy, 1971).

Kinetic isotope fractionation, however, is expressed by irreversible transition between two phases. Most stable isotope fractionation processes in nature are dominated by kinetic fractionation. Rapid degassing as well as evaporation may promote kinetic isotope fractionation in speleothems (Mickler et al. 2004).

Mickler et al. (2004) point out that stable isotope fractionation in speleothems may occur under equilibrium or kinetic (disequilibrium) conditions. Therefore, a test has been proposed to verify whether speleothem calcite was deposited under equilibrium or kinetic conditions. This so-called "*Hendy Test"* (Hendy 1971) is based on following key assumptions:

1. The $\delta^{18}O$ values remain constant along single growth layer.
2. No relationship between $\delta^{18}O$ and $\delta^{13}C$ along a single growth layer is visible.

However, Dorale & Liu (2009) question the key assumptions of the Hendy Test. In

recent publications it has been suggested that not only stable isotope values of speleothems that were deposited under equilibrium conditions but also stable isotope values of speleothems that were deposited under disequilibrium conditions may be used to reconstruct peleoclimate variability (e.g. Mühlinghaus et al. 2009; Scholz et al. 2009).

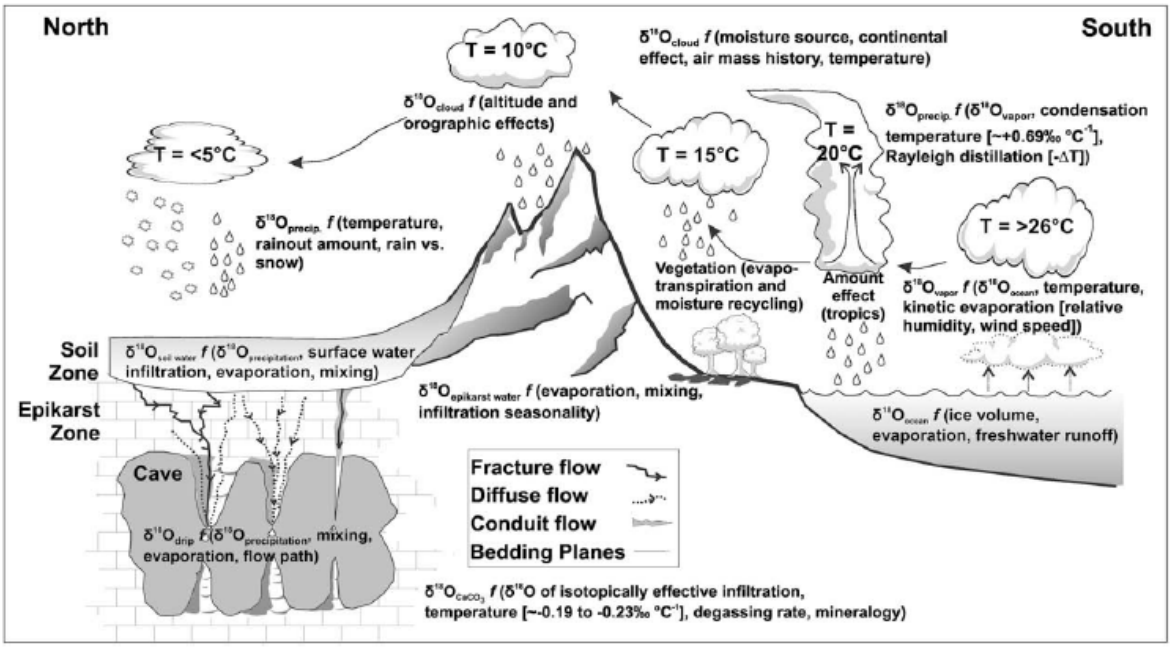

Figure 2.4: Figure adopted from Lachniet et al. (2009), which illustrates the primary processes affecting $\delta^{18}O$ variations in speleothems. It is indicated that the dominant driver of $\delta^{18}O$ variability is temperature and relative humidity as a function of changes in the ocean, atmosphere, hydrosphere, soil and epikarst zone.

The most important processes that influence the stable isotope signatures in speleothems are:

1. Atmospheric processes
2. Soil-related processes
3. Cave-related processes

$\delta^{18}O$

For $\delta^{18}O$, these processes are summarized in Fig. 2.4. Atmospheric processes only affect the $\delta^{18}O$ value of precipitation. These signals are affected by a large number of different effects such as *the ice volume effect, the altitude effect, the temperature effect, the*

continental effect and the amount effect (Lachniet et al 2009; Dansgaard 1964; Rozanski et al 1992).

In the following these processes are shortly described:

The ice volume effect:
The stable oxygen isotope value of the ocean is not stable on geological and orbital time scales. Thus, during the Quaternary, its $\delta^{18}O$ value varied between glacial-interglacial as well as between interstadial-stadial conditions as a consequence of changing ice volume in high northern latitudes.

The continental effect:
This effect is based on the isotopic depletion as a consequence of progressive rainout.

The latitude effect:
This effect explains the isotopic depletion ratios with increasing distance from the equator.

The altitude effect:
This effect points out that an isotopic depletion is related to increasing altitude.

The amount effect:
This effect describes an isotopic depeltion due to heavy rainfall. This effect is particularly important in monsoon-influenced areas where isotopic ratios become more depleted with increasing precipitation amount.

Other processes such as prior calcite precipitation (PCP) (Fairchild et al. 2000), changing evapotranspiration rates (Fohlmeister et al. 2012; Wackerbarth et al. 2010), and post-depositional diagenesis (PDD) may also influence the oxygen isotope composition of speleothems.

$\delta^{13}C$
The $\delta^{13}C$ value of speleothems is mainly influenced by soil related processes (McDermott, 2004). These processes include changes in pH, pCO_2, soil type,

temperature and changes in open/closed system conditions (McDermott, 2004).
The temperature and precipitation regime governs the type of vegetation, which in turn also controls the $\delta^{13}C$ composition in speleothems (McDermott, 2004; Baldini et al. 2005). However, one has to distinguish between the different plant types. C3 plants (trees and shrubs) have, in comparison to C4 plants (grasses), a different $\delta^{13}C$ signature. Therefore, the plant type population determines to a large extent the $\delta^{13}C$ value in the pedosphere and, thus, in speleothems (McDermott, 2004; Baldini et al. 2005). Drier and cooler climates favor a higher $\delta^{13}C$ value in speleothems (Fairchild, 2006).

Another potential driver of the $\delta^{13}C$ value of speleothems is kinetic isotope fractionation during calcite precipitation. Such effects are for example described by Mickler et al. (2004), Mühlinghaus et al. 2009 and Scholz et al. (2009).

Trace elements:
The incorporation of trace elements into speleothems underlies diverse processes (Fairchild and Treble, 2009). Trace element incorporation into speleothems can occur through three different processes:

1. During speleothem formation, cation exchange is leading to the exchange of Ca with other elements, such as Ba, Mg and Sr, and their incorporation into the crystal lattice of $CaCO_3$. In solution, Ca forms the bivalent cation Ca^{2+}. Thus, the cation exchange process leads to a substitution of Ca^{2+} with other bivalent cations, such as Ba^{2+}, Mg^{2+} and/or Sr^{2+} (Fairchild and Treble, 2009).
2. Closely related to that are elements, such as P, Na and F, which are incorporated into the crystal lattice of $CaCO_3$ by filling crystal defect points.
3. Some elements, such as Na and Cl may also be associated with aqueous inclusions in speleothems.

To relate solution and mineral composition for trace elements, the partition coefficient can be used (Morse and MacKenzie 1990):

$$\frac{c(Tr)}{c(Ca)}_{CaCO_3} = K_{Tr} \frac{c(Tr)}{c(Ca)}_{solution} \qquad (2.17)$$

In equation (2.17), *Tr* is representing the trace ion, while K_{Tr} indicates the partition (distribution) coefficient, which may also vary with increasing or decreasing temperature, precipitation rate, crystal structure and morphology as well as other aspects of solution composition (Fairchild and Treble, 2009).

It is important to mention that partition coefficients are different for aragonite and calcite. However, the Ca ion in the aragonite crystal lattice is substituted by larger bivalent cations, such as Sr (Terakodo & Masuda, 1988), while Mg trace element incorporation is less abundant in aragonite. Therefore, the Mg level decreases significantly when aragonite precipitation initiates (McMillan et al., 2005). Fig. 2.5 displays the possible pathways of trace element incorporation. Trace elements can be transported by solutes, colloids and particles. Higher concentrations of trace element in speleothems, which are transported by collides and particles, are expected during intervals of higher infiltration. However, Tooth and Fairchild (2003) point out, that trace element fluctuations based on a changing hydrology are not related to faster or slower flows. In contrast, these fluctuations may be related to the contribution of different aquifers with different porosity.

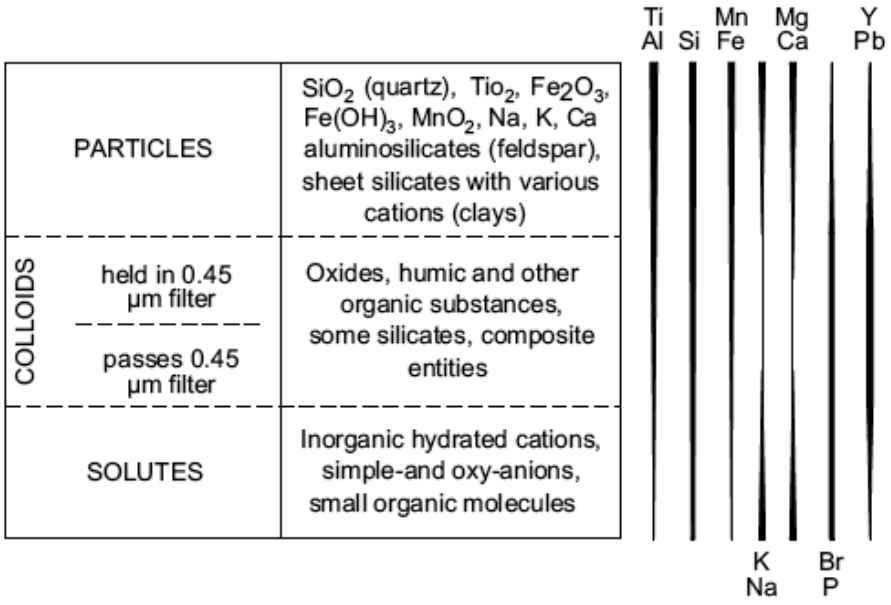

Figure 2.5: Adopted from Fairchild and Treble (2009), which indicates the possible transport modes of trace elements by particles, colloids and solutes in karstic waters.

Additionally, different sources may influence the composition of trace elements in speleothems (Fig. 2.6). Treble and Fairchild (2009) state that the most important source, that governs the geochemical composition of speleothems, is the geochemical hostrock composition. The soil and the epikarst zone, however, have the highest pCO_2 and, thus,

reflect the largest amounts of elements to the solution. In addition, the trace element signature of the speleothems is influenced by soil type, vegetation and the karstic aquifer. Secondary alteration, such as post-depositional diagenesis (PDD), can also influence the geochemical composition of speleothems (Fairchild et al. 2006; Fairchild and Treble, 2009).

Another important mechanism influencing the geochemical composition of speleothems is prior calcite precipitation (PCP). PCP occurs when saturated drip water enters an air-filled cavity, which has a lower pCO_2 than the drip water. As a consequence, the drip water becomes supersaturated and calcite precipitates prior to entering the cave. This will lead to an enrichment of Sr/Ca, Mg/Ca and $\delta^{13}C$ in the speleothems. PCP is a common process observed in speleothems and is related to dry climate periods (Fairchild and Treble. 2009).

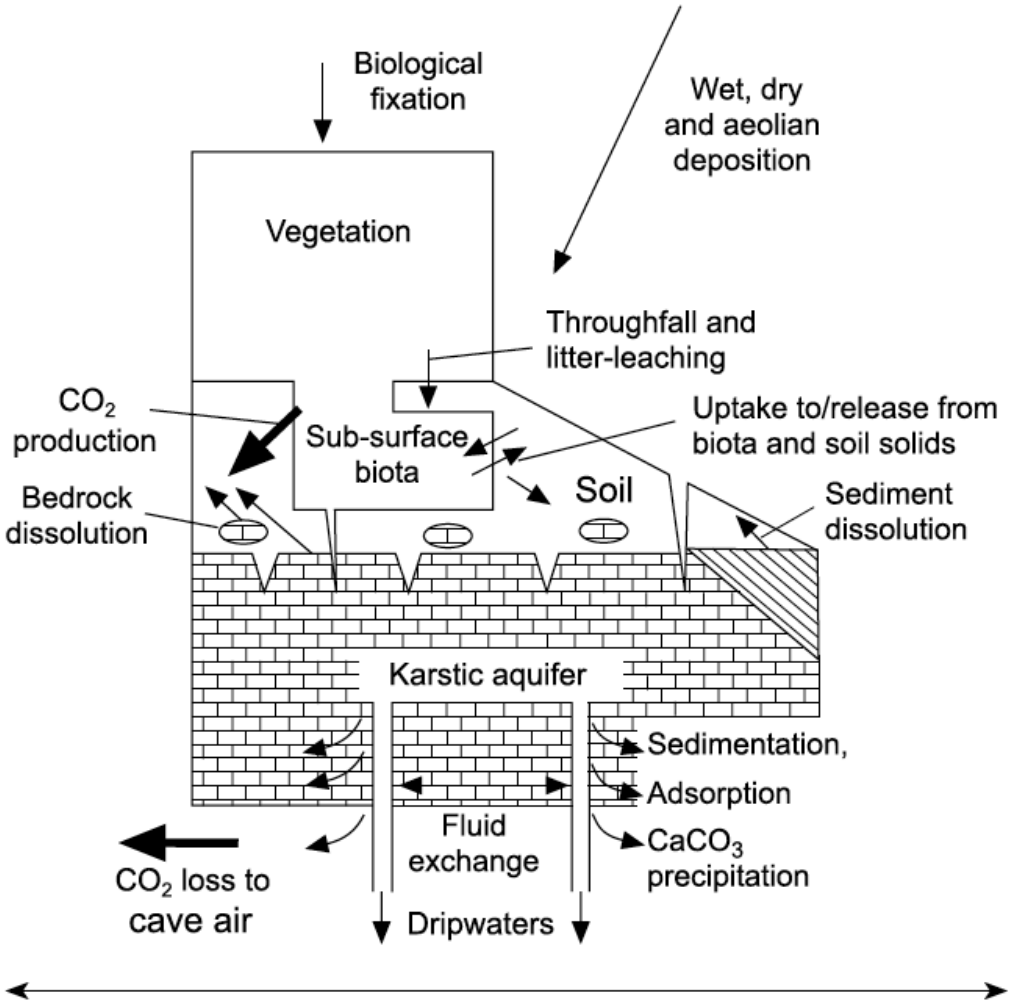

Figure 2.6: Adopted from Fairchild and Treble (2009). Schematic overview of the element sources and processes, which are involved in the deposition of different elements in speleothems.

2.3 Past climate variability

Depending on the specific research question and on the climate archive, it is possible to study past climate variability on different time scales. Specifically, past climate variability can be performed on tectonic, orbital and millennial to centennial time scales. For reconstruction of climate variability on tectonic time scales, the $\delta^{18}O$ record of benthic foraminifera in sediment cores can be used (e.g. Zachos et al., 2001; Lisiecki and Raymo, 2005). To reconstruct past climate variability on orbital time scales different climate archives can be used. For example past climate variation on orbital scale can be observed in sediment cores (e.g. Raymo and Lisiecki, 2005; Lea et al. 2000 or Martrat et al. 2007), in ice cores (e.g. Lüthi et al 2008; Jouzel et al. 2007; Wolff et al. 2010) as well as in speleothems (e.g. Drysdale et al., 2009; Feitmann et al., 2009; Cheng et al., 2009, 2012).

For reconstruction of past climate variability on millennial scales, also different climate archives such as sediment cores (e.g. Sirocko et al., 2005; Raymo and Lisiecki, 2005 or Bauch et al. 2011), ice cores (e.g. Capron et al. 2010b, 2012; Steni et al. 2010 or Landais et al. 2010), tree ring analyes (e.g. Esper et al 2010 or Cherubini et al., 1996) as well as speleothems (e.g. Boch et al. 2011; Mangini et al 2007; Bardertscher et al. 2011; Holzkämper et al., 2009 or Spötl et al., 2006) can be used.

For past climate reconstructions on centennial scale, observations on tree rings (e.g. Touret et al., 2009; Esper et al. 2010), speleothems (e.g. Meyer et al 2012) and in shells (e.g. Maurer et al., 2012 or Hallmann et al. 2012) can be used.

Here a short overview of past climate variability during the last 3 Ma is given followed by a more detailed in

troduction of different concepts of climate variability on millennial time scales as observed for the RBH stalagmites.

2.3.1 Climate variability over the past 3 million years

The Earth's climate is underlying cyclical changes that are coherent with changes of orbital configurations in time (Milankovitch, 1941). In the context of transitions between *glacials* and *interglacials* on orbital time scale, Milankovitch (1941)

introduced the following key terms, which are seen as orbital forces that drive climate change:

Eccentricity: The Earth's orbit describes a slow shift of its shape from nearly circular and gently elliptical within approximately 100ka. This cycle is predominant for the last 700 ka and, therefore, seen as the responsible driver of glacials and interglacials.

Obliquity (Tilt): The Earth's axial tilt varies between 22.1° and 25.5° with a periodicity of approximately 42ka. Prior to 700ka, ice ages occurred with a periodicity of 42ka and, therefore in dependency of obliquity.

Precession: The tendency of the Earth revolution to change the direction of motion of its axis in time. The earth describes such a cycle in about 23ka.

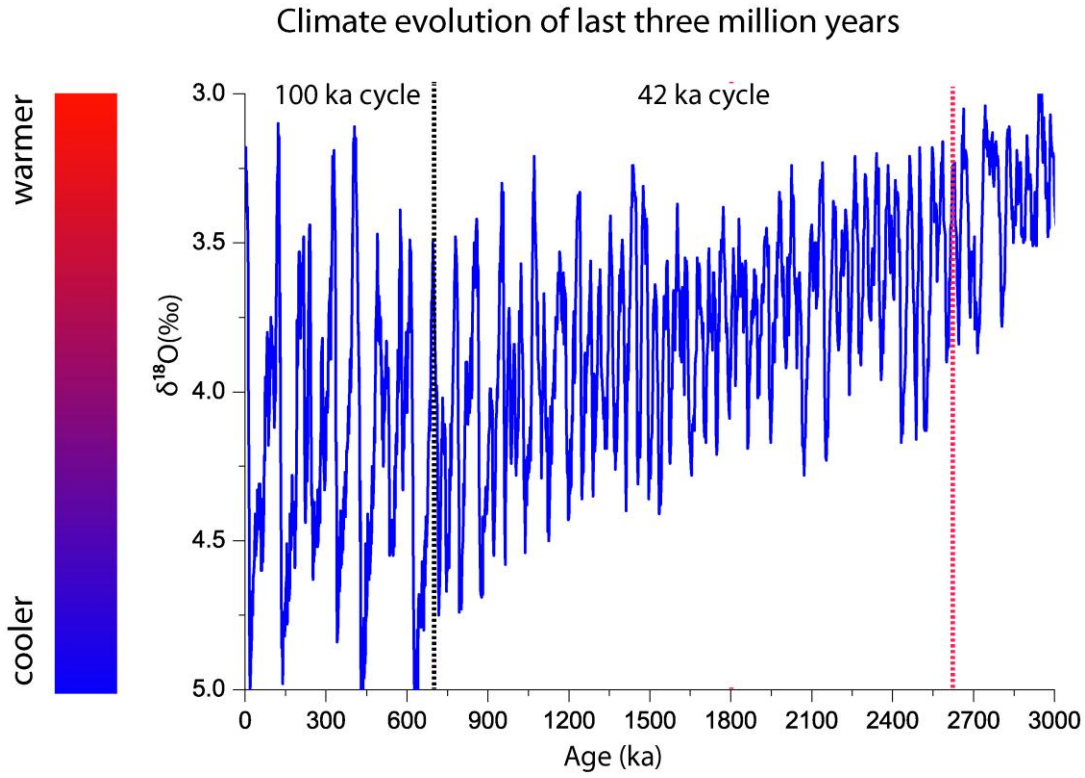

Figure 2.7: The benthic $\delta^{18}O$ LR04 stack of Lisiecki & Raymo (2005) displayed for the last 3Ma. Note that peaks of lower $\delta^{18}O$ values indicate warmer periods (interglacials and interstadials), whereas maximum $\delta^{18}O$ values indicate cooler periods of glacial or stadial maxima. The red dashed line indicates the inception of the Quaternary at 2.6 Ma, whereas the black dashed line indicates the Mid-Pleistocene climate transition.

Figure 2.7 exposes the $\delta^{18}O$ LR04 stack of Lisiecki & Raymo (2005), which reveals the cyclic global climate change of the last three million years and the transition from the Neogene to the Quaternary at approximately 2.6 Ma (red dashed line). The Mid-Pleistocene climate transition (Raymo et al. 1997) describes the shift from the 42 ka ice age cycles to the 100 ka cycles as indicated by the black dashed line. However, the cause for the transition between both cycles remains an open question.

In Figure 2.7, lower $\delta^{18}O$ values represent warmer phases in time, i.e., so-called interglacials or interstadials, while higher $\delta^{18}O$ signatures represent cooler time periods, which indicate so-called glacial or stadials. Here, a general shift from shorter intervals of warmer periods to longer and cooler periods can be observed. This cooling might be related to the emergence of the Isthmus of Panama at 2.75 Ma (e.g. Lunt et al. 2007; Maier-Raimer et al. 1990), which is seen as the trigger of arctic glaciations because the Gulf Stream was redirected to high northern latitudes transporting enough humidity for precipitation. Thus a closer look into climate change of the last three million years does not only reveal climate change on orbital time scales (i.e. change from a 42 ka cycle to 100 ka cycle) but also global climate change on tectonic scales.

2.3.2 Climate change observed for the last 800 ka

After the Mid-Pleistocene climate transition, the glaciations were driven by eccentricity resulting in a 100 ka cycle, which can be also observed in Figure 2.8.

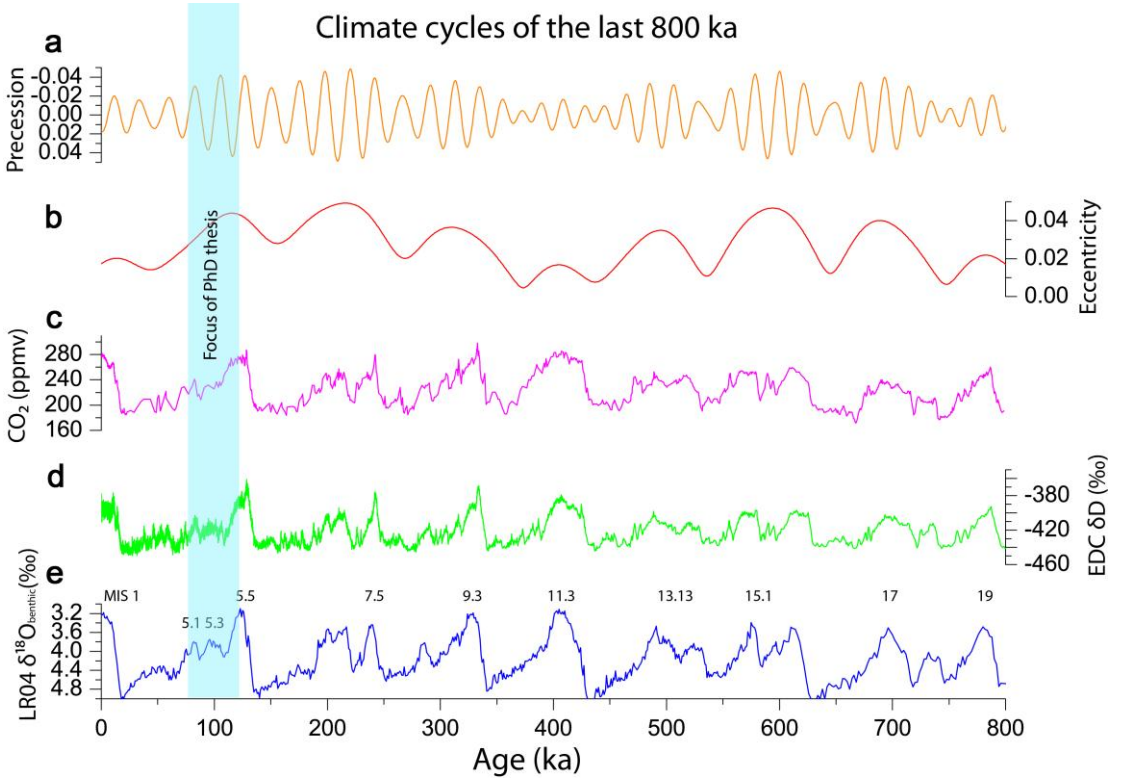

Figure 2.8: Figure 2.8 reveals the compilation of the LR04 stack (Lisiecki & Raymo, 2005) with the δD (Jouzel et al. 2007), the CO_2 record of the EPICA ice core (Lüthli et al. 2008) and the precession and eccentricity (Berger & Loutre, 1991) for the last 800 ka (MIS 19-1).

After 700 ka BP, the interglacials occur within a periodicity of 100 ka and are expressed by distinct shifts from relatively low to relatively high CO_2 values, steep increases in δD from comparatively negative to less negative values and pronounced swings in $\delta^{18}O$ from rather high to rather low values. All these distinct shifts arise at times of highest eccentricity and lowest precession configurations. Thus, including the Holocene, nine pronounced Interglacials are for example observed in the EPICA ice core (EPICA community members, 2004) as well as in the LR04 stack (Lisiecki and Raymo, 2005) as displayed in Fig. 2.8. These pronounced warm periods are separated from each other by eight distinct glacial periods, which were driven by the 100 ka eccentricity cycle. Thus, Fig. 2.8 reveals orbitally forced long-term climate variability.

2.3.3 Potential mechanisms of Greenland Interstadials (GIS) and millennial to submillennial climate variability during MIS 5

In chapter 2.3.1 and 2.3.2, climate variation on tectonic and orbital time scales has been shown. Here, the most common concepts of millennial scale GIS variability are shortly introduced and displayed.

During the last glacial, spanning a time period from MIS 5d to MIS 2, rapid climate shifts from relatively cold (*stadials*) to relatively warm (*interstadials*) periods, can for example observed in the NGRIP ice core (NGRIP community members, 2004). For the last glacial (115-14ka) 25 of these rapid climate shifts are observed, which were first detected by Dansgaard et al. (1993). Such intra-climatic variations are known as the Greenland Interstadials (GIS).

The focus of this PhD thesis is on stalagmite growth periods observed during the Last Interglacial (MIS 5e) and the early glacial period (MIS 5d-a). Hence, here it is postulated that the growth periods observed during MIS 5d-a in RBH stalagmites are related to the pronounced GIS 25 to 19 (compare Figure 2.8). The following paragraph gives an overview of the most common approaches, which explain the rapid climate shifts (GIS).

The GIS are characterized by Ganopolski & Rahmstorf (2001) as periods of an abrupt warming within a few decades, followed by a warm plateau phase, a gradual cooling phase and a rapid cooling at the end of each GIS. During MIS 5d-a, these GIS observed in NGRIP are associated with rapid increasing temperatures of 2 to 16.5°C +/- 2.5°C (Landais et al., 2004, 2006; Capron et al., 2010, 2012).

Figure 2.8 displays the $\delta^{18}O$ curve of the NGRIP ice core (NGRIP members, 2004) on the GICC05modelext time scale (Wolff et al. 2010) plotted with sea level (Martinson et al., 1987) and the July solar insolation curve at 65°N (Berger and Loutre, 1991) for the time period of 125 to 65 ka. Pronounced peaks detected in the NGRIP $\delta^{18}O$ record display the Last Interglacial (Eemian, MIS 5e) or the GIS (25-19), which are dedicated to be warmer periods.

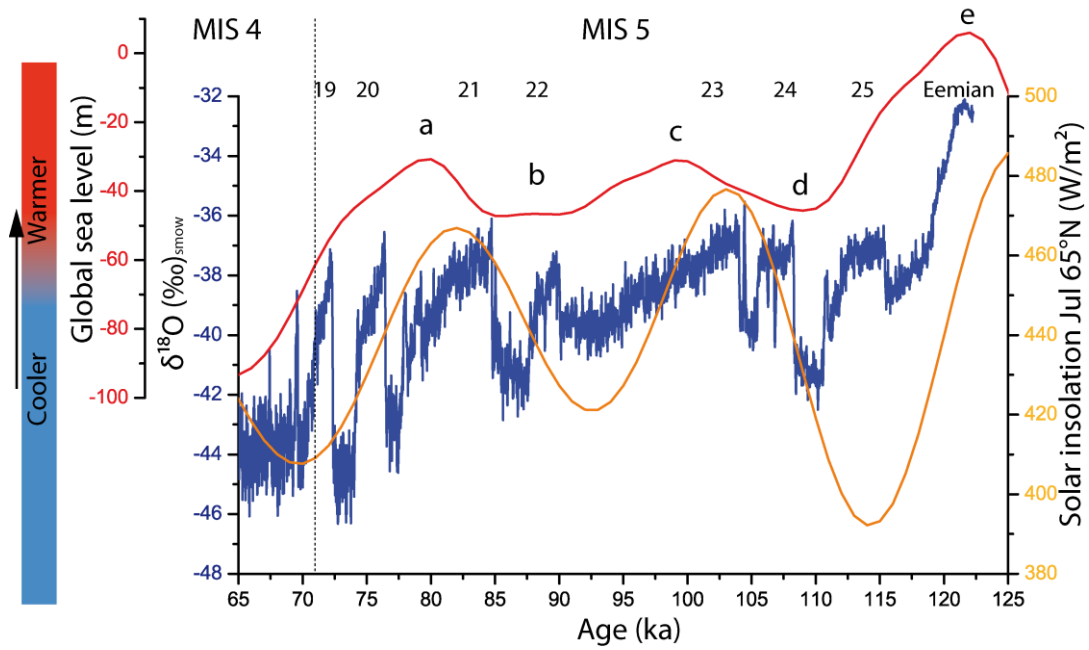

Figure 2.9: Figure 2.9 displays the $\delta^{18}O$ curve of the NGRIP ice core shown in blue (NGRIP community members, 2004) for time period of 125 to 65 ka plotted together with sea level variations displayed in red (Martinson et al., 1987) and the July solar insolation curve at 65°N indicated in orange (Berger and Loutre, 1991). Pronounced peaks detected in the NGRIP $\delta^{18}O$ record display the Last Interglacial (Eemian, MIS 5e) or the GIS (25-19), which are dedicated to be warmer periods. The letters e-a are indicating the substages of MIS 5, whereas a, c and e represent warmer periods with sea level high stands, b and d are substages of cooler climate periods with sea level minima.

The GIS are often seen to be triggered by the intensity and extent of sea ice formation (Wang and Mysak, 2006), ice sheet size controlling iceberg discharge (MacAyeal, 1993) or orbitally forced July solar insolation changes at 65°N (e.g. Loutre and Crucifix, 2002), which in turn triggers the reorganization of the Atlantic Meridional Overturning Circulation (AMOC).

Rahmstorf (2002) postulates that the GIS are triggered by transitions of the Atlantic Ocean circulation, which in turn originates from stochastic resonance. In the model of Ganopolski & Rahmstorf (2001), the transition from a cold to a warm mode is triggered by decreasing freshwater input in high northern latitudes as displayed in Fig 2.10. As a result, a movement of warm, salty Atlantic water occurs that cools down in high northern latitudes, sinks down and triggers convection (A). According to the authors, the transition back to the cold mode (B) is established when a specific threshold is reached where convection in high northern latitudes stops. During the “off mode” (C), the NADW (North Atlantic Deep Water formation) is almost shut down, and Antarctic water fills the Atlantic Basin (Rahmstorf 2002). The “off mode” is represented by

Heinrich Events, which are associated with pronounced cold phases and IRD layers in sediment cores (e.g. Chapman et. al. 1999).

The model of Ganopolski & Rahmstorf (2001) can be combined with an additional model of Braun et al. (2008), which assumes that the GIS might be related to quasi-periodic solar forcing plus noise. However, there are no proxies in any climate archives revealed that give a sufficient evidence for the model of Braun et al., (2008).

Broecker (2003) sums up that the GIS are most likely related to a reorganization of the AMOC, which in turn is a function of seawater density, salinity and freshwater input into the North Atlantic Ocean. In addition, the length of each GIS might be associated in turn with the orbitally forced July insolation intensity at 65°N and sea level high stands (Capron et al. 2010a).

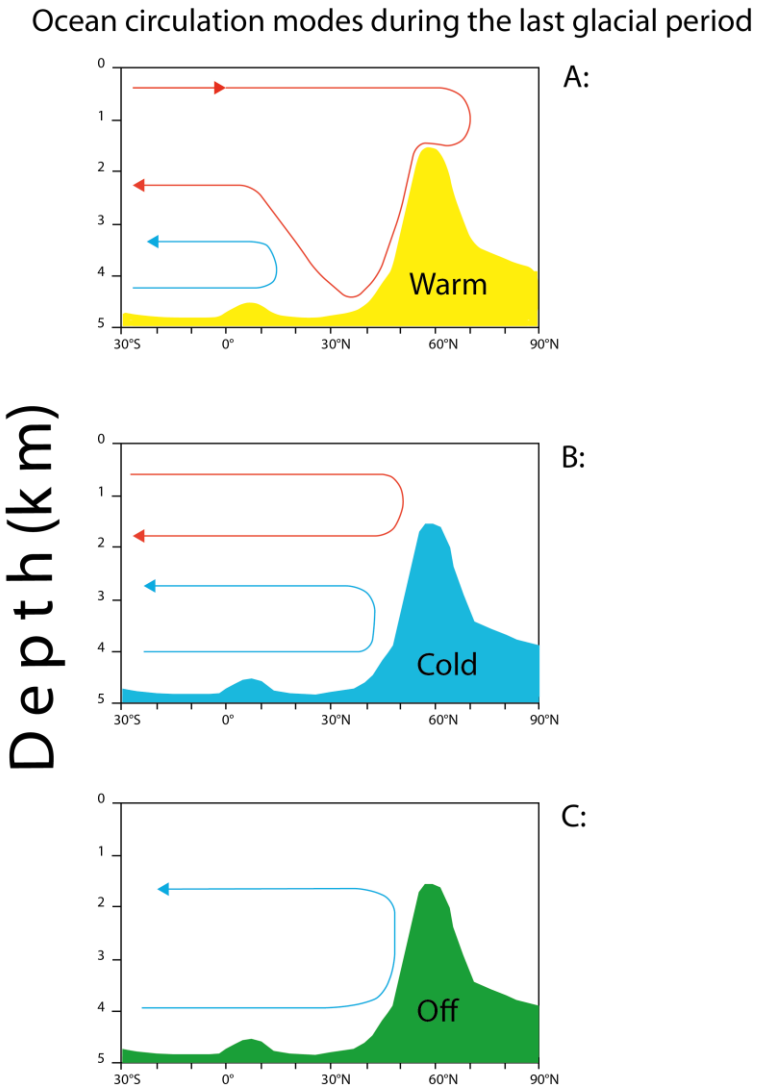

Figure 2.10: Figure adopted from Rahmstorf (2000) indicating the three modes of ocean circulation. Mode A: Ocean circulation mode during interglacial conditions. Mode B: Ocean circulation mode during glacial conditions. Mode C: Ocean circulation mode during Heinrich events.

3. Material and methods

3.1 Location and geological setting

3.1.1 Geographical setting

The Riesenberghöhle (RBH, 52° 12´ N, 9° 21´ E, 260-270 m above sea level) is located in the Süntel, which is part of the east-west trending Weser Hills, Germany (Fig. 3.1 map: A). It is one of the northernmost flowstone and stalagmite caves in Germany and is developed in Jurassic limestone. Figure 3.2 shows the geological map of lower Saxony and indicates the cave location (red box).

Figure 3.1 map: B shows a selected section of the Topographische Karte 25 (TK 25) Kathrinhagen to demonstrate the extension and location of the Riesenberghöhle as indicated in the red box. A map Riesenberghöhle (RBH) itself is shown in Fig. 3.1 map: C. The red dots in the map show the location of the stalagmites retrieved for this PhD thesis.

The climate of the area is relatively wet throughout the year, with an average annual precipitation of 720 mm and a mean annual temperature of 9.2°C (Deutscher Wetter Dienst (DWD), mean values between 1961 and 1990, derived from the meteorological station Hameln), reflecting the typical humid-temperate climate in northern Germany influenced from the North Atlantic Ocean.

The RBH stalagmites were retrieved by local cavers and subsequently stored in the Deutsches Archiv für Sinterchronolgie (DASC), which is an archive located in Langenfeld (Weser Hills region) providing stalagmites for scientific research.

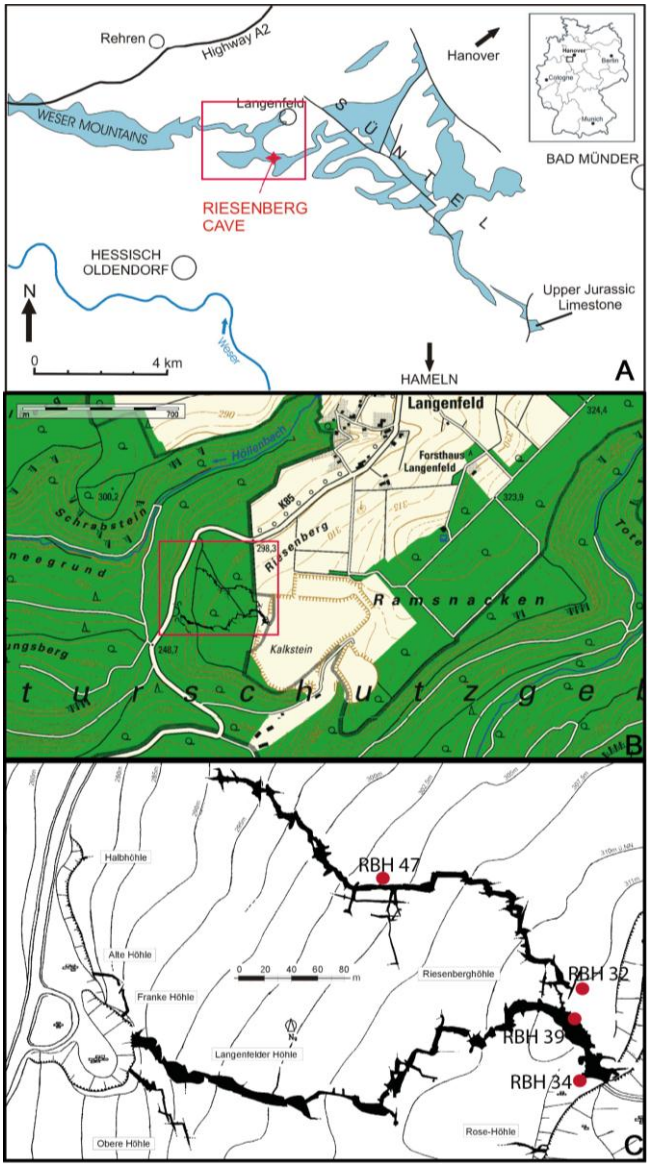

Figure 3.1: Overview of research site. Map A: Adopted from Richter et al. (2012), overview of the cave location in Germany (Süntel, Weser Hills). Map B: Selected section of topographic map 1:25000, 2018 Kathrinhagen. The red box is locating the cave location. Map C: Cave map of the Riesenberghöhle (RBH) and location of RBH stalagmites studied in this thesis. The investigated RBH stalagmites are indicated with red dots.

3.1.2 Geological setting

The host rock of the RBH consists of coral oolite that was deposited during the upper Jurassic on top of the Ornaten mudstone (Grupe, 1933; Schülke, 1993). The RBH is a relatively shallow cave with one vertical level and has an extension of approximately 1127 m. The host rock above the cave reaches a thickness of 30-45 m. The soil cover

consists of cambisols, the vegetation is a beech forest. The cave had no natural entrance in the past and was therefore, only weakly ventilated.

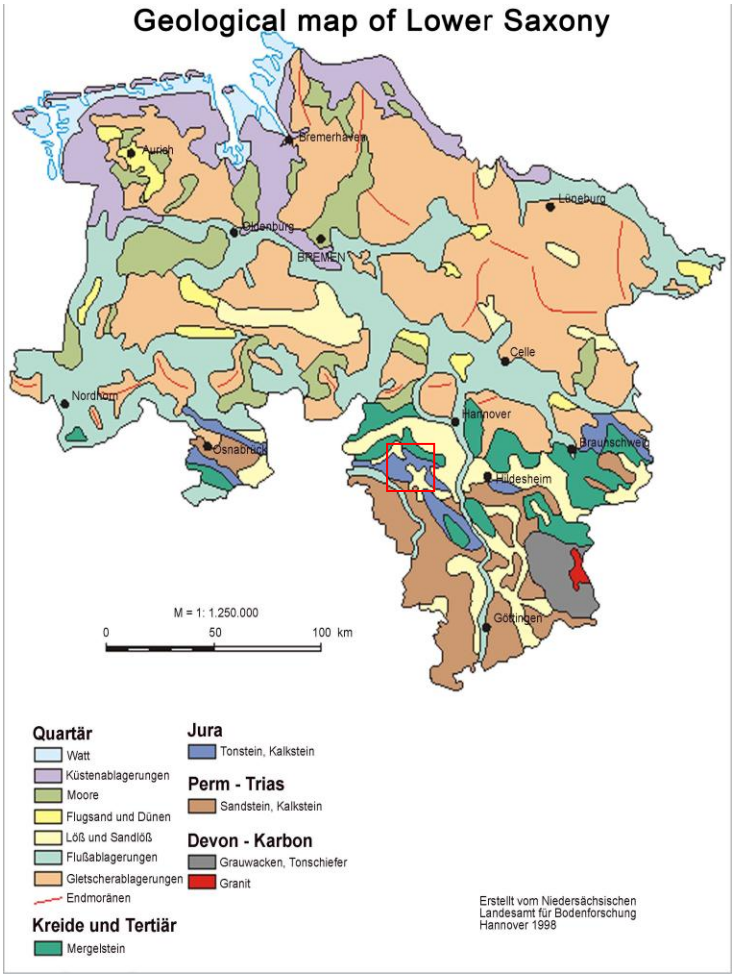

Figure 3.2: Adopted from Landesamt für Bodenforschung, Lower Saxony, Hannover (1998). The red box indicates the location of the Weser Hills.

As illustrated in Fig. 3.3, the Riesenberghöhle is located within a layer that belongs stratigraphically to the lower coral oolite formation, which was deposited during the Upper Jurassic (Grupe, 1933).

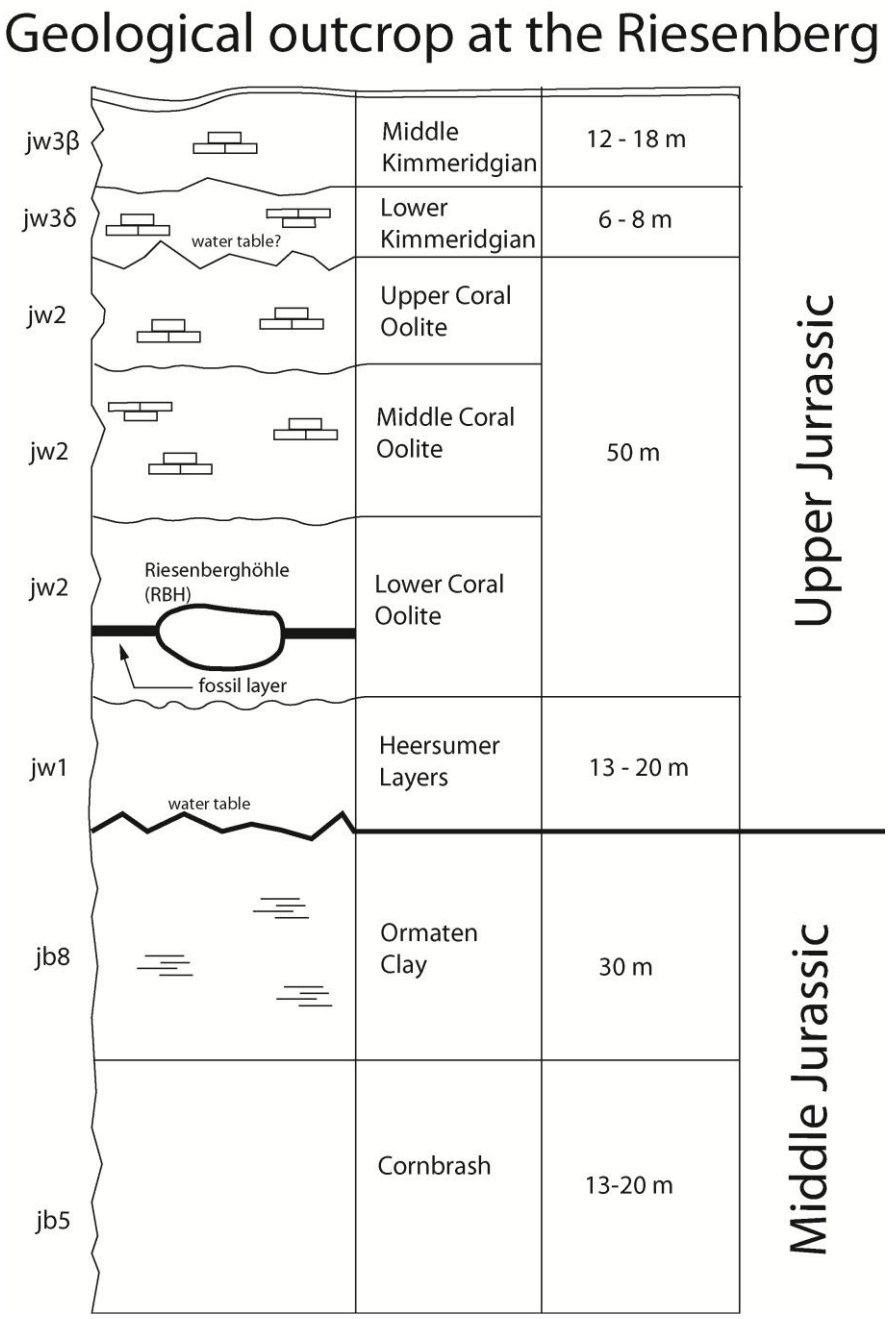

Figure 3.3: Figure adopted and modified from Grupe (1933). Geological layers above and below the RBH. Note that today the lower coral oolith layer is at the bottom of large outcrop, which was cleared by a mining company.

Figure 3 and 4 show the different geological layers in an outcrop scheme (Fig. 3.3) and as a cross section (Fig. 3.4). The description of the subsequent layers is adopted from Grupe (1933).

The ***Cornbrash (jb5)*** formation represents the oldest layer and was deposited during the middle Jurassic. It consists of ferrous calcareous massive banks with individual clayey intercalations. This sequence is followed by ***Ornaten Clay (jb6-8)***, which describes dark, marly, sometimes sandy clay shale with partly larger nodule deposits. The

Heersumer Layers (jwi) describe the subsequent layers and belong to the upper Jurassic. Dark calcareous sandstone intercalations of sandy merl clay are typical for this layer type. The ***Coral Oolite (jw2)*** represents the subsequent layer and is characterized by massive oolite calcite banks with individually weak Hematite beds. In this layer also represents the Riesenberghöhle has developed. The next layer is represented by the ***Lower Kimmeridgian (Jw3α)*** formation and is characterized by a layer of calcite, marl calcite clay, marl, clay and sandstone. The ***Middle Kimmeridgion (jw3β)*** represents the top of the outcrop and is characterized by solid calcite banks, marl calcite, marl, clay and sandstone.

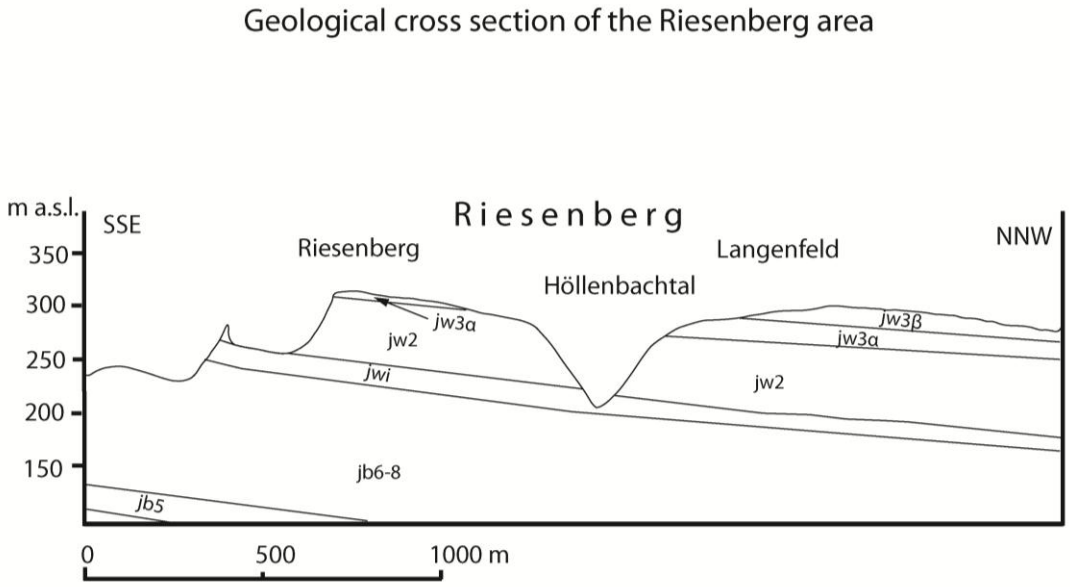

Figure 3.4: Geological cross section of the Riesenberghöhle Area. Figure modified from Grupe (1933).

3.2 RBH stalagmites

Four stalagmites were chosen from the DASC (Deutsches Archiv für Sinterchronologie, Langenfeld) for paleoclimatic and investigated at the Johannes-Gutenberg-University of Mainz (preparation for: U-series dating, trace elements and stable isotopes, thin section analysis), Max-Planck-Institute for Chemistry, Mainz (U-series dating and trace element analysis), CENIEH, Burgos (U-series dating) and at the University of Innsbruck (stable isotope analysis).

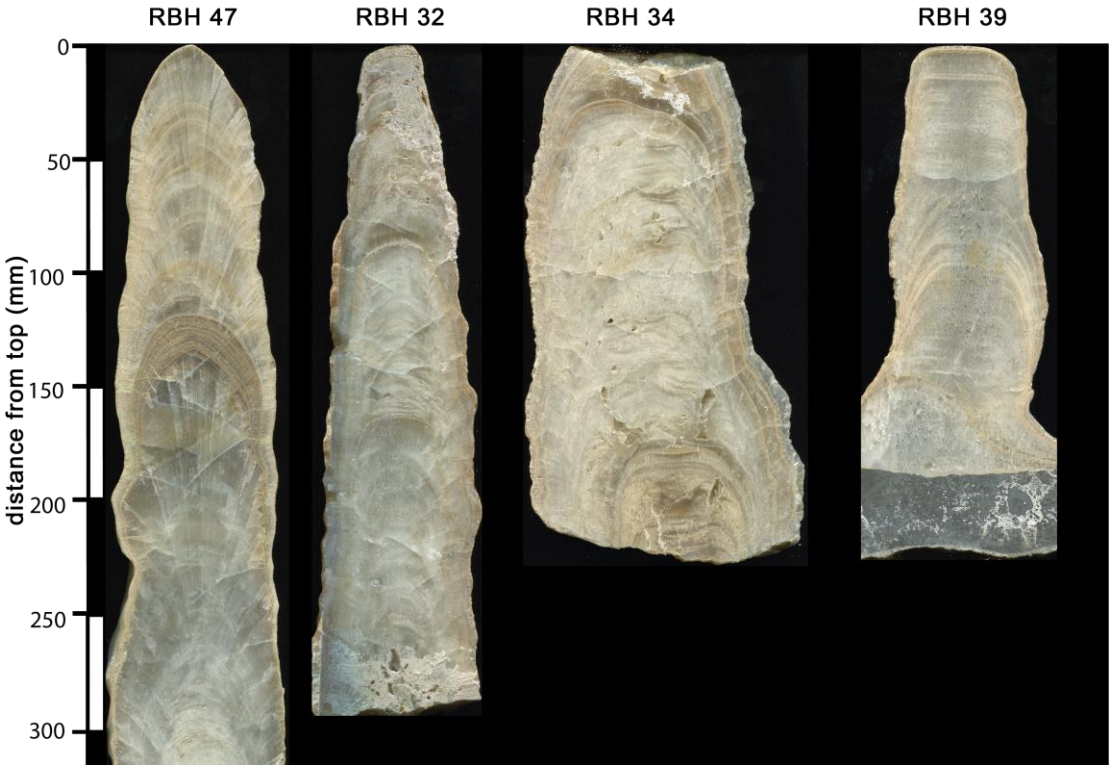

Figure 3.5: Overview of the stalagmites studied in this PhD thesis. From left to right: Stalagmite RBH 47 (310mm), stalagmite RBH 32 (285mm), stalagmite RBH 34 (224mm), stalagmite RBH 39 (195mm).

The stalagmites RBH 32 (285mm), 34 (224mm) and 39 (195mm) were located close to each other, whereas stalagmite RBH 47 (310mm) was retrieved from a different part of the cave (compare Figure 3. 1 map: C). These stalagmites are shown in Fig. 3.5.

Figure 3.6 provides an overview of the sampling strategy. Note that for sampling reasons all stalagmites have been cut along their growth axis. One half was preserved for Th/U dating, while the other half was used to sample trace elements and stable isotopes.

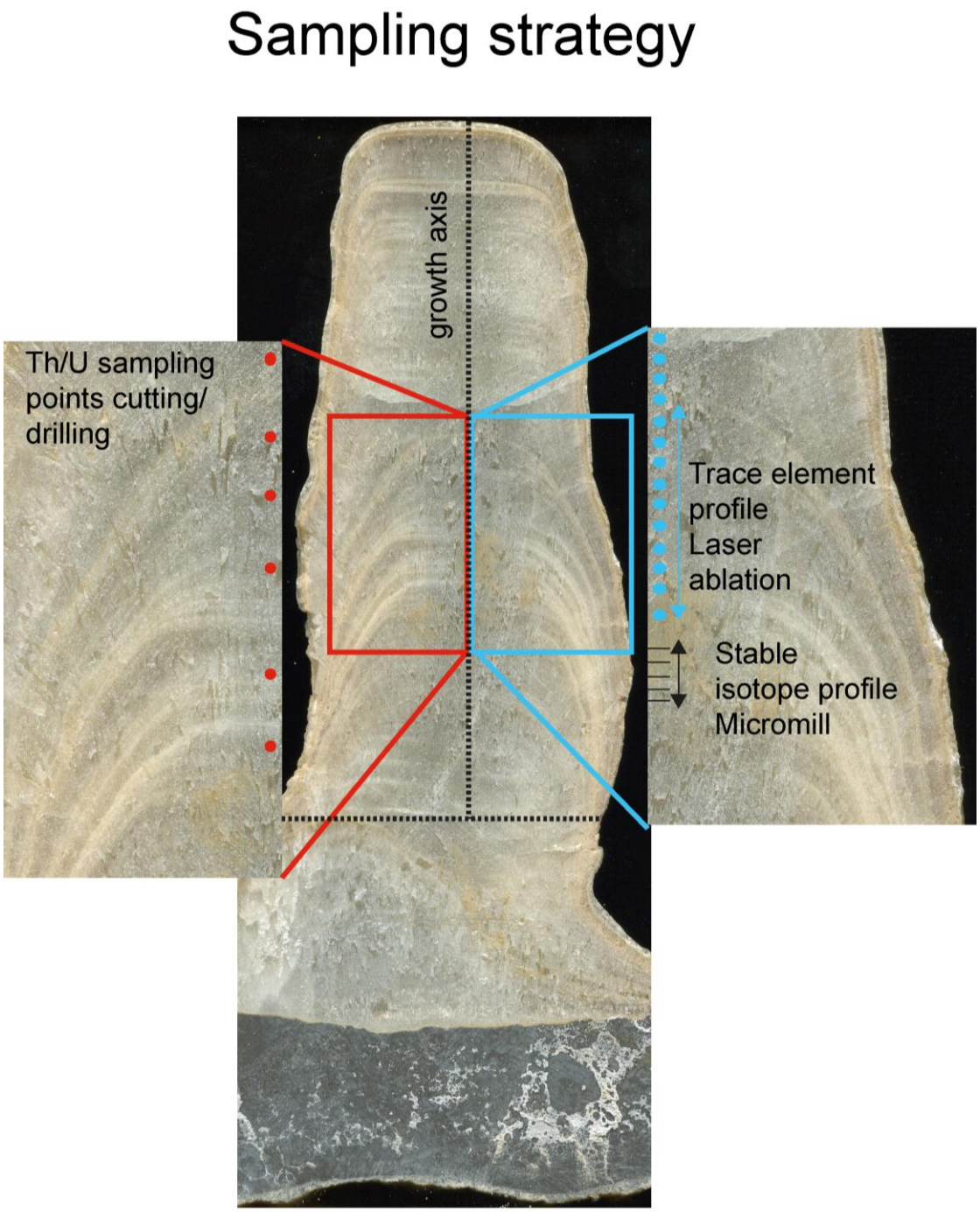

Figure 3.6: Sampling scheme for the RBH stalagmites, here exemplarily shown for stalagmite RBH 39. All stalagmite samples were taken along the growth axis of each stalagmite. Thus, stalagmites were cut into two halves (sample half and archive half) and then cut again along the growth axis on one half Th/U dating was performed on the other half, stable isotope and trace element samples were taken.

3.3 U-series dating method

3.3.1 Sampling strategy and sample preparation

Sub-samples for U-series dating (50-100mg) were drilled as powders or cut as small pieces along the growth axis of RBH stalagmites. Sample preparation was similar as described in Hoffmann et al. (2007). Dating was performed by MC-ICPMS at the Max-Planck-Institute for Chemistry (MPIC), Mainz, Germany, and at CENIEH, Burgos, Spain. The first samples were taken from the base and top of each stalagmite in order to estimate the whole duration of stalagmite growth. These first samples were prepared and measured at CENIEH. Further samples were taken above and below visible growth layers in order to assess the growth of specific periods and their timing, in individual stalagmites.

Prior to further preparation, the surface of the samples was purified by brief leaching in suprapure 0.1 N HNO_3 and dried. Then the samples were dissolved HNO_3, before the Th/U solution was added. Column chemistry was applied to separate the Th and U fractions. Columns were filled with ion exchange resin, and several column steps were performed. After both fractions have been separated, each fraction was dissolved in 2ml of 0.8 N HNO_3 and ready for analysis for *Multi Collector ICP Mass Spectrometry*.

3.3.2 The Nu MC-ICPMS

The Th/U measurements were performed using a *Multi Collector Inductively Plasma Mass Spectrometer (Nu Plasma, MC-ICPMS)* designed in Nier Johnson geometry. The Nu Plasma, MC-ICPMS uses a variable mass dispersion “zoom lens” to direct ion beams into a fixed arrangement of twelve Faraday cups (for higher masses) and three ion counters (IC) to measure lower intensities (Hellstrom, 2003). Here, a short description of the basic principles of MC-ICPMS will be given (compare Fig. 3.7). For a more detailed description see for example Goldstein and Stirling (2003).

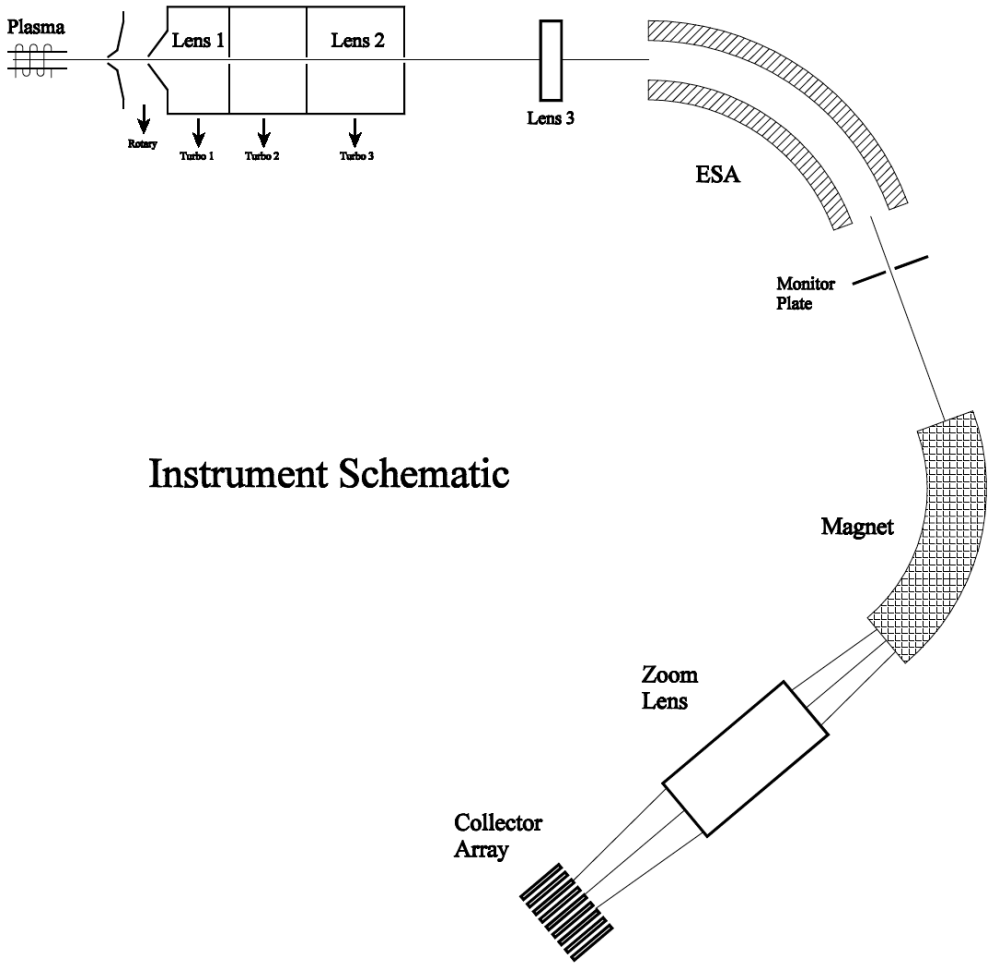

Figure 3.7: Nu Plasma MC-ICPMS instrument scheme. Adopted from Nu Instruments.

The sample solution was induced into the system with a CETAC Aridus desolvating nebulizer system (Goldstein and Sterling, 2003). In the Aridus, the solution is transformed into a dry aerosol in the spray chamber.

Then, the aspirated sample is transported as a dry aerosol by the Ar carrier gas into the center of the torch. Here, the sample becomes immediately dissociated and ionized due to the hot (≈6000K) temperature of the surrounding Ar plasma (compare Goldstein and Sterling, 2003). At the cones most of the samples are lost. Behind the skimmer cone, a series of ion lenses focus the ions optically onto the entrance slit into the ESA (Electro Static Analyzer) unit. The ESA is an energy filter that focuses the analyte ions and leads them into a magnetic field. The magnetic field separates all ions depending on a specific mass-to-charge ratio and allows them to access the detection system, led by further of zoom lenses.

3.3.3 The measuring program and data correction

Prior to the measurements, the instrument was tuned in order to establish highest intensity (1) and to maintain optimal peak shapes (2).
For the establishment of highest intensities (1), a U-standard solution was used. To provide the best peak shapes (2), the quad values were adjusted using a Th-standard solution (containing the ^{229}Th spike) and a U-tune-mix solution for Uranium containing both ^{233}U and ^{236}U.

For optimal results for U and Th measurements the following masses were tuned:

Uranium:
1. H1 = ^{238}U L2 = ^{235}U IC0 = ^{234}U (intensity, peak shape).
2. H2 = ^{238}U Ax = ^{236}U L1 = ^{235}U IC0 = ^{233}U (peak shape with U-tune-mix solution).

Thorium:
1. H1 = ^{238}U L2 = ^{235}U IC0 = ^{234}U (intensity)
2. Ax = ^{232}Th IC0 = ^{229}Th (peak shape)
3. L1 = ^{232}Th IC0 = ^{230}Th (peak shape)
4. IC0 = ^{232}Th (peak shape)

Analytical MC-ICPMS procedures in the laboratories in Mainz and Burgos involve a standard-sample bracketing procedure to derive correction factors for mass fractionation and Faraday cup to ion counter gain as described in Hoffmann et al. (2007). All samples and standards had to be corrected for: dark noise (background noise), tailing in the U fraction, mass fractionation and yield.

- **Dark noise (background):** Prior to each analysis the dark noise is the background noise, which is always measured. It is an interfering voltage measured on the both ICs and Faraday cups. Thus, it must be subtracted from the measured signal.

- **Tailing:** The mass of ^{234}U is so low that it can only be measured on the ion counters. During the measurements the tail of the relatively large peak of ^{238}U superimposes the signal of ^{234}U. Therefore, the tail must be calculated and subtracted from the measured signal of ^{234}U.

- **Mass fractionation factor:** All isotopes undergo mass spectrometer specific mass-fractionation-processes. Therefore, a mass fractionation factor has to be calculated, which is used to correct all measured ratios.

- **Yield:** The yield is the amplification factor of the ion counter, which connects the signal of the Faraday Cups with that of the IC.

Once the optimal intensities and peak shapes were established, the samples were screened for the intensity of the isotopes of interest and the spike intensity expected for the sample. Therefore, we screen each fraction separately. The IC and Faraday Cup arrangement where:

1. ^{232}Th on the axial (Ax) and ^{229}Th on the Ion Counter 0 (IC0) for the Th fraction and ^{230}Th on the IC0.
2. ^{238}U on the Faraday Cup H2, ^{236}U on the axial cup (Ax) and ^{233}U on the IC0.

The background noise is estimated by measuring on half masses (e.g. $^{234.5}U$) on the cups and the ICs in a cycle prior to measurements of the sample or standard, which is called the "Zero". The resulting signals were subtracted from the measured signals, in a first correction step. For the different measuring programs, different *magnet delay* times and *integration times* have been used. The magnet delay time describes the time needed for the magnet sector field to reestablish after a mass jump, and thus reflects the time where no signals can be measured. The integration time is the time applied to measure the masses during one single cycle. Usually 50 cycles have been measured.

The individual measuring program of each fraction are described as follows (compare Table 3.1):

U-standard:

The configuration used a magnet delay time of two s including integration times of 60s (zero) and 4s (cycle 1). For cycles 2 and 3, a magnet delay time of 1s was applied.

U-sample:

Depending on the ^{238}U signal in the sample the U fraction must be diluted or can be measured directly. If the measured signal is higher than 8V, the sample fraction must be diluted, if it is lower than 8V the solution can be measured directly. For all measurements, a program configuration with a magnet delay time of 2s including integration times of 60s (zero) and 4s (cycle 1 and 2) were used.

Th-standard:

The Th standard is measured using the same Cup/IC arrangement as used for *Th-static* program including the same integration time and magnet delay times.

Th sample:

Depending on the ^{232}Th intensity, two different programs were applied. If the ^{232}Th signal above is 5mV, the measuring program *"Th-static*" was applied. If the measured signal is below 5mV the measuring program *"Th-jump"* was applied (compare table 3.1).

Th-static:

The measuring program *Th-static* implies that the signal of ^{232}Th is large enough to be measured on Faraday Cups. Thus ^{232}Th on the Ax (cycle 1) and the L1 (cycle 2) Faraday Cup. In addition, a magnet delay time of 2s and integration times of 60s (Zero) and 4 s (cycle 1 and 2) were applied.

Th-jump-sample:

The measuring program *"Th-jump"* implies that the masses ^{229}Th, ^{230}Th and ^{232}Th are measured in three different cycles on the IC0. Here, a magnet delay time of 0.5s and integration times of 30s (zero), 4s (cycle 1 and 2) and 1s (cycle 3) were used.

Table 3.1: Nu MC-ICPMS Faraday Cup and Ion Counter arrangement for sample and standard measurements of Thorium (Th) and Uranium (U) during the different cycles. Note that H2, H1, Ax, L1 and L2 are Faraday Cups, while IC0 is an Ion Counter.

	Cycle	H2	H1	Ax	L1	L2	IC0
Thorium-STD	Zero			$^{232.5}$Th	$^{231.5}$Th		$^{229.5}$Th
	1			^{232}Th			^{231}Th
	2				^{232}Th		^{232}Th
Thorium- Sample jump	Zero						$^{230.5}$Th
	1						^{229}Th
	2						^{230}Th
	3						^{232}Th
Thorium-Sample static	Zero			$^{232.5}$Th	$^{231.5}$Th		$^{229.5}$Th
	1			^{232}Th			^{229}Th
	2				^{232}Th		^{230}Th
Uranium- STD	Zero		$^{237.5}$U			$^{234.5}$U	$^{233.5}$U
	1		^{238}U			^{235}U	^{234}U
	2						$^{233.5}$U
	3						$^{234.5}$U
Uranium Sample	Zero	$^{238.5}$U	$^{237.5}$U	$^{236.5}$U	$^{235.5}$U	$^{234.5}$U	$^{233.5}$U
	1		^{238}U		^{236}U	^{235}U	^{234}U
	2	^{238}U		^{236}U	^{235}U		^{233}U

To assure highest quality and sample purity intensive wash out times have been performed after each standard and applying the following wash-out protocol:

1. MQ H_2O
2. Mixed solution of 0.8N HNO_3 and 0.05N HF
3. 0.8N HNO_3

3.3.4 Potential errors

Here all potential errors are described in detail. However, a careful, accurate and precise sample handling regarding the sample preparation as well as the chemical sample treatment, was performed. This, of course, is self-evident for all work performed in a

chemical laboratory. Thus, here most of the errors, described in this chapter, could be avoided.

However, errors may arise, which will lead to imprecise and inaccurate Th/U-ages. These errors can be threefold:

1. *Potential errors during the sampling procedure.*
2. *Potential errors, which may occur during chemical procedures, e.g. column chemistry.*
3. *Potential errors during MC-ICPMS measurements.*

During the sample-taking procedure it is possible to produce mixed Th/U-ages. Such ages will appear whenever samples are taken along visible growths layers or when a single sample is cut representing a small part above and below the growth layer. Such errors can be easily avoided using a hand-held drill, drilling the samples closely above and below visible growth layers. However, some stalagmites reveal a very complex microstructure. Thus, sampling these stalagmite sections will enlarge the potential to produce mixed Th/U-ages.

Furthermore, it is indispensable to investigate the stalagmite for diagenetically altered fabrics via thin section analysis and to avoid sampling these sections. Diagenetically altered sections will lead to altered Th/U-age, which may be reflected as age inversions.

During *chemical procedures*, mistakes may arise that also possibly lead to incorrect Th/U-ages. For instance, some of the sample might be lost during dry down steps between column chemistry when sample beakers are overheated and as consequence some quantities of the sample jump out of the beaker. Furthermore, it is possible that quantities that jump out of the sample might jump inside the neighbored beaker and will eventually cause wrong Th/U-ages because samples are mixed. To prevent such potential errors, it is important not to overheat the beakers and to deposit the individual beakers as far as possible apart from each other during dry down procedures. However, the dry down steps bear the highest risk of losing sample quantities and/or to generate mixed Th/U-ages.

Also highly important is that no Ca residue is left inside the beaker after the final dry down step in order to prevent further complications during the measurements.

During *MC-ICPMS measurements*, it is important to tune the instrument as well as possible in order to guarantee reproducibility and highest precession during the sample and standard measurements. However, due to internal intensity fluctuations, this cannot

be always guaranteed. As mentioned before, impurities, such as residual Ca, inside the sample solution will cause potential problems during MC-ICPMS measurements because depending on the impurity degree it will block the Aridus and/or the cones. As a consequence, this will lead to wrong Th/U ratios. Therefore, intensive wash out times are required after each sample or standard is measured. However, impurities can be large and as a consequence, wash out times might be insufficient to prevent a blocked Aridus and/or cones when the chemistry was not performed well beforehand.

3.4 Stable Isotopes ($\delta^{18}O$ and $\delta^{13}C$)

All stable isotope analyses have been conducted at the University of Innsbruck. However, at the University of Mainz, samples for stable isotope analyses have been micromilled using an ESI New Wave Micromill, which operates with a high-resolution stereomicroscope and a color OCD video camera for imaging and digitizing the sample. Samples have been milled of the stalagmites with a conventional dentist drill of 0.3mm in diameter. To provide optimal milling conditions, a drilling depth of 50-200µm combined with a drill speed of 40 – 50% have been applied. Each stalagmite has been milled twice along their growth axis in 3mm and 500µm spatial resolution in 2.5mm long isotope tracks. The sample size ranged from 0.05 – 0.37mg

Subsequently all sample were measured at the University of Innsbruck, Austria following the measuring procedure of Spötl and Wennemann (2003).

3.5 Trace elements

Altogether 34 different elements of each stalagmites have been analyzed with a Thermo Finnigan Element 2 ICP-MS single-collector sector-field mass spectrometer coupled with a New Wave Research Nd: YAG UP 213nm laser system at the Max Planck Institute for Chemistry, Mainz, Germany. Samples were ablated with energy of 15.7J/cm^2. A 100µm spot size was used for all measurements along the growths axis in 500µm and 1mm resolution. A detailed description of the instruments used for LA-ICPMS has been given by Jochum et al. (2007). The reference glass NIST 612 was measured every 30 sample-points as a reference material in order to correct for instrumental fractionation. For all analyzes, we followed the analytical protocol described by Jochum et al. (2012). However not all elements could be used as

paleoclimate proxies. Therefore only the following elements have been used for paleoclimate investigations: Mg, Ba, P, Sr, Th, Al and U.

3.6 Thin section preparation

Petrographic investigation on thin sections was conducted under crossed polarized light at the University of Mainz using an Olympus BX51 system microscope in order to identify the different calcite fabrics and micromorphology of RBH 34.

The sample preparation has been performed at the Johannes-Gutenberg-University Mainz, following the sample-preparation-procedure of Tucker (1988).

4. Results

In the following, the results of the investigation of stalagmites RBH 32, 34, 39 and 47 are shown. These include a description of the stratigraphy and petrography (4.1), the Th/U-ages (4.2), the stable isotope- (4.3) and the trace element profiles (4.4).

4.1 Stratigraphy and petrography of the RBH stalagmites

Four different types of calcite fabrics have been observe in the RBH stalagmites, which are symbolized in Fig. 4.1. Later in this chapter, these symbols are plotted against distance from top (dft) for each of the RBH stalagmites to indicate the fabric composition.These types are defined after Frisia and Borsato (2010) as follows:

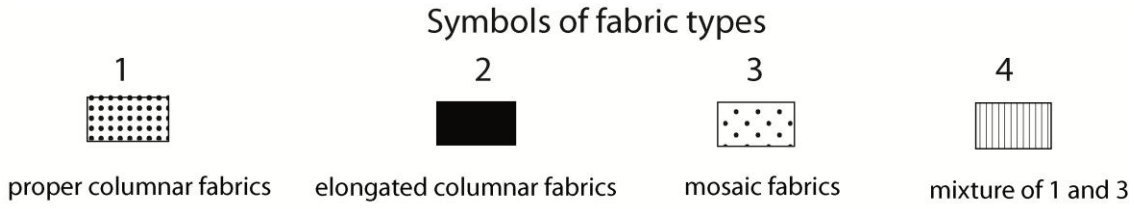

Figure 4.1: Symbols used to indicate the four types of calcite fabrics in the observed RBH stalagmites in this PhD thesis.

Type 1 (Proper columnar fabrics): The proper columnar fabrics display a characteristic length-to-width ratio of approximately 6:1, are elongated along the c-axis and show uniform extinction (Frisia and Borsato, 2010).

Type 2 (Elongated columnar fabrics): In contrast to Type 3, elongated columnar fabrics have a higher length-to-width ratio and are elongated along the c-axis. (Frisia and Borsato, 2010).

Type 3 (Mosaic fabrics): Mosaic calcite fabrics show no elongation along the c-axis, but reveal a chaotic arrangement of small, “mosaic like” fabrics.

Type 4 (Mixture of type 1 and 3): This type of calcite fabric represents a mixture of types 1 and 2.

Figures 4.2 – 4.5 show the same arrangement. Each figure is subdivided into an upper and a lower part**.** The upper part of the figures is subdivided again into panels A, B, C and D and plotted against distance from top (cm). Panel A displays the growth phase (GP) based on macroscopic all visible layers and remain in agreement with panel B. Panel B reveals the stalagmite itself. Panel C symbolizes the distribution of the different types of fabrics within each stalagmite and is based on the observations given in panel D and indicated in Fig. 1. Panel D exposes the thin section profile of each stalagmite under double crossed polarized light. The lower part of each figure exhibits the magnification of the most abundant fabric types based the on observations of panels C and D.

4.1.1 Stalagmite RBH 32

Stalagmite RBH 32 is 285mm long. In the lower part of Fig. 4.2 shows that stalagmite RBH 32 is subdivided into three pronounced growth phases (GP): GP 32-1 (0-85mm), GP 32-2 (86-160mm) and GP 32-3 (159-285mm). A thin visible whitish layer separates each phase from the other as is visible in panel 2B. These interruptions are designated growth stops and identified as hiatuses. Each GP displays a mixture of a brown-whitish color and prominent layers (Fig. 4.2, panel B). However, GP 1 and 3 reveal some small voids in the middle and lower part of each unit. These voids appear to be larger in GP 3 as can be seen in Fig. 4.2, panel B. None of these macroscopically observed voids seem to have impact on the structure of the fabrics detected in the thin sections.

Unfortunately, it is not known if the base of the stalagmite RBH 32 corresponds to the beginning of the initial growth phase.

Thin section analyses (Fig. 4.2, panel D) reveal that stalagmite RBH 32 only consists of calcite minerals and allows identification of the abundance of two different calcite fabric types. Columnar proper fabrics and elongated columnar fabrics types are visible, whereas their distribution in stalagmite RBH 32 is shown in panel 2C. Examples for sections of columnar proper fabrics and elongated columnar fabrics in stalagmite RBH 32 are given in the lower part of Fig. 4.2. Elongated columnar fabrics are the predominant type exhibited in stalagmite RBH 32 (Fig. 4.2, panel C).

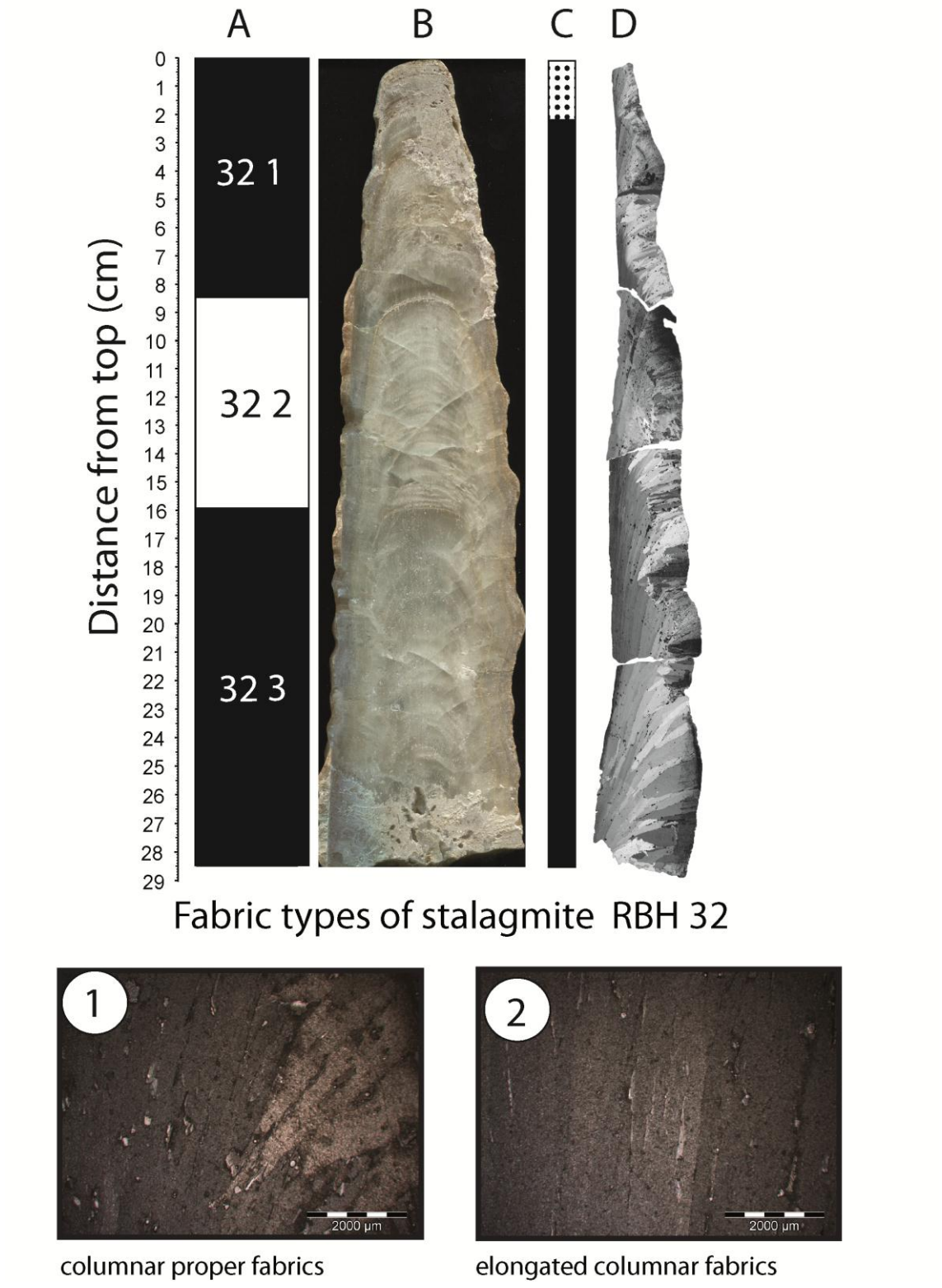

Figure 4.2: Subdivision: Upper Figure 4.2: Panel A: reflects the divisions into growth phases (GP). Panel B: shows the stalagmite itself. Panel C: symbolizes the distribution of the calcite fabric types in RBH 32. Panel D: illustrates a thin section profile of RBH 32 under double crossed and polarized light. Lower

Figure 4.2: two thin section examples of RBH 32 are given, presenting the two prevailing calcite fabric types of RBH 32. 1: columnar proper fabrics. 3: elongated columnar fabrics.

4.1.2 Stalagmite RBH 34

Stalagmite RBH 34 is 224mm long and consists of pure calcite (upper part of Fig. 4.3, panel B). The nature of the surface at the top of the speleotheme indicates that the uppermost section of RBH 34 most probably broke off or was already missing when the stalagmite was retrieved. RBH 34 can be subdivided into three growth phases (GP 34-1-3) as indicated in Fig. 4.3, panel B, which shows three distinct stalagmite growth phases. GP 34-1 (0–18mm dft) is separated from GP 34-2 (19–173mm dft) by a pronounced brownish layer at 18-19mm dft (DL). GP 34-3 (174–224mm dft) is clearly separated from GP 34-2 by a single milky, opaque layer at 173.0-174mm dft.

GP 34-1 only consists of mosaic fabrics. GP 34-2 represents the longest GP, and the predominant fabrics in this unit are mosaics and a mixture of mosaics and proper columnar fabrics. There are only two sections in GP 34-2 at 42-55 and 152-160mm dft showing proper columnar fabrics (Fig 4.3, panel C and D). GP 34-2 is also characterized by high porosity as indicated by the large numbers of voids. These voids have different dimensions ranging from 4 to 25mm.

GP 34-3 only consists of elongated columnar fabrics, which are primary crystals as proper columnar fabric with a pronounced elongation along the c-axis. For stalagmite RBH 34, it is not known whether the base of GP 34-3 represents the start of initial growth of the stalagmite. Note that types 3 and 4 represent the predominant fabrics, which is the reason why they were set in front at the lower part of Fig. 4.3. The nature of these fabrics will be discussed in detail in chapter 5.1.

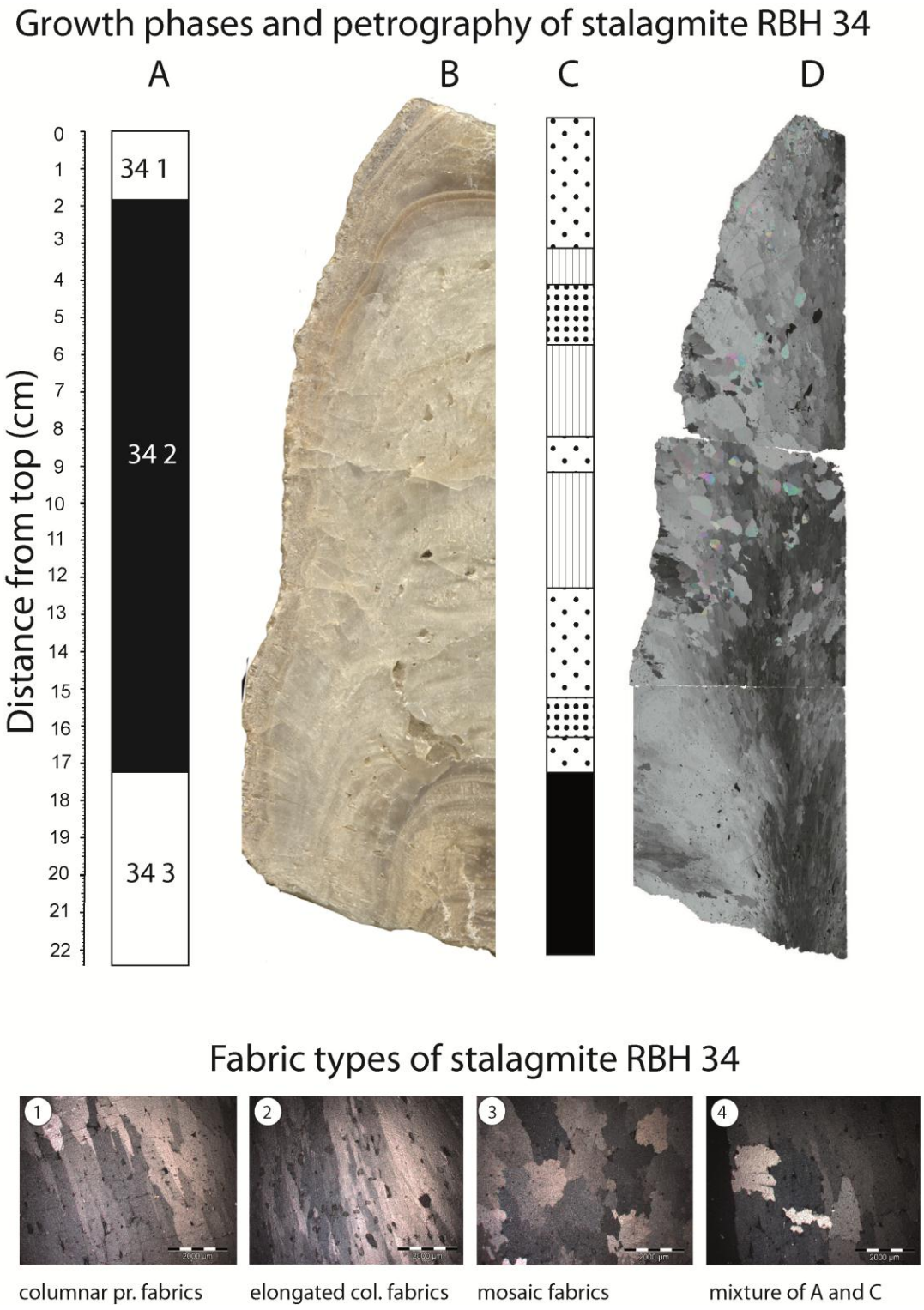

Figure 4.3: Subdivision: Upper Figure 4.3: Panel A: reflects the divisions into growth phase (GP). Panel B: shows the stalagmite itself. Panel C: symbolizes the distribution of calcite fabric types in RBH 34. Panel D: illustrates a thin section profile of RBH 32 under double crossed and polarized light. Lower Figure 4.3: four thin section examples of RBH 34 are given, presenting the four prevailing calcite fabric types of RBH 34. 1: columnar proper fabrics, 2: elongated columnar fabrics, 3: mosaic fabrics, 4: mixture 1 and 3.

4.1.3 Stalagmite RBH 39

Stalagmite RBH 39 is 195mm long and is subdivided into five GP (Fig. 4.4, panel B): GP 39-1 (0-10mm), GP 39-2 (10-65mm), GP 39-3 (66-130mm), GP 39-4 (131-150mm) and GP 39-5 (151-195mm). In comparison to stalagmite RBH 32 and RBH 34, RBH 39 reveals a more complex structure (Fig. 4.4). Thus, stalagmite RBH 39 reveals two stalagmites composed in one. The GP 39-1-4 represent stalagmite RBH 39, while GP 39-5 represents an older stalagmite, which is called RBH 39a. A light yellow-brownish thin layer represents the transition from RBH 39 to RBH 39a (compare Fig. 4.4, panel B, dashed line). However, since stalagmite RBH 39a represents a new stalagmite and it is not known whether stalagmite RBH 39a was cut exactly along its growth axis, all proxy measurements of GP 5 were neglected for climate reconstruction. The shape of the stalagmite expresses a candle form as described by Dreybrodt and Romanov (2008). All subdivisions are clearly separated from each other by pronounced white layers. These layers represent growth stops and are identified as hiatuses. The transition from GP 39-1 to GP 39-2 exhibits a very thin layer of mosaic fabrics as denoted in Fig. 4.4, panel C, D and indicated at the lower part of Fig. 4.4 by type 3. The two predominant fabric types of RBH 39 are proper columnar and elongated columnar fabrics (Fig. 4.4, type 1 and 2). Furthermore, all GP are characterized by a whitish color and a pronounced arrangement of fine layers. GP 39-5 shows a different structure. First of all the arrangement of fine layers is missing in GP 5. In fact, the crystal structure of GP 5 seems to be rather coarse (Fig. 4.4, panel B). This finding, however, is not observed in the thin section analysis. As visible in the thin section profile of stalagmite RBH39 (panel 4D), mosaic fabrics represent the base of GP 39-5 in stalagmite RBH 39a. The base of GP 39-5 characterizes a transition between stalagmite RBH 39a and the pronounced fossil layer, which was described earlier. This indicates that the base of RBH 39 corresponds to the beginning of the initial growth phase of stalagmite RBH 39a.

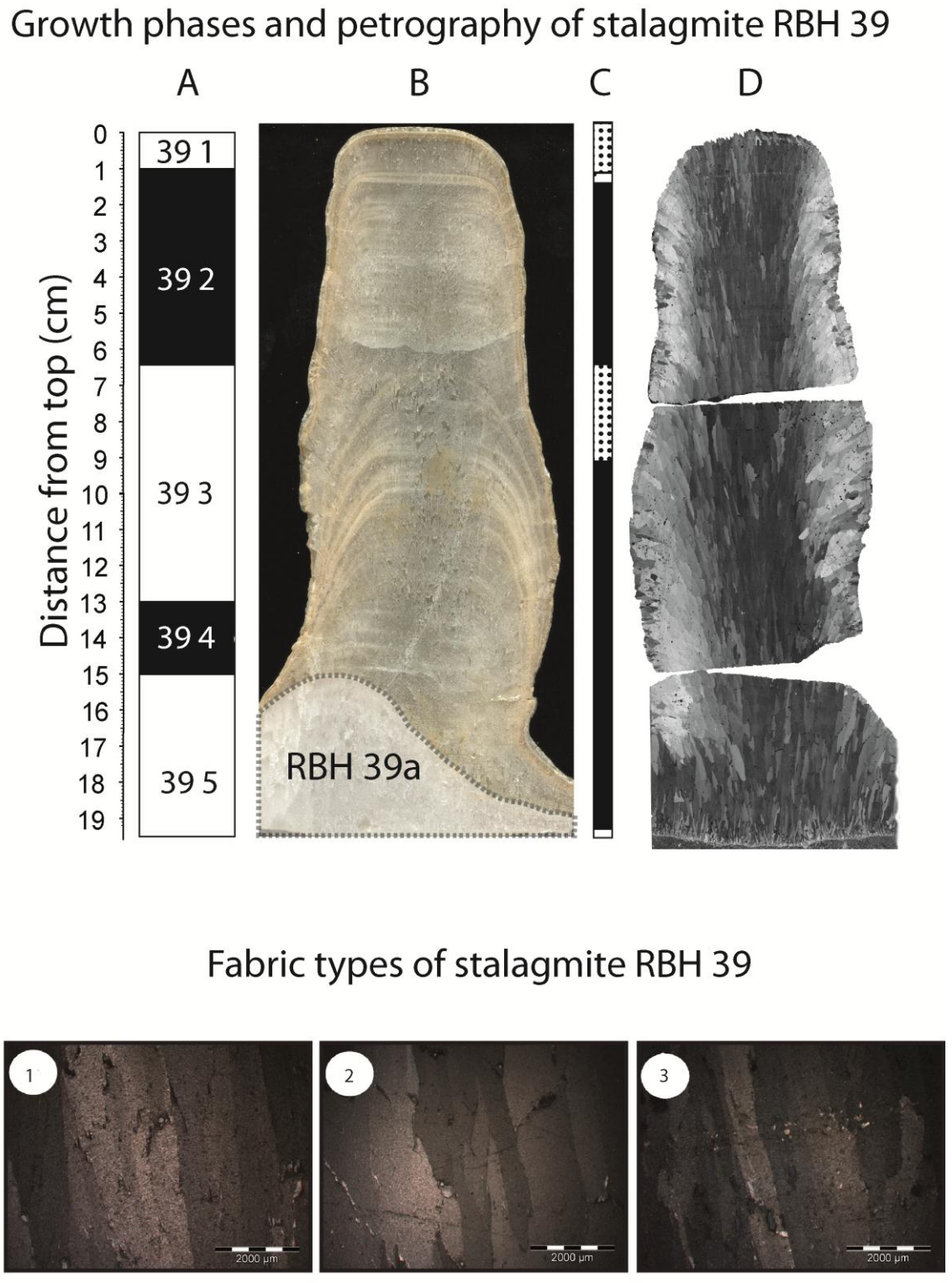

Figure 4.4: Subdivision: Upper Figure 4.4: Panel A: reflects the divisions into growth phase (GP). Panel B: shows the stalagmite itself. Panel C: symbolizes the distribution of calcite fabric types in RBH 39. Panel D: illustrates a thin section profile of RBH 32 under double crossed and polarized light. Lower Figure 4.4: three thin section examples of RBH 39 are given, presenting the three prevailing calcite fabric types of RBH 39. 1: columnar proper fabrics, 2: mosaic fabrics, 3: elongated columnar fabrics.

4.1.4 Stalagmite RBH 47

Stalagmite RBH 47, is with 310mm, the longest stalagmite studied for in this PhD thesis and reveals the most complex structure as displayed by six GP. The upper part represents GP 47-1 (0-15mm), GP 47-2 (16-40mm) and GP 47-3 (41-108mm) as indicated in Fig. 4.5 (panel A and B). The basic characteristics of this part are its dark whitish color and its frequently changing structure from strong to faint arrangement of pronounced layers. Predominant fabric types are columnar proper fabrics and elongated columnar fabrics as illustrated in Fig. 4.5, panel C and D and by fabric types 1 and 2. The middle section of stalagmite RBH 47 is revealed by GP 47-4 (109-150 mm) and is characterized by intercalated brown, coarse and fine layers (upper part of Fig. 4.5, panel B) as well as an arrangement of predominant mosaic fabrics (type 3). In addition, the unit represents a less dense structure. The transition from GP 4 to GP 5 (151-192 mm) shows a distinct white layer and delineates the intersection to the lower part of stalagmite RBH 47.

In contrast to the upper units, GP 47-5 does not expose any layers but is exposed by a more compact and dense structure. The thin section analysis of this unit reveals that the entire unit consists of elongated columnar fabrics (Fig. 4.5, panel C and D).

The intersection to GP 47-6 (193-310 mm) shows a faint and barely visible layer (upper part of Fig. 4.5, panel B). The unit exhibits to broad extent, the same characteristics as described for GP 47-5. However, major differences of both units are:

1. GP 47-6 reveals a constant set of poorly developed layers.
2. In the lower part of GP 47-6 these layers demonstrate a higher density and also small macroscopically visible voids, which have no effect on the structure of the fabrics.
3. The columnar proper fabric type is the only one observed for GP 47-6.

However, as with stalagmites RBH 32 and 34 it is not known whether the base of stalagmite RBH 47 represents the beginning of the initial growth phase. There is no information available on how the stalagmites were recovered because these stalagmites were provided by the DASC. In addition, the base of the stalagmite RBH 47 sample half was very thin. Thus, for the very last few millimeters of stalagmite RBH 47 no stable isotpe and trace element data exist.

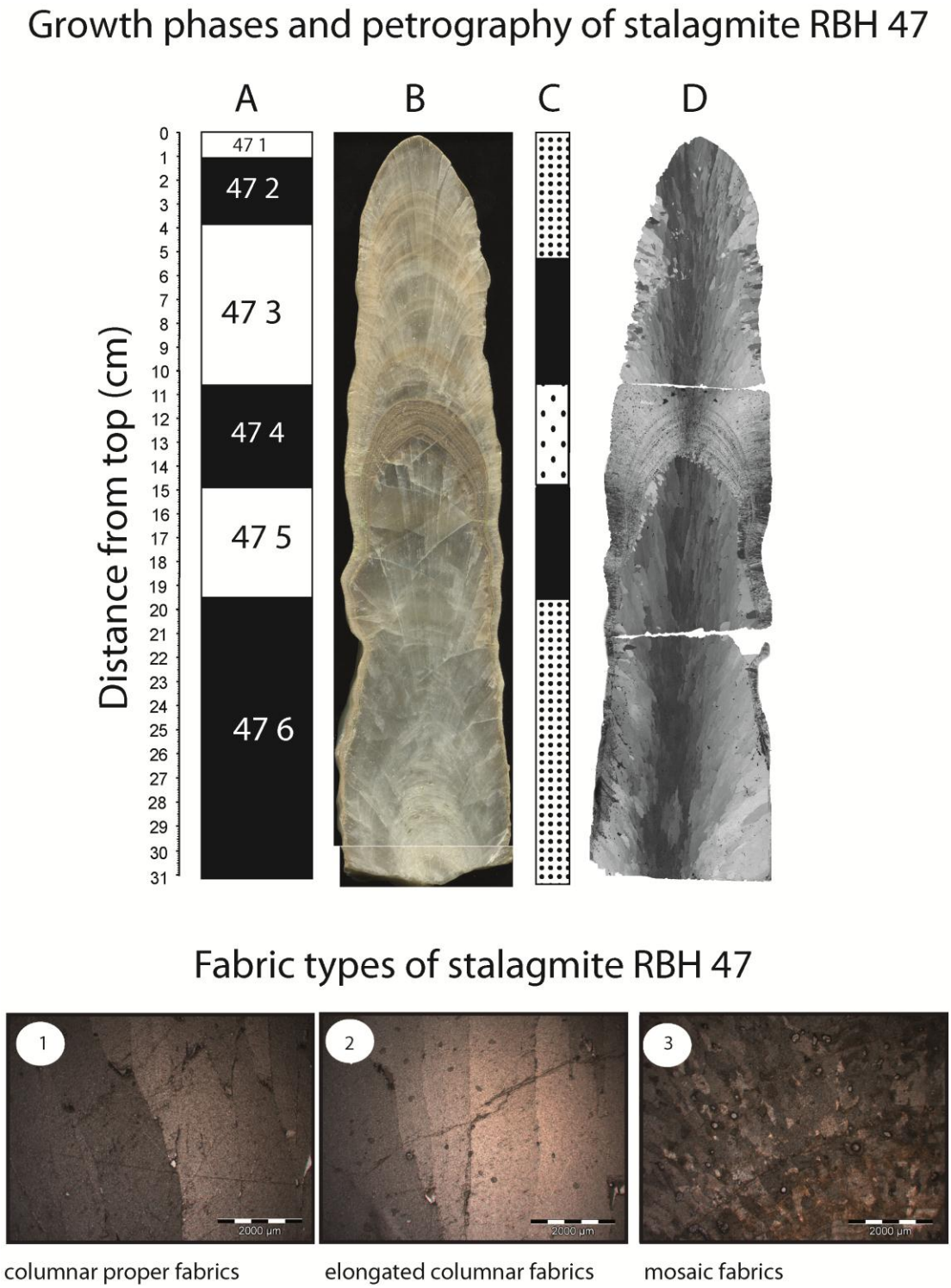

Figure 4.5: Subdivision: Upper Figure 4.5: Panel A: reflects the divisions into growth phase (GP). Panel B: shows the stalagmite itself. Panel C: symbolizes the distribution of calcite fabric types in RBH 47. Panel D: illustrates a thin section profile of RBH 47 under double crossed and polarized light. Lower Figure 4.5: three thin section examples of RBH 32 are given, presenting the three prevailing calcite fabric types of RBH 47. 1: columnar proper fabrics. 3: elongated columnar fabrics.

4.2 Th/U-ages of RBH stalagmites

In this chapter the measured Th/U-ages are displayed and plotted against the distance from top (dft) for each RBH stalagmite. These Th/U-ages are given in tables x to y, which can be found in Appendix.

In addition, the calculated Th/U-ages are compared with the NGRIP ice core $\delta^{18}O$ record (NGRIP members, 2004) on the GICC05modelext timescale to identify stalagmite growth phases during Greenland Interstadials (GIS). The nature of these ages is presented and discussed in more detail in chapter 5.2, which also includes the discussion of analytical errors. Here, the corrected Th/U-ages are presented together with the designated growth phases (GP) and compiled to phases of pronounced GIS.

4.2.1 Th/U-ages and growth phases of stalagmite RBH 32

For stalagmite RBH 32, 18 Th/U ages have been measured in total, which are shown in Fig. 4.6. Three different age phases of stalagmite RBH 32 could be identified, which coincide with the distinct growth phases (GP 32-1, 32-2 and 32-3). For the first growth phase GP 32-3, eight Th/U-ages have been measured. The transition from GP 32-2 to GP 32-3 is characterized by a distinct hiatus, which can be identified in Fig. 4.6 through a pronounced shift. In GP 32-2 four Th/U-ages were measured. The transition from GP 32-2 to GP 32-1 is characterized again through a hiatus. In GP 32-1, six Th/U-ages were measured.

Once these growth phases are compared to the GIS, it can be observed that the stalagmite growth of RBH 32 occurred during phases of GIS. GP 32-3 is representative for a distinct growth phase during the late Eemian. GP 32-2 represents a phase during GIS 23, while GP 32-1 represents to a large extent GIS 21.

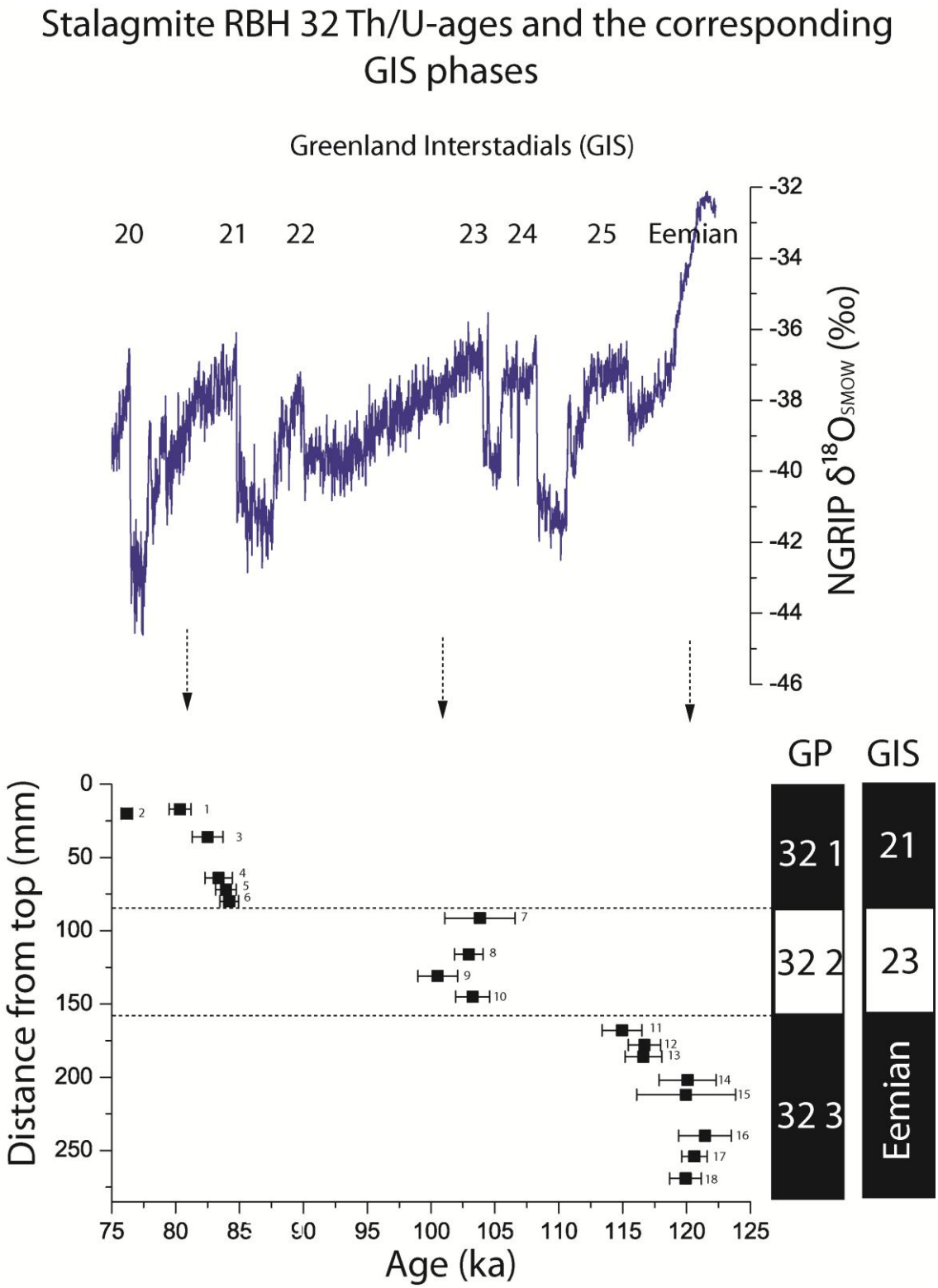

Figure 4.6: Presentation of the 18 Th/U-ages, which were measured for stalagmite RBH 32, and comparison to Greenland Interstadials (GIS) as reflected in the $\delta^{18}O$ record of the NGRIP ice core. These Th/U-ages cluster in distinct the growth phases described in chapter 4.1.1, which in turn can be allocated to the corresponding phases during the GIS as indicated by the dashed lines.

4.2.2 Th/U-ages and growth phases of stalagmite RBH 34

Twelve ^{230}Th/U-ages were determined along the growth axis of RBH 34 (Fig. 4.7). The U-series data are shown in Appendix A. The corrected ^{230}Th/U-ages range from 74 to 123ka and indicate that RBH 34 grew during the warmer phases of Marine Isotope Stage (MIS) 5, i.e., MIS 5a, c and e.

Two ^{230}Th/U-ages were determined for GP 1 at 3 and 18mm dft, respectively. The sample at 18mm dft was probably taken at double layer (DL), and the age probably reflects a mixture between GP 1 and 2. Thus, this age is not considered reliable. The remaining age determined for GP 1 is the youngest age of the whole stalagmite suggesting that this section most likely grew during MIS 5a. Six ages were determined for GP 2. Fig. 4.7 clearly shows that the ages in GP 2 do not increase with increasing dft as expected from the stratigraphy. In contrast, the ages scatter around a mean age of 102.7 ka, and exhibit various age inversions along the growth axis (i.e., ages that are younger/older than expected from the stratigraphy). The youngest age of this section (98.6 ± 0.7ka at 168mm dft) is obtained at the bottom section of GP 2 (Fig. 4.7). The ages determined for GP 3 range from 119.3 to 123.4ka indicating a Last Interglacial origin. We observe only one age inversion for GP 3, which consists only of elongated columnar fabrics.

Despite of the dating problems reflected by the apparent age inversions, we suggest to assign the observed three growth sections to the three major warm phases of MIS 5: GP 1 (mean age: 74.7ka) corresponds to MIS 5a, GP 2 (mean age: 102.7ka) corresponds to MIS 5c, and GP 3 (mean age: 120.9ka) grew during Last Interglacial (MIS 5e).

However, due to the observed age inversions it was not possible to allocate distinct growth phases with corresponding GIS. The origin of the age inversion and its implication of post depositional diagenesis (PDD) on the U-series system is discussed in detail in a later chapter 5.1.

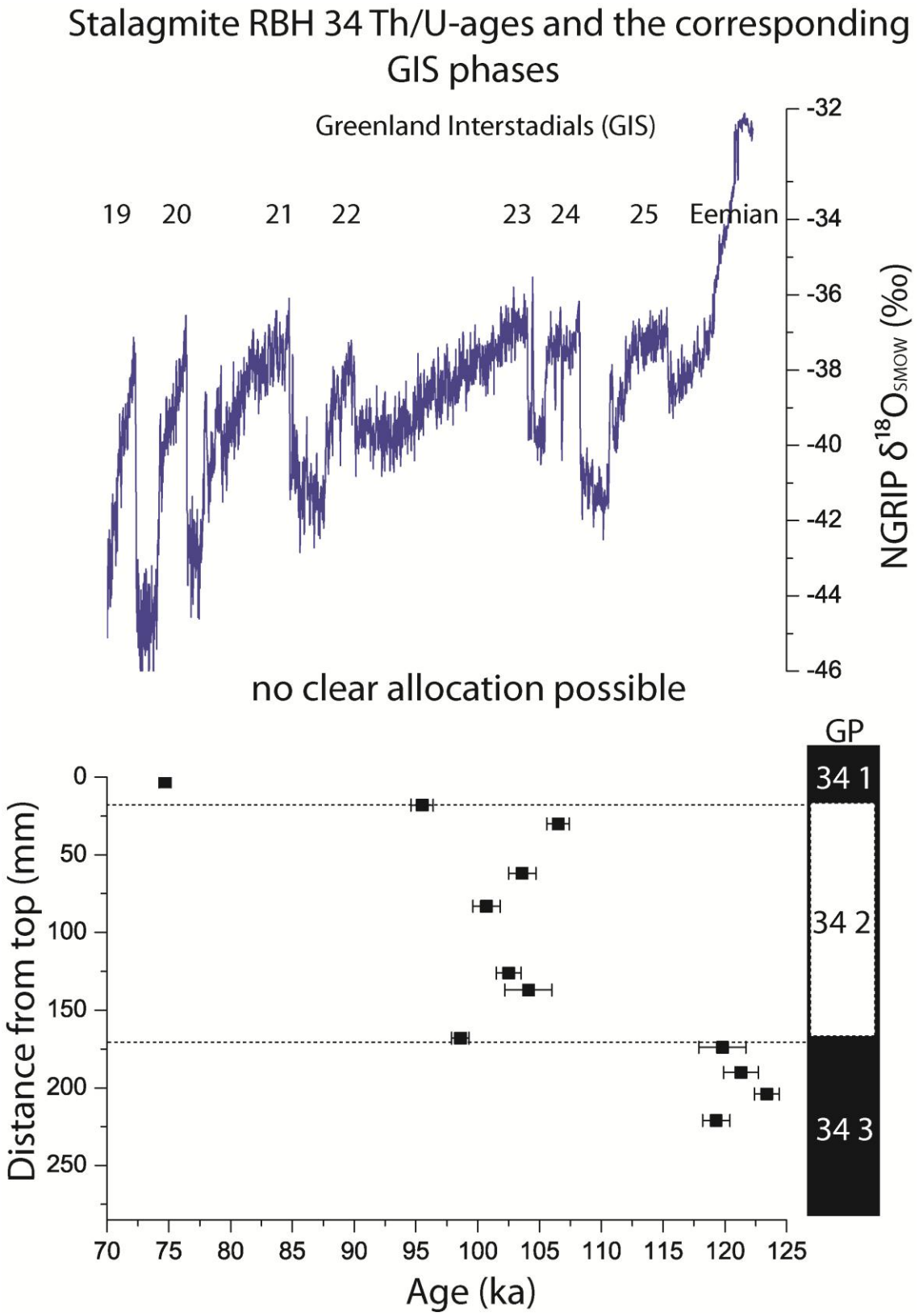

Figure 4.7: Presentation of the 12 Th/U-ages, which were measured for stalagmite RBH 34 and comparison to Greenland Interstadial (GIS) as reflected in the $\delta^{18}O$ record of the NGRIP ice. These Th/U-ages cluster in distinct the growth phases described in chapter 4.1.2 Note that due to large age inversions no clear allocation to phases during GIS was possible.

4.2.3 Th/U-ages and growth phases of stalagmite RBH 39

For stalagmite RBH 39 altogether 24 Th/U ages have been measured, which are shown in Fig. 4.8. Five different age phases of stalagmite RBH 39 could be identified, which coincident with the distinct growth phases (GP 39a, 39-4, 39-3, 39-2 and 39-1). All growth phases are separated from each other by distinct hiatuses.

Note that the Th/U-ages measured for GP 39a were not taken into account for later age modeling, because it has been shown that this GP represents an entire different stalagmite (stalagmite RBH 39a) and that it can be assured that this stalagmite was cut along it growth axis, which was set as one requirement for Th/U-age dating. Nonetheless, six Th/U-ages were measured for stalagmite RBH 39a, which most likely represents a growth phase during the Eemian also when characterized by two distinct age inversions located close to the base of stalagmite RBH 39a. For GP 39-4 four Th/U ages have been measure, while in GR39-3 and GP 39-2 six and seven Th/U-ages have been measured. GP 39-1 is represented by two Th/U-ages.

Once these growth phases are compared to the GIS as displayed for example in the NGRIP $\delta^{18}O$ ice core record (NGRIP members, 2004) it can be observed that the stalagmite growth of RBH 39 occurred during distinct phases of Greenlandinterstadials (GIS). Thus GP 39-4 is representative for a phase of GIS 24. GP 39-3 represents a phase during GIS 23, while GP 39-2 represents GIS 21 and GP 39-1 represents a phase during GIS 20.

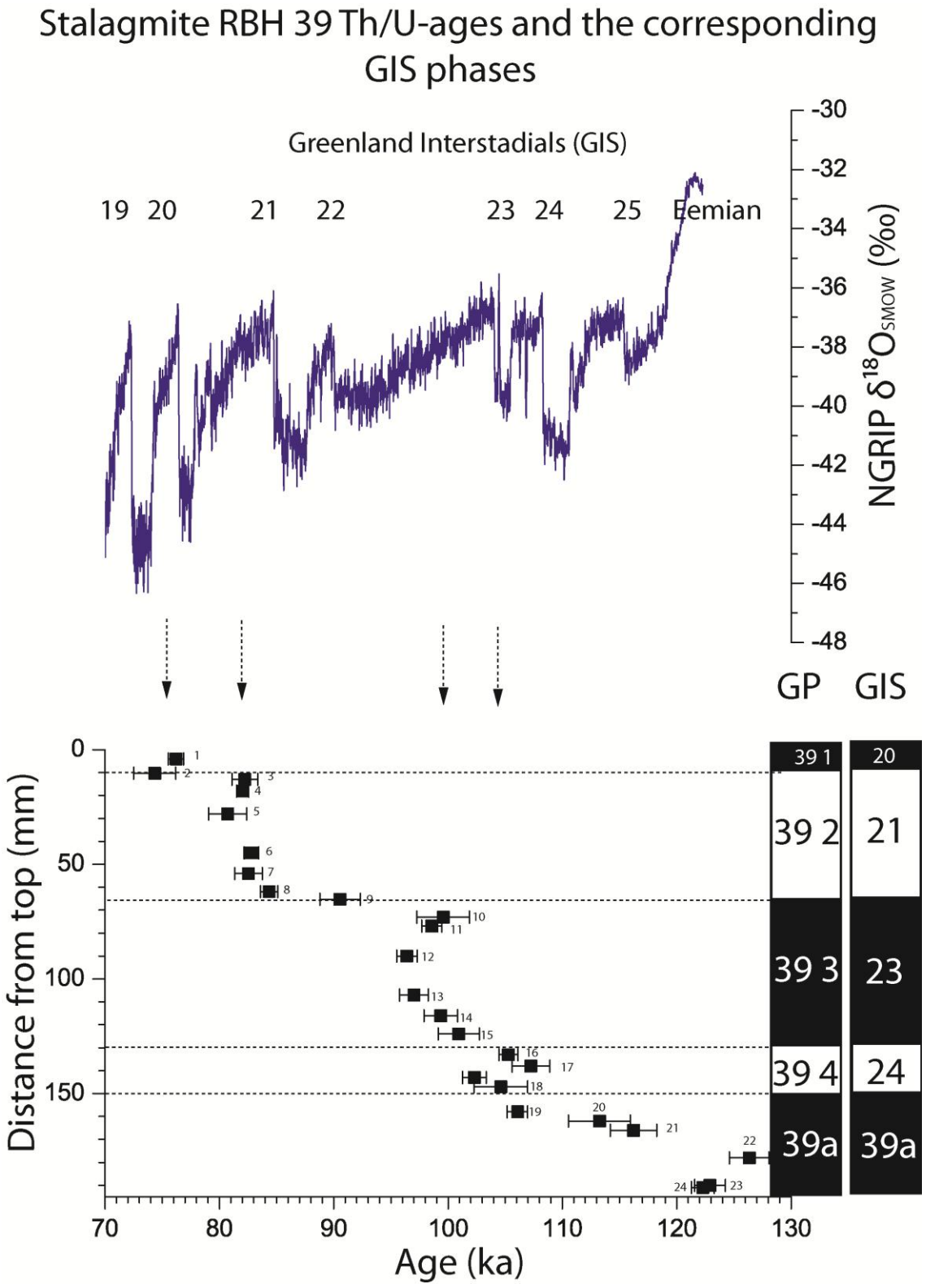

Figure 4.8: Presentation of the 24 Th/U-ages, which were measured for stalagmite RBH 39, and comparison to Greenland Interstadials (GIS) as reflected in the $\delta^{18}O$ record of the NGRIP ice core. These Th/U-ages cluster in distinct the growth phases described in chapter 4.1.3, which in turn can be allocated to corresponding phases during the GIS as indicated by the dashed lines. Note that RBH 39a represents a different stalagmite and thus no allocation to designated phases of GIS could be performed.

4.2.4 Th/U-ages and age phases of stalagmite RBH 47

For stalagmite RBH 47, in total 18 Th/U ages have been measured, which are shown in Fig. 4.9. Five different age phases of stalagmite RBH 74 could be identified, which coincident with the growth phases (GP 47-6, 47-5, 47-4, 47-3, 47-2 and 47-1). All growth phases are separated from each other by distinct hiatuses. It is noteworthy that for GP 47-4 large age inversions are detected, which might be related to the fabric type of this growth phase, which be discussed in chapter 5.1.1.4.

For GP 47-6 six Th/U-ages have been measured, while for GP 47-5 only one Th/U-age was measured. For GP 47-4 five Th/U ages have benn measured.

Once these growth phases are compared to the GIS, it can be observed that the stalagmite growth of RBH 47 occurred during distinct phases of GIS. GP 47-6 is representative for a phase during the late Eemian. GP 47-5 represents a phase during GIS 24. GP 47-4 cannot be allocated to the designated GIS phases due to the large number of age inversions. However, it can be speculated that this phase represents a phase during GIS 23. The proceeding growth phases GP 47-3, GP 47-2 and GP 47-1 GIS 21, 20 and 19.

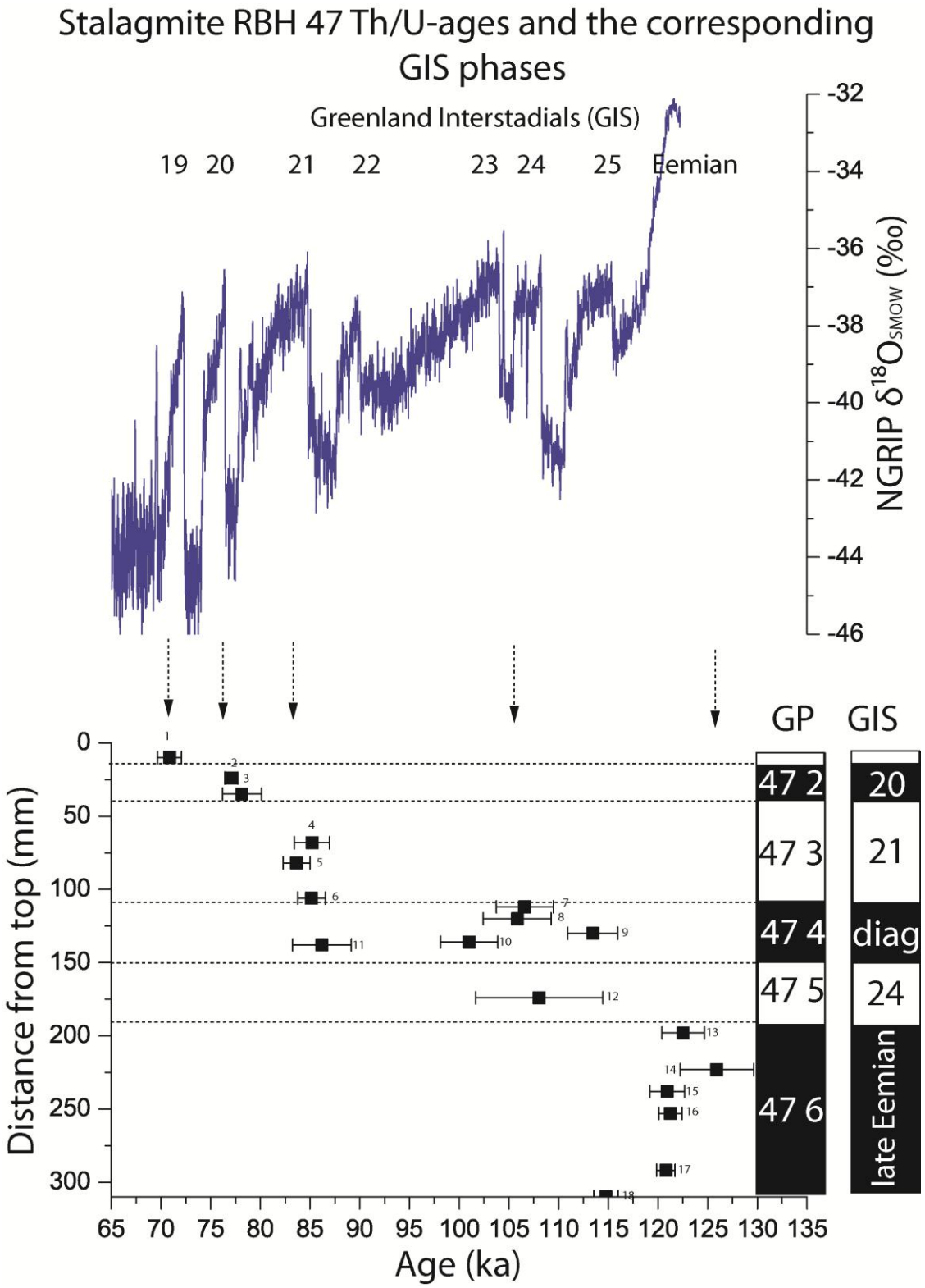

Figure 4.9: Presentation of the 18 Th/U-ages, which were measured for stalagmite RBH 47, and comparison to Greenland Interstadial (GIS) as reflected in the $\delta^{18}O$ record of the NGRIP ice core. These Th/U-ages cluster in distinct the growth phases described in chapter 4.1.4, which in turn can be allocated to the corresponding phases during the GIS as indicated by the dashed lines. Note that for GP 47-4 no clear allocation was possible.

4.3 Stable isotope profiles of RBH stalagmites

In the following, the stable isotope profiles of the examined RBH stalagmites are presented. All figures show the same structure. The stable isotope profiles are plotted against dft (distance from top), and on top the growth phases (GP) are shown. Blue lines represent $\delta^{13}C$-value, whereas stable isotope profiles indicated in red lines represent $\delta^{18}O$-values.

4.3.1 Stable isotopes of RBH 32

For the whole profile, the average $\delta^{13}C$ value represents -5.8‰, while the average $\delta^{18}O$ value is -6.1‰. As shown in Fig. 4.10, a stepwise increase of $\delta^{13}C$ can be observed. Thus, the average $\delta^{13}C$ vale of the late Eemian phase displays the lowest average $\delta^{13}C$ value of -7.03‰, while the GIS 23 phase displays an average $\delta^{13}C$ value of -6.16‰ and the GIS 21 phase an average value of -5.58‰. The maximum value of $\delta^{13}C$ of 1.03‰ is reached at the end of the GIS 21 phase.

In contrast to the $\delta^{13}C$ characteristics, the $\delta^{18}O$ record of stalagmite RBH 32 shows a diverse pattern. The GIS 23 phase represents the lowest average $\delta^{18}O$ value of -6.52‰ and also shows the $\delta^{18}O$ minimum of -7.01‰. It is also obious that the $\delta^{18}O$ record of stalagmite RBH 32 shows an increasing trend in the late Eemian phase and is than characterized by a significant decline of $\delta^{18}O$ at the transition to the GIS 23 phase. Then, a slight increase can be observed during the GIS 23. In contrast the transition from the late Eemian phase to GIS 23 phase, the transition from GIS 23 phase to GIS 21 is characterized by an abrupt shift to more positive values and reaches its maximum value of $\delta^{18}O$ -4.81‰ at the end of GIS 23. The inception of the GIS 21 phase is characterized by a significant decline in $\delta^{18}O$ and then shows a gradual decrease until an abrupt increase of $\delta^{18}O$ can be observed.

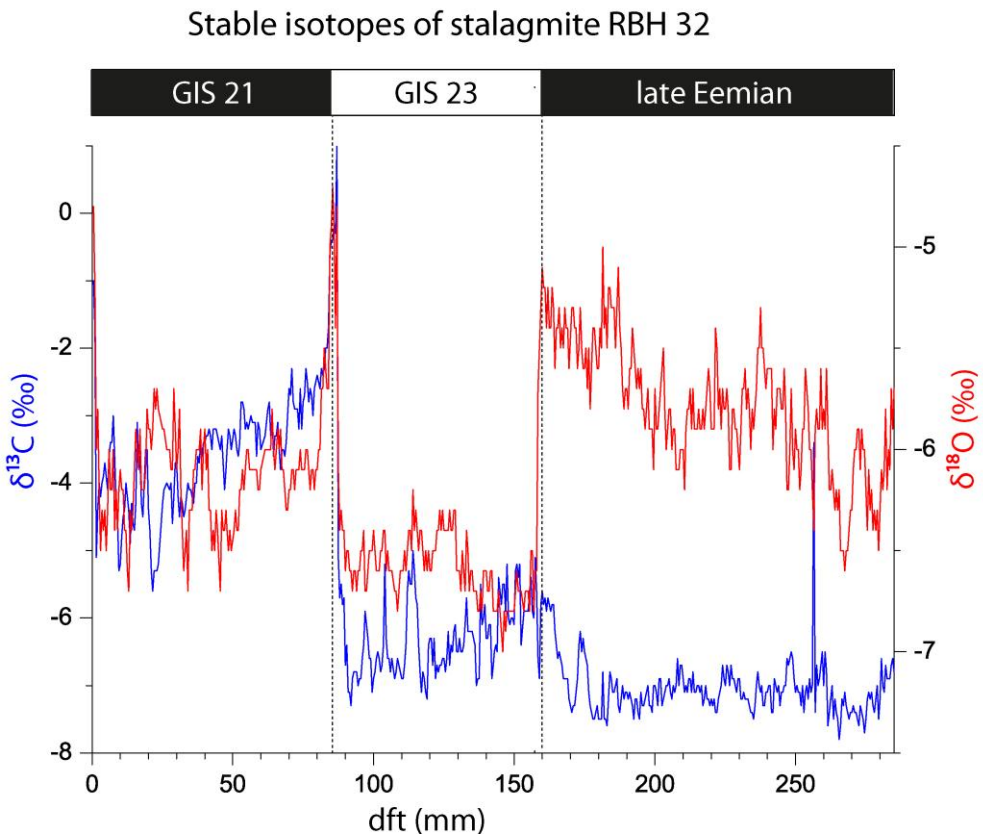

Figure 4.10: Figure 4.10 displays the stable isotope profile of RBH 32 ($\delta^{13}C$, blue and $\delta^{18}O$, red in ‰) plotted against distance from top (dft) in mm and to the designated growth phases during GIS including the late Eemian. The dashed lines indicate the agreement between these phases, which coincident with changes in the stable isotope profile.

4.3.2 Stable isotopes of RBH 34

In contrast to the other RBH stalagmites, stalagmite RBH 34 can only be characterized by its growth phases. This is a consequence of the large age inversions observed in GP 34-2. Thus, the growth phases of stalagmite RBH 34 could not be assigned to individual GIS. Implications of stalagmite RBH 34 will be discussed in a later section. The first impression of stalagmite RBH 34 is that the growth phases do not correlate with changes in the stable isotope record. The transition from GP 34-3 as well as from 34-2 and GP 34-2 to 34-1 is characterized by significant changes in both stable isotope records (compare Fig. 4.11). Nonetheless, both records also reveal large variability in each growth phase. In general, the $\delta^{13}C$ record is characterized by a large shift from -8‰ to -6‰ in GP 34-3. In contrast, the $\delta^{18}O$ values decrease from -6.3‰ to -6.5‰ in the same growth phase, but are characterized by a large variability that shows shifts from -6.9‰ to -5.1‰. In the first phase of GP 34-2, the $\delta^{13}C$ values show a plateau, which can also be observed in the $\delta^{18}O$ record. In the second phase of GP 34-2, however, $\delta^{13}C$ and $\delta^{18}O$ show opposite trends. While the $\delta^{18}O$ values increase before they decrease again, the $\delta^{13}C$ values keep decreasing until the absolute $\delta^{13}C$ minimum (-7.98‰) is reached. Then, a gradual increase can be observed. The transition from GP 34-2 to GP 34-4 is characterized by large increase in $\delta^{13}C$ from -6.5‰ to -3.5‰ before a distinct decline from -3.5‰ to -7.0‰ is observed. The $\delta^{18}O$ record does not show similar large changes.

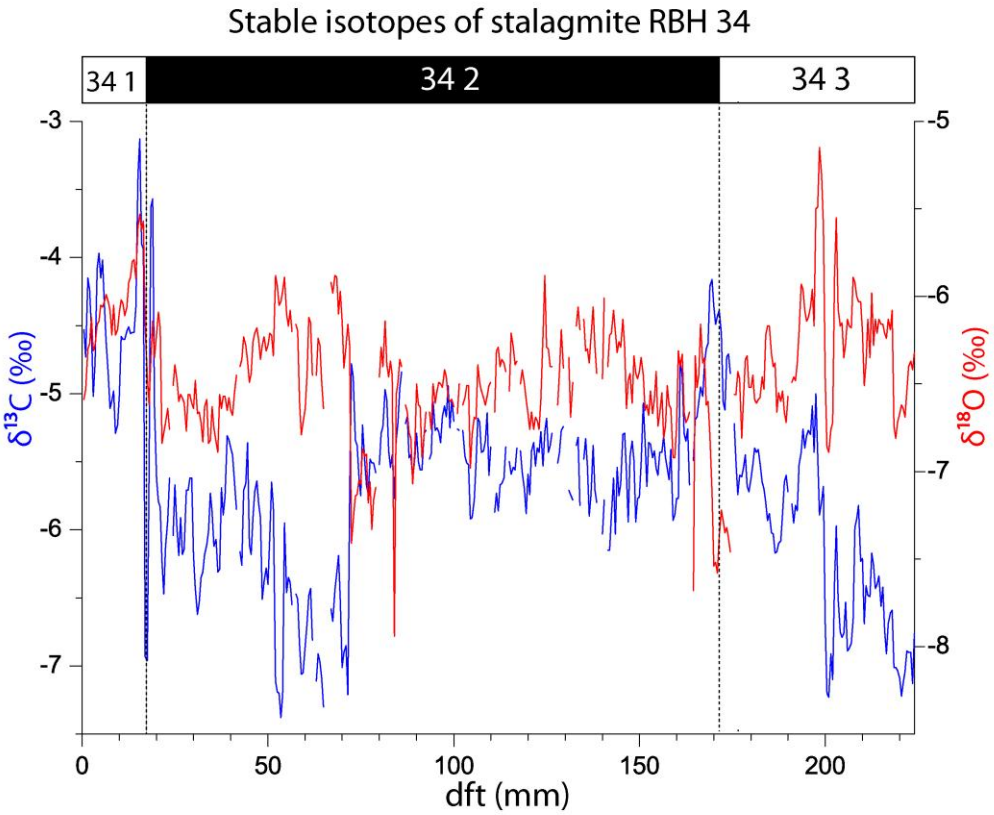

Figure 4.11: Figure 4.11 displays the stable isotope profile of RBH 34 ($\delta^{13}C$, blue and $\delta^{18}O$, red in ‰) plotted against distance from top (dft, mm) and to the designated growth phases during GIS including the late Eemian. The dashed lines indicate the agreement between these phases, which coincident with changes in the stable isotope profile.

4.3.3 Stable isotopes of RBH 39

In Fig. 4.12, stalagmite RBH 39a is shown in the light yellow box. It is noteworthy that in general, an increasing $\delta^{13}C$ trend can be observed throughout the record. However an exception of this is the GIS 20 phase. In contrast, no clear trend can be observed for the $\delta^{18}O$ values. In RBH 39a an incline of 1‰ a $\delta^{13}C$ from approximately -7‰ to approximately -6‰ can be observed, while a decline of $\delta^{18}O$ that reaches from -5‰ to -6‰ is detectable. Then, in the GIS 24, phase a rapid increase in $\delta^{13}C$ from -4 to approximately +1‰ characterizes the transition to the GIS 23 phase, while $\delta^{18}O$ does not show similar characteristics during GIS 24 and displays an average $\delta^{18}O$ value of - 6.25‰. Apart from the pronounced decline of the $\delta^{13}C$ signal in the first few mm after the inception of GIS 23, the general trend of both isotopes is rather uniform during GIS 23. This uniform pattern of both isotopes is still observed during the first half of GIS 21. In the second half of GIS 23 however, the $\delta^{13}C$ signal describes a pronounced positive

shift of about 1.5‰ from -3.2‰ to -1.7‰ before it sharply declines again from approximately -1.7 ‰, to approximately -4.2‰ at the end of the GIS 21 phase. In contrast, the $\delta^{18}O$ values in general decline during the second half of GIS 21. In the GIS 20 phase, a general decline of the $\delta^{13}C$ values can be observed, while the $\delta^{18}O$ values show the opposite trend.

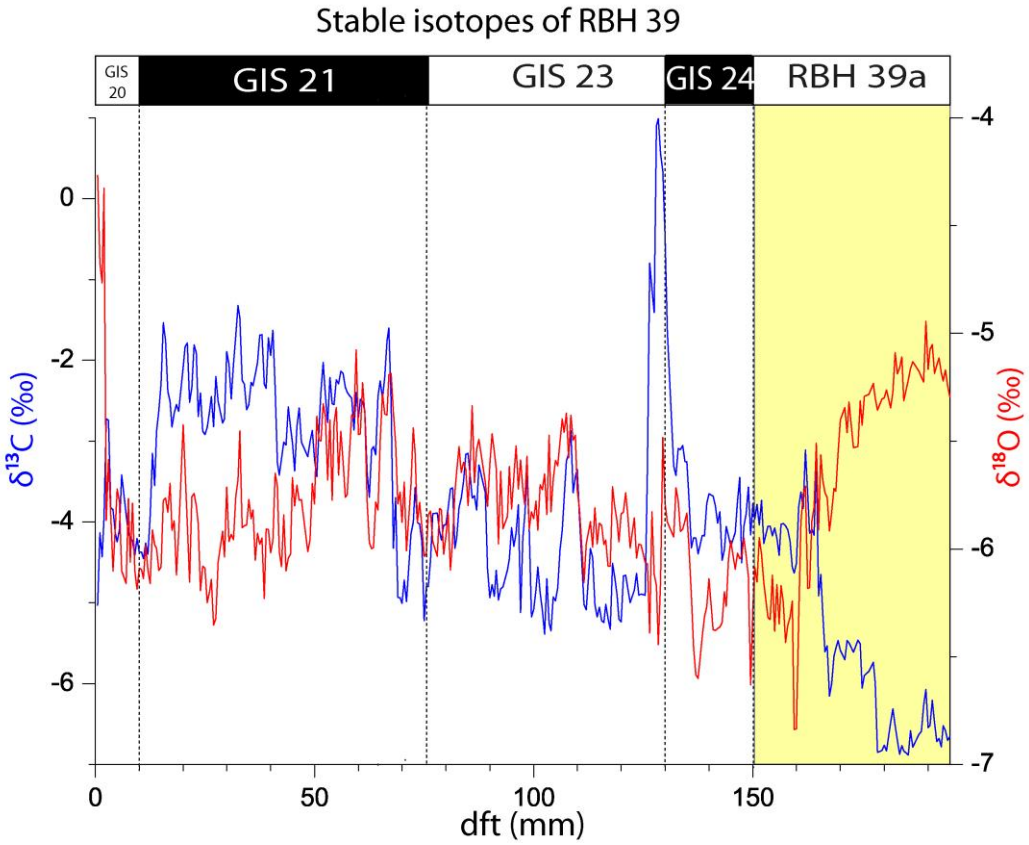

Figure 4.12: Figure 4.12 displays the stable isotope profile of RBH 39 ($\delta^{13}C$, blue and $\delta^{18}O$, red in ‰) plotted against distance from top (dft) in mm and to the designated growth phases during GIS including the late Eemian. The dashed lines indicate the agreement between these phases, which coincident with changes in the stable isotope profile. The yellow box signalizes the transition to RBH 39a.

4.3.4 Stable isotopes of RBH 47

As demonstrated in Fig. 4.13, the general $\delta^{13}C$ trend is increasing, while the general $\delta^{18}O$ trend displays a rather decreasing pattern. In stalagmite RBH 47, the lowest $\delta^{13}C$ values of all RBH stalagmites are observed. In addition, the $\delta^{13}C$ values do not exceed - 3‰, which is similar to the $\delta^{13}C$ values of stalagmite RBH 34.

The average $\delta^{13}C$ value along the profile is -6.9‰, while the average $\delta^{18}O$ value is - 6.0‰. The maximum $\delta^{13}C$ value is -2.9‰ at 1.5mm (dft). The minimum value is

- 9.2‰ at 194.5mm (dft), shortly after the transition from the late Eemian phase to GIS 24 phase. During the late Eemian phase, constant is declining $\delta^{13}C$ isotopes can be observed. This trend changes with the inception of the GIS 24 phase and continues to increase throughout the record during each phase. A similar trend for $\delta^{18}O$ is not observed. Instead, during the Eemian phase, a $\delta^{18}O$ plateau is observed. In GIS 24, the $\delta^{18}O$ characteristics can be described by a constant decrease of the $\delta^{18}O$ values. This trend also continues during the diagenetic disturbed phase. In the proceeding two GIS phases 21 and 20, a distinct $\delta^{18}O$ plateau is established, while in the GIS 19 phase a rapid increase of the $\delta^{18}O$ values from -7.5 to -4‰ is recognized.

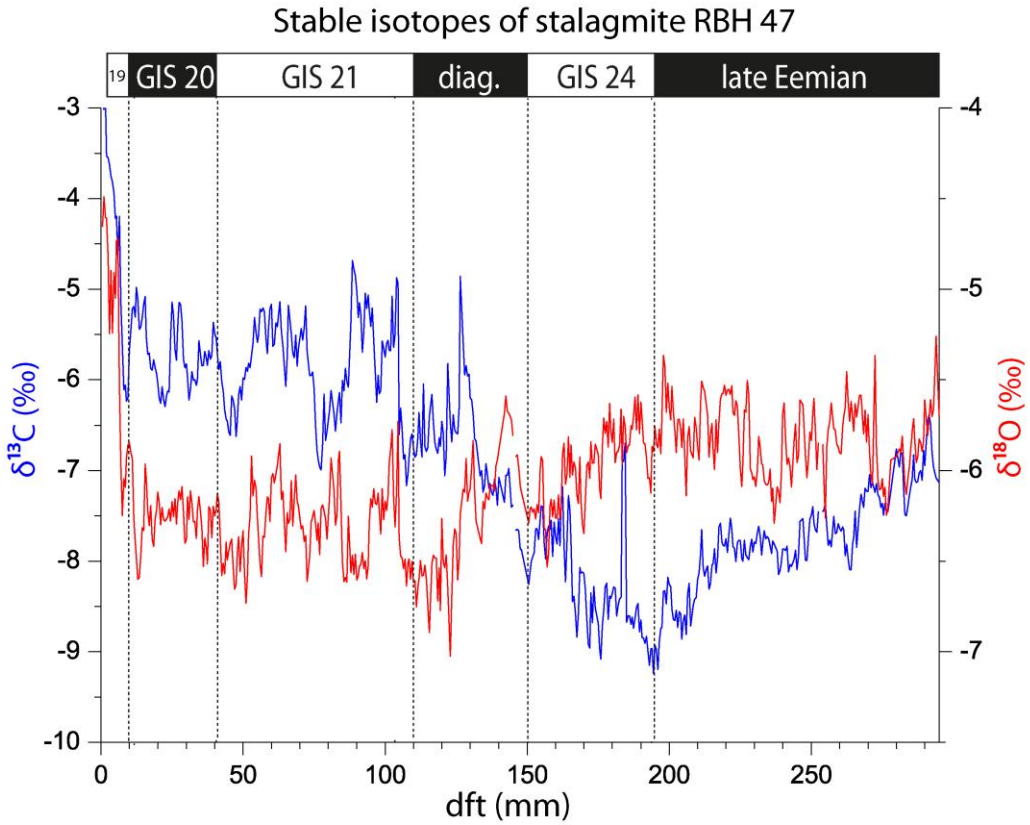

Figure 4.13: Figure 4.13 displays the stable isotope profile of RBH 32 ($\delta^{13}C$, blue and $\delta^{18}O$, red in ‰) plotted against distance from top (dft) in mm and to the designated growth phases during GIS including the late Eemian. The dashed lines indicate the agreement between these phases, which coincident with changes in the stable isotope profile.

4.4 Trace element profiles of RBH stalagmites

The figures presented in the following showthe same arrangement of five selected trace elements plotted against dft. From bottom to top these trace elements are: Mg (orange),

Sr (pink), Ba (black), U (olive) and P (brown). It is notable again the GIS phases (chapter 4.2) are in positive agreement with distinct shifts in trace element profiles.

4.4.1 Trace elements of RBH 32

Figure 4.14 shows that during the late Eemian phase, the P concentration shows apart from a few peaks, average values below 10µg/g. However, a weak gradual increase in P can be observed during the late Eemian and GIS 23. During the GIS 21 phase, P reflects strong variability and concentrations that vary from 5-300µg/g.

The U concentrations decline constantly from 1.25 to almost 0.25µg/g during the late Eemian phase. At the onset of the GIS 23 phase, a sudden increase in U can be observed followed by gradual is declining U concentration. A similar pattern can be observed during the GIS 21 phase. The only exception is reflected in a short excursion back to relatively high U concentrations of 1.5µg/g that is followed by a sudden decline to approximately 0.25µg/g. The same characteristic patterns can be observed in Sr and Ba concentrations along the profile. The exception is Ba during the GIS 21 phase. Here, the Ba concentration remains constantly below 30µg/g. Then, two short sudden increasing shifts in Ba concentrations can be observed, which show maximum Ba concentrations of 110µg/g in the middle of the GIS 21 phase. This sequence is followed by a drastic shift back to Ba concentrations below 30µg/g.

The Mg concentration of stalagmite RBH 32 is increasing constantly during the late Eemian phase before a rapid decrease can be observed. In the proceeding GIS 23 phase, the Mg concentration remains rather stable and reveals only a weak variation. During the GIS 21 phase, the Mg concentration reveals higher variability and reaches maximum concentrations. Additionally, the Mg concentration pattern is inverse to the U and Sr concentrations.

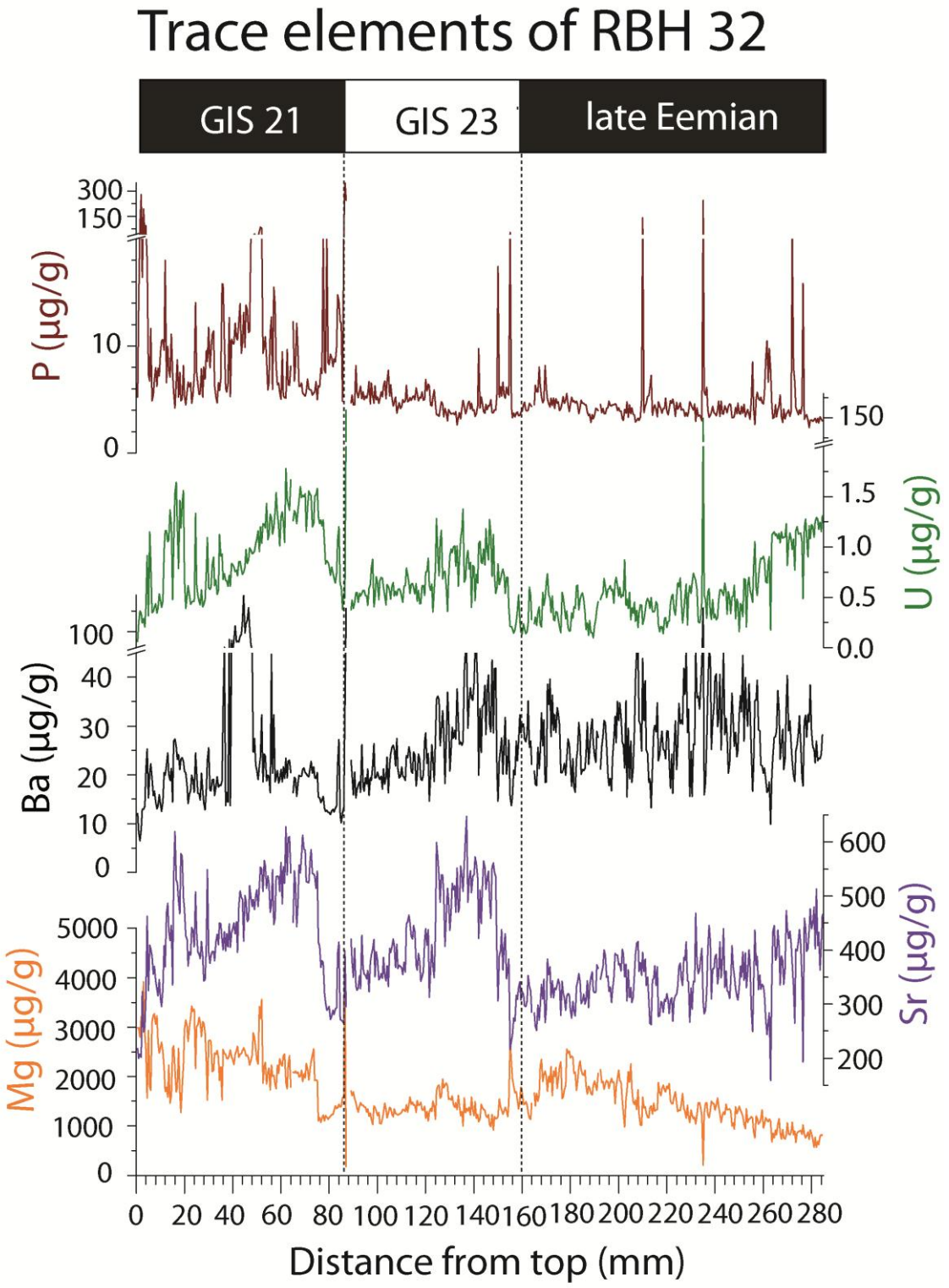

Figure 4.14: Figure 4.14 displays the distribution of selected trace elements plotted against distance from top (dft) and allocated to the designated GIS phases as described in chapter 4.2.1 for stalagmite RBH 32. Color code: Orange: Magnesium (Mg), Pink: Strontium (Sr), Black: Barium (Ba), Olive: Uranium (U) and Brown: Phosphorous (P).

4.4.2 Trace elements of RBH 34

In Fig. 4.15, generally low P concentrations below 5µg/g can be observed during GP 34-3. This trend continues during the first half of GP 34-2 but is interrupted by a short excursion that describes a rapid increase of P during the transition of GP 34-3 to GP 34-2 that reaches a maximum concentration of 20µg/g. The second half of GP 34-2 is characterized by frequent and rapid shifts in P, which reach its maximum concentration of 360µg/g at the transition of GP 34-2 to GP 34-1. In the proceeding GP 34-1 the P pattern does not change the trend in comparison to the second half of GP 34-2.

During all GP, the characteristics of U, Sr and Ba are similar. These elements reveal a frequent fluctuation during GP 34-3, and vary from 1.7-0.01µg/g for U, 10-37µg/g for Ba and 30-390µg/g for Sr concentrations. In the first half, the U, Ba and Sr concentrations are relatively stable and do only show minor fluctuations, while in the second half of GP 34-2 these fluctuations are larger and more pronounced. This is evident in maximum concentrations reached in the second half for Ba and Sr concentrations of 550µg/g and 43µg/g as well as in minimum concentrations of 200µg/g and 8µg/g respectively. During GP 34-1A general increase of the U, Ba and Sr concentrations can be observed. The Mg concentrations are decoupled from this pattern. The general trend of Mg shows a slight decrease during all GP.

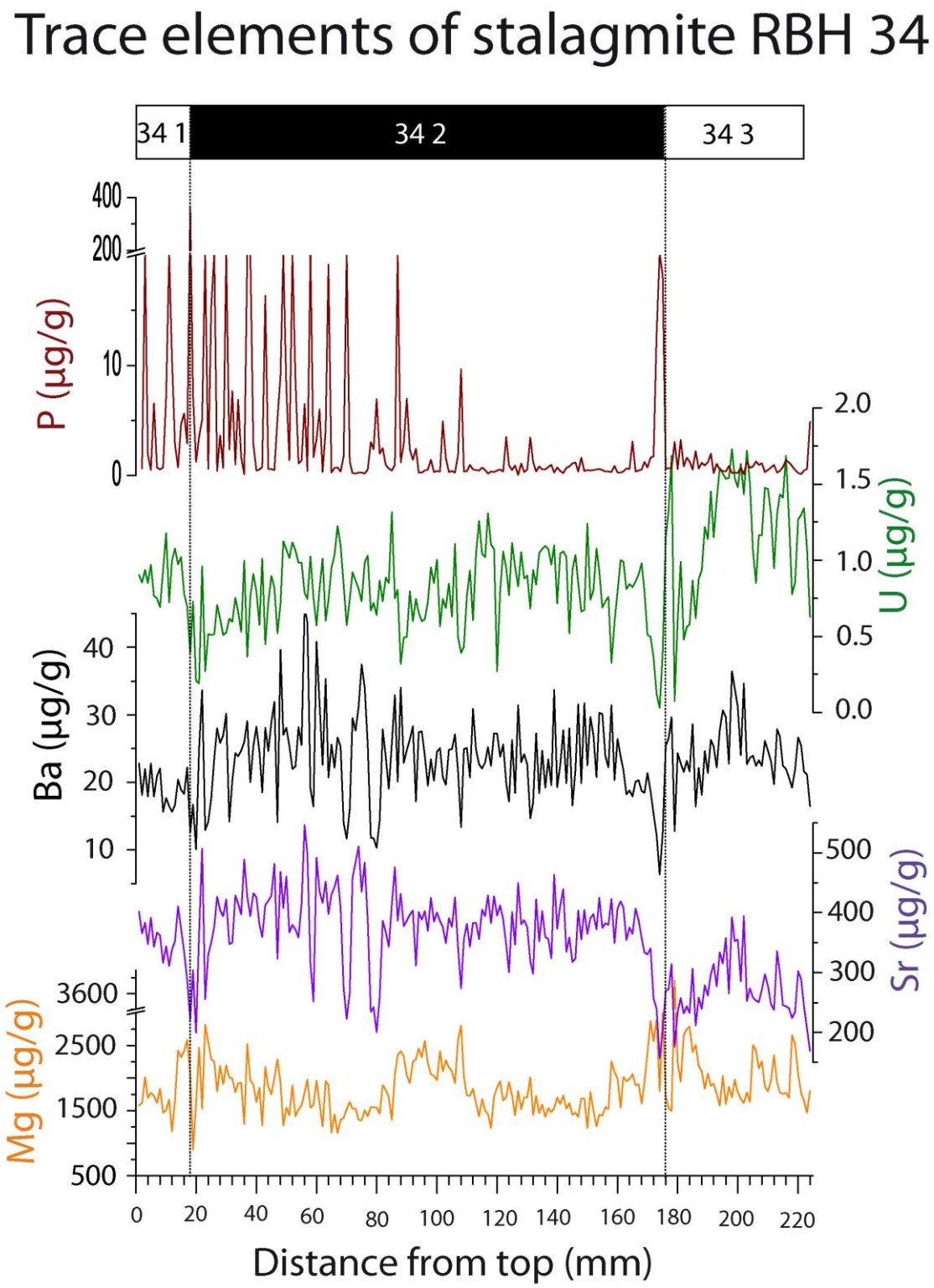

Figure 4.15: Figure 4.15 displays the distribution of selected trace elements plotted against distance from top (dft) and allocated to the designated GIS phases as described in chapter 4.2.2 for stalagmite RBH 34. Color code: Orange: Magnesium (Mg), Pink: Strontium (Sr), Black: Barium (Ba), Olive: Uranium (U) and Brown: Phosphorous (P).

4.4.3 Trace elements of RBH 39

As observed for stalagmite RBH 34, U and Sr characteristics reveal similar patterns along the whole profile. Fig. 4.16 demonstrates that all elements displayed are depleted in RBH 39a and show minimum concentrations. However, except for P, all elements experience a sharp concentration increase shortly before the transition to the GIS 24 phase. Large fluctuations in all elements can be observed during the GIS 24 phase. During the GIS 23 phase, the Ba pattern shows the largest variability. In this phase Mg is in anti-phase to the U and Sr characteristics.

The GIS 21 phase is characterized by large rapid and shifts in U, Sr and Ba and reach maximum concentrations of 1.42µg/g, 390µg/g and 41.4µg/g, respectively. Mg however, does not show similar characteristics and reveals an anti-phase pattern to U, Ba and Sr during the pronounced peak. The P concentrations during the GIS 23 phase are characterized by a high and frequent fluctuation, but do not reveal any specific pattern. The GIS 20 phase is characterized by a large positive shift in all elements. However, this is not the case for Ba. Here, a rapid decrease of 6µg/g can be observed.

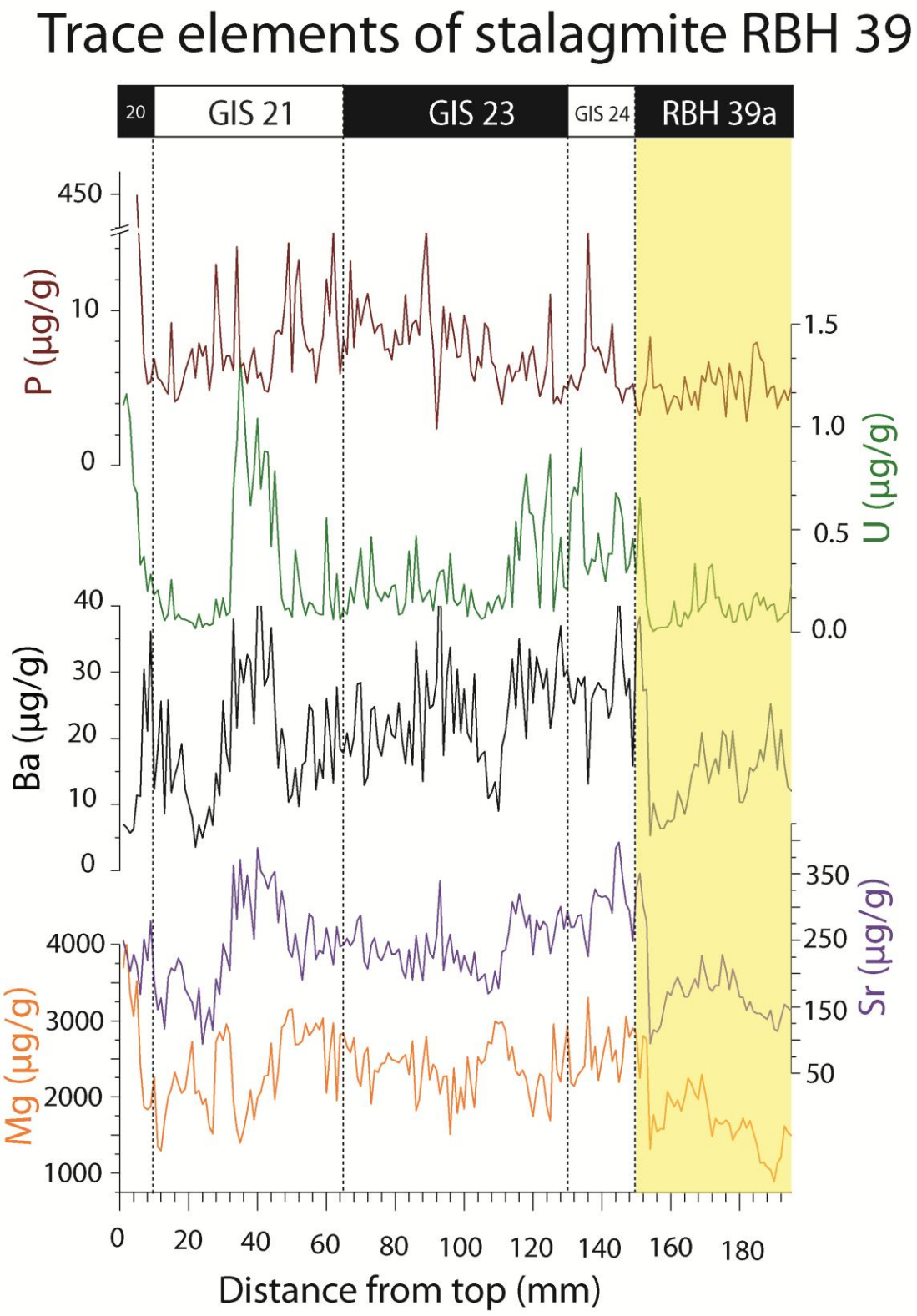

Figure 4.16: Figure 4.16 displays the distribution of selected trace elements plotted against distance from top (dft) and allocated to the designated GIS phases as described in chapter 4.2.3 for stalagmite RBH 39. Color code: Orange: Magnesium (Mg), Pink: Strontium (Sr), Black: Barium (Ba), Olive: Uranium (U) and Brown: Phosphorous (P). The yellow box signalizes the transition to stalagmite RBH 39a.

4.4.4 Trace elements of RBH 47

In general it can be observed that the Mg concentration of stalagmite RBH 47 is lower than in the other RBH stalagmites. Fig. 4.17 reveals a decrease in U, Sr and Mg concentrations during the late Eemian phase, while P shows only low concentrations between 5-10µg/g. Ba scatters between 15 and 30µg/g. During the GIS 24, phase all concentrations are relatively low. Ba is an exception shows large scatter but an overall decreasing trend. In the subsequent, diagenetic disturbed phase, an increase in all elements can be observed. In this phase, P reflects highest concentrations and reaches its maximum concentration of 300µg/g. As shown in chapter 4.1.4, this phase coincides with the occurrence of brownish dark layers and a high content of organic matter.

During the GIS 21 phase a general decrease in P, U, Ba and Sr concentrations can be observed, while an increase of Mg shows the opposite trend. In the GIS 20 phase, a large variation of P, Ba, Sr and Mg is detectable, while the U concentration remains relatively stable and presents concentrations that scatter around 0.5µg/g. During the GIS 19 phase, most elements show a decreasing trend, while Mg and P concentrations are increasing.

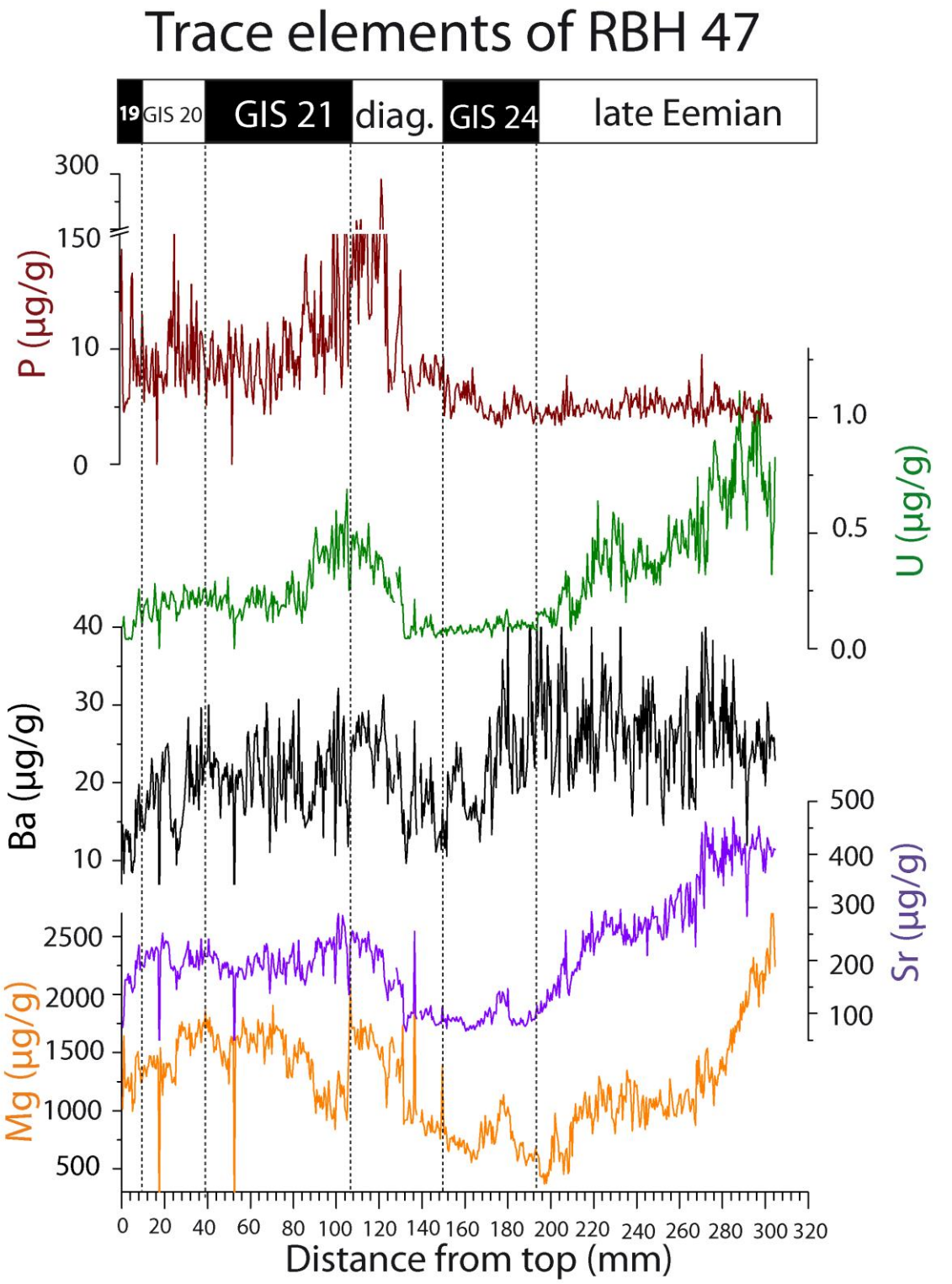

Figure 4.17: Figure 4.17 displays the distribution of selected trace elements plotted against distance from top (dft) and allocated to the designated GIS phases as described in chapter 4.2.4 for stalagmite RBH 47. Color code: Orange: Magnesium (Mg), Pink: Strontium (Sr), Black: Barium (Ba), Olive: Uranium (U) and Brown: Phosphorous (P).

5. Discussion

The discussion is divided into four parts. Chapter 5.1 reveals the potential Th/U-age dating problems of stalagmites due to post-depositional diagenesis (PDD). These problems are related to age inversions. Therefore here a conclusion of (Tolzmann et al. 2012, under review) is given, which addresses these problems based on observations of stalagmite RBH 34 and models the effect of PDD on the U-system. In addition, stalagmite RBH 47 reveals also signs of PDD. However, in contrast to stalagmite RBH 34 PDD in stalagmite RBH 47 is only restricted to a small section. Nonetheless this section is presented and discussed in terms of PDD.

5.1 Diagenetic influence on 230Th/U-ages

5.1.1 Diagenetic processes in speleothems

Post-depositional diagenesis (PDD) of speleothems cannot occur under the 'normal' conditions, which were described in chapter 2.1 because supersaturation of the drip water precludes post-depositional dissolution of speleothem calcite and, as a consequence, mobilization of U-series isotopes. Based on the definition provided by Frisia and Borsato (2010), Borsato et al. (2003) and Frisia et al. (1993; 1996), all potential processes resulting in dissolution and re-precipitation of speleothem calcium carbonate are refer as post-depositional diagenesis (PDD). Corrosive water is required in order to dissolve previously deposited speleothem calcite. There are three potential scenarios how corrosive drip waters may arise.

The first scenario is mixing corrosion (Bögli, 1978; Gabrovsek and Dreybrodt, 2000). Mixing corrosion arises when two solutions, which are both saturated with respect to calcite but with different chemical compositions, are mixed. Due to the non-linear relationship between pCO_2 and the Ca concentration of the drip water, the new (mixed) solution may be undersaturated with respect to calcite and have the potential to dissolve carbonate again (Bögli, 1978). Considering the complex network of fissures occurring in a karst aquifer, mixing corrosion may occur at different times and different drip sites in the same cave system. However, this process only represents a valid assumption for post-depositional dissolution in stalagmites if cave pCO_2 is in the range of the pCO_2 of

the solution itself. Establishment of relatively high cave pCO_2 requires poor air ventilation inside the cave. As described in section 2, the RBH has no natural entrance and was, thus, only poorly ventilated. This may lead to high cave pCO_2 values inside the cave. Therefore, it is possible for RBH that mixing corrosion triggered post-depositional speleothem dissolution, which in turn led to altered ^{230}Th/U-ages.

The second potential scenario resulting in corrosive water is fast flow of water through the epikarst. Fast flowing water, which has previously equilibrated with high soil pCO_2, does not have enough time for calcite dissolution and may still be undersaturated with respect to calcite when it enters the cave (Kaufmann, 2003). This might be the case if the water flows through large fissures caused, for instance, by dissolutional widening (Bögli, 1978; Gabrovsek and Dreybrodt, 2000). Dissolutional widening of primary fractures does not only result in faster flow velocities resulting in corrosive waters, but may also establish preferential flow paths for percolating water in the karst. As a consequence, dissolutional widening may result in a change from supersaturated to undersaturated drip water, simply due to a change in the karst aquifer characteristics.

The third potential scenario may occur if cave pCO_2 is higher than the pCO_2 in the soil zone. In this case, the drip water would take up CO_2 from the cave air, become undersaturated with respect to calcium carbonate and dissolve speleothem calcite. This scenario may be found for very poorly ventilated cave systems with less vegetation cover (e.g., in high altitude areas or during glacial/stadial conditions). This scenario would result in speleothem growth during warm conditions (interglacials and interstadials) and post-depositional dissolution of the same speleothems during cold (glacial/interstadial) conditions. All three scenarios are, in principle, possible for the RBH.

The uranyl ion $(UO_2)^{2+}$ is highly soluble in corrosive waters (Langmuir, 1978; Kelly et al., 2003). Thus, U may be re-mobilized from the calcite crystal lattice when corrosive water enters the cave and drips onto the stalagmites surface (Railsbeck et al., 2002). In contrast, Th will most likely not be re-mobilized by corrosive waters because it is highly particle reactive and rapidly adsorbed onto particles. Thus, Th will usually remain in the surrounding calcium carbonate matrix during post-depositional dissolution of speleothem calcite (Scholz et al., 2004).

As a consequence, post-depositional diagenesis in stalagmites may have a large effect on (^{230}Th/^{238}U) ratios leading to both apparently older and younger ^{230}Th/U-ages. If the sample used for U-series dating suffered net U loss, the (^{230}Th/^{238}U) ratio will be higher

than expected from its age. If the sample gained U that was mobilized from other parts of the speleothem or originates from host rock dissolution, the (^{230}Th/^{238}U) ratio will be lower than expected. Both processes affect the radiometric clock and consequently lead to apparently wrong ^{230}Th/U-ages. A similar U-redistribution scenario has been described for fossil reef corals (Scholz and Mangini, 2007).

Post-depositional dissolution of speleothem calcite by corrosive waters does not only affect the U-series system, but also alters speleothem fabrics. According to Frisia and Borsato (2010), mosaic fabrics (e.g., Fig. 5.3A) are the clearest indicator of post-depositional diagenesis in spelothems. The corrosive drip waters dissolve the calcite at the speleothem surface and particularly along the crystal boundaries due to the reduced coalescence between single columnar crystals (Kendall and Broughton, 1978). This progressively leads to dissolution of speleothem calcite resulting in relatively large voids.

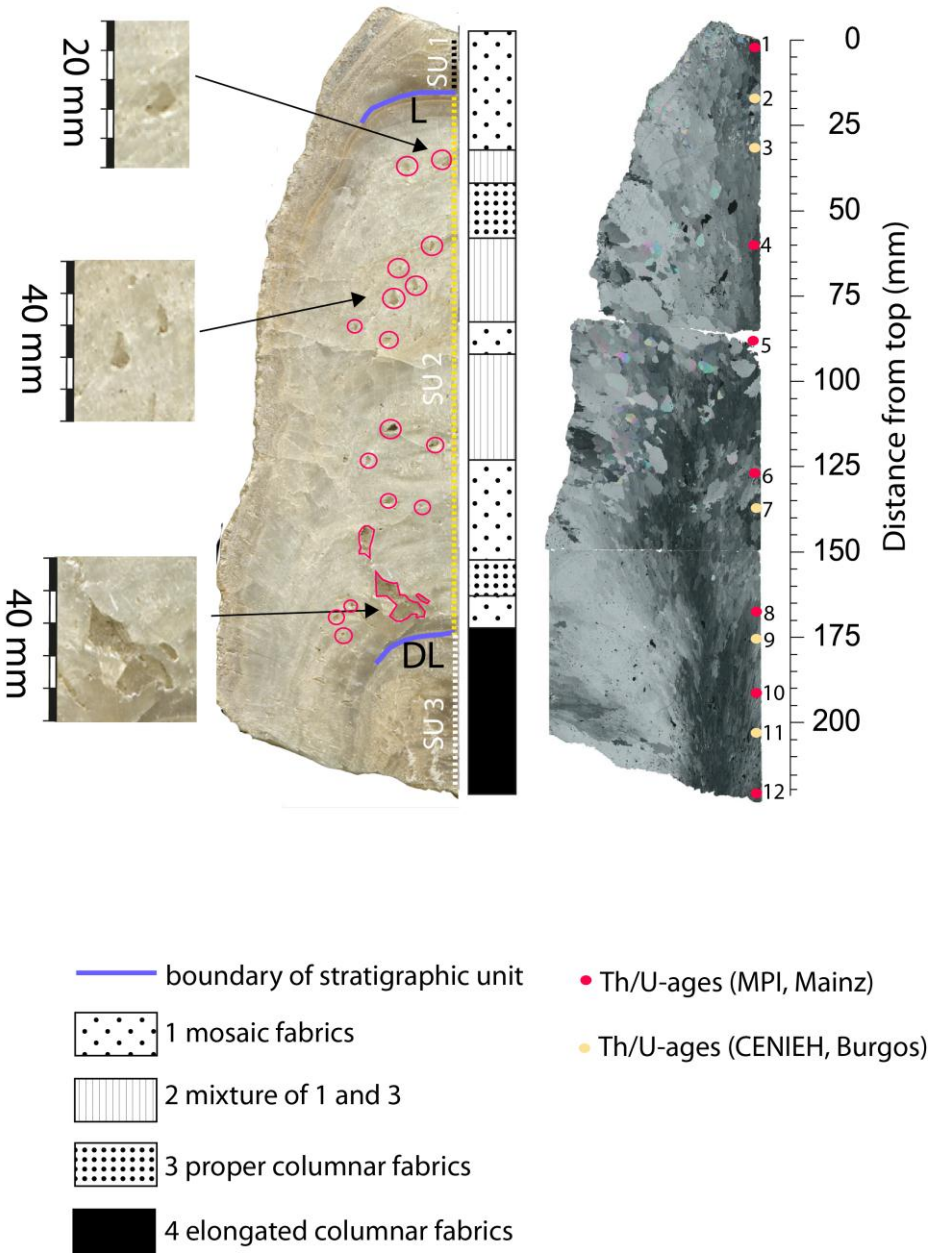

Figure 5.1: Stratigraphy and morphology of stalagmite RBH 34. The right panel shows stalagmite RBH 34 under crossed polarized light. Red dots indicate where samples for ^{230}Th/U-dating at MPIC have been taken. Yellow dots show the position of the ^{230}Th/U-dating samples for CENIEH.

Speleothem petrography is shown in the middle panel. Stalagmite RBH 34 is sub-divided into three growth phases (GP 1-3) as indicated by the dashed lines in the left panel. The transition from one growth phase to another is highlighted by two layers (DL and L) indicated by the blue lines.

The sample exhibits several voids. For better visualization of the structure and dimension of these voids, the left panel shows enlarged pictures of selected voids.

The relicts of these dissolution voids are still visible in stalagmite RBH 34 (Fig. 5.1). Subsequent to dissolution due to one of the scenarios described above, a change to supersaturated drip waters may result in filling of the voids with water and re-precipitation of calcite. The mosaic fabric without a uniform orientation results from the growth of new calcite crystals on the surfaces of the voids with randomly oriented c-axes (Hill and Forti, 1993). These crystals grow until the voids are filled, which leads to the observed mosaic fabrics or a mixture of mosaic and proper columnar fabrics (Fig. 5.1).

5.1.1.1 Identification of diagenetically altered sections in stalagmite RBH 34

Stalagmite RBH 34 shows several voids along the growth axis (e.g., at 145-170mm dft, Fig. 5.1). These are interpreted as post-depositional dissolution features, which may be the result of infiltration of corrosive waters along crystal boundaries. The porous structure of Stalagmite RBH 34, thus, provides a first indication for the influence of diagenesis on this speleothem.

Furthermore, GP 1 and 2 of stalagmite RBH 34 are mainly characterized by mosaic fabrics. According to Frisia and Borsato (2010), mosaic fabrics are typical for post-depositional replacement of columnar fabrics due to dissolution and re-precipitation processes and are, therefore, clear evidence for post-depositional diagenesis in speleothems. The frequent occurrence of mosaics and the mixture of mosaics and proper columnar fabrics in GP 1 and 2 consequently most likely mirrors post-depositional diagenesis in stalagmite RBH 34. Mosaic fabrics are the result of secondary calcite crystals filling the voids and may, thus, be considered as the final product of the dissolution/re-precipitation processes in speleothems (Frisia and Borsato, 2010).

As described in section 5.1, GP 3 only shows elongated columnar fabrics. According to Frisia and Borsato (2010), this type of fabric indicates unaltered speleothem calcite, which should be appropriate for ^{230}Th/U-dating.

Thus, summarizing the macroscopic and microscopic observations on stalagmite RBH 34, it is concluded that GP 1 and 2 have suffered strong post-depositional diagenetic alteration. This is expected to be also reflected in the U-series system. The effect of post-depositional diagenesis on the ^{230}Th/U-ages of stalagmite RBH 34 is discussed in the following section.

5.1.1.2 Identification of the diagenetically altered section in stalagmite RBH 47

As has been stated in chapter 4, the entire GP 47-4 (109-150mm, dft) is characterized by age inversions. Within this GP a section of fain to thick brownish growth layers is exposed. The 1st panel of Fig. 5.2 shows an image of GP 47-4, whereas in the 2nd panel of Fig. 5.2 a thin section image of same GP is shown. The 2nd panel also reveals that mosaic fabrics are predominant fabric type. These mosaic fabrics and consequently the age inversions might be related to the processes discussed in chapter 5.1.2.

The age inversions reported for the brownish layer might be additionally related to a different process. Frisia et al. (2000) point out that stalagmite layers might be associated with climate (e.g. heavy rain events). Thus, these layers might be formed organic colloids, which are mainly deposited during wetter phases. It is possible that a degassing of organic material occurs after its subsequent deposition. Post depositional degassing of organic material may lead to open system conditions, which in turn would lead to age inversions indicated by mosaic fabrics. In that case, the brownish layers should contain organic material and additionally, should be characterized by mosaic fabrics. The sample treatment with H_2O_2 for ^{230}Th/U-age dating revealed that the section of the brownish layers is associated with a high content of organic material and reveals mosaic fabrics as predominant type. Thus it is possible that the post depositional degassing of the organic material caused the age inversions, at least for the section with the dark brownish layers.

However, in the following chapters the focus of PDD is based on observations of stalagmite RBH 34.

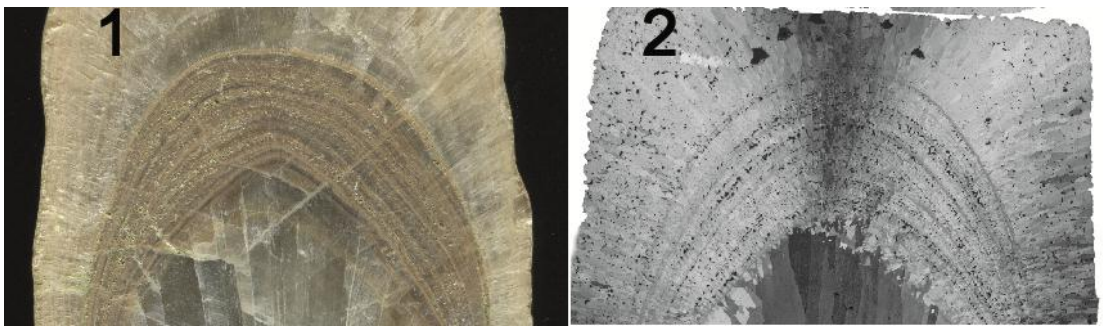

Figure 5.2 The 1st panel of Fig. 5.2 reveals a simple image of GP 47-4 (109-150mm, dft) of stalagmite RBH 47, whereas the 2nd panel shows the thin section of the same GP. As revealed in panel 2, mosaic fabrics are the predominant fabric type.

5.1.2 Influence of post-depositional diagenesis on the ^{230}Th/U ages of stalagmite RBH 34

Even though stalagmite RBH 34 shows clear evidence for post-depositional diagenesis and at least some of the determined ^{230}Th/U-ages are, thus, not reliable, it is possible to deduce that the sample grew during MIS 5. Due to the location of the RBH in northern Germany, it is presumed that stalagmite RBH 34 grew only during warm climate phases of MIS 5, i.e., MIS 5a, c and e. This is in agreement with the findings of other studies showing that speleothem growth is sensitive to the climatic conditions above the cave (Spötl et al., 2002; Holzkämper et al., 2004). According to Lisiecki and Raymo (2005), MIS 5e lasted from 130 to 118ka. MIS 5c lasted from 108 to 95ka, whereas MIS 5a lasted approximately from 85 to 71ka. While MIS 5e represents the Last Interglacial, MIS 5a and c reflect warmer periods within MIS 5.

The ^{230}Th/U-ages reveal age inversions in GP 2 and 3 of stalagmite RBH 34 (Fig. 5.1). Age inversions are independent of the laboratory where the ages have been determined because they are also observed in the individual subsets measured at CENIEH and the MPI, Mainz (compare Appendix A and Fig. 5.4). These age inversions in GP 2 result from post-depositional diagenesis as suggested by the mosaic fabrics (Figs. 5.1 and 5.3 A) observed in the MIS 5a and c growth phases. In contrast, the petrography of GP 3, corresponding to MIS 5e, shows no evidence for diagenesis (Fig. 5.1). Thus, based on the petrography, it is expected that the ^{230}Th/U-ages of GP 3 show no evidence for diagentic alteration. However, the age at the bottom section of stalagmite RBH 34 (221mm dft, Appendix A) of 119.3 ± 1.1ka is significantly younger than the sample at 204mm dft (123.4 ± 1.0ka). Thus, even this petrographically unaltered section shows one age inversion.

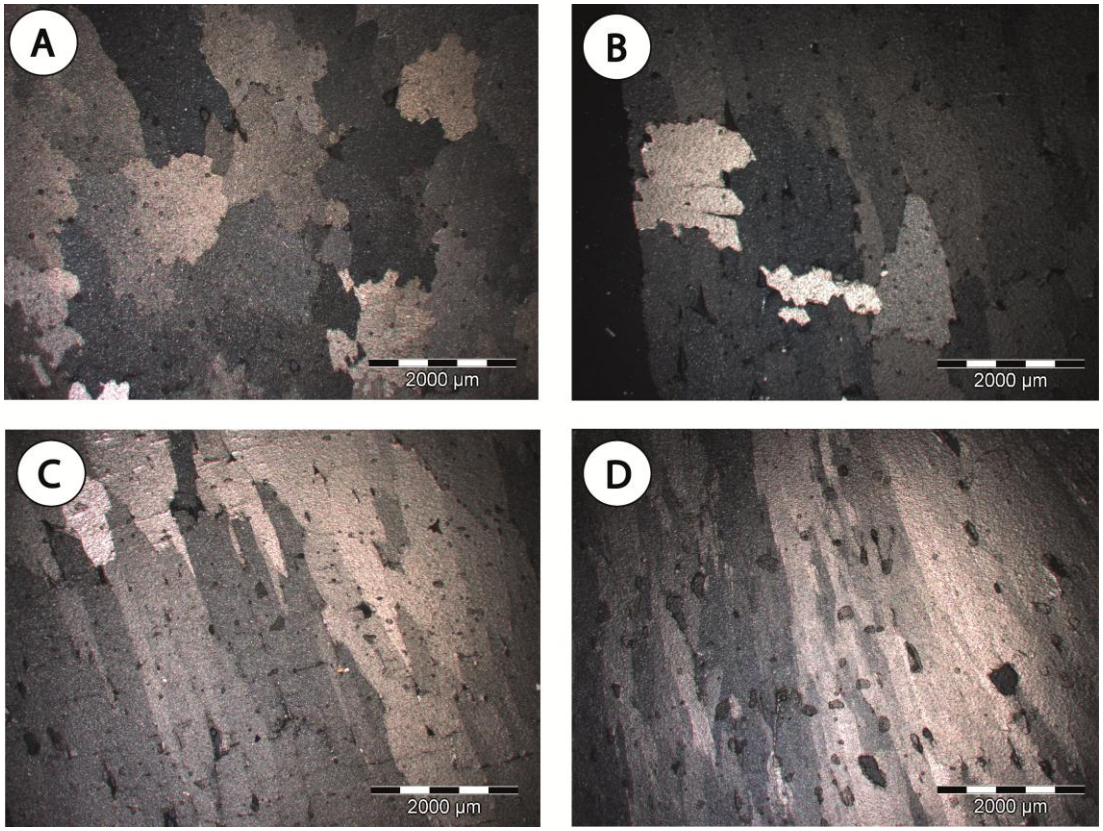

Figure 5.3: Examples for the four observed different types of calcite fabrics in stalagmite RBH 34. A: mosaic fabrics, B: mixture of mosaic and proper columnar fabrics, C: proper columnar fabrics, D: elongated columnar fabrics

One possible explanation for this observation might be that the U-series system is more sensitive for post-depositional diagenetic alteration than any other parameter as has been observed for fossil reef corals (Chen et al., 1991; Scholz et al., 2007). Despite from this age inversion, the three upper ages of GP 3 (ages 9-11, Appendix A) are in stratigraphic order and provide a chronology for the late MIS 5e.

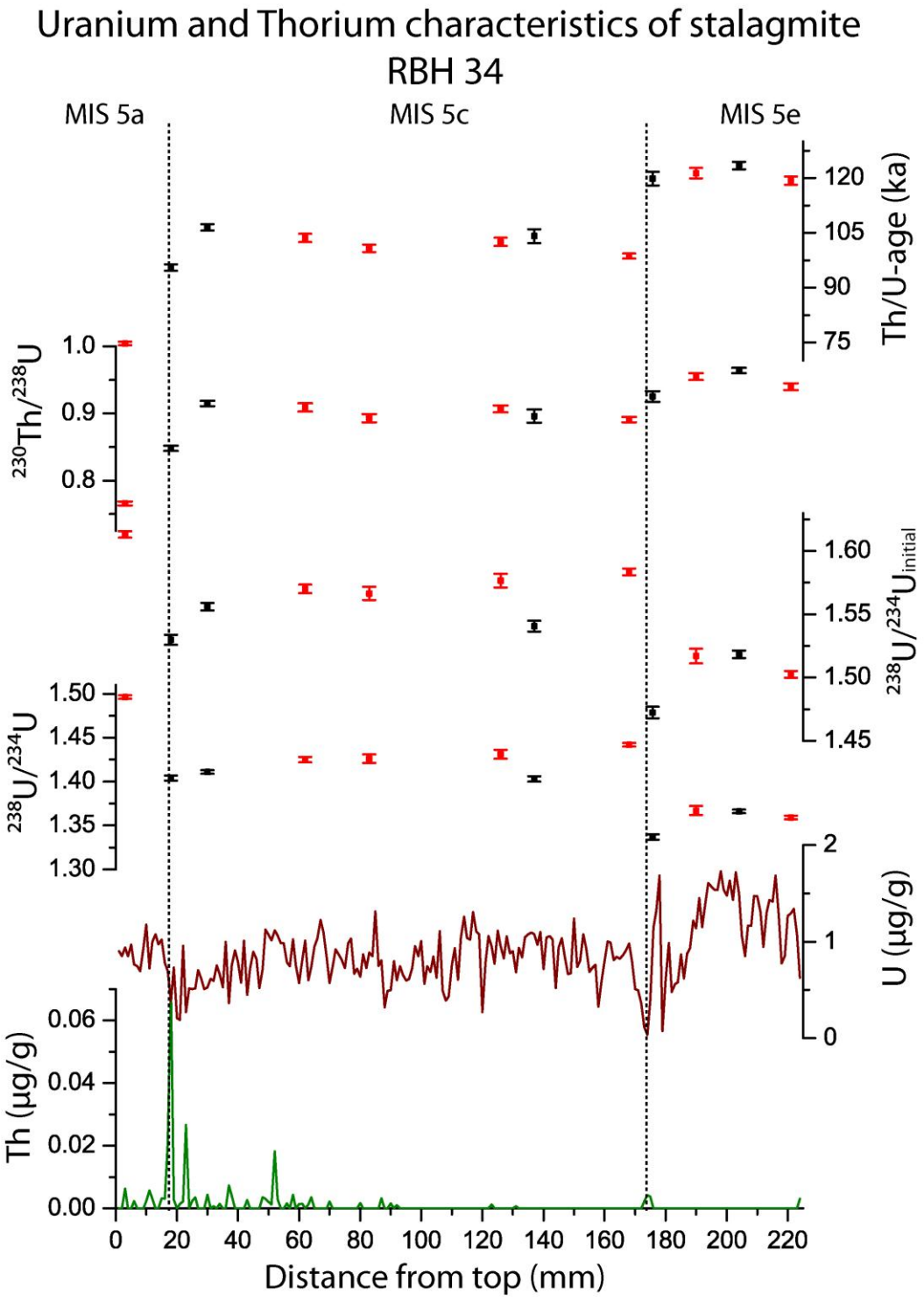

Figure 5.4: Compilation of the U-series data and comparison with the different types of observed fabrics. U and Th concentration, ^{230}Th/U-ages, (^{234}U/^{238}U), (^{234}U/^{238}U)$_{initial}$ and (^{230}Th/^{238}U) activity ratios are shown against dft of the speleothem. The dashed lines represent the hiatuses between GP 1, 2 and 3 corresponding to MIS 5a, c and e.

Both the initial and the measured (^{234}U/^{238}U) activity ratio are lower for GP 3 compared to GP 1 and 2. There are two possible explanations for this: The first explanation is that

the ($^{234}U/^{238}U$) activity ratio of the drip water was lower during MIS 5e compared to MIS 5c and a due to a change of environmental conditions. For instance, Hellstrom and McCulloch (2000) suggested that ($^{234}U/^{238}U$) activity ratios in speleothems are related to the amount of precipitation above the cave with lower activity ratios indicating more humid conditions. The lower ($^{234}U/^{238}U$) activity ratios observed during MIS 5e may, thus, reflect wetter conditions during the Last Interglacial compared to the subsequent interstadials. The second explanation is that the ($^{234}U/^{238}U$) activity ratio was initially similar for all GPs and has subsequently been altered towards higher ratios in GP 1 and 2 by diagenesis. If the second explanation is true, one would expect a higher variability in ($^{234}U/^{238}U$) in the altered sections compared to the unaltered sections. However, this is not the case for the diagenetically altered sections of stalagmite RBH 34 (Fig. 5.4). Thus, it seems more plausible that drip water ($^{234}U/^{238}U$) activity ratio was lower during the end of the Eemian than during MIS 5a and c.

The 157mm long section GP 2 represents the largest part of stalagmite RBH 34 (Fig. 5.1). In total, seven $^{230}Th/U$-ages have been determined for this section. Fig. 5.1 clearly reveals that the complete unit is characterized by prominent age inversions. Nevertheless, the ages indicate that GP 2 largely formed during MIS 5c. The apparent age inversions are in line with the observed dominant mosaic fabric, which are considered as the final product of post-depositional diagenetic calcite dissolution induced by corrosive waters and subsequent re-precipitation. The magnitude of age inversions of GP 2 rarely exceeds 2 ka (Fig. 5.4 and 5.5) with the only exception at 168mm dft (98.6 ± 0.7ka, Appendix A), which is approximately 5 ka younger than the age above (137mm dft, 104.1± 1.9ka, Appendix A).

GP 1 is 18 mm long and the shortest section of stalagmite RBH 34 (Fig. 5.1). The clear predominance of mosaic fabrics in GP 1 indicates post-depositional diagenesis and puts the reliability of the determined $^{230}Th/U$-ages in question. Only one $^{230}Th/U$-age has been determined for this section (at 3mm dft, 74.7 ± 0.5ka, Appendix A) suggesting that GP 1 was deposited during MIS 5a. The hiatus between GP 1 and 2 (DL, Fig. 5.1) probably represents the transition between MIS 5c and 5a in stalagmite RBH 34.

5.1.3 Hypothetical age model for stalagmite RBH 34

The intention of this paper is to investigate and model the influence of post-depositional diagenesis in speleothems on the U-series system. GP 2, which corresponds to MIS 5c,

is the longest section of stalagmite RBH 34 and reveals the most age inversions (Fig. 5.4). Thus, it is focused on this section. The 'true' age of GP 2 is unknown due to diagenetic alteration and its effect on the ^{230}Th/U-ages. Therefore, a hypothetic age model is constructed for GP 2.

Figure 5.5 shows the ages determined for GP 2 (numbered 3 to 8, compare also Figs. 5.1 and 5.4 as Appendix A) connected with black lines. It is obvious that the ages scatter around an age of 103ka in contrast to what would be expected from the stratigraphy. In addition, a hypothetic age model is shown (red line), which assumes a phase of continuous growth for 3ka during Dansgaard/Oeschger (D/O) event 23(also called GIS 23). One could also assume linear growth during entire MIS 5c. However, this scenario this scenario is not further discussed because constant growth of stalagmites is relatively unlikely in nature. Also shown in Fig. 5.5 is the δ^{18}O record of the North GRIP ice core (NGRIP members, 2004) on the GICC05modelext time scale (Wolff et al. 2010) showing both cooler (stadials) and warmer (interstadials) phases during MIS 5c.

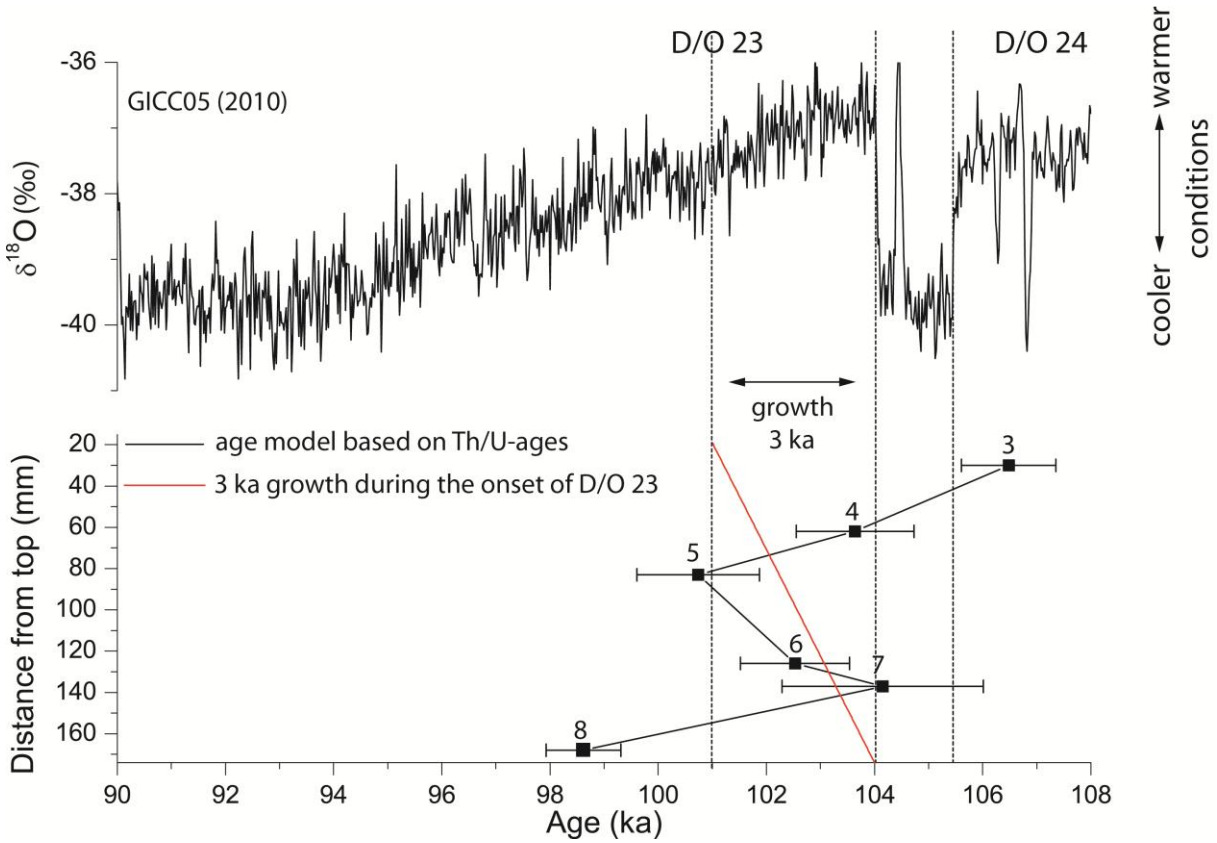

Figure 5.5: Determined ^{230}Th/U-ages and comparison with the hypothetic age model. Straight black lines connect the observed ages for stalagmite RBH 34, and the red line denote the hypothetic age model. Also shown is the δ^{18}O record of the NGRIP ice core (NGRIP members, 2004).

In the hypothetic age model, it is assumed that speleothem growth at RBH is sensitive to millennial scale climate variability during MIS 5c (i.e., the GIS). Such a scenario is not unlikely because relatively short growth phases are often observed in speleothems (e.g., Holzkämper et al., 2004; Couchoud et al., 2009; Fleitmann et al., 2009; Boch et al., 2011; Cheng et al., 2012). The GIS were first described by Dansgaard et al. (1993) and are characterized by abrupt shifts from cool (stadial) to warm (interstadial) conditions. After rapid warming, the GIS show an unstable plateau and gradual cooling prior to a final, rapid cooling representing the transition to stadial conditions.

According to Lisiecki and Raymo (2005), MIS 5c lasted for about 15.5ka from 105.5 to 90ka, and GIS 23 is the most prominent warm event during MIS 5c. GIS 23 has a duration of 14ka lasting from 104 to 90ka.

Most of the ^{230}Th/U-ages determined in GP 2 are within a relatively small range of 3ka, which is approximately in agreement with the inception of GIS 23 at 104ka. Therefore, an age model that implies constant and linear growth for about 3ka after the onset of GIS 23 is suggested. This suggests a growth rate of 51.7µm/a. The corresponding hypothetic ages at the positions of the ^{230}Th/U-age determinations are given in Tab. 5.1. Subsequent to this growth phase, climate conditions might have changed again towards drier and cooler conditions, as suggested by NGRIP δ^{18}O values (Fig. 5.5), and stalagmite RBH 34 may have stopped growing.

Ages 6 and 7 agree within error with the hypothetical age model (Fig. 5.5). This is not surprising regarding the fact that both ages scatter around 103ka. Ages 4 and 5 are also in the range of the corresponding hypothetic ages (Tab. 5.1). Two ages show a larger deviation from the hypothetic age model. Age 3 at 30mm dft is 106.5±0.9ka and, thus, approximately 5.3ka older than suggested by the age model. Age 8 at 168mm dft is with 98.6±0.7ka the youngest age of GP 2 and 5.3ka younger than suggested by the hypothetic age model.

Table 5.1: Corresponding hypothetic ages for stalagmite RBH 34.

age point	depth (mm)	age corr.	±	hyp GIS 23	Δ.age diff.
3	30	106.5	0.9	101.2	5.3
4	62	103.6	1.1	101.8	1.8
5	83	100.7	1.1	102.2	-1.5
6	126	102.5	1	103.1	-0.6
7	137	104.2	1.9	103.3	0.9
8	168	98.6	0.7	103.9	-5.3

5.1.4 ^{230}Th/U-age alteration model

The study reveals post-depositional diagenetic alteration of stalagmite RBH 34, which results in both apparently older and younger ^{230}Th/U-ages. Here, a conceptual model calculating the effects of post-depositional open-system behavior for a better understanding of the potential effects of diagenesis on the U-series system is presented.

The model relies on the following assumptions:

1. During initial speleothem growth, only U is incorporated, and the U-series system remains closed until diagenetic alteration occurs for the first time.
2. If corrosive drip water occurs, U may be mobilized. Thus, a specific fraction of the U initially incorporated in the speleothem is lost. Th, in contrast, is not mobilized due to its high particle reactivity.
3. Subsequently, drip water supersaturated with respect to calcite may enter the cave, and re-precipitation of speleothem calcite in the voids and channels produced by the corrosive water may occur. This would result in mosaic fabrics and post-depositional addition of U. Th is assumed to be not contained in the drip water and is, thus, not added.

The model has five important variables:

1. Time of formation (real age of the stalagmite).
2. Timing of speleothem dissolution by corrosive drip water (i.e., the dissolution time, given in years after speleothem deposition) - ΔT_1 (time between formation and dissolution).
3. Timing of re-precipitation of calcite by supersaturated water (i.e., the re-precipitation time, given in years after calcite dissolution occurred) - ΔT_2 (time between dissolution and re-precipitation).
4. The amount of loss of U relative to the initial U content of the sample - ΔU_1.
5. The amount of subsequent addition of U relative to the initial U content of the sample - ΔU_2.

For reasons of simplicity, it is assumed that both calcite dissolution and re-precipitation occur instantaneously and that the (^{234}U/^{238}U) activity ratio is not influenced by diagenesis. Also more complex scenarios with multiple phases of dissolution and re-

precipitation cannot be excluded a priori. However, in order to qualitatively demonstrate the effect of the diagenetic processes and to estimate the associated age bias, this simple model is adequate.

The effect of diagenesis on the ^{230}Th/U-ages strongly depends on the timing of dissolution and re-precipitation after initial deposition. The magnitude of U loss and subsequent addition is also important. In general, post-depositional U loss leads to increased (^{230}Th/^{238}U) activity ratios and, thus, apparently older ages. In contrast, post-depositional addition of U results in decreased (^{230}Th/^{238}U) activity ratios and, thus, apparently younger ages.

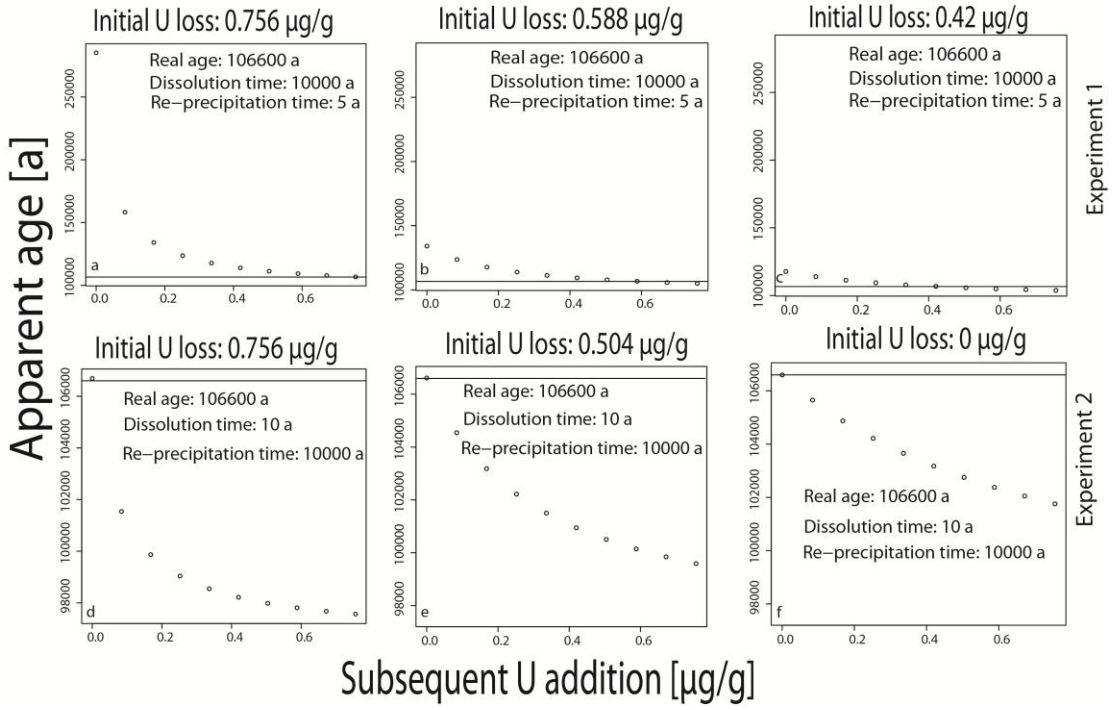

Figure 5.6: Application of ^{230}Th/U-age alteration model to demonstrate extreme scenarios for age inversions for apparently too old (experiment 1) and apparently too young ages (experiment 2). The plots show the relationship between apparent age and subsequent U addition during re-precipitation of calcite. The amount of initial U loss associated with calcite dissolution is shown at the top of the individual plots. The horizontal straight line represents the true age of the sample.

Two extreme scenarios for post-depositional diagenesis in Fig. 5.6 for both apparently older and younger ^{230}Th/U ages are presented. An initial (^{234}U/^{238}U) activity ratio of 1.57, a U concentration of 0.84µg/g and a true age of 106.6ka for both cases was used. Figs. 5.6a - c show experiment 1, where the ^{230}Th/U-age alteration model with a relatively long ΔT_1 of 10 ka and a very short ΔT_2 of 5a is applied. Three different amounts of U loss associated with dissolution of calcite are shown: 90% (0.756µg/g,

Fig. 5.6a), 70% (0.588µg/g, Fig. 5.6b) and 50% (0.42µg/g, Fig. 5.6c). It is obvious that all scenarios associated with net U loss (i.e., more U has been lost than is subsequently added) result in apparently older ^{230}Th/U-ages. All scenarios with net U gain result in younger ages. The magnitude of the alteration strongly depends on the amount of initial U loss. For an initial loss of 90% of U, the effect is up to 173ka (Fig. 5.6a), for an initial loss of 50%, the effect is much smaller and varies between 2 and 15.5ka.

Figs. 5.6d – f show experiment 2, which demonstrates how to produce apparently younger ages. In this scenario, ΔT_1 is very short (10a), and ΔT_2 is relatively long (10ka). Again three different amounts of initial U loss of 90% (0.756µg/g, Fig. 5.5d), 60% (0.504µg/g, Fig. 5.5e) and 0% (0µg/g, Fig. 5.6f) are shown. It is obvious that such a scenario always results in apparently younger ^{230}Th/U-ages. The magnitude of the alteration mainly depends on both the amount of initial U loss and the amount of U added during re-precipitation of speleothem calcite (Figs. 5.6d-f). For an initial U loss of 90% (0.756µg/g) and subsequent U addition of 0.756µg/g, the maximum age difference between the "true" and the altered ^{230}Th/U-age is 9ka (Fig. 5.6d). For an initial U loss of 0µg/g and subsequent addition of 0.756µg/g (90%), the age difference between altered and true age is 4.8ka (Fig. 5.6f). Although both experiments represent extreme scenarios, they cannot exclude such extreme cases in nature are priori. However, such extreme scenarios for stalagmite RBH 34 are not assumed because the magnitude of the age inversions observed in GP 2 rarely exceeds 2ka (Fig. 5.4).

5.1.5 Application of the ^{230}Th/U-age alteration model for stalagmite RBH 34

The processes discussed above can be used to explain both the apparently older and younger ^{230}Th/U-ages. Based on the hypothetic age model (Fig. 5.5 and Tab. 5.1), the ^{230}Th/U-age alteration model should be able to produce apparently older as well as apparently younger ^{230}Th/U-ages. Thus, two further experiments are conducted. Experiment 3 results in apparently older ages, whereas experiment 4 produces apparently younger ages.

For experiment 3, it is assumed that age 3 is approximately 5.3ka older than the age suggested by the hypothetical age model at the equivalent depth (106.5 ± 0.9ka compared to 101.2ka, Fig. 5.4 and Tab. 5.1). There are several scenarios using an initial

($^{234}U/^{238}U$) activity ratio of 1.57 and a U concentration of 0.84µg/g, resulting in an age, which is apparently older by 5.3ka. For instance, if identical values for ΔT_1 and ΔT_2 of 1.5 ka are considered and an initial U loss of 90% (0.756µg/g), subsequent U addition of 10% (0.084µg/g) is required to produce an age apparently older by 5.3ka (Fig. 5.6a). Another possible scenario assumes an initial U loss of 60% (0.504µg/g), no subsequent U addition, ΔT_1 = 3ka and ΔT_2 = 2ka (Fig. 5.7b).

In experiment 4, it is assumed that ^{230}Th/U-age number 5 is approximately 1.5 ka younger than suggested by the hypothetical age model for the equivalent depth (Tab. 5.1). If a ΔT_1 of 10a, a ΔT_2 of 5ka is assumed, an initial U loss of 30% (0.252µg/g) and subsequent U addition of 30 % (0.252µg/g), the effect would be approximately 1.5ka (Fig. 5.7c).

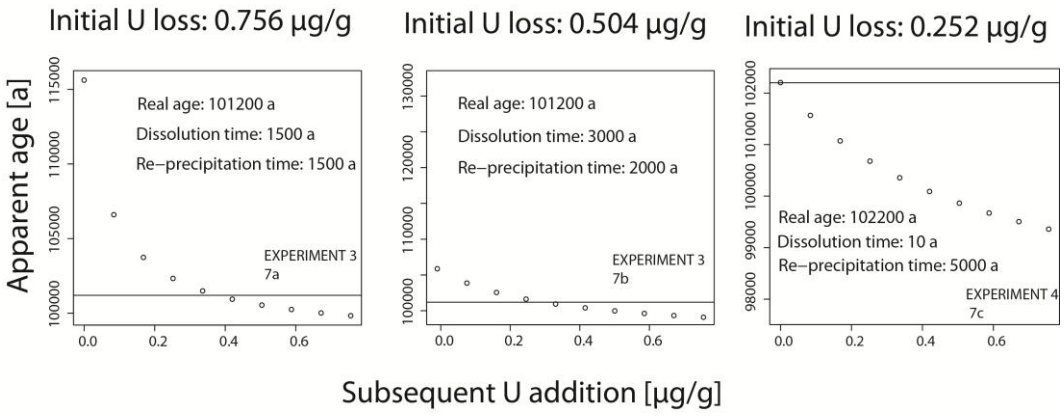

Figure 5.7: Application of ^{230}Th/U-age alteration model for stalagmite RBH 34. Figs. 5.7a and b (experiment 3) show how apparently older ages can be produced, whereas Fig. 5.7c provides a scenario for apparently younger ages (experiment 4).

Comparison of the age data with the hypothetic age models shows that the model is generally able to explain the observed effects. Furthermore, the data suggest that the largest alteration effect on Th/U-ages can be seen at the beginning and at the end of the stalagmite RBH 34 growth phases during MIS 5c (Fig. 5.5).

5.1.6 Climatic forcing of diagenesis in RBH speleothems?

It is hypothesized that speleothem growth at RBH is linked to the onset of the D/O

events assuming that speleothem growth is sensitive to climate forcing. Is it possible that speleothem diagenesis is also triggered by climatic parameters? During warm periods, high soil pCO_2 values are observed due to root respiration and soil bacteria (Baldini et al., 2006). However, this is not the case for cold phases due to the reduced vegetation cover. During transitions from cold to warm periods, it is possible that the vegetation is not sufficiently developed yet to produce high soil pCO_2 values (Baldini et al., 2005). In this case, cave pCO_2 may be higher than soil pCO_2, and when the drip water enters the cave it may become undersaturated with respect to calcite and dissolve the stalagmite surface.

Experiment 3 (Fig. 5.7a) reflects such a scenario. Before the onset of GIS 23, cold and dry conditions above the cave resulted in reduced vegetation and probably soil degradation. Furthermore, the dry conditions may have led to the drip site running dry. These conditions lasted for ca. 1.5ka (Fig. 5.5). After the onset of GIS 23, drip water entered the cave, became corrosive because cave pCO_2 was higher than the low pCO_2 in the soil zone and dissolved the speleothem surface. The basic requirement for such a scenario would be a poorly ventilated cave in order to preserve high cave pCO_2. That is the case for the Riesenberghöhle because it probably had no natural entrance. Subsequently (i.e., 1500 a later), when the soil above the cave has been re-established, drip water, which is oversaturated with respect to calcite, enters the cave, and calcite precipitation starts again.

There is no petrographic evidence for constant supply of corrosive waters over long time-scales (i.e., several 100a). However, stalagmite RBH 34 shows several voids along the whole profile (e.g., in 30mm dft, Fig. 5.1), which may indicate infiltration of corrosive water along crystal boundaries. This suggests that even if corrosive drip water was only supplied during rather short events (e.g., at the beginning of the GIS), lower sections of the stalagmite could have been affected by dissolution. In this case, supply of corrosive waters may have been induced by climate change above the cave.

However, there are also two potential scenarios (e.g., experiment 4, Fig. 5.7c) indicating that corrosive waters are not related to climate change:

1. Mixing corrosion may have generated corrosive water (Bögli, 1978). This may occur when high amounts of precipitation cause overflow of storage reservoirs as described by Tooth and Fairchild (2003).
2. Another explanation for corrosive drip water, as explained above, is

dissolutional widening of primary fractures. This may also be forced by high precipitation amounts, which generate higher fluxes of percolating water through the aquifer causing both dissolutional widening and storage overflow.

5.2 Conduction of RBH stalagmite age models

In chapter 5.1 it has been proved that some RBH stalagmites suffered of post-depostional diagenesis (PDD) (Tolzmann et al., 2012 in review). The conclusion was drawn that stalagmite growths not always took place under closed conditions, which in turn violates one basic requirement for Th/U-age dating.

However, not all stalagmites show evidence for PDD. Thus, here the age models of three selected RBH stalagmites are presented and discussed.

5.2.1 Age model framework requirements

The results of Th/U dating have been shown in chapter 4.2. In this chapter, the conduction of the age model is going to be discussed. However, the conduction of reliable age models for RBH stalagmites is difficult, due to large Th/U-age errors and non-optimized conditions for age modeling. These features are deriving on the one hand from impurities represented partly by high ^{232}Th concentrations and bad counting rates during measurements. On the other hand, some growth sections are represented by fairly poor Th/U-age data sets. The reason for that is that some growth intervals were simply too small for a huge collection of Th/U-age samples. Another reason is that some ages have been not taken into account for age modeling because they were identified as mixed Th/U-ages or due to problems that occurred during the chemistry sample preparation. In addition to that, it is also highly questionable if the RBH stalagmites were stored at the DASC under ideal conditions for Th/U-age dating. With these difficult starting conditions for age modeling, here RBH Th/U-models are presented that might reflect the real duration of RBH stalagmite growths phases at least to a certain extent.

Figure 5.8 generalizes the required steps, which have to be taken into account prior to establish an age model using StalAge (Scholz and Hoffmann, 2011). In the following these steps will briefly introduced and later discussed in more detail for stalagmites RBH 32, 39 and 47.

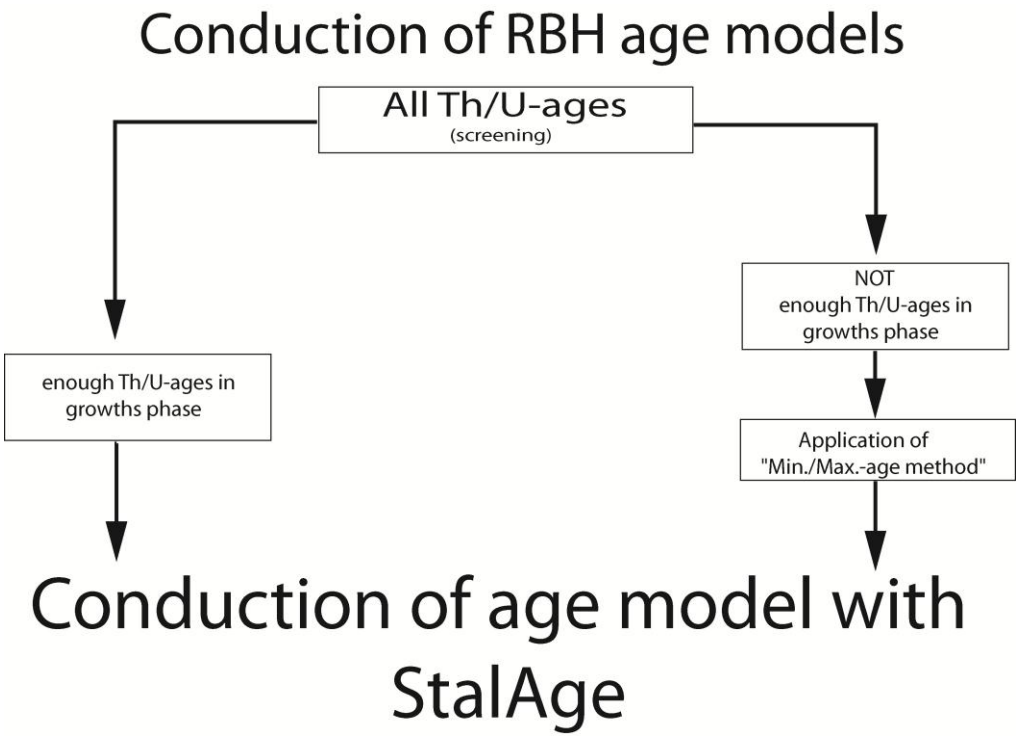

Figure 5.8: Schematic overview of the individual steps, which have to be taken into account prior to the establishment of an age model for RBH stalagmites using StalAge (Scholz and Hoffmann, 2011).

Step 1: Screening. In this first step, all Th/U-ages are plotted. Then, based on notes during chemistry sample preparation and comparison with visible hiatuses along the stalagmites it was decided, which Th/U-ages had to be removed. Although it is not common to neglect specific Th/U-ages, in two cases it is strictly essential to do so. In the first case it is necessary to remove specific Th/U-ages whenever mixed Th/U-ages are identified. Drilling or cutting along pronounced layers enhances the likelihood of producing such mixed Th/U-ages.

In the second case, it is essential to remove Th/U-ages when they are not reliable due to problems occurring during chemistry sample preparation. These laboratory uncertainties include a number of different analytical laboratory errors, which have been addressed in chapter 3.3.4. However, to identify potential analytical errors reflected as apparent strange Th/U-ages it is fundamental to take notes whenever such potential errors are recognized.

To meet the principal requirements to model the timing of specific growth phases with StalAge, it is important to provide at least three Th/U-ages per growth phase. Unfortunately, depending on the vertical length interval of specific growths phases, it is not always possible to meet this principal requirement. For instance, this is the case

when the growth phase measures just a few millimeters. Thus, the application of StalAge must be seen in context with the number of calculated Th/U-ages per growth phase. Whenever there is a sufficient number of calculated Th/U-ages per growth phase, the direct use of StalAge is possible (**Step 3**). This procedure is discussed in detail in Scholz and Hoffmann (2011). In RBH stalagmites, this was the case for most growth phases.

However, for growth phases with only one or two calculated Th/U-ages or to avoid "over-extrapolation" generated by StalAge is binding to apply the "Min./Max.-age method" to conduct "Edge-ages" (**Step 2**). The "Edge-ages" are artificially conducted ages calculated for the beginning and end of specific growth phase using the average of minimum- maximum ages, which were calculated assuming specific max./min. growth rates. The errors of these "Edge-Ages" are simply taken from the measured age. A simplified scheme of this method is displayed in Fig. 5.9.

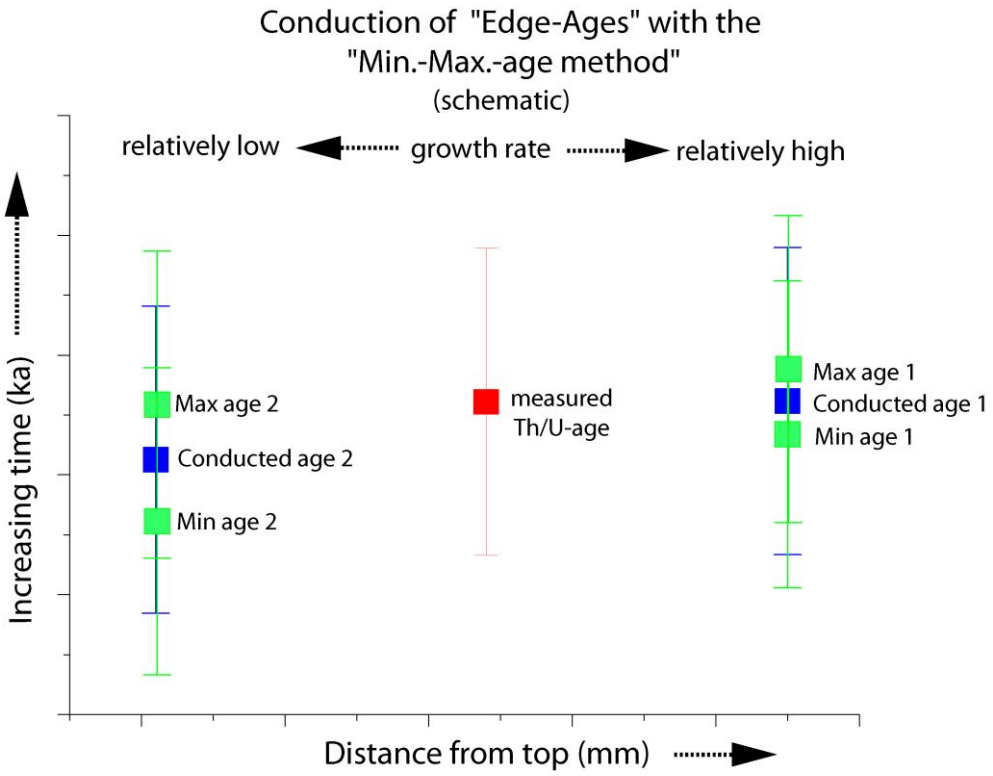

Figure 5.9: Simplified scheme of the "Min.-Max.-age method".

More specifically, the "Min.-Max.-age" method is based on the assumption of specific minimum and maximum growth rates, which differ considerably at the beginning and at the end of each growth phase. Thus, here a minimum growth rate of 500 µm/a and a maximum growths of 1000µm/a at the beginning of the growth phases was assumed

whereas at the end of the growth phases a minimum growth rate of 5 µm/a and a maximum growth rate of 100µm/a at the end of the growths phases was assumed. The assumption of such very high growths rates does not fit necessarily with real observations in nature. However, they were necessary to avoid an overlapping of the time scales in the age model conducted by StalAge.

For this purpose, all growth rates, which are normally displayed in µm/a, have to be converted into ka/mm in a first step. Based on one measured Th/U-age (indicated by the red age in Fig. 5.9), the minimum and maximum ages have to be calculated for the beginning and end of the specific growth phase. This is done by multiplying the distance (mm) of the measured Th/U-ages to the end or start point of the growths phase with the converted growth rate (ka/mm).

Once this was being done, the average of the performed minimum and maximum ages (labeled as green ages in Fig.5.9) were calculated to estimate these "Edge-age" (indicated by blue ages in Fig. 5.9).

After this short introduction to the framework requirements that have to be met for the conduction of the RBH age models, in the next section the establishment of the RBH age models is being discussed for each stalagmite.

In the following the RBH stalagmite growth phases are dedicated to the Greenland Interstadials (GIS) as displayed in the extended NRGIP ice core chronology GICC05modelext (Wolf et al. 2010). The GIS 25-19 are shown in Fig. 5.10.

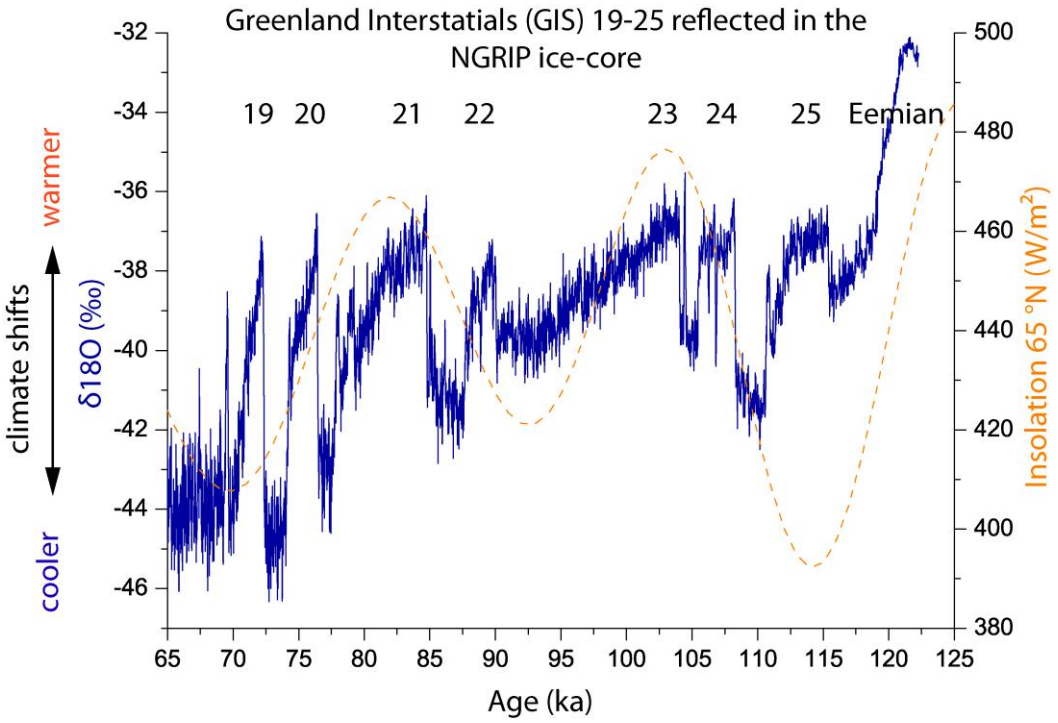

Figure 5.10: Greenland interstadials (GIS) 19-25 reflected in the $\delta^{18}O$ of the NGRIP ice-core with the chronology GICC05modelext (Wolff et al. 2010) displayed in blue and compared with the July solar insoloation curve at 65° N of Berger and Loutre (1991) as displayed in the orange dashed line.

Table 5.1 displays the duration of GIS 25-21 observed in different climate archives.

Table 5.1: Modified after Capron et al 2010. Table 5.1 gives an overview for the timing of GIS 25-21 as observed in different climate archives. The ages displayed in Table 1 are given in kilo years (ka). EDML-NGRIP[1]: (Wolff et al., 2010); (Capron et al., 2010b), MD95-2042[2]: (Matrat et al., 2004), NEAP-18K[3]: (Chapman and Shackelton, 1999), Samboa Cave[4]: (Wang et al., 2008), Monticchino[5]: (Brauer et al., 2007). Note that GIS 20 and 19 are not displayed in Tab. 6.1.

GIS	EDML-NGRIP[1]	MD95-2042[2]	NEAP-18K[3]	Samboa Cave[4]	Monticchino[5]
25	5.53	3.95	2.99	3.97	2.61
24	4.85	4.13	4.94	5.15	4.82
23	12.57	11.19	11.53	13.9	9.46
22	5.87	6.3	4.94	6.75	5.34
21	9.35	6.46	9.7	7.36	

5.2.2 Th/U-age screening of RBH stalagmites

Here, the Th/U-ages (black and red boxes) are plotted together with their errors against distance from top (dft) and are arranged according to the corresponding GIS on the upper x-axis. The Th/U-ages labeled in red are those, which were removed, in a later step before conducting the final age model. All analytical errors are at the 95%

confidence level, whereas the dashed lines represent the hiatuses between the individual GIS (Figs. 5.11-5.13). A table giving a full overview of all Th/U-ages calculated and corresponding values for RBH stalagmites is shown in appendix A.

5.2.2.1 Th/U-ages of RBH 32

For RBH 32, 18 Th/U-ages have been measured, which are shown in Fig 5.11. According to the sample ages of stalagmite RBH 32, three growth intervals have been detected: A growth phase during the late Eemian as well as distinct growth phases during GIS 23 and 21. For the phase that grew during the late Eemian eight samples (samples 18-11), were analyzed for the interval that grew for some extent during GIS 23 four samples (samples 10-7) and for a phase that grew during GIS 21 six samples (samples 6-1). Nonetheless, Th/U-age sample 2 had to be removed because it was identified as a mixed age, which was conducted during the drilling procedure along a pronounced layer. All three growths phases contain a sufficient number of Th/U-ages (at least three per growth phase) for the application of StalAge (Scholz & Hoffmann, 2011). The ^{238}U concentration of the samples ranges from 1.73 – 0.11µg/g and represent an average of 0.70µg/g. The Th/U-age errors vary from 0.6-3.2 % and represent an average of 1.4 %. These errors are, compared to errors reported by Boch et al. (2011) of 0.2-0.6%, relatively high. The relatively large errors may be related to the detritus correction. The ^{232}Th concentration of the sample is a direct proxy for detritus contamination (Scholz & Hoffmann, 2008). Therefore, ^{232}Th concentrations should be high and differences between corrected and uncorrected Th/U-ages should be large if the detritus correction was responsible for large errors. The Th/U-age samples of stalagmite RBH 32 are represented by low ^{232}Th concentrations that range from 2.35-0.11 ng/g. In addition, no age difference larger as 0.08 ka between uncorrected and corrected Th/U-ages can be detected. Thus, the larger errors do not result from detritus contamination.

However, it is also possible that the relatively large errors derive from blockades of the Aridus and/or the cones during the measurements. If that is the reason, the error of the ^{230}Th/^{229}Th ratios higher than 1 % should be elevated. In stalagmite RBH 32 samples, an error of ^{230}Th/^{229}Th ratios as high as 1.84 % (sample 15) is displayed. This could be explained by insufficient count rates for ^{230}Th. However, adequate count rates should display values not lower than $8*10^{-6}$ V. In the Th/U-age samples of stalagmite RBH 32

count rates as low as $2.17*10^{-6}$ V (sample 7) have been observed. This gives evidence that the larger age errors in stalagmite RBH 32 are indeed, related to insufficient count rates, which in turn most likely was caused by blockades of the Aridus during the measurements.

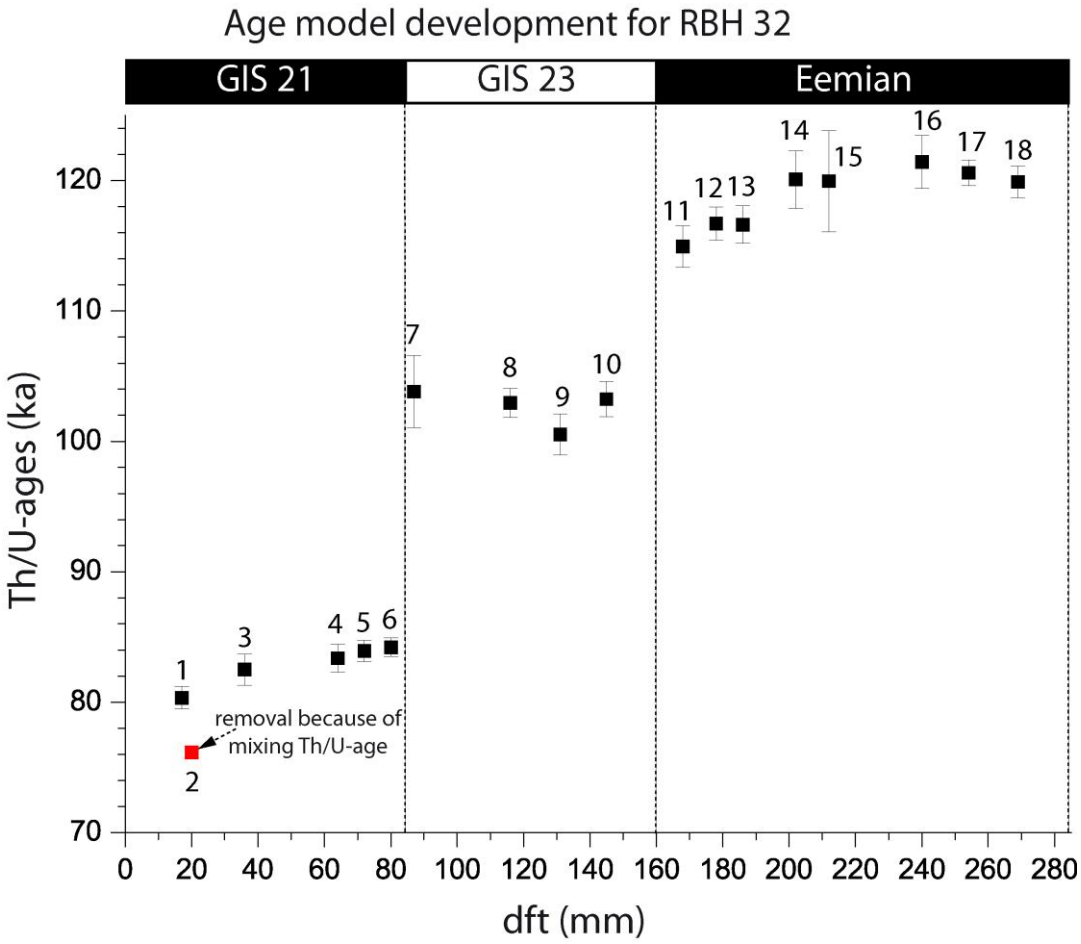

Figure 5.11: All Th/U-ages measured at CENIEH, Burgos and at the Max-Planck-Institute for Biogeochemistry, Mainz, for stalagmite RBH 32 plotted against distance from top. The red age point indicates the age that has been removed. The dashed lines indicate hiatuses. Thus, stalagmite RBH 32 has grown during three distinct growth phases during GIS 21, 23 and the late Eemian.

5.2.2.2 Th/U-ages of RBH 39

For RBH 39, 19 Th/U-ages have been measured and are shown in Fig. 5.12. As displayed in Fig. 5.12, altogether four ages (red symbols) had to be removed because of the following reasons: Both Th/U-age samples 2 and 8 were drilled too close to the hiatuses causing a mixture of two separated growth phases in one age sample.

Therefore, they were identified as mixed ages similar to age sample 2 of stalagmite RBH 32. For the other two Th/U-age samples 18 and 11, problems occurred during sample preparation during the dry down procedure of U for sample 18 and Th for sample 11. Hence after the first "age-screening", 15 Th/U-ages samples are left for Th/U-age modeling. Consequently the direct application of StalAge was possible for the growth phases during GIS 21, 23 and 24, while GIS 20 was only represented by Th/U-age sample 1. Hence, the Min./Max.-age method was applied before StalAge was carried out.

With ^{238}U concentrations that range from 0.69-0.04µg/g with an ^{238}U average of 0.29µg/g, stalagmite RBH 39 represents the lowest U concentrations of the RBH stalagmites being investigated. The errors Th/U-ages display a variety of 0.8-2.5% with an average error of 1.5 %. These errors are compared to Boch et al. (2011) also relatively high. The reasons for this are similar as for RBH 32. The samples being investigated are represented by low ^{232}Th concentrations that range from 4.05-1.42ng/g. In direct comparison to RBH 32, these concentrations are slightly higher, but not high enough to be reflected in large Th/U-age differences due to the ditrital correction. Indeed, the age difference between uncorrected and corrected Th/U-ages range from 0.02-0.09ka. Thus the relatively high error does not originate from detritus correction.

In analogy to the large errors of RBH 32, the errors may also derive from blockades of the Aridus or the cones during the measurements. Again, the errors of the $^{230}Th/^{229}Th$ ratios should be higher than 1% in sample 10, 17 and 19, respectively. This requirement is valid with 1.35% for sample 10. The $^{230}Th/^{229Th}$ ratios of samples 17 and 19 also have relatively high errors with 0.9% (sample 17) and 0.89% (sample 19) compared to sample 6, which displays an error of 0.49%. However, whether such errors derive from the suggested blockage can be verified or falsified by controlling the count rates of ^{230}Th. Again, insufficient count rates below $8*10^{-6}$ V would indicate such blockings. As expected for sample 6 the count rate of ^{230}Th presents $4.7*10^{-5}$ V, whereas sample 10 with $2.75*10^{-6}$ V presents low count rates. Consequently relatively large age error in Th/U-age sample 10 derives most likely from blockades of the Aridus. The same conclusion is valid for Th/U-age samples 17 and 19 because both samples represent low count rates of $6.67*10^{-6}$ V (sample 17) and $1.45*10^{-6}$ V (sample 19) respectively.

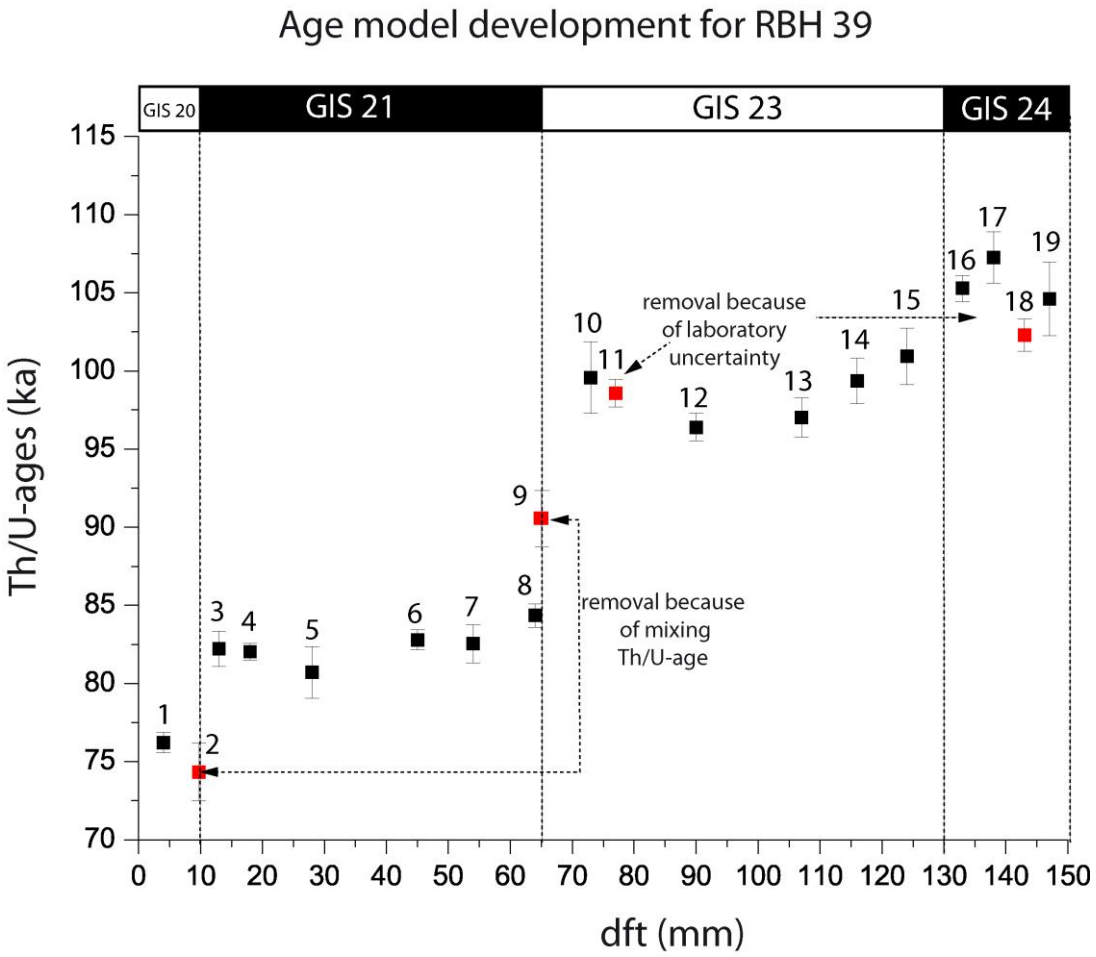

Figure 5.12: All Th/U-ages measured at CENIEH, Burgos and at the Max-Planck-Institute for Biogeochemistry, Mainz, for stalagmite RBH 39 plotted against distance from top. The red age points indicate the age that has been removed. The dashed lines are indicating pronounced hiatuses. Thus, stalagmite RBH 39 has grown during four distinct growth phases during GIS 20, 21, 23 and 24.

5.2.2.3 Th/U-ages of RBH 47

The stratigraphical structure of stalagmite RBH 47 is very complex. Altogether, 18 Th/U-ages have been measured and calculated for six distinct growth phases, which represent to some extent the late Eemian, GIS 24, possibly GIS 23, 21, 20 and GIS 19. The growth phase that most likely represents GIS 23 was identified as a section that suffered of a PDD modification as described in the previous chapter 5.1. Hence, all Th/U-ages measured for the phase, which is labeled as "disturbed" in Fig. 5.13, are invalid for Th/U-age modeling. Moreover, Th/U-age samples 18 and 14 had to be removed because of similar reasons as discussed in Chapter 5.2.2.2 As a consequence, only to the growth interval that grew to some extent during the Eemian, the application

of StalAge was possible because three Th/U-ages are the minimum requirement for the direct application of StalAge. However, an exception of that can be found for the three Th/U-age samples 4, 5 and 6, which reflect the growth phase during GIS 21. Here, the "Min./Max.-age method" was applied for the end of the growth phase although three Th/U-ages are available. This is reasonable because a potential over-extrapolation conducted by StalAge and in this context a potential age overlap with the next growth phase is avoided.

The average ^{238}U concentration of RBH 47 is 0.45µg/g and displays maximum and minimum values of 0.95 and 0.13µg/g respectively. The ^{232}Th concentration of stalagmite RBH 47 demonstrates with 24.06ng/g the highest average values observed in the RBH stalagmites. This high average ^{232}Th concentration can be explained by the very high ^{232}Th concentration in the disturbed section of RBH 47. This section displays with 212.52 ng/g the highest ^{232}Th concentration (sample 7) observed in all RBH stalagmites. In addition, the disturbed section is also characterized by large contents of organic material as observed during sample treatment with H_2O_2. In contrast, in GIS 21 sample 6 represents with 0.38ng/g the lowest ^{232}Th concentrations observed for stalagmite RBH 47.

The relatively large age errors as demonstrated in the disturbed section might originate from the very high ^{232}Th concentration (e.g. 212.52ng/g in sample 7 or 138.2ng/g in sample 8). For both ages, a high age difference of 3.69ka for sample 7 and 4.66ka for sample 8 between uncorrected and corrected Th/U-ages is observed. The fact that the error of the $^{230}Th/^{229}Th$ ratios of are with 0.5 % for both samples below the 1 % threshold and that the ^{230}Th concentrations for both samples are above 8.10^{-6} V allows the conclusion that in this case the large errors must derive from the ^{232}Th concentration and its correction.

In contrast, the large Th/U-age error of 6.41ka (5.9%) for sample 12 in GIS 24 may derive from blocked cones. In that case, the error of the $^{230}Th/^{229}Th$ ratio should be larger as 1% and the count rate of ^{230}Th should be smaller than $8*10^{-6}$ V. Indeed, for sample 12 the observed error of the $^{230}Th/^{229}Th$ ratio reflects 3.62% and the ^{230}Th count rate is as small as $2.80*10^{-7}$. Therefore, it is possible to draw the conclusion that the large error derives from contaminated samples, which may still have carried to some extent some organic material in addition to the large ^{232}Th concentration as reflected for sample 7 and 8. In that case, the blockage of the cones would have been derived in time

from contaminated samples, which were measured beforehand as observed for sample 7 and 8.

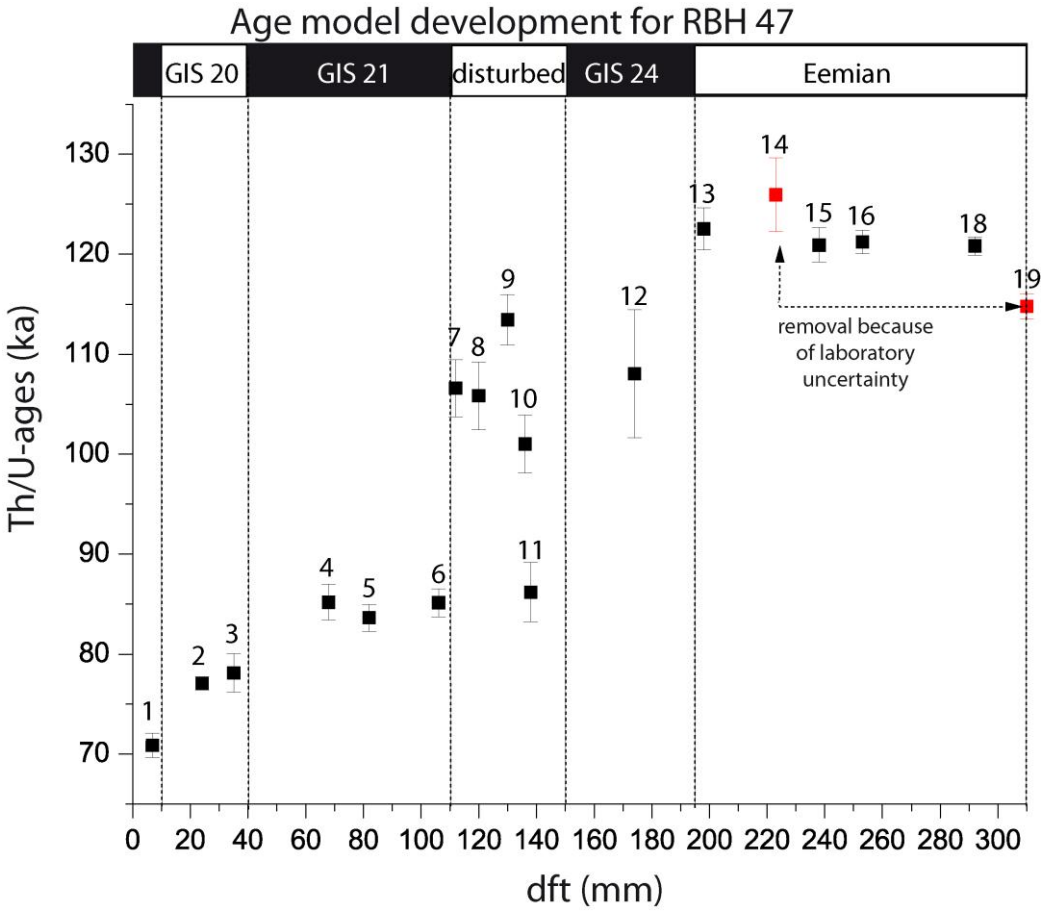

Figure 5.13: All Th/U-ages measured at CENIEH, Burgos, and at the Max-Planck-Institute for Biogeochemistry, Mainz, for stalagmite RBH 47 plotted against distance from top. The red age points indicate the age that has been removed. The dashed lines indicate hiatuses. Thus stalagmite RBH 47 has grown during six distinct growth phases during GIS 19, 20, 21, one disturbed growth phase, GIS 24 and the late Eemian.

5.2.3 Establishment of the age models for the investigated RBH stalagmites

Here, the conduction of the age models for RBH stalagmites with StalAge and the Max./Min.-age method are described and discussed. The growth phases of RBH stalagmites occur during the GIS (Greenland Interstadials). The final age models are conducted with StalAge. In all figures shown in Chapter 5.2.3, the green lines represent the final age model, whereas the red lines indicate the corresponding 95%-confidence

limits. Additionally, the final age models are displayed with the original –and the screened errors. StalAge may have enlarged the original construction of errors for the final age model whenever it has been necessary to do so.

5.2.3.1 Final age model of stalagmite RBH 32

In the following the stalagmite RBH growth phases for the late Eemian, GIS 23 and GIS 21 are displayed and discussed.

5.2.3.1.1 The Eemian in stalagmite RBH 32

In the final age model of stalagmite RBH 32, the Eemian represents a growth interval of 7.34ka in 124mm during 122.17-114.82ka with a growth rate of 21.92µm/a (Fig. 5.14). Although very unlikely, it is also possible that stalagmite RBH 32 reflects maximum growth duration of 11.20ka during 123.88-112.68ka within the corresponding 95% confidence limits. In both scenarios, the growth phase of stalagmite RBH 32 is reflected throughout the late Eemian and for some time of GIS 25. However, there is no visual indication for a hiatus, neither in the stalagmite itself nor in the data that could justify a separation of the growth duration of stalagmite RBH 32 for the late Eemian between Th/U-age samples 14 and 13. This allows the assumption that stalagmite growth was continuous throughout the late Eemian and for some time during GIS 25. Nonetheless, it is also possible within the corresponding 95% confidence intervals, that the growth phase stops at 116.25ka. Capron et al. (2012) report the onset of GIS 25 at 116ka. This shows that it also possible that stalagmite RBH 32 grew during the cooling phase of the late Eemian (123-116.25ka) and stopped 0.2 ka before the onset of GIS 25. This also reflects the interpretation difficulties of RBH stalagmite growth phases and their corresponding proxies.

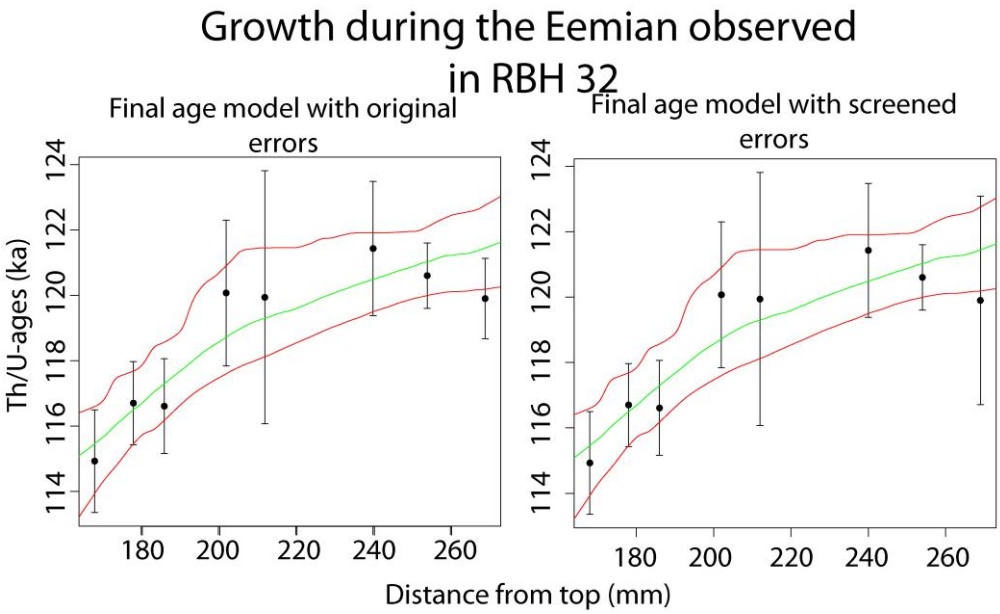

Figure 5.14: Age model conducted by StalAge for RBH 32 for the end of the Last Interglacial period (Eemian) displayed as age model with original- and screened errors plotted against distance from top (dft) in mm. The green line reflects the final age model and the red lines are the corresponding 95 % confidence limits.

5.2.3.1.2 GIS 23 in stalagmite RBH 32

The final age model for stalagmite RBH 32 during GIS 23 lasts from 102.88-102.08ka for 0.8ka in 74mm and demonstrates a relatively high average growth rate of 92.84µm/a (Fig. 5.15). A comparison of all RBH stalagmite growth phases will be shown in Chapter 5.2.4. The high growth rate reflected for the growth duration during GIS 23 could also represent an artifact from application of StalAge due to the relatively large error bars in addition to the insufficient number of Th/U-age samples to conduct a reliable age model for that interval. Consequently, this shows again the difficulty of the interpretation of RBH stalagmites. However, within the corresponding 95% confidence limits it is also possible to conduct a model that reflects a growth duration of 1.28 ka from 103.13-101.85 ka. In this case, the growth rate would reflect 74.08µm/a.

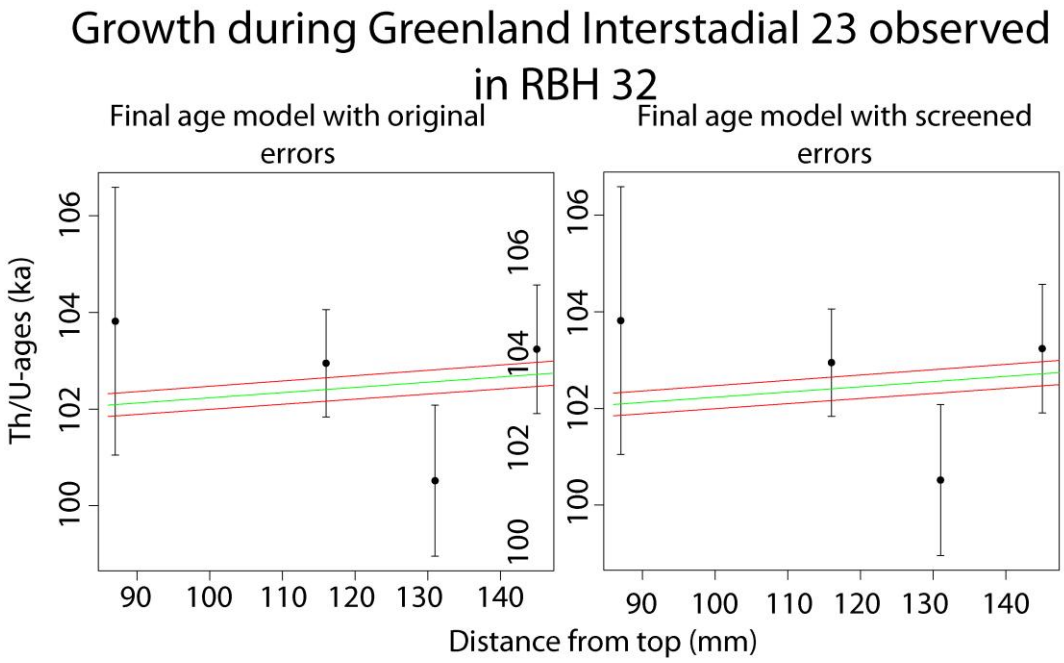

Figure 5.15: Age model conducted by StalAge for RBH 32 for (Greenland Interstaldial) GIS 23 displayed as age model with original- and screened errors plotted against distance from top (dft) in mm. The green line reflects the final age model and the red lines are the corresponding 95 % confidence limits.

5.2.3.1.3 GIS 21 displayed in stalagmite RBH 32

The final age model of RBH 32 reflects a growth duration of 4.87 ka at 84.52-79.65 ka with a growth rate of 17.71µm/a during GIS 21 (Fig.5.16). This reflects in comparison to the growth of GIS 23 in stalagmite RBH 32 a relatively slow growth rate. However, it is possible to conduct a similar growth rate as observed in GIS 23 for RBH 32 within the corresponding 95% confidence limits. Within these limits, it is also possible to conduct a growth period of 6.74ka during 85.3 – 78.56ka, which reflects a corresponding growth rate of 12.53µm/a. Once again this demonstrates the high uncertainties for the RBH stalagmites being investigated.

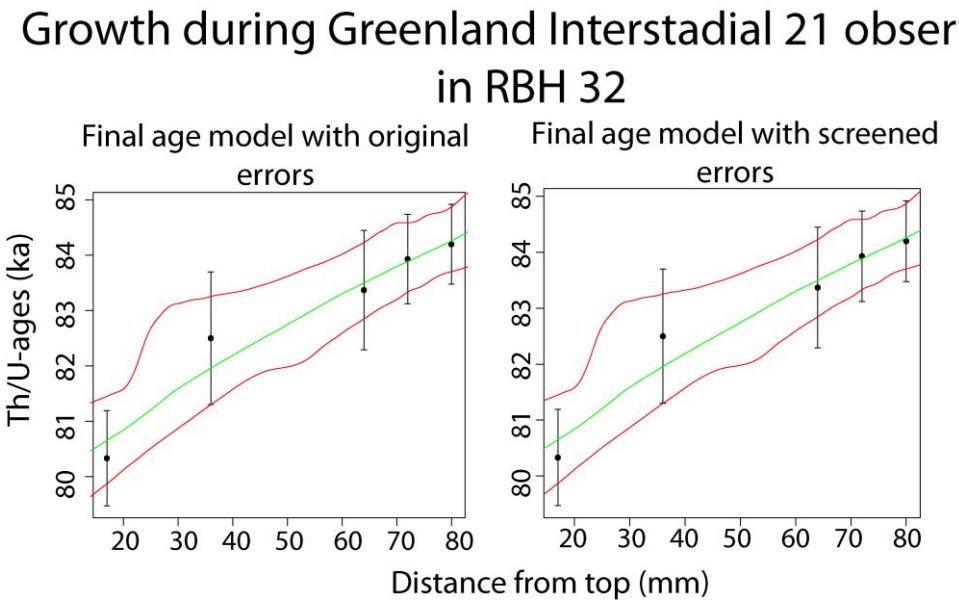

Figure 5.16: Age model conducted by StalAge for RBH 32 (Greenland Interstaldial) GIS 21 displayed as age model with original- and screened errors plotted against distance from top (dft) in mm. The green line reflects the final age model and the red lines are the corresponding 95 % confidence limits.

5.2.3.2 Final age model of RBH 39

For stalagmite RBH 39, the potential age models for four growths phases during GIS 24, 23, 21 and GIS 20 are displayed and discussed.

5.2.3.2.1 GIS 24 displayed in stalagmite RBH 39

The final age model of RBH 39 during GIS 24 demonstrates a growth period of 1.07ka in 20mm during 106.46-105.39ka and hence a growth rate of 22.92µm/a. In spite of this, within the 95% confidence limit, it is possible to conduct a longer growth period for this interval of 4.33ka during 109.0-104.63ka (Fig. 5.17). This demonstrates the large uncertainties of the age model of this phase and suggests investigating one or two more Th/U-age samples for that interval in a later study. Nonetheless, at that stage this represents the final age model of RBH 39 for GIS 24, which will be discussed in detail in chapter 5.4 when being compared to NGRIP and the solar insolation curve.

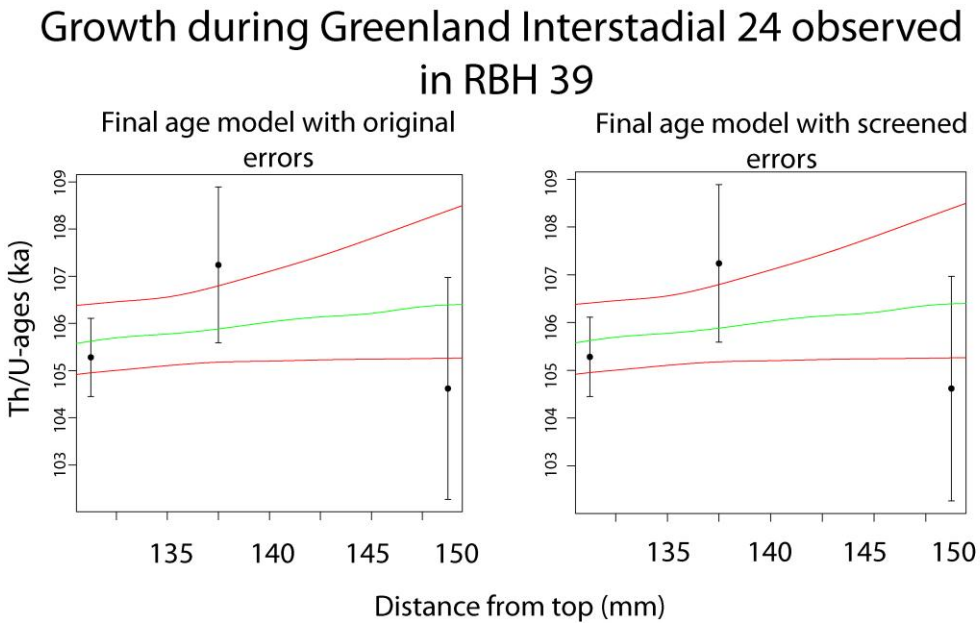

Figure 5.17: Age model conducted by StalAge for RBH 39 for the (Greenland Interstaldial) GIS 24 displayed as age model with original- and screened errors plotted against distance from top (dft) in mm. The green line reflects the final age model and the red lines are the corresponding 95 % confidence limits.

5.2.3.2.2 GIS 23 displayed in stalagmite RBH 39

In the final age model of RBH 32 a growth duration of 5.78ka in 63.5mm is suggested during 101.5-95.71ka for GIS 23. This age model reflects an average growth rate of 16.05µm/a (Fig. 5.18). However, almost no increasing ages are displayed between 78-83.5mm (dft) reflecting an extremely high growth rate of 3667µm/a. This very large growth rate is an artifact conducted by StalAge and can be explained by comparison of the age model with the original errors to the one with the screened errors. The age model that displays the screened errors enlarges the error of Th/U-age sample 10. However, within the 95% confidence limits, it is possible to enlarge the growth duration to 11.16ka during 104.04-92.89ka for this period.

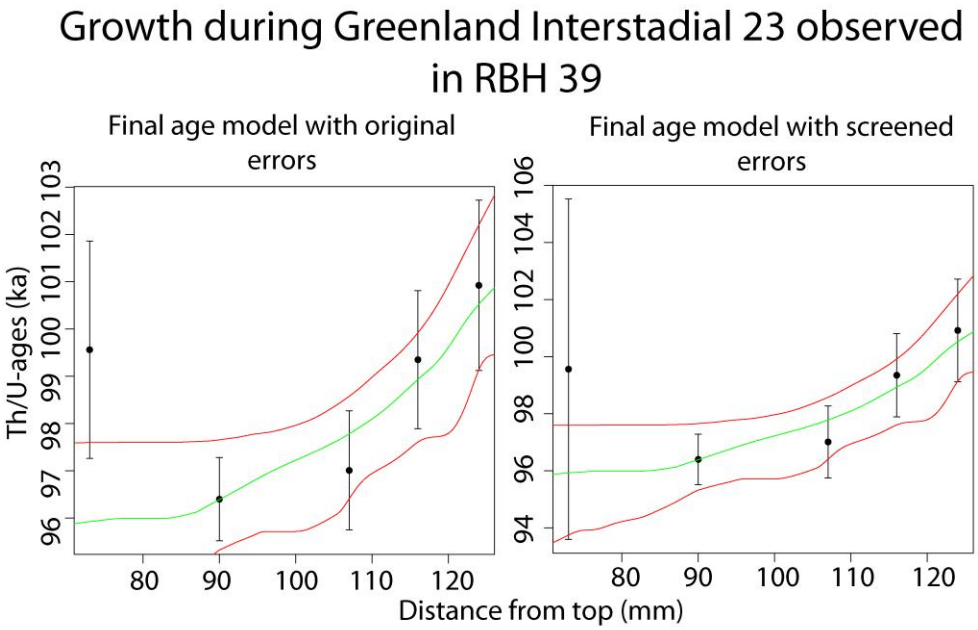

Figure 5.18: Age model conducted by StalAge for RBH 39 for the (Greenland Interstaldial) GIS 23 displayed as age model with original- and screened errors plotted against distance from top (dft) in mm. The green line reflects the final age model and the red lines are the corresponding 95 % confidence limits.

5.2.3.2.3 GIS 21 displayed in stalagmite RBH 39

The final age model of RBH 39 reflects with 84.00-81.59ka a growth duration of 2.41ka in 54mm for GIS 21 and, hence, a growth rate of 29.36µm/a (Fig. 5.19). Nonetheless, it is possible to extent the growth period in time to 4.14ka from 84.9ka to 80.76ka. The largest difference between the final age model with the original errors and the one with the screened errors is a strong enlargement of the error of Th/U-age 7.

Figure 5.19: Age model conducted by StalAge for RBH 39 for the (Greenland Interstaldial) GIS 21 displayed as age model with original- and screened errors plotted against distance from top (dft) in mm. The green line reflects the final age model and the red lines are the corresponding 95 % confidence limits.

5.2.3.2.4 GIS 20 displayed in stalagmite RBH 39

The final age model of stalagmite RBH 32 that grew for some extent during GIS 20 reflects a duration of 0.54ka in 10mm from 76.36-75.82ka with an average growth rate of 17.5µm/a. Within the 95% confidence interval it is possible to enlarge this duration in time to 1.63ka from 76.96 to 75.33ka.

For that interval it was necessary to apply the Min./Max.-age method (for further explanations see chapter 5.2.1). Consequently, an age of 76.21ka for the inception of GIS 20 at 10mm dft and another age of 75.78ka for the ending of GIS 20 at 0.5mm (dft) have been estimated. In Fig. 5.20, these ages are displayed as blue spots.

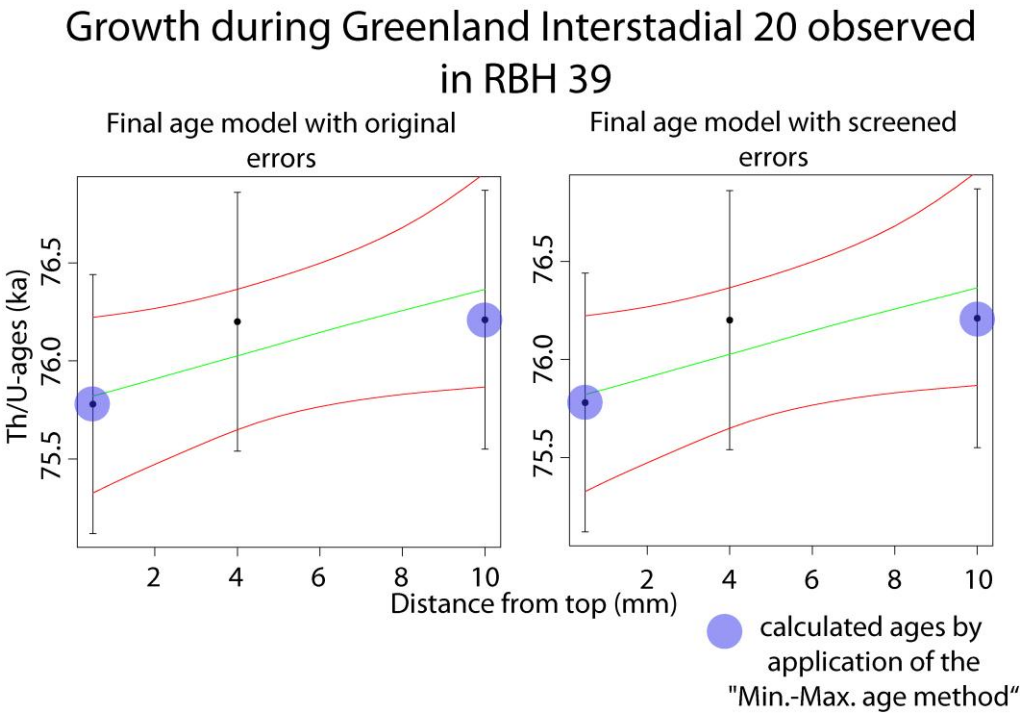

Figure 5.20: Age model conducted by StalAge for RBH 39 for the (Greenland Interstaldial) GIS 20 displayed as age model with original- and screened errors plotted against distance from top (dft) in mm. The green line reflects the final age model and the red lines are the corresponding 95 % confidence limits. The blue spots indicate the artificially estimated data points with the "Min.-Max age method".

5.2.3.3 Final age model of RBH 47

Stalagmite RBH 47 represents the most growths phases of RBH stalagmites being investigated in this thesis. In addition, for stalagmite RBH 47, the "Min./Max.-age growth method" had to be applied most often. Only for the growth phase that grew for some extent during the end of the late Eemian, StalAge could be applied directly. Apart from that, stalagmite RBH 47 is represented by growth phases that grew during time intervals of GIS 24, 21, 20 and GIS 19. Thus stalagmite RBH 47 is the only stalagmite that grew for some extent during GIS 19. Although the Th/U-ages would have been sufficient enough in numbers for the direct application of StalAge for GIS 21 it has been avoided to do so, to obviate over-extrapolation by StalAge and hence to artifacts in the final age model.

5.2.3.3.1 The Eemian displayed in stalagmite RBH 47

The final age model of RBH 47 reflects a growth period of only 1.02ka during 122.34-121.47ka in 114mm and reveals the largest growth rates of 1000µm/a being observed in RBH stalagmites for this thesis in the Eemian (Fig. 5.21). Such growth rates are presented nowhere in the literature for these regions. Therefore, these large growth rates can be explained best, if one takes a combination of an artifact conducted by StalAge advantaged by large error bars and the possibility of an age plateau formation. Nonetheless, within the 95% confidence interval it is possible to enlarge that growth period by almost 3ka to 3.97ka during 122.34-118.37ka.

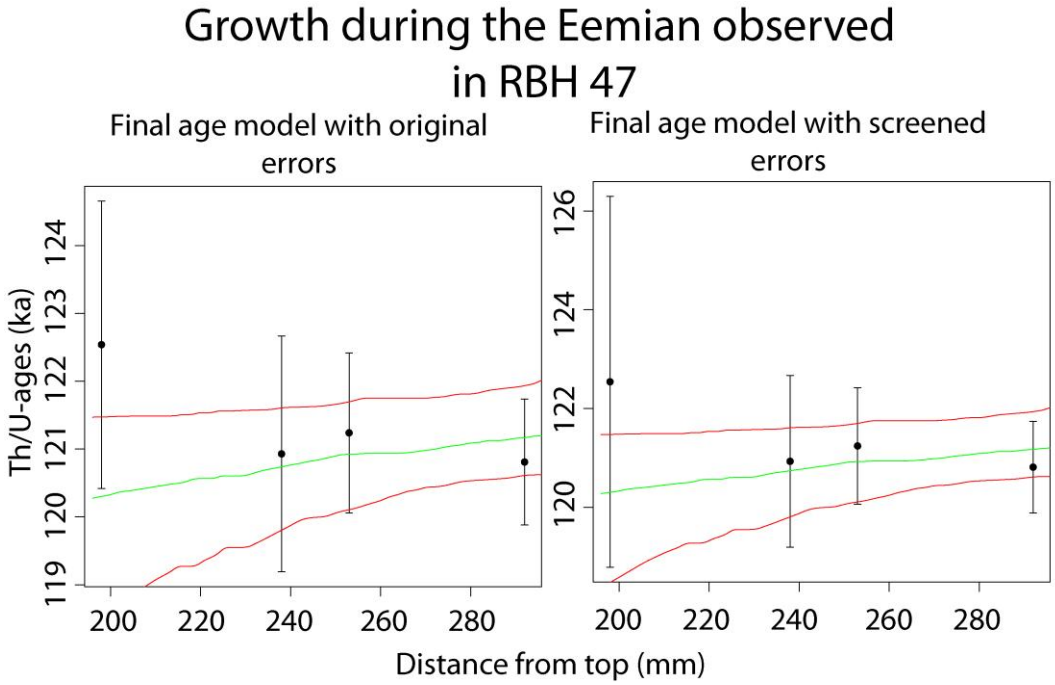

Figure 5.21: Age model conducted by StalAge for RBH 47 for the end of the Last Interglacial period (Eemian) displayed as age model with original- and screened errors plotted against distance from top (dft) in mm. The green line reflects the final age model and the red lines are the corresponding 95 % confidence limits.

5.2.3.3.2 GIS 24 displayed in stalagmite RBH 47

In the final age model, which displays growth during GIS 24, two extra artificially conducted age tie point had to be accomplished performing the "Min.-Max. age method" for the later application of StalAge. In this context an artificially conducted ages of 108.08 ka and 105.64 ka for the inception and the ending of the growths duration can be reported for the growth period during GIS 24 and are displayed as blue spots in Fig. 5.22. For this interval, a growth period of 4.22ka in 44mm from 109.22-

104.87ka can be observed displaying an average growth rate of 12.03µm/a. However, the large errors reflected in the Th/U-ages for that period reveal that it might be possible within the corresponding 95% confidence limits to enlarge this growth period up to 13.37ka from 114.20-105.06ka. This period would span the entire GIS 25 and 24 without displaying a growth stop and is, therefore, highly unlikely.

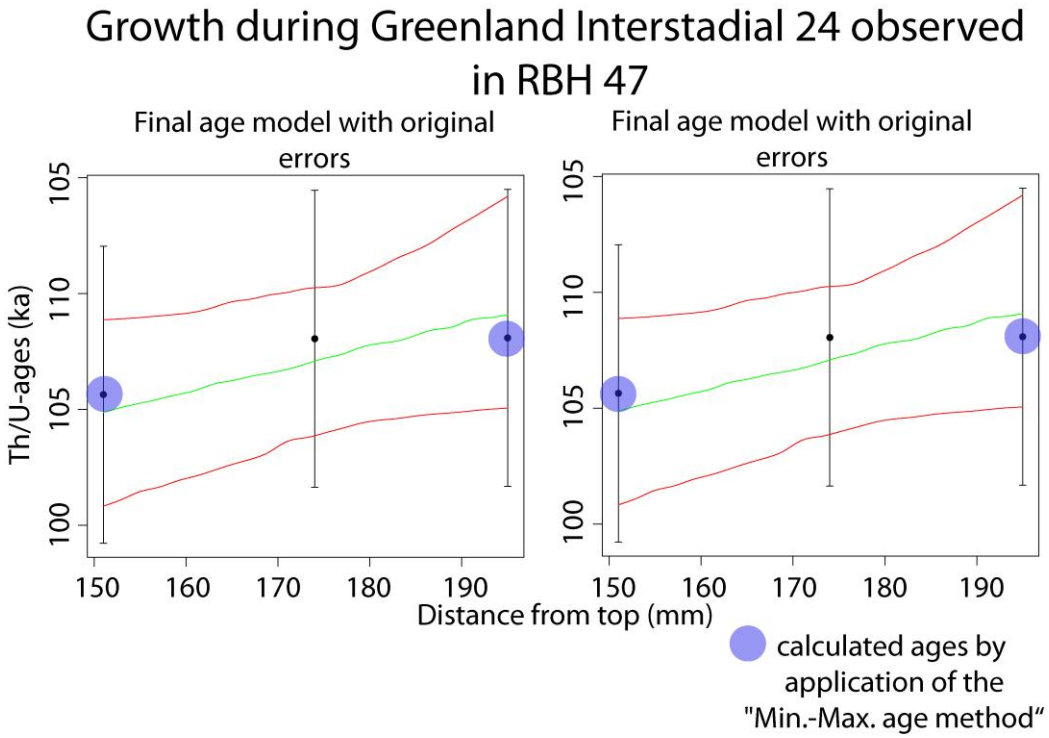

Figure 5.22: Age model conducted by StalAge for RBH 37 for (Greenland Interstaldial) GIS 24 displayed as age model with original- and screened errors plotted against distance from top (dft) in mm. The green line reflects the final age model and the red lines are the corresponding 95 % confidence limits. The blue spots indicate the artificially estimated data points with the "Min.-Max age method".

5.2.3.3.3 GIS 21 displayed in stalagmite RBH 47

As exposed in Fig. 5.23 for the final age model that displays growth during GIS 21, one artificially conducted age tie point had to be accomplished performing the "Min.-Max. age method" for the later application of StalAge at the end of the growth period and reflects 82.36ka (blue spot Fig 5.23). The step was necessary in order to avoid over-extrapolation and overlapping age models conducted by StalAge. Hence, the growth duration of 2.53ka in 69 mm between 85.20-82.77ka is reflected, which displays a growth rate of 28.58ka. In spite of this, within the 95% confidence interval, it is possible

to enlarge the growth duration by approximately another 2.5ka. In that case, the growth period would reflect 5.08ka during 86.49-81.37ka.

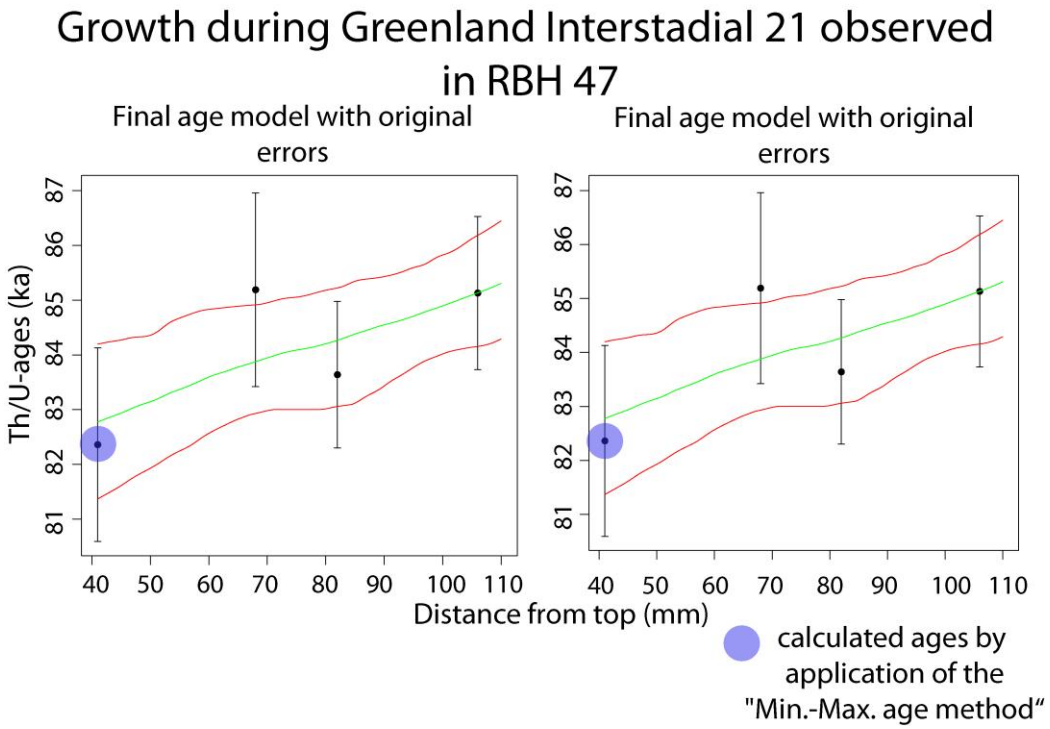

Figure 5.23: Age model conducted by StalAge for RBH 47 for the (Greenland Interstaldial) GIS 21 displayed as age model with original- and screened errors plotted against distance from top (dft) in mm. The green line reflects the final age model and the red lines are the corresponding 95 % confidence limits. The blue spots indicate the artificially estimated data points with the "Min.-Max age method".

5.2.3.3.4 GIS 20 displayed in stalagmite RBH 47

As indicated by the blue spots in Fig. 5.24, for the RBH 47 growth period during GIS 20 it was also necessary to conduct two artificially conducted ages. These tie-points are 77.10 ka for the inception of the growth phase and 75.72ka for the end of the growth phase. Thus, a growth period of 1.62ka has been estimated in 29mm from 77.49 to 75.87ka, which is reflected by an average growth phase of 20.86µm/a. Within the 95% confidence interval, it is possible to enlarge the duration by another 1.28ka.

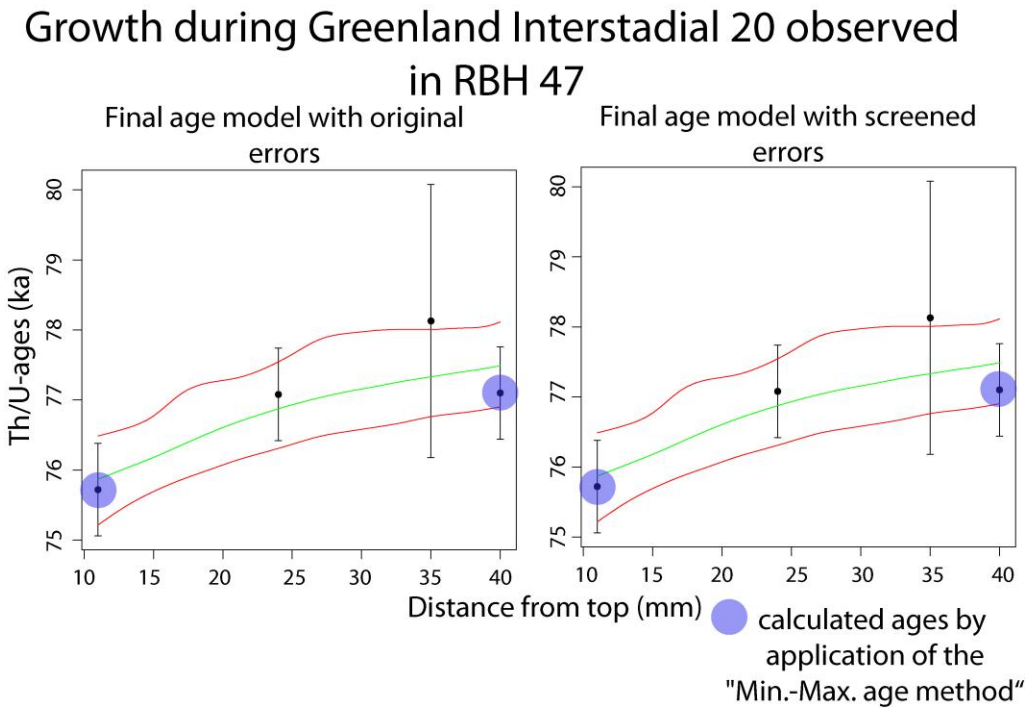

Figure 5.24: Age model conducted by StalAge for RBH 47 for (Greenland Interstaldial) GIS 20 displayed as age model with original- and screened errors plotted against distance from top (dft) in mm. The green line reflects the final age model and the red lines are the corresponding 95 % confidence limits. The blue spots indicate the artificially estimated data points with the "Min.-Max age method".

5.2.3.3.5 GIS 19 displayed in stalagmite RBH 47

Regarding the fact that only one Th/U-age was measured for this period it was necessary to estimate two artificially conducted Th/U-ages with the application of the Min.-Max. age method as indicated by the blue spots of Fig. 5.25. These ages can be denoted with 70.89 and 69.94ka for the onset and ending of the growth phase. Hence, the timing of the growth duration can be denoted with 1.07ka within 10mm between 70.97 and 69.89ka displaying a growth rate of 8.87µm/a. Again, within the corresponding 95 % confidence limits it is possible to enlarge the duration of growth in time by approximately 2.14ka. In that scenario, stalagmite RBH 47 would have shown growth between 71.74 and 68.53ka.

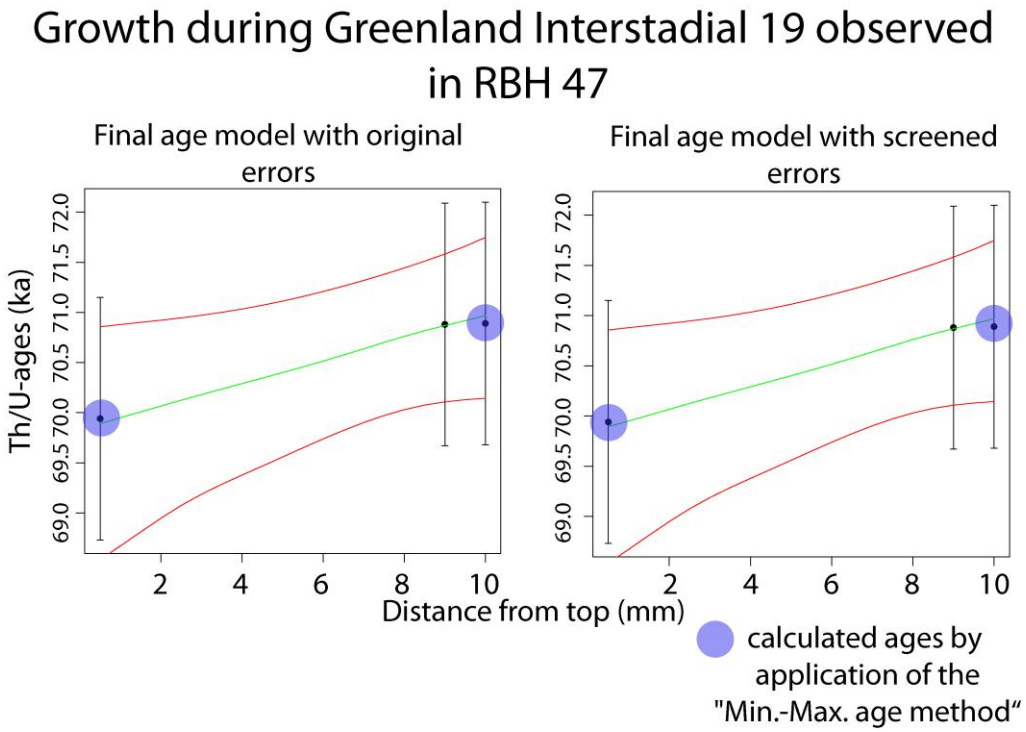

Figure 5.25: Age model conducted by StalAge for RBH 47 for the (Greenland Interstaldial) GIS 19 displayed as age model with original- and screened errors plotted against distance from top (dft) in mm. The green line reflects the final age model and the red lines are the corresponding 95 % confidence limits. The blue spots indicate the artificially estimated data points with the "Min.-Max age method".

5.2.4 Comparison of RBH stalagmite growth phases

In chapter 5.2.3 the final age models of RBH stalagmites were introduced. These age models represent the basis for the further discussion. In this chapter the duration of these age models will be compared to each other as well as to the duration of pronounced GIS displayed in the $\delta^{18}O$ record of NGRIP (NGRIP members, 2004) for the extended GICC05modelext ice core record (Wolff et al., 2010) and the July solar insolation curve at 65° N (Berger and Loutre, 1991). In addition the potential errors of these age models are displayed, which is displayed by the dashed lines.

5.2.4.1 The RBH stalagmite growth during the Eemian

The Eemian (Fig. 5.26) is represented by growth phase of stalagmite RBH 32 and RBH 47. However, Fig. 5.26 displays that in comparison to stalagmite RBH 47 the growth phase of stalagmite RBH 32 in the final age model is much longer. In the final age model both stalagmites are overlapping in time for 1.02ka during 122.34-121.47ka, which reflects the entire growth phase of stalagmite RBH 47 in the final age model. Nonetheless within the 95% confidence limit it is also possible that both age models might overlap for 3.97ka during 122.34-118.37ka.

Still, in the final age model the growth of stalagmite RBH 32 stops shortly after the onset of GIS 25. Within the 95% confidence limit it is also possible that the growth stop of stalagmite RBH 32 coincident with the onset of GIS 25 or that it continues to grow almost during the entire duration of GIS 25 as revealed in the $\delta^{18}O$ record of NGRIP. In the final age model of stalagmite RBH 47 growth stop occurs at 120.28ka but within the 95% confidence limit might also stop growing at 118.36 or already at 121.47ka.

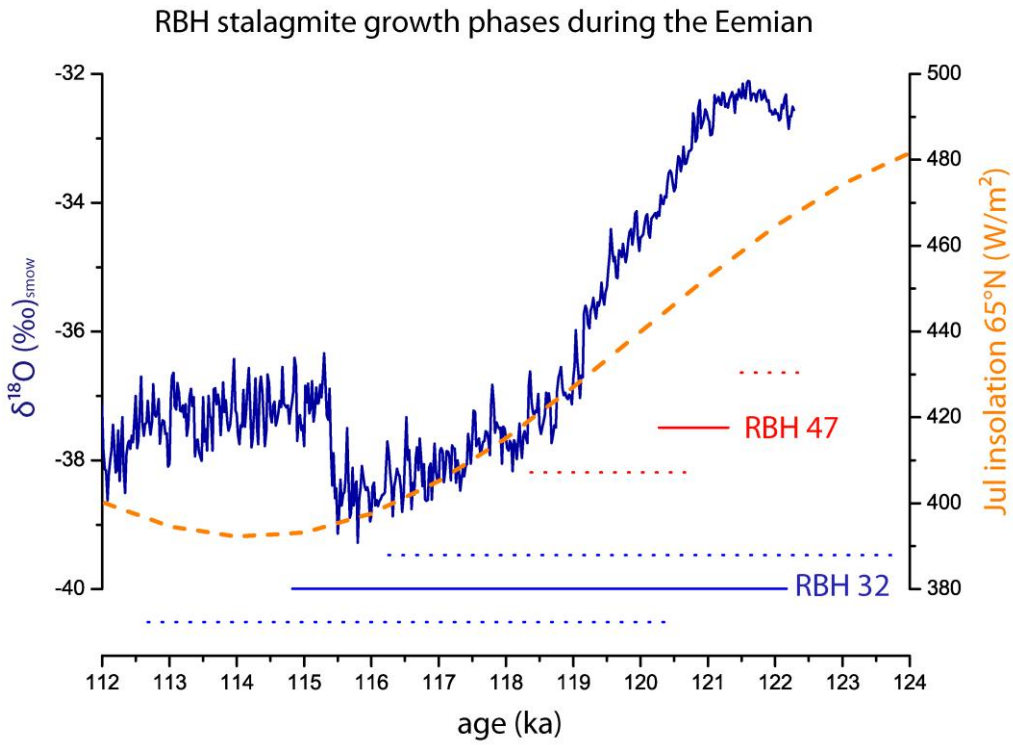

Figure 5.26: Growth phases during the Eemian of stalagmites RBH 32 (light blue) and 47 (red), compared with the NGRIP $\delta^{18}O$ ice core record (NGRIP, members, 2004), displayed in a dark blue line and the July solar insolation curve at 65°N (Berger and Loutre, 1991), displayed in a dashed orange line. Note that for RBH stalagmites the corresponding dashed lines indicate the maximum and minimum age models, whereas the straight line indicates the final age model. All RBH age models were conducted with StalAge (Scholz and Hoffmann, 2011).

5.2.4.2 The RBH stalagmite growth during the GIS 24

Stalagmite RBH 47 and stalagmite RBH 39 represent the GIS 24 (Fig. 5.27). The growth phase of stalagmite RBH 47 is longer in comparison to the growth phase of stalagmite RBH 39. Both stalagmites overlap in the final age model for 1.07ka during 106.46-105.39ka. The growth duration of stalagmite RBH 47 exceeds the duration of the GIS 24 as reflected in the NGRIP $\delta^{18}O$ ice core record. Moreover within the 95% confidence limits it is also possible that stalagmite RBH 47 has grown during the second part of GIS 25 and beyond or at the beginning of GIS 23.

However the growth phase of stalagmite RBH 39 shows a clearer picture. Thus within the 95% confidence limits it is possible that stalagmite RBH 39 has drown during the entire duration of the GIS 24. The GIS 24 itself is associated with an increasing July insolation at 65°N.

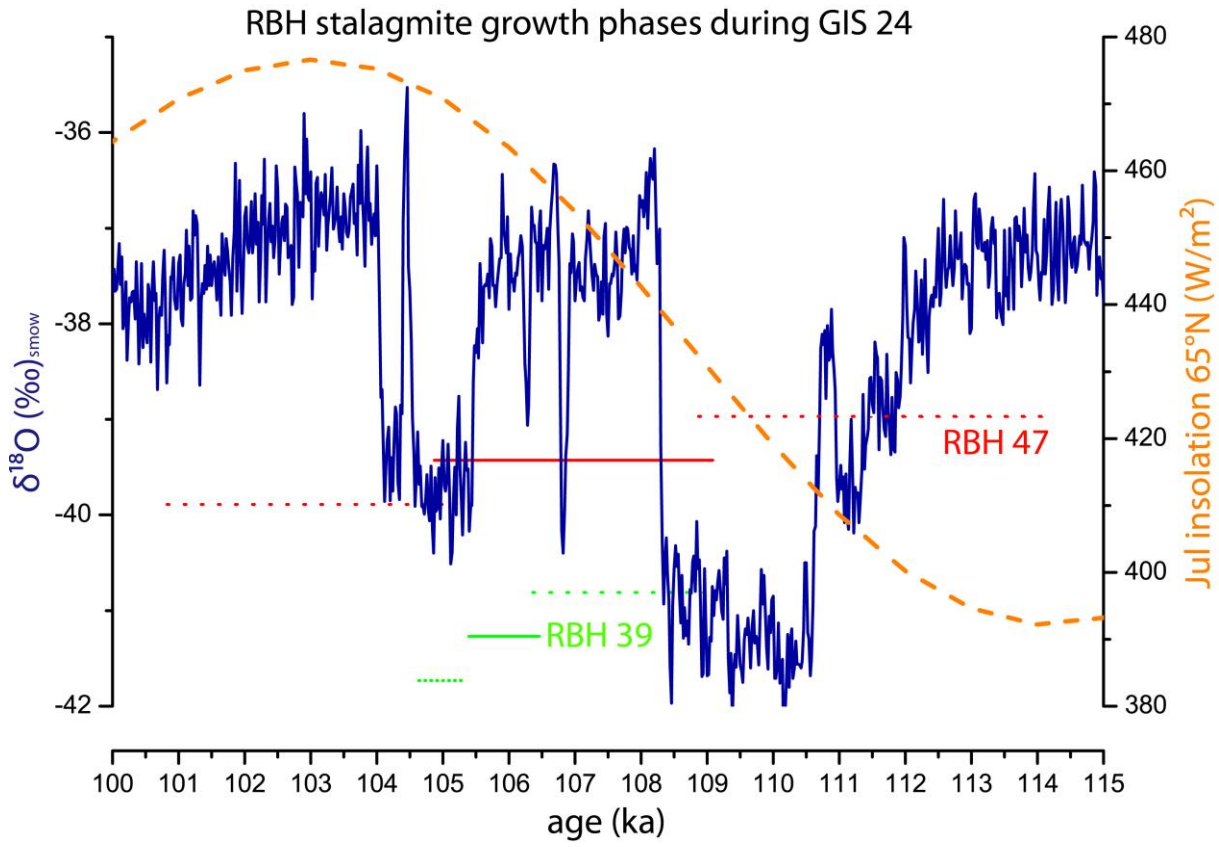

Figure 5.27: Growth phases during GIS 24 of stalagmites RBH 39 (light green) and 47 (red), compared with the NGRIP $\delta^{18}O$ ice core record (NGRIP, community members, 2004), displayed in a dark blue line and the July solar insolation curve at 65°N (Berger and Loutre, 1991), displayed in a dashed orange line. Note that for RBH stalagmites the corresponding dashed lines indicate the maximum and minimum age

models, whereas the straight line indicates the final age model. All RBH age models were conducted with StalAge (Scholz and Hoffmann, 2011).

5.2.4.3 The RBH stalagmite growth during the GIS 23

The stalagmites RBH 39 and RBH 32 represent a phase during the GIS 23 since both stalagmites do not represent the entire duration of GIS 23. The growth duration of RBH 32 is in comparison to the growth duration of RBH 39 much shorter and its inception commence shortly after the onset of the GIS 23. The final age models of both stalagmites do not overlap each other. As displayed in the NGRIP $\delta^{18}O$ record (NGRIP members, 2004) (Fig. 5.28) it might be possible that within the 95% confidence limit the growth phase of stalagmite RBH 39 coincident with the inception of the GIS 23 and stops when July solar insolation at 65°N has reached a value of approximately 430W/m^2.

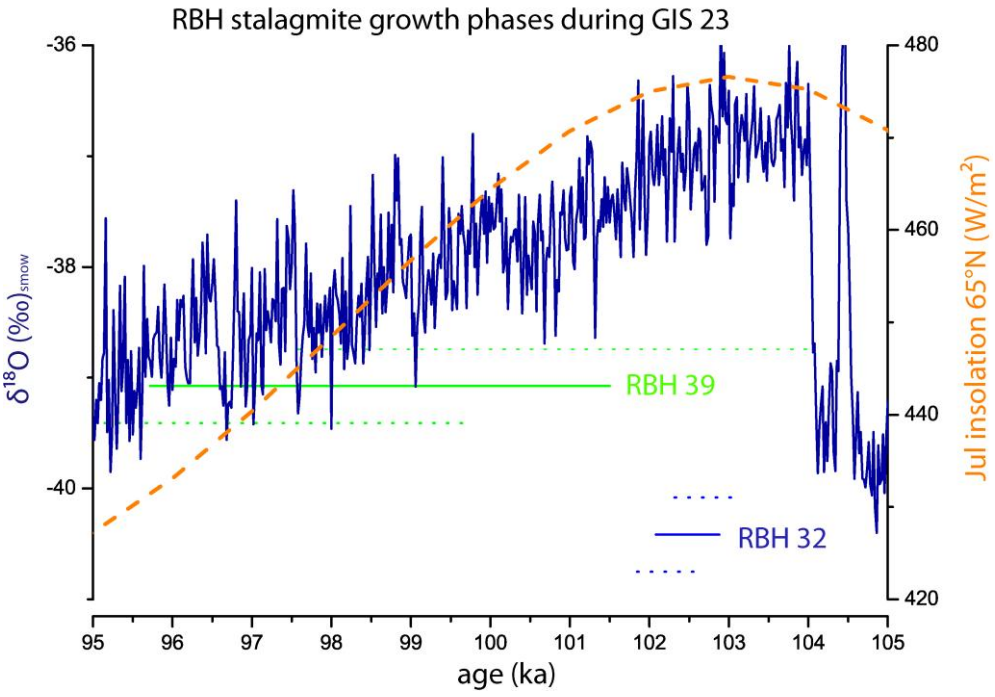

Figure 5.28: Growth phases during GIS 23 of stalagmites RBH 32 (light blue) and 39 (light green), compared with the NGRIP $\delta^{18}O$ ice core record (NGRIP, community members, 2004), displayed in a dark blue line and the July solar insolation curve at 65°N (Berger and Loutre, 1991), displayed in a dashed orange line. Note that for RBH stalagmites the corresponding dashed lines indicate the maximum and minimum age models, whereas the straight line indicates the final age model. All RBH age models were conducted with StalAge (Scholz and Hoffmann, 2011).

5.2.4.4 The RBH stalagmite growth during the GIS 21

The GIS 21 is the only Greenland Interstaldial, in which all RBH stalagmites investigated grow at the same time (compare Fig. 5.29). This might be associated with highest orbital forced July solar insolation values after the Eemian for MIS 5. However stalagmite RBH 39 reveal the shortest growth phase but within the 95% confidence limit it is possible that growth inception coevals with the inception of the GIS 21 as displayed in the NGRIP $\delta^{18}O$ ice core record. The final age model of stalagmite RBH 47 commences with a pronounced precursor event. Stalagmite RBH 32 reveals the longest growth phase during the GIS 21. Within the 95% confidence limits it is also possible that stalagmite RBH 32 covers the entire GIS 21 including the precursor and rebound event.

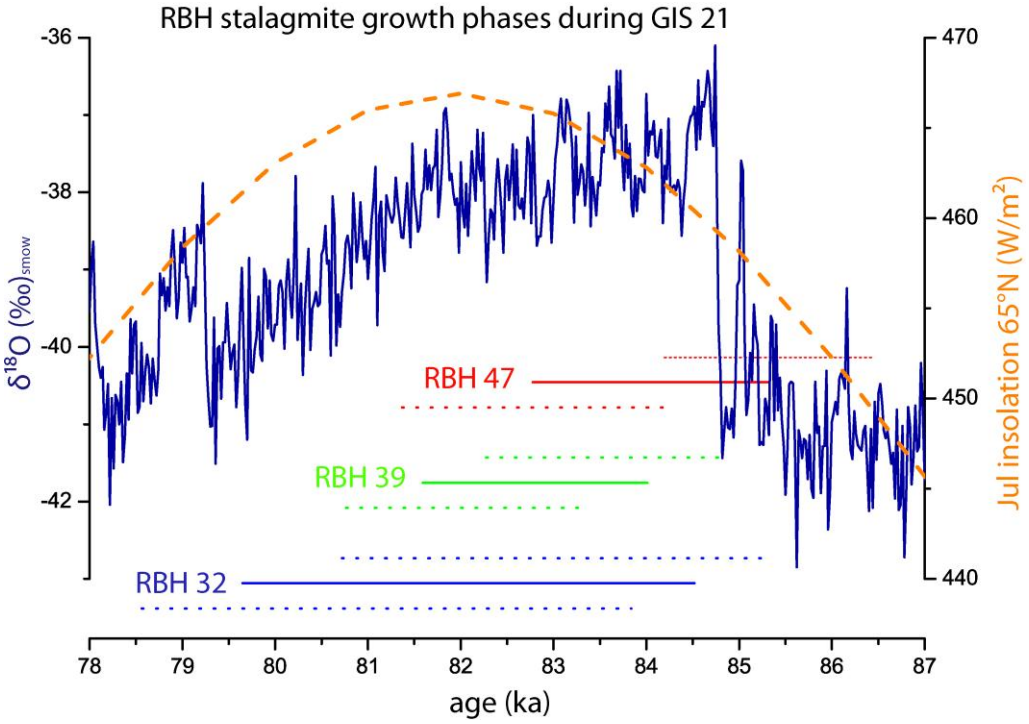

Figure 5.29: Growth phases during GIS 21 of stalagmites RBH 32 (light blue), 47 (red) and 39 (light green) compared with the NGRIP $\delta^{18}O$ ice core record (NGRIP, members, 2004), displayed in a dark blue line and the July solar insolation curve at 65°N (Berger and Loutre, 1991), displayed in a dashed orange line. Note that for RBH stalagmites the corresponding dashed lines indicate the maximum and minimum age models, whereas the straight line indicates the final age model. All RBH age models were conducted with StalAge (Scholz and Hoffmann, 2011).

5.2.4.5 The RBH stalagmite growth during the GIS 20

The two stalagmites RBH 32 and RBH 47 represent a phase during the GIS 20 but both stalagmites do not cover the entire GIS 20. The growth phase of stalagmite RBH 32 is much shorter and coincident with the inception of the GIS 20, which is characterized by a rapid shift in the $\delta^{18}O$ record of the NGRIP ice core as displayed in Fig. 5.30. However the final age model of stalagmite RBH 47 reveals might also growth during the Greenland stadial (GS). The entire GIS 20 is associated with decreasing solar insolation values.

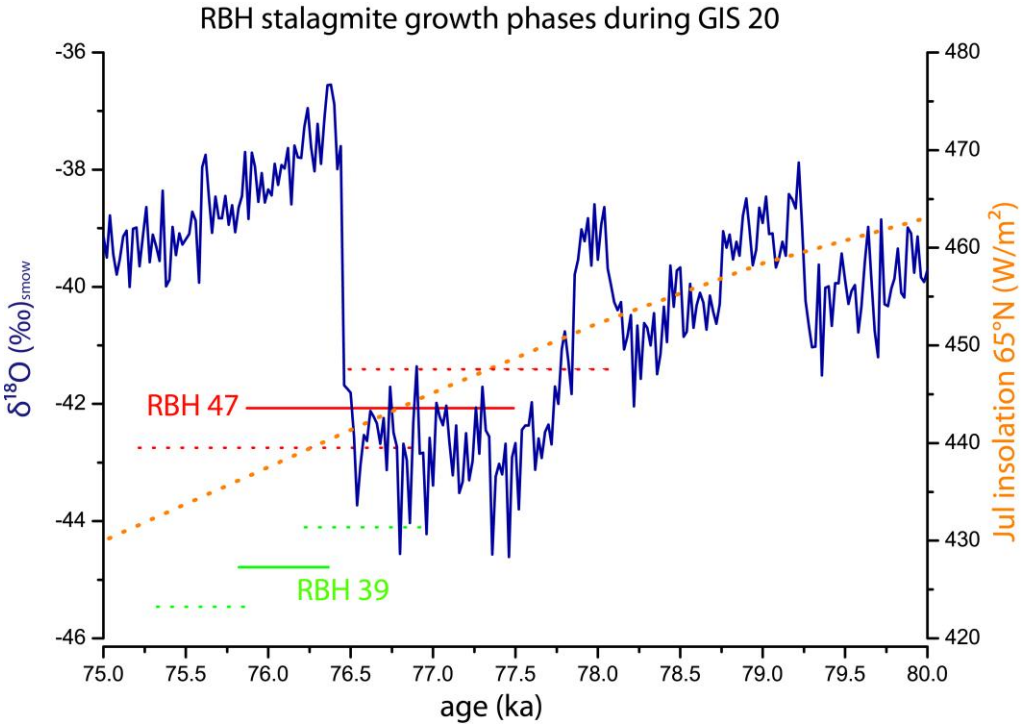

Figure 5.30: Growth phases during GIS 20 of stalagmites RBH 39 (light green) and 47 (red), compared with the NGRIP $\delta^{18}O$ ice core record (NGRIP members, 2004), displayed in a dark blue line and the July solar insolation curve at 65°N (Berger and Loutre, 1991), displayed in a dashed orange line. Note that for RBH stalagmites the corresponding dashed lines indicate the maximum and minimum age models, whereas the straight line indicates the final age model. All RBH age models were conducted with StalAge (Scholz and Hoffmann, 2011).

5.2.4.6 The RBH stalagmite growth during the GIS 19

Stalagmite RBH 47 is the only stalagmite that reveals growth during the GIS 19. In the final age model the growth duration is with 1.07ka rather short (compare Fig. 5.31). The

GIS 19 is associated with decreasing solar insolation values at 65°N and reaches the lowest values at the end of the phase.

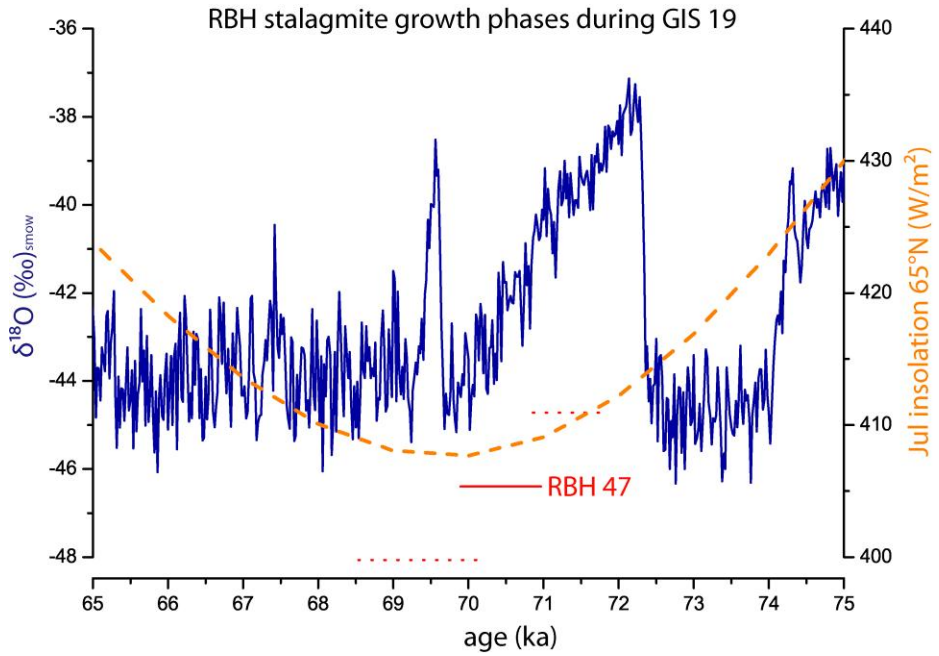

Figure 5.31: Growth phases during GIS 19 of stalagmite RBH 47 (red), compared with the NGRIP $\delta^{18}O$ ice core record (NGRIP, members, 2004), displayed in a dark blue line and the July solar insolation curve at 65°N (Berger and Loutre, 1991), displayed in a dashed orange line. Note that for RBH stalagmites the corresponding dashed lines indicate the maximum and minimum age models, whereas the straight line indicates the final age model. All RBH age models were conducted with StalAge (Scholz and Hoffmann, 2011).

5.3. Mechanisms of past climate variability during MIS 5 reflected in RBH stalagmites

In chapter 5.3 it is shown that general trends of trace elements and stable isotopes recorded in RBH stalagmites indicate that similar processes influence their concentration changes. These processes will be discussed and general mechanisms described. Thus, in the following correlation coefficients are discussed. Note that all correlation coefficients are displayed in correlation matrixes, which can be found in Appendix B in this PhD thesis.

5.3.1 Trace Elements

Here the most common processes, which describe the variation of trace elements in stalagmites, are displayed and interpreted in terms of paleoclimate variability. Nonetheless a difference in the trace element distribution in RBH stalagmites can be observed. However, it must be taken into account that the distribution of trace element variability in stalagmites might be controlled by different processes in different stalagmites of the same cave, even if deposited during the same time interval. This is a consequence of different drip water aquifers and drip rates feeding the stalagmites and reveals that caves are very dynamic systems, which undergo a constant state of change (Fairchild and Baker, 2012).

Therefore, it is not very surprising that the trace element values, e.g. in stalagmite RBH 47, show to some degree different patterns than in stalagmites RBH 32 and stalagmite RBH 39. The reason for that may also be that stalagmite RBH 47 was retrieved from a different part of the cave, whereas the other two stalagmites were located closer together to each other. Thus, it is hypothesized that different control mechanisms were responsible for trace element signals that might differ in RBH 47 from the two stalagmites to some degree in some growth phases. Figures 5.32-5.34 show the trace element distribution of stalagmite RBH 32 (Fig. 5.32), RBH 39 (Fig. 5.33) and RBH 47 (Fig. 5.34) plotted against time.

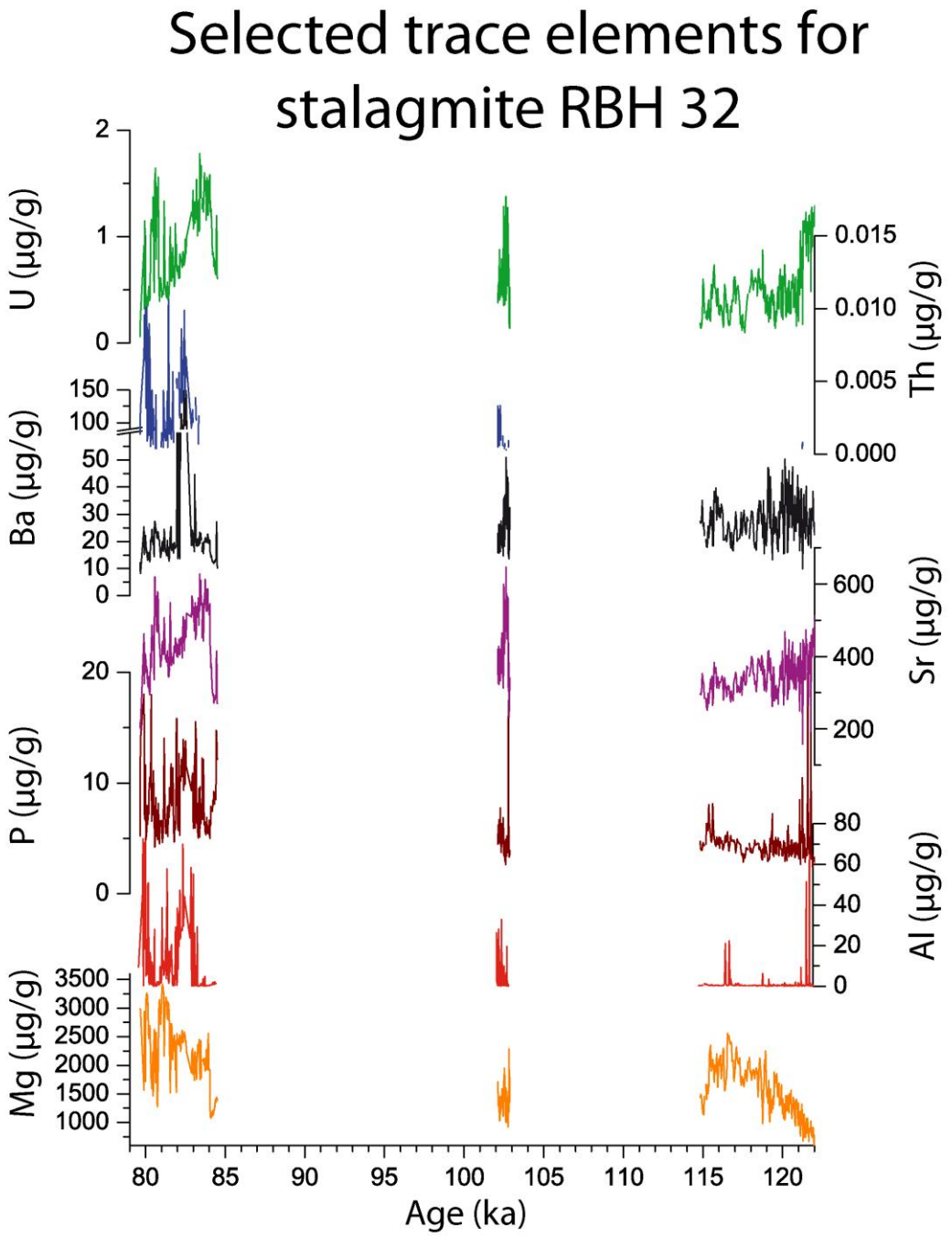

Figure 5.32: Distribution of selected trace elements in stalagmite RBH 32: late Eemian, GIS 23 and GIS 21. Color code for selected trace elements: Mg: orange, Al: red, P: brown, Sr: pink, Ba: black, Th: blue, U: olive.

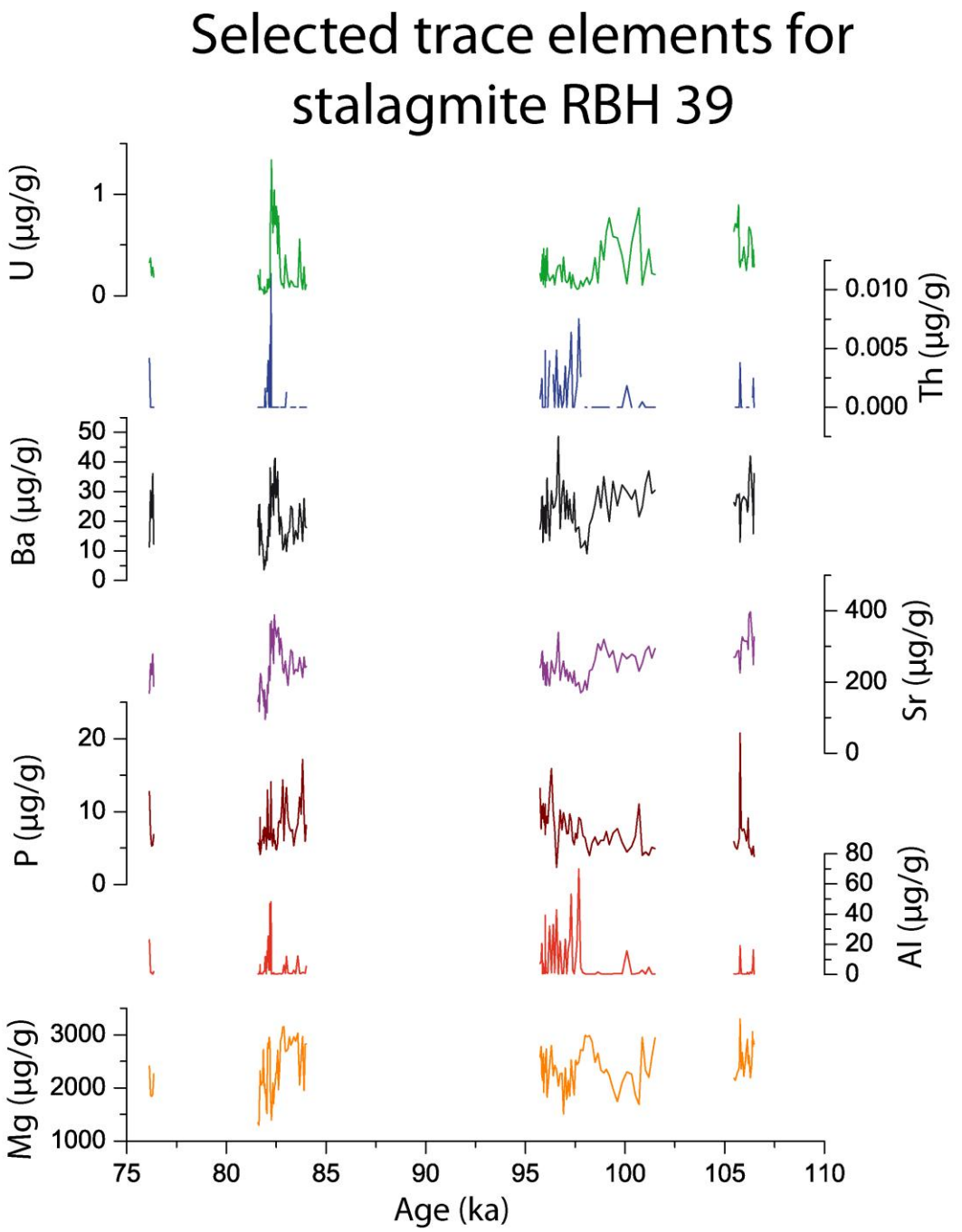

Figure 5.33: Distribution of selected trace elements in stalagmite RBH 39: GIS 24, GIS 23, GIS 21 and GIS 20. Color code for selected trace elements: Mg: orange, Al: red, P: brown, Sr: pink, Ba: black, Th: blue, U: olive.

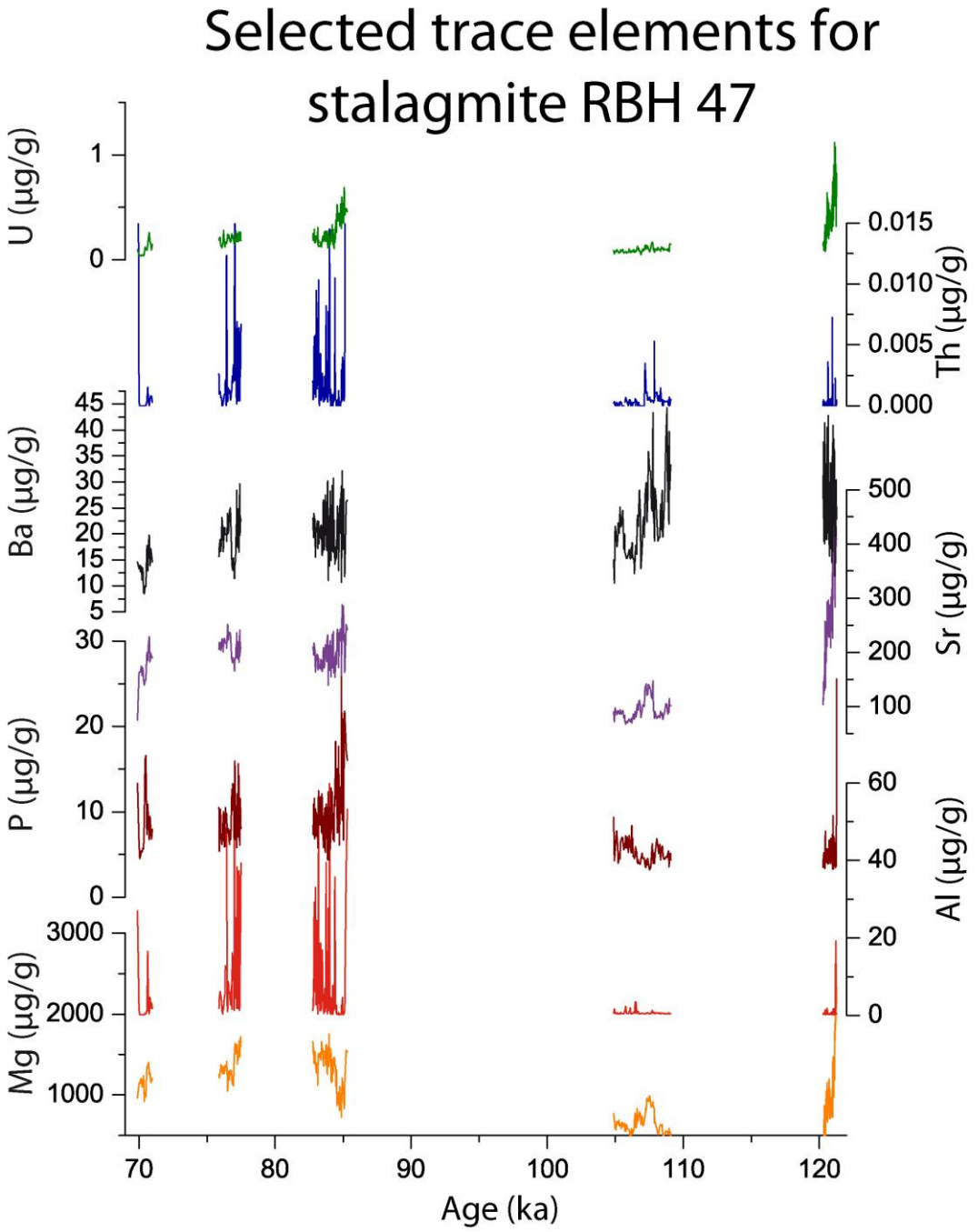

Figure 5.34: Distribution of selected trace elements in stalagmite RBH 47: late Eemian, GIS 24, GIS 21, GIS 20 and GIS 19. Color code for selected trace elements: Mg: orange, Al: red, P: brown, Sr: pink, Ba: black, Th: blue, U: olive.

5.3.1.1 Aluminum and Thorium

In all RBH stalagmites investigated within this PhD thesis, a significant positive correlation as high as r=1 (compare Appendix B, RBH 39, GIS 20) between Al and Th has been observed for all growth phases. These highly significant correlations indicate that similar processes have influenced the concentration of both elements and that they are most likely transported by particles (Fairchild and Treble, 2009). This is not surprising because both elements are known to be indicators of detrital layers and occur in largest quantities at the end of each growth phase. Thus, both elements are interpreted as proxies for detritus that indicate hiatuses between distinct growth phases. However, to avoid falsifications of the correlation matrixes between the trace elements and stable isotopes, all Al concentrations above 100 have been neglected for further correlations and for all records of RBH stalagmites.

5.3.1.2 Strontium, Barium, Uranium and Phosphorous

A prominent covariance between Ba and Sr can be observed in all RBH stalagmites investigated for all growth phases, which is indicated by positive correlation coefficients as high as r=0.99 (compare Appendix B, RBH 39, GIS 20). Both elements belong to the group of the alkaline earth elements and have similar ion radii and divalent cations, which can be substituted for Ca in the carbonate crystal lattice of the stalagmites (Fairchild and Treble, 2009).

Hellstrom and McColloch (2000) point out that in soils, Ba is known to be a rather immobile element due to the high cation exchange selectivity for Ba^{2+} (Peek et al. 2012). Ba may become mobilized in soils when a climate shift from cooler and drier to wetter and warmer conditions occurs. Such shifts may trigger a cascade of processes that lead to the incorporation of Ba and Sr in the crystal lattice of the stalagmite. A sudden climatic shift from colder and drier to wetter and warmer conditions triggers the growth of vegetation and influences its density above the cave. Additionally, physical and chemical weathering will be amplified. As a consequence, this generates higher microbiological activity in and above the soil and increases soil pCO_2. The vegetation above the cave also assimilates nutrition, which is provided from cations in the hostrock or soil. Via complex cation exchange processes this in turn leads to an increase of

carbonic acid in soils. Consequently, nominally rather immobile elements, such as Ba, may be mobilized by increased leaching of soil cations. As a result, the observed shifts in Ba and Sr concentrations in RBH stalagmites are interpreted as a consequence of climate change from drier and cooler to wetter and warmer climate conditions and vice versa. Thus, more humid conditions with phases of stronger precipitation favor the transport of elements such as Ba and its incorporation into the stalagmite. This finding is associated with a high correlation between U and Sr as high as r=0.83 (compare Appendix B, RBH 47, Eemian) in all stalagmites for almost each growth phase and, to a lesser degree, by a positive correlation between U and Ba. Changing U concentrations in stalagmites are dependant on changing redox conditions in the soil and hostrock. Blume et al. (2010) note that under oxidized conditions, U is relatively mobile as UO_2^{2+} in aqueous solution, whereas under reduced environments, U^{4+} is less soluble in soils and the host rock. In this context, it is surprising that opposite observations have been made by Hellstrom and McColloch (2000). They point out that a reduction of the U concentration observed in a stalagmite from New Zealand indicates a change from more oxidizing conditions during the late glacial to less oxidizing conditions during the Holocene, resulting in a reduction in the U concentration. In addition, the decrease in U concentration is inverse to an increase of Ba and Sr concentrations in the record of Hellstrom and McColloch (2000). They come to the conclusion that these elements are not controlled by the same mechanisms.
However, RBH stalagmites reveal a positive covariance between Ba, Sr and U concentrations, which indicates that these elements are controlled by the same mechanisms. Uranium mobilization in soils and the hostrock that leads to an incorporation of U in speleothems is a function of hostrock characteristics, weathering intensity, soil type and soil ventilation, as well as the precipitation regime.

In the case of RBH stalagmites precipitation rates might be the key control mechanism. Thus, an increase in U, Sr and Ba concentrations may represent a rapid precipitation increase associated with a temperature increase from cooler to warmer climate represented in higher element concentrations and vice versa.

Fairchild and Treble (2009) state a potential linkage between paleoclimate and incorporation of P in speleothems. Also, Treble et al. (2003) and Baldini et al. 2002 report such a link and demonstrate that the P concentration in speleothems decreases

with decreasing rainfall. In this case, if U, Ba and Sr concentrations represent past changes in precipitation and temperature, P concentrations in RBH stalagmites should show a positive relation with these elements.

However, this is not the case for RBH stalagmites (compare Appendix B). Thus, the value of P as a proxy of precipitation and temperature variations can be excluded, which indicates that different more complex processes drive P. However, for vegetation, phosphorus is an important nutrition source to produce proteins, DNA and ATP (Blume et al., 2010). It follows that more P should be incorporated into vegetation during wetter and warmer time periods, whereas in cooler and drier time periods, less P should be incorporated in vegetation resulting in opposite findings in speleothems. If this assumption is valid, a strong anticorrelation between P and the denoted trace elements should be detectable, expressed in negative correlation coefficients. However, a negative correlation between P and Ba, Sr and U concentrations cannot be observed in all stalagmites. This, in turn, leads to the conclusion that P in RBH stalagmites, unlike Ba, Sr and U is not directly linked to past precipitation and temperature changes. Hence, it may only be speculated that P is a potential indicator for vegetation density and/or vegetation type.

5.3.1.3 Magnesium

Mg in stalagmites can be an indicator for various processes suggesting changes of precipitation regimes (Fairchild and Treble, 2009; Treble et al. 2003; McDonald et al., 2004, Fohlmeister et al. 2012).

In the RBH stalagmites being investigated, two different mechanisms influencing the Mg concentrations are observed. Thus, the emplacement mechanism of Mg concentrations in stalagmite 47 differs in some phases from those of stalagmites RBH 32 and RBH 39 (compare Fig. 5.32-5.34). This finding is not surprising because stalagmite RBH 47 was retrieved from a different part of the cave, while stalagmites RBH 32 and RBH 39 were closely located to each other. This in turn shows again the sensitivity of the processes, which lead to the incorporation of trace elements in stalagmites. Therefore, the processes of Mg concentration emplacement is first explained and interpreted for stalagmites RBH 32, RBH 39, which are also observed for some of the growth phases in stalagmite RBH 47.

Cruz Jr. et al. (2007) reveal a positive relationship between Mg and $\delta^{18}O$ in a South American stalagmite and interpret this as an indicator of past rainfall veriability driven by changing summer insolation. In RBH stalagmites a general correlation between Mg and $\delta^{18}O$ cannot be drawn (compare Appendix B). However, as revealed in Appendix B, in stalagmites RBH 32 and RBH 39, a significant positive covariance of r=0.64 and r=0.52 between Mg and $\delta^{18}O$ during the Eemian (stalagmite RBH 32) and GIS 21 (stalagmite RBH 39) is striking. Thus, this can be interpreted as an indicator for past rainfall variability, if $\delta^{18}O$ is a proxy for past rainfall. This mechanism might be enhanced when summer insolation is strong as reported for GIS 21 by Berger and Loutre (1991). A similar covariance in stalagmite RBH 47 during the same time interval is not observed. However, this shows again that more than a single parameter may drive Mg concentrations in stalagmites.

It has also been shown that in drier periods, more Mg can be incorporated in stalagmites due to the longer residence time of water and its capacity to dissolve Mg in the hostrock, while the opposite is true for wetter periods (Treble et al., 2003; McDonald et al., 2004; Fohlmeister et al. 2012). In such cases, Mg can be seen as proxy for past rainfall variability. If Mg concentrations reflected in RBH stalagmites also represent past rainfall variability, an increase of Mg concentrations during transitions from wetter to drier conditions should be detected in the RBH stalagmites and vice versa. Short-term variations of Mg concentrations are detected in stalagmites RBH 32 and 39, which are in anti-phase with U concentration expressed by negative correlation coefficients as low as r=-0.63 (compare Appendix B; RBH 39, GIS 24 and Figs. 5.32 and 5.33). Earlier in section 5.3.1.2 it has been shown that U mainly represents past rainfall variations on a local scale.

Thus, phases with low or decreasing Mg concentrations are interpreted here as wetter phases with higher rainfall amounts, while the opposite is true during phases of high or increasing Mg concentrations for stalagmites RBH 32 and RBH 39. This finding is supported by the anti-correlation of U with concentration in both stalagmites.

Similar observations are not observed for all growth phases of stalagmite RBH 47. Consequently, one or more different control mechanisms must have governed the incorporation of Mg. A potential candidate would be Prior Calcite Precipitation (PCP) (e.g. Hellstrom and McColloch, 2000; Tooth and Fairchild, 2003; Fairchild et al. 2006; McMillian et al. 2005; Fairchild et al. 2006; Treble et al., 2003). According to Fairchild and Treble (2009) PCP occurs when to calcite saturated drip water enters a cavity,

which is filled with air that has a lower pCO2 than the drip water. As a consequence, the drip water becomes supersaturated and calcite precipitates prior to entering the cave. In turn, this will lead to an enrichment of Sr/Ca, Mg/Ca and $\delta^{13}C$ and to a decrease of Ca in speleothems. PCP is a common process observed in speleothems and is related to dry climate periods (Fairchild and Treble. 2009).

Only stalagmite RBH 47 shows signs of PCP. However, constant covariations of Mg, Sr and $\delta^{13}C$ cannot be detected in stalagmite RBH 47 (compare Appendix B). Nonetheless, a strong covariance of these elements can be detected during the Eemian, where additionally, highest Mg and Sr concentrations are reached. Hence, PCP is a possible mechanism that could describe the strong covariance between such elements. In that case PCP would be related particularly to stalagmite RBH 47 and would appear as unique event in stalagmite RBH 47. However, PCP only occurs in stalagmite RBH 47 and only during the Eemian. Thus, it can be stated that PCP, in RBH stalagmites, is not a predominant process.

5.3.2 Stable isotopes

In chapter 2 it has been shown that stable isotopes ($\delta^{18}O$ and $\delta^{13}C$) can be affected by several different mechanisms that influence their signals in speleothems and that these signals may be influenced by equilibrium or kinetic isotope fractionation processes. Mickler et al. (2006) have shown that most stable isotope records may be influenced by kinetic fractionation. In this case both isotopes should show similar signals (Mühlinghaus et al. 2009). Moreover, Mühlinghaus et al. (2009) stated that kinetic fractionation might be enhanced by slow drip water rates, which in turn results in higher $\delta^{18}O$ values (Mühlinghaus et al. 2009; Scholz et al. 2009; Scholz and Dreybrodt, 2011). However, to estimate the isotope fractionation types, as described e.g. y Friedmann and O'Neil (1977); Kim and O'Neil (1997); O'Neil et al. (1969), cave monitoring data such as drip water composition and cave temperature are needed. As has been mentioned before, the RBH is considered as nature reservoir with limited excess. Therefore, a RBH cave monitoring was not possible and hence, it was not possible to estimate the predominant isotope fractionation type mathematically in this thesis. However, Mickler et al. (2006) state that if $\delta^{18}O$ and $\delta^{13}C$ are positively correlated to each other, kinetic fractionation may have been the predominant process. Consequently, the fractionation processes can also be illustrated graphically (Figs. 5.35-5.37).

The correlation coefficients calculated for the different RBH stalagmite growth phases as displayed in Figs. 5.35-5.37 suggest that equilibrium fractionation has been the predominant controller of RBH stalagmite stable isotope signals, at least for most phases (compare Appendix B). In all stalagmites, growth phases can be observed, in which kinetic fractionation processes dominate. It is striking that none of these phases is observed in individual stalagmites at the same time. However, it has been suggested by Mickler et al. (2006) that same processes influence both isotope signals.

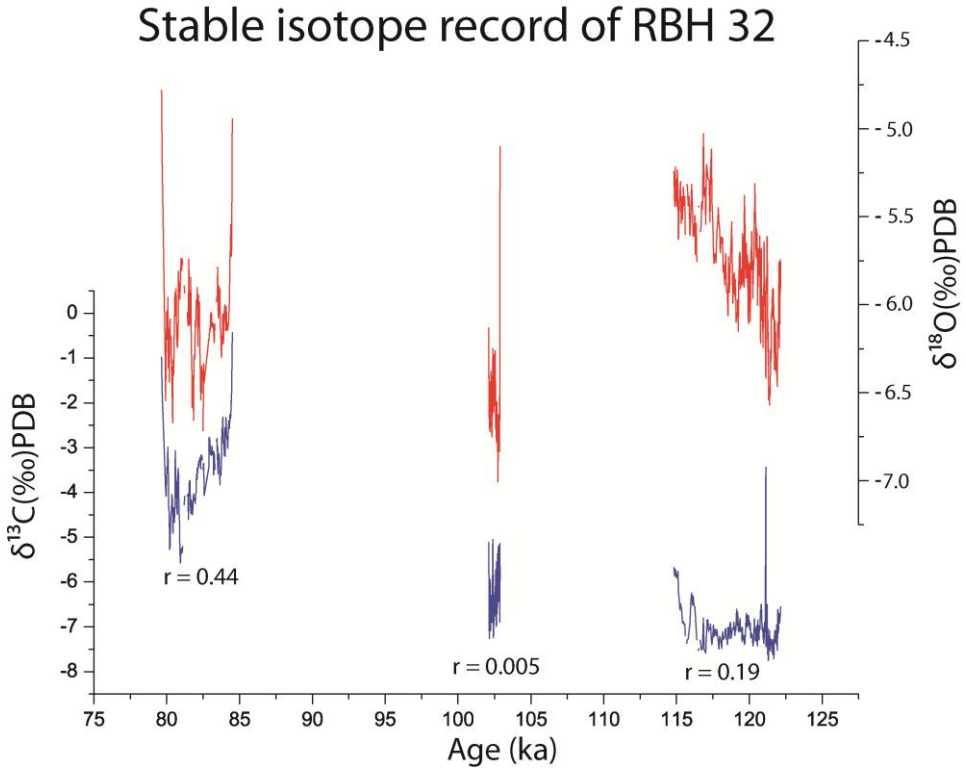

Figure 5.35: The stable isotope record ($\delta^{18}O$ and $\delta^{13}C$) of stalagmite RBH 32 displayed with correlation coefficients for the late Eemian, GIS 23 and GIS 21.

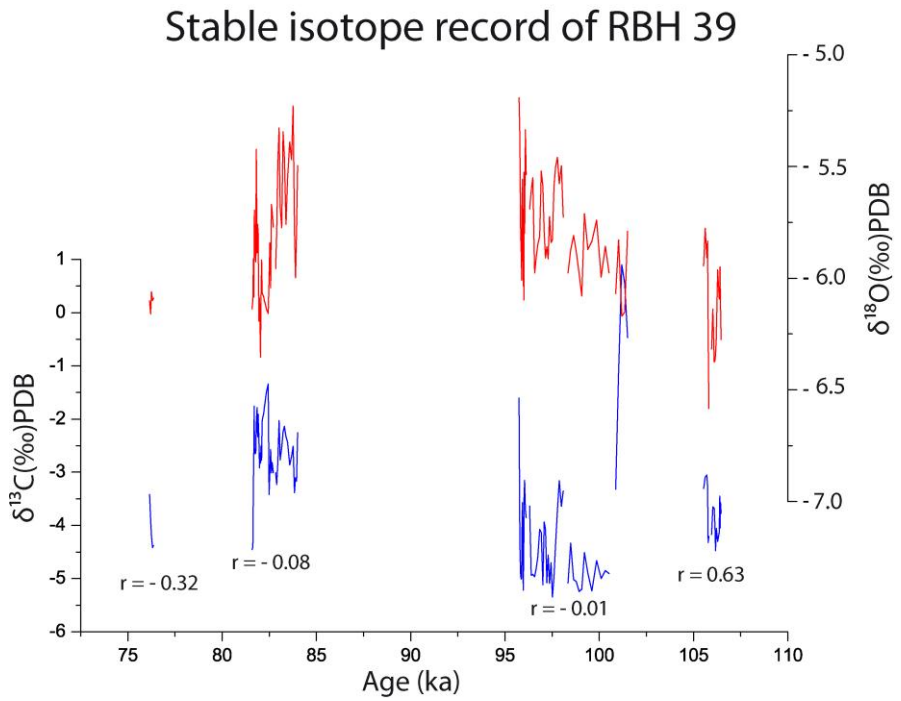

Figure 5.36: The stable isotope record ($\delta^{18}O$ and $\delta^{13}C$) of stalagmite RBH 39 displayed with correlation coefficients for GIS 24, GIS 23, GIS 21 and GIS 20.

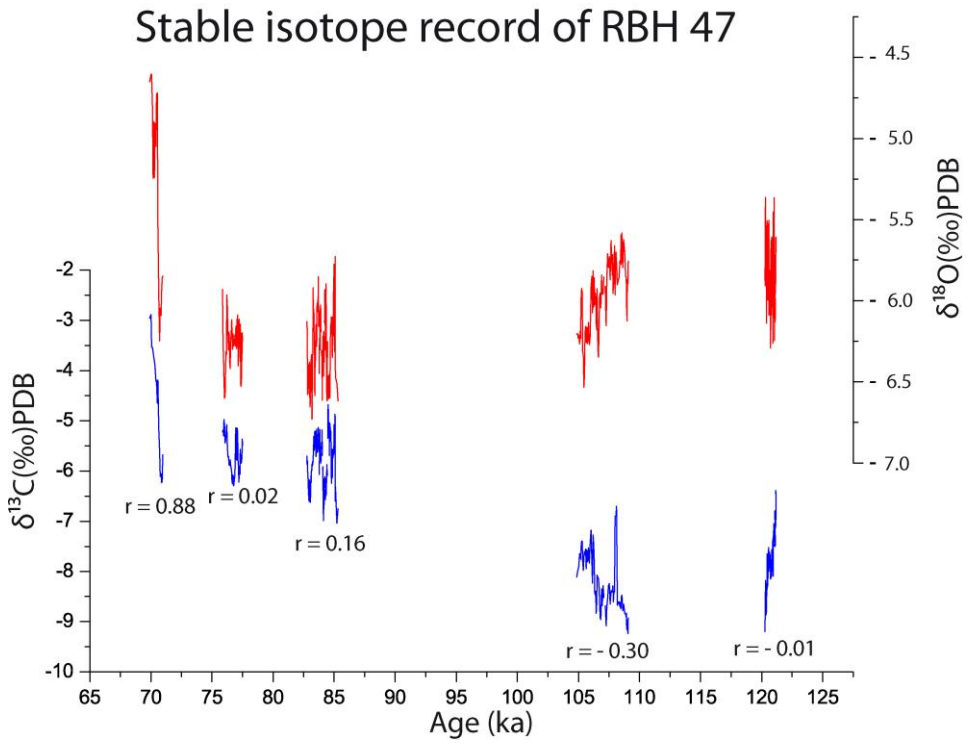

Figure 5.37: The stable isotope record ($\delta^{18}O$ and $\delta^{13}C$) of stalagmite RBH 47 displayed with correlation coefficients for the late Eemian, GIS 24, GIS 21, GIS 20 and GIS 19.

5.3.2.1 The $\delta^{18}O$ records of the RBH stalagmites

It has been shown in previous studies that $\delta^{18}O$ records of speleothems are reliable proxies for paleoclimate variability (e.g. Cheng et al., 2012; Fohlmeiser et al., 2012; Boch et al. 2011, Drysdale 2009; Cruz Jr. et al., 2007; Fleitmann et al., 2006; Mangini et al., 2005).

Nonetheless, in comparison to $\delta^{18}O$ records from monsoon-influenced regions, the variability in stable isotope signals in Central and Northern European speleothems is rather small. Therefore already small changes in such records may indicate climate variability, which may, however, be superimposed by cave internal processes. Consequently, the interpretation of $\delta^{18}O$ records for stalagmites in these regions is not straightforward.

Recently, Fohlmeister et al. (2012) demonstrated that four Holocene stalagmites from Bunkercave, which is located 200 km southwest of the RBH, reveal valuable insights of paleoclimate variability. Fohlmeister et al. (2012) argue that the main moisture source of the cave site is the North Atlantic Ocean. Thus, the $\delta^{18}O$ signature of RBH stalagmites should also be sensitive to changes in past climate conditions, due to the cave location, which is located in higher latitudes than Bunkercave and closer to the North Atlantic.

There are four potential drivers that can influence the $\delta^{18}O$ signature of stalagmites (Couchoud et al. 2009):

1. Calcite precipitation temperature: In this case, the relation of the $\delta^{18}O$ value to the temperature is about -0.23‰/°C (Friedmann and O'Neil, 1977; Kim and O'Neil, 1997; O'Neil et al. 1969), when the $\delta^{18}O$ values are reflected by equilibrium fractionation conditions.

2. Additionally, the $\delta^{18}O$ signature could reflect seepage water and is, thus, a proxy for rainfall $\delta^{18}O$ recharge, which can potentially be forced by changes of the condensation temperature, vapor source and/or the amount effect (Lachniet et al. 2009). Another potential driver could be triggered by air mass trajectories.

Fohlmeister et al. (2012) interpret the $\delta^{18}O$ variability of Bunkercave stalagmites to as a proxy for rainfall $\delta^{18}O$. This interpretation is also very likely for the $\delta^{18}O$ variations observed RBH stalagmites.

3. Moreover the amount effect (Daansgard, 1964) is an additional candidate to govern the signal of $\delta^{18}O$ variations in RBH stalagmites, which would in turn be triggered by significant changes in rainfall amounts resulting in increasing $\delta^{18}O$ values in an order of magnitude that is described by several ‰ (e.g. Cruz Jr. et al. 2006). Thus more rain would cause an increase of $\delta^{18}O$ reflected in stalagmites and vice versa. This effect is an important driver for $\delta^{18}O$ values in stalagmites from tropical latitudes but minor for temperate regions. Therefore, the amount effect in the stable isotope signature in RBH stalagmites can be neglected.

4. Also, the temperature effect, first described by Daansgard (1964), is a potential driver to regulate the $\delta^{18}O$ signature of RBH stalagmites, which may generate a positive relationship between increasing temperature and increasing rainfall $\delta^{18}O$ and vice versa. Lachniet et al. (2009) remark that this process might be a predominant driver of $\delta^{18}O$ in more continental regions and/or regions of higher latitudes due to sharper isotope-temperature gradient. Consequently, this process can be an important driver for $\delta^{18}O$ variability in RBH stalagmites.

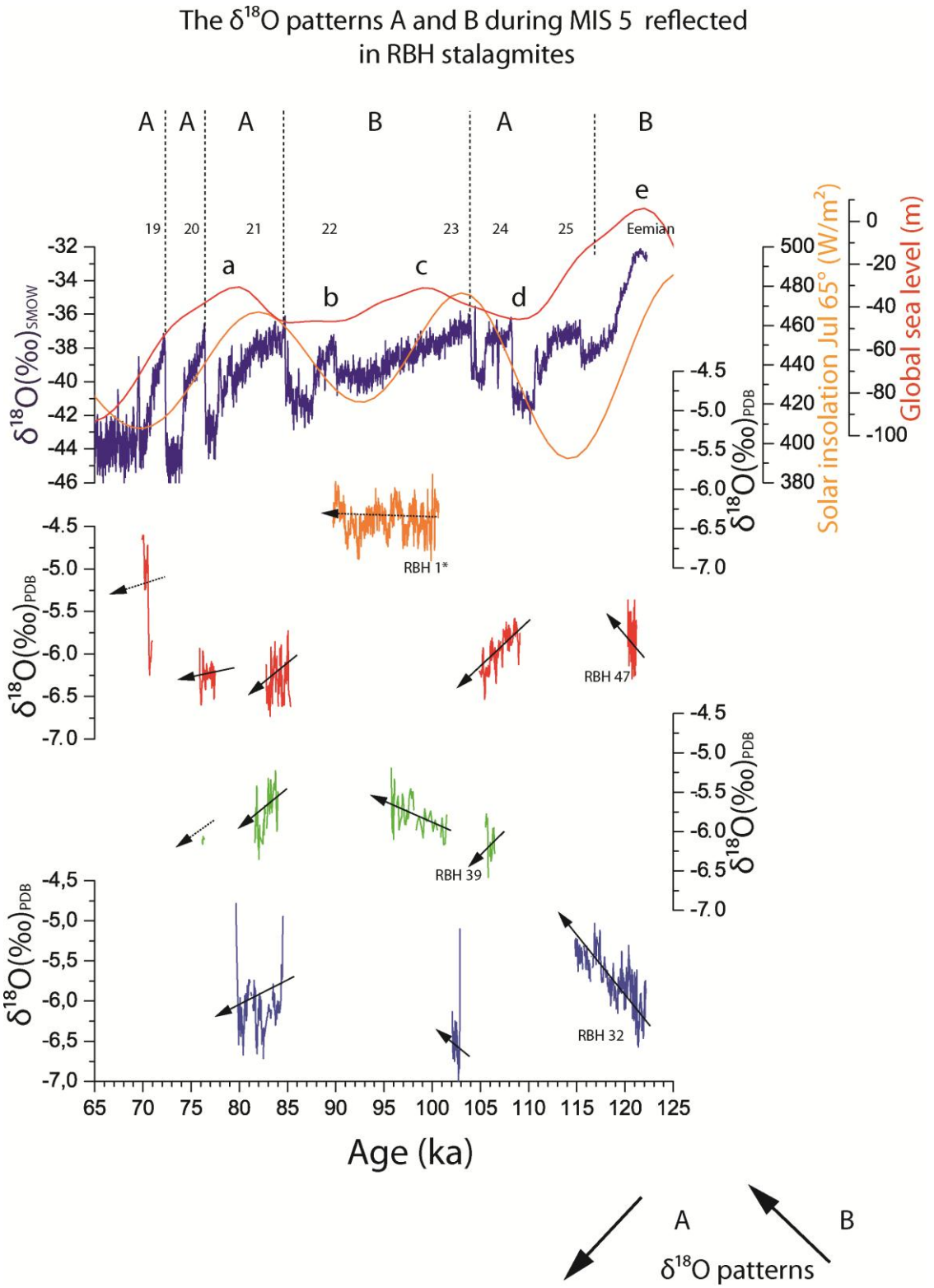

Figure 5.38: The relationship between orbital time scale variations and the $\delta^{18}O$ record reflected by the two different pattern types A and B plotted against the NGRIP δ18O record displayed in navy blue (Wolff et al., 2010), Sea level curve displayed in red (Martinson et al., 1987) and the July solar insolation curve at 65°N displayed in orange (Berger and Loutre, 1991). Color code for RBH stalagmites: blue: stalagmite RBH 32, green: stalagmite RBH 39, red: stalagmite RBH 47 and an additional stalagmite of an unpublished RBH dataset (Niggemann) displayed in orange.

In RBH stalagmites, no climate variability on orbital time scale can be observed in $\delta^{18}O$ records. Thus, here it is postulated that the $\delta^{18}O$ signature of RBH stalagmites is be modulated by millennial climate variability. In Fig. 5.38, it is suggested that the $\delta^{18}O$ variability, observed in RBH stalagmites, is primarily driven by two different pattern types, which are inverse to each other. The trend of these pattern types are indicated with arrows. In most cases the arrows are conducted by linear regression fits. However, due to a spare data base for GIS 19 a trend for the $\delta^{18}O$ pattern for this growth phase could only be assumed.

Pattern A Type: Growth phases with decreasing $\delta^{18}O$ values with time. This type is linked to GIS 24, 21, 20 and 19.
Pattern B Type: Growth phases with increasing $\delta^{18}O$ values with time. In turn this type is reflected during the late Eemian growth phases.

The pattern A type is observed more often in the RBH stalagmites. This type suggests that decreasing $\delta^{18}O$ values in speleothem calcite are linked to decreasing temperature and, thus, represents “normal” (i.e., expected) $\delta^{18}O$ variations (Lachniet et al. 2009, McDermott et al. 2004). During these “normal” conditions, it is expected that the $\delta^{18}O$ compositions displayed in stalagmites results from summer recharge as well as from winter recharge. Additionally, it is suggested that during summer, the evapotranspiration rates, in comparison to the pattern B type, may be reduced. Consequently, lower evapotranspiration rates during summer do not lower the recharge of summer precipitation. In turn, summer and winter precipitation recharge would both be the key controllers feeding the $\delta^{18}O$ values of RBH stalagmites. Thus, the $\delta^{18}O$ value is a signal that also may represent the amount of summer precipitation when accounting for a positive relationship between summer temperature and amount of summer precipitation. Consequently, the $\delta^{18}O$ pattern A type variation is interpreted to reflect both surface temperature and precipitation variation.

Here it is hypothesised that the transition from pattern type A to type B, at least during MIS 5, is modulated by changes of orbitally forced solar insolation patterns and changes of the AMOC. Consequently, during periods, which are characterized by a prevailing pattern B type, the $\delta^{18}O$ values in the RBH stalagmites are strongly influenced by winter

recharge. Thus, in comparison to the pattern A type, the pattern B type represents phases in speleothems suggesting an inverse relationship between speleothem $d^{18}O$ values and temperature (i.e., lower $d^{18}O$ values corresponding to higher temperatures). This may be due to a positive relationship between the amount of winter precipitation and winter temperature, which has been suggested and modeled for Holocene stalagmites from Bunkercave (Wackerbarth et al. 2010; Fohlmeister et al. 2012). The authors show that high evapotranspiration during summer lowers and probably inhibits recharge during summer. Thus, summer precipitation does not contribute to the recharge water. Furthermore, more positive $\delta^{18}O$ values would represent cold and dry winters and wetter summers, whereas more negative $\delta^{18}O$ values would represent more humid and warmer winters but drier summers. Hence, the amount of winter precipitation would be the key controller of the $\delta^{18}O$ signals of the drip water feeding the stalagmites. Consequently, following the findings for Bunkercave (Fohlmeister et al. 2012); Wackerbath et al. 2010), pattern B type $\delta^{18}O$ variations are interpreted as reflecting changes in winter surface temperature and amount of winter precipitation.

Hence, in times when summer insolation decreases and the strength of the AMOC diminishes, the influence of summer recharge on the $\delta^{18}O$ values of the RBH stalagmites will be enhanced. This, in turn, will lead to more positive $\delta^{18}O$ values resulting in an increasing $\delta^{18}O$ trend, which is anti-proportional to the $\delta^{18}O$ trend observed in the NGRIP ice core during the late Eemian and MIS 23 (pattern B types during MIS 5) (Fig. 5.38). Thus, during periods of highest summer solar insolation at 65°N combined with strong and stable phases of the AMOC, evapotranspiration during summer is amplified (compare Fig. 5.38, Eemian and GIS 23).

5.3.2.2 The $\delta^{13}C$ records of RBH stalagmites

Similar trends of the $\delta^{13}C$ values investigated in the RBH stalagmites cannot be observed in the individual growth phases. However, a long-term trend towards less negative values in time is observed. Generally, these patterns could indicate a long-term climate-cooling trend.

Genty et al. (2001) point out that most carbon in speleothems originates from soil pCO_2. Taking into account this precondition, Couchoud et al. (2009) note that it is likely that

speleothem $\delta^{13}C$ is controlled by biogenic soil CO_2 productivity. Similar findings have been reported by Gascoyne (1992), Hellstrom et al. (1998) and Genty et al. (2006). The authors conclude that biogenic soil activity is controlleded by vegetation density via root respiration, photosynthetic activity and microbiological activity. Vegetation density in turn is a function of local temperature. Warmer and wetter periods enlarge the vegetation density and so the soil productivity. Consequently, the $\delta^{13}C$ values represented in speleothems are more negative during warmer and wetter and less negative during cooler and drier climate periods. Hence, the $\delta^{13}C$ signature in RBH stalagmites may be influenced on millennial and orbital time scales.

On the millennial time scale, the $\delta^{13}C$ variations of individual RBH stalagmites demonstrate contradicting patterns, which do not show any systematic patterns related to millennial scale temperature variability. This observation can be explained with a non-homogeneous microbial activity as well as with non-homogeneous vegetation coverage. Consequently, both may lead to different $\delta^{13}C$ signals in speleothem. Additionally, cave internal processes such as PCP, kinetic isotope fractionation, slower or faster drip rates at individual cave sites (Dreybrodt 2008; Mühlinghaus et al., 2009; Scholz et al., (2009); Scholz and Dreybrodt (2011), which influence the growth rates as well as different drip water residence times may superimpose at least to some degree the $\delta^{13}C$ signature observed in RBH stalagmites. Thus, the $\delta^{13}C$ record of individual RBH stalagmites on the millennial scale remains difficult to compare and to interpret.

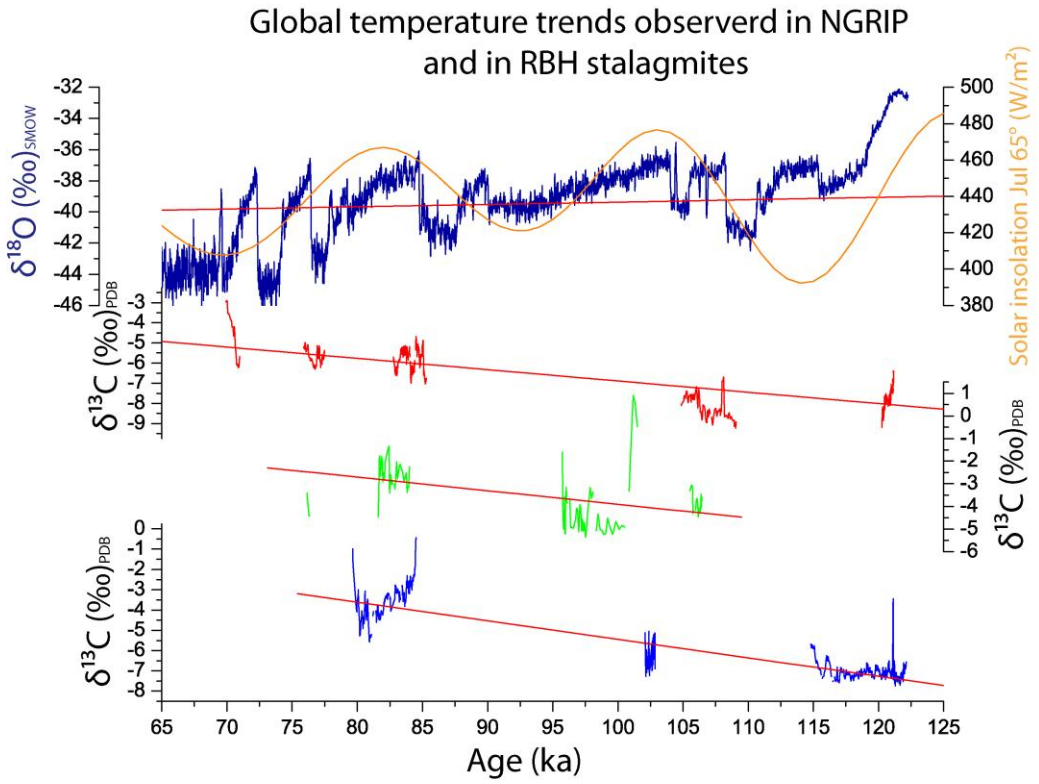

Figure 5.39: Orbitally forced changes of the climate variability of $\delta^{13}C$ records observed in RBH stalagmites and the $\delta^{18}O$ record of NGRIP (Wolff et al. 2010) displayed in navy blue and plottet against the July solar insolation curve at 65° N (Berger and Loutre,1991) displayed in orange. Color code for RBH stalagmites: blue: stalagmite RBH 32, green: stalagmite RBH 39 and red: stalagmite RBH 47.

On orbital time scales, however, the $\delta^{13}C$ records of the RBH stalagmites represent local temperature changes and show a gradual cooling in time as indicated in Figure 5.39. The red lines displayed in Fig. 5.39, demonstrate these gradual cooling trends, which are observed in each individual RBH stalagmite. Similar cooling trends are for example observed in the NGRIP ice core record (NGRIP members 2004), in the LR04 stack (Lisiecki and Raymo, 2005) as well as in the sea surface temperature record (SST) (Martrat et al. 2007) and to a less degree in the Gröbern pollen record (Kühl et al. 2007) for the same time period from 125-65ka before present. This allows the assumption that the general $\delta^{13}C$ patterns of the RBH stalagmites are not only following local but also the global cooling trends at least on an orbital time scale. Thus, for the observed RBH stable isotope records it can be summarized that:

1. The $\delta^{13}C$ records represent potentially predominant climate variability on orbital time scales.

2. The $\delta^{18}O$ values represent potentially prevalent climate variability on the millennial time scale. However, orbital forcing additionally influences the millennial scale $\delta^{18}O$ variability, which is reflected by pattern type A and B.

5.4. Reconstruction of millennial scale climate variability during MIS 5 based on RBH stalagmites

The mechanisms investigated in chapter 5.3 are now studied in detail in order to reveal climate variability of Northern Germany. As has been shown, the growth phases correspond to the late Eemian and the pronounced GIS 24, 23, 21, 20 and 19 (Fig. 5.40). However, due to the relatively large age uncertainties, the interpretation of millennial scale variability revealed by RBH stalagmites remains difficult.
Particularly here, the climate reconstruction for GIS 24 and 23 remains speculative, due to relatively large $^{230}Th/U$-age errors combined with only few data points. Nonetheless, to a certain degree, RBH stalagmites represent past millennial climate variability for Northern Germany but, due to the discussed problems, one has to be careful with statements in order to avoid over interpretation.

Thus, disregarding the difficulties stated above, it is hypothesized that:

1. In most cases, a threshold of $\delta^{18}O$ = -38‰ in the NGRIP ice core must be exceeded to trigger the growth of RBH stalagmites.
2. The growth phases of RBH stalagmites correspond to the GIS, but they rarely grow during the entire GIS.
3. Considering the large age uncertainties, it is assumed that some RBH stalagmites might reflect the “precursor-type” and “rebound-type” events, which were first introduced by Capron et al., (2010a) for the NGRIP ice core and also found in high alpine stalagmites (Boch et al. 2011).

According to Capron et al. (2010a) precursor and rebound events can be defined as follows:

Precursor-type events:

Short-term and rapid warming to interstadial conditions followed by a sudden flash back to stadial conditions, which are observed during MIS 5 for GIS 23 and GIS 21. The nature of these precursor events can be best illustrated considering that in comparison to MIS 2, 3 and 4 much smaller ice sheets were present during MIS 5 (Bintanja et al. 2005; Colleoni et al. 2012). Capron et al. (2010a) point out that the ice sheets during MIS 5 react much more sensibly to changes of solar insolation. The authors point out, that strong summer insolation at 65°N may trigger sporadic freshwater discharge, which in turn would trigger a rapid transition of the state of the AMOC. The short excursion back to stadial conditions might be due to a relatively unstable AMOC mode. Finally, when solar insolation increases, a sudden shift back to interstadial conditions is displayed reflecting a much more stable AMOC situation.

Rebound-type events:

Fast switchbacks to warmer interstadial conditions after a long cooling phase, which occur shortly followed by a change to stadial conditions observed at the end of the late Eemian, GIS 23 and GIS 21. Capron et al. (2010a, 2012) also identify GIS 22 and GIS 25 to be rebound-type events, triggered by feedbacks of e.g. sea ice formation. Capron et al. (2011) suggest these rebound effects to be associated with the sea ice feedback mechanism (Cruzifix and Loutre, 2002). Capron et al. (2010a) conclude, that the relatively long cooling phase of proceeding GIS warm phases (late Eemian, GIS 23 and GIS 21) are causing the reduction of river runoff combined with increasing sea ice formation. Consequently, this causes the salinity enrichment below the sea ice formation in relatively cold waters. Cool, salty water display a much higher density than cool but less salty waters. Hence, at a certain point, a saltwater plume triggers the re-advection of the AMOC, which in turn triggers the appearance of prominent rebound events.

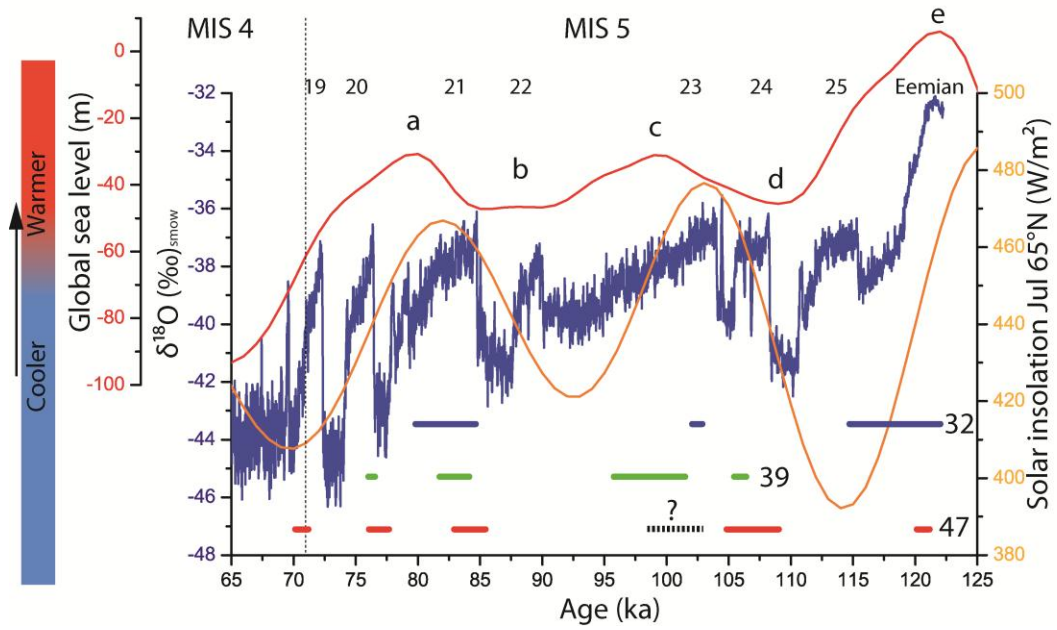

Figure 5.40: Overview of RBH stalagmite growth phases reflecting the late Eemian and GIS 24, 23, 21, 20 and 19 plotted against the NGRIP δ18O record displayed in navy blue (Wolff et al., 2010), Sea level curve displayed in red (Martinson et al., 1987) and the July solar insolation curve at 65°N displayed in orange (Berger and Loutre, 1991). Color code for RBH stalagmites: blue: stalagmite RBH 32, green: stalagmite RBH 39, red: stalagmite RBH 47. The black dashed line indicates the diagentically disturbed section in stalagmite RBH 47, which represents a phase during GIS 23 but could not be accurately dated due to PDD (Post Depositional Diagenesis)

5.4.1 The end of the late Eemian

The $\delta^{18}O$ records of RBH stalagmites displayed in Fig. 5.38, demonstrate that the pattern B type is predominant during the Eemian. Stalagmite RBH 32 was chosen to show the climate evolution during the late Eemian and the inception of the early last glacial period. Thus, in Fig. 5.41 the climate evolution from 122.15-114.84ka is shown as displayed by stalagmite RBH 32. This stalagmite has been chosen because stalagmite RBH 32 is the only RBH stalagmite that reveals the longest record for the late Eemain. Here, the evolution Sr and U is compared with the $\delta^{18}O$ record of NGRIP (Wolff et al. 2010), the solar insolation curve displayed at July 65°N (Berger and Loutre, 1991) and the SST (Martrat et al. 2007). The dashed black line indicates that within the 95% confidence interval, it is also possible that the growth inception of stalagmite RBH 32 started at 124 ka and stopped at 116.25 ka. This scenario is plausible considering that the inception of GIS 25 is recorded at 116 ka as reflected in NGRIP (Capron et al. 2012). In addition, an alpine stalagmite also estimates the end of the Eemian at 116 ka

(Holzkämper et al. 2004). However for stalamite RBH 32 is unlikely that the growth inception occurred later than 122.15 ka because there are no sedimentological, petrographic or Th/U ages that would justify this assumption. This scenario is, thus, excluded and not displayed in Fig. 5.41. A gradual decrease of U and Sr can be observed. As discussed in chapter 5.3.1, both elements are here interpreted as proxies for past temperature variability and hence would indicate a temperature decrease. The cascade of impacts revealed in chapter 5.3.1 now shifts in a different direction resulting in a regional decrease of temperature and precipitation. This decrease in temperature and precipitation is also observed elsewhere (e.g. Kühl et al., 2007; Sirocko et al. 2005). Accordingly, the regional temperature and precipitation decrease coincides with a synchronized SST temperature reduction of 2.2°C observed at the Iberian Margin (Martrat et al., 2007), a reduction in summer insolation intensity by 80 (W/m^2) (Berger and Loutre, 1991) and a decrease of -7‰ in the $\delta^{18}O$ signal in NGRIP. Therefore, it is stated that the regional temperature reduction as observed for the RBH cave site reflects a global temperature and precipitation reduction. Moreover stalagmite RBH 32 reflects the last glacial inception.

A long term cooling trend from 123-116 ka is associated with decreasing obliquity and a precession forced insolation as reported for NGRIP by Carpon et al. (2012). This can also be observed in stalagmite RBH 32. Prior to the glacial inception a sharp decline in the Sr and U concentration occurs during 121 and 119 ka +/- 2 ka, which indicates a sudden shift to cooler temperatures. This temperature shift could be associated with an annual mean cooling of 5°C between 122 and 120 ka and a gradual appearance of perennial arctic sea ice cover at about 122 ka as reported by Cricifix and Loutre (2002) for high Northern latititudes.

This hypothesis agrees with the findings in stalagmites of the RBH. Thus, after 120ka +/- 2ka the Sr and U concentrations are rarely exceeding 400 and 0.8µg/g in stalagmite RBH 32. This suggests that temperatures remain lower at the cave site after 120ka. Additionally, the $\delta^{18}O$ record of stalagmites RBH 32 suggests that gradual cooling of the strong evatransoporation during summer forced by a potential cold spell at 121ka +/ 2ka resulting in a $\delta^{18}O$ shift of +0.5‰ (Fig 5.41).

Based on modeling results, Lohmann (2007) speculates that the glacial inception is introduced by the direct effect of insolation combined with a negative phase of the NAO (North Atlantic Oscillation). Thus, a negative NAO would be associated with a reduced intensity of the westerlies allowing northeastern cold spells to trigger colder winters

(Wanner et al. 2001). This, in turn, establishes a climate regime, where cold and dry temperatures prohibit sufficient precipitation to trigger the growth of RBH stalagmites. This scenario characterizes the glacial inception reflected by RBH stalagmites at about 114.82ka. Within errors glacial inception at 116.25ka seems to be more plausible compared with the findings of others.

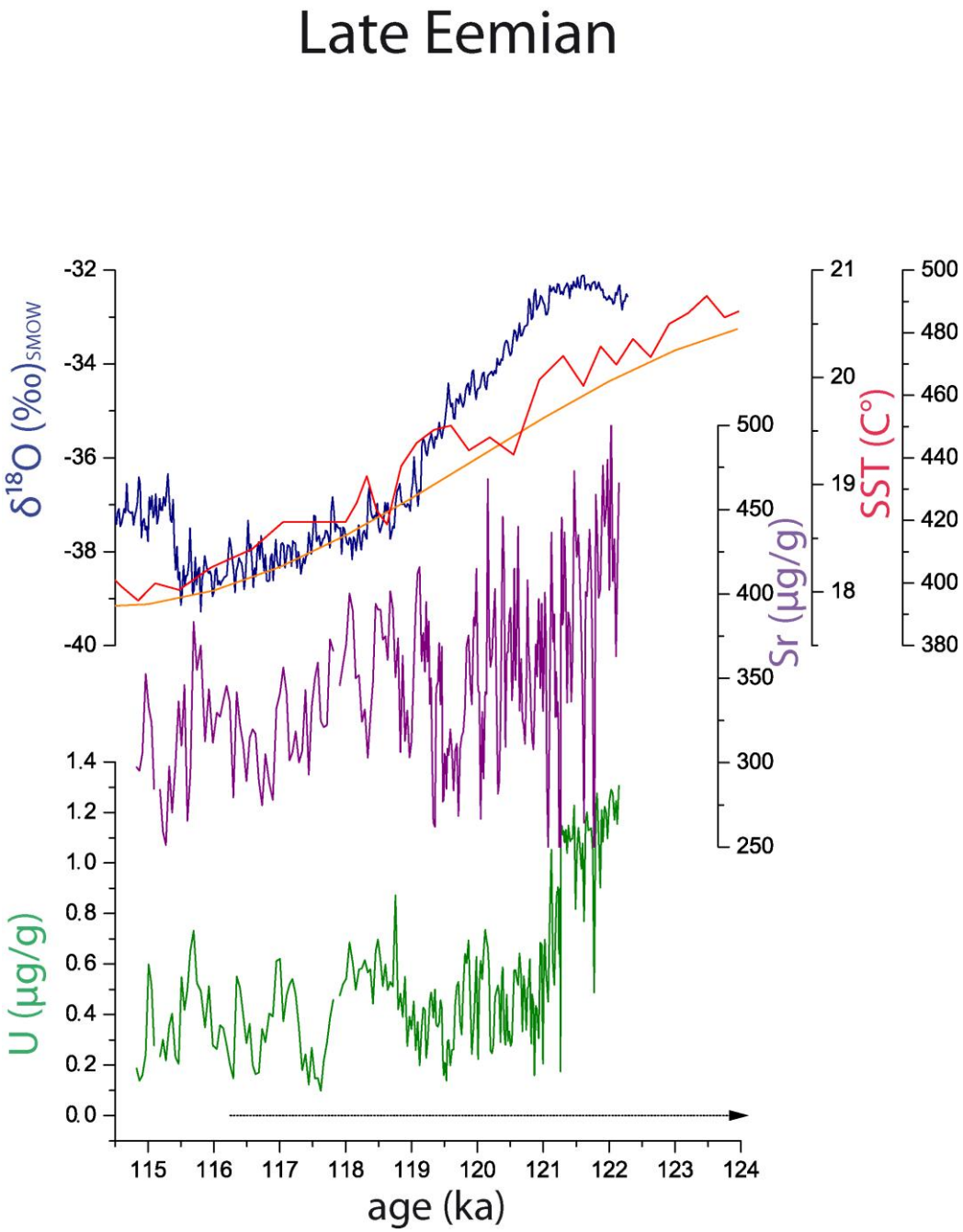

Figure 5.41: Climate variability of the late Eemian period represented by stalagmite RBH 32 compared to the $\delta^{18}O$ record of NGRIP (Wolff et al., 2010), the July solar insolation curve at 65°N (Berger and Loutre, 1991) and the MD95-2042 SST record of the Iberian Margin (Martrat et al., 2007). Color code: olive: U concentration, pink: Sr concentration.

5.4.2 Past climate variability during GIS 24

As shown in Fig. 5.38, the $\delta^{18}O$ pattern A type is predominant during GIS 24. The climate reconstruction for GIS 24 is difficult due to large age uncertainties in stalagmite RBH 47 for GIS 24. It is considered to represent GIS 24 best because it comprises the longest growth period. However, to construct the age model of GIS 24 in stalagmite 47, the maximum/minimum age method was applied because only one Th/U age was measured during that time interval for RBH 47. One big disadvantage of this method was that the relatively large error of 4 ka was reproduced for each Th/U-age conducted with StalAge. Therefore, stalagmite RBH 47 was excluded from the representation of GIS 24. Instead, RBH 39 was chosen to represent the climatic evolution of GIS 24 as far as possible. Stalagmite RBH 39 reveals the better age model but is represented by much shorter growth duration within GIS 24.

GIS 24 spans 4.85ka in NGRIP as reported by Capron et al. (2010a). As has been demonstrated in chapter 5.2, stalagmite RBH 39 reveals a duration of growth of 1.07 ka from 106.46-105.39ka during GIS 24. This reveals that the growth of stalagmite RBH 39 may have started when the hypothesized threshold of -38‰ $\delta^{18}O$ is exceeded (compare Fig. 5.40). That can be explained considering cave internal cave processes (Fairchild and Baker, 2012), which might have prevented the direct inception of growth in stalagmite RBH 39 after this threshold was reached. Fig. 5.42 shows the Ba and Sr concentration of stalagmite RBH 39 during GIS 24. The black dashed line close to the x-axis indicates that growth inception might have commenced earlier considering the 95% confidence interval. Although possible within the 95% confidence interval, it is unlikely that growth inception commenced later than 106.46ka considering that the RBH growth phases are related to Greenland Interstadials as postulated earlier. Thus, this scenario is not displayed in Fig. 5.42.

The Sr and Ba concentration of stalagmite RBH 39 demonstrate high oscillation patterns. The patterns might be related to abrupt cooling excursions during GIS 24 as suggested by Capron et al. (2010a). The authors state that the pronounced cold spell observed during GIS 24 can be compared to the 8.2ka event as described by Alley et al. (1997) and observed e.g. in stalagmites from northeastern China by Wu et al. (2012). Within the 95% confidence limit, it is possible to wiggle match these oscillation patterns with the oscillation patterns of NGRIP as indicated by the arrows (Fig. 5.42). This scenario suggests that the growth inception of stalagmite RBH 39 commenced after this

short cold reversal in the second half of GIS 24. During that phase, a rapid negative shift of 100µg/g Sr and 15 µg/g Ba concentrations accompanied by a large shift of 0.5‰ in the $\delta^{18}O$ can be observed in stalagmite RBH 39 (compare Fig. 5.38). Here, it is suggested that these large shifts observed in Fig. 5.42 represent a temperature decrease, which is also observed in NGRIP, as described by Capron et al. (2010a). However, the large shifts can also observed, even so less pronounced and earlier, in the SST record of the sediment core obtained at Iberian margin. The insolation curve for Jul at 65° N is continues increasing after GIS 24. Thus, the sudden North Atlantic freshwater input has a larger influence on climate variability than orbital forcing similar to the observations of Lohmann (2006) for the onset of GIS 25. However, in comparison to the proceeding GIS during MIS 5 (except GIS 22), the AMOC seems to be much more unstable during GIS 24 resulting in pronounced cold spells. These sub-millennial cold spells are triggered by strong modifications of freshwater input as suggested by Capron et al. (2012). This in turn could be related to a complex interplay between freshwater discharge (von Grafenstein et al., 1998; Rahmstorf et al., 2005; Clark et al., 2004) and enhanced precipitation (Khordi et al., 2001), which might be favored by small ice sheets (Eisenmann et al., 2009).

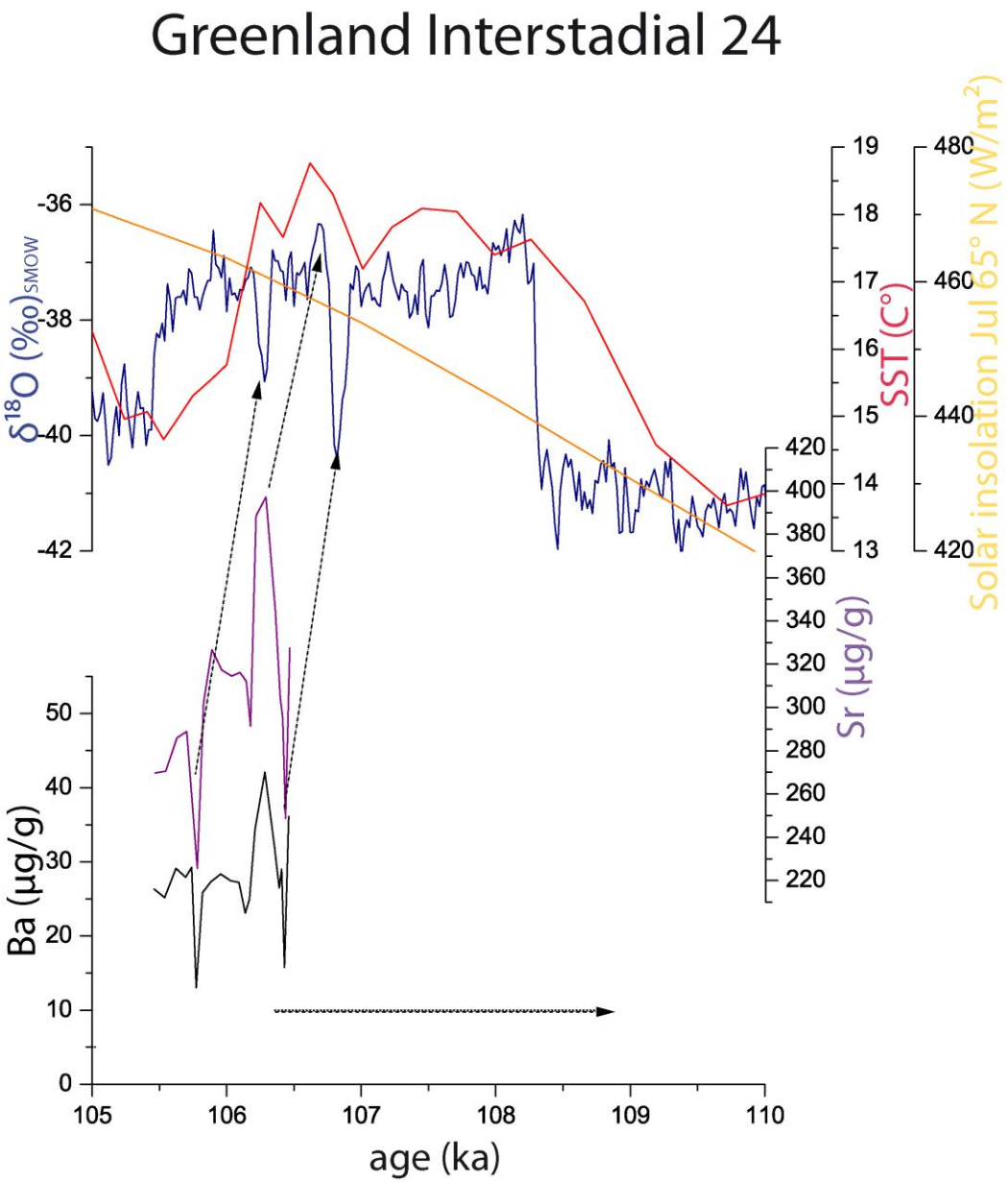

Figure 5.42: Climate variability of GIS 24 represented by stalagmite RBH 39 compared to the $\delta^{18}O$ record of NGRIP (Wolff et al., 2010), the July solar insolation curve at 65°N (Berger and Loutre, 1991) and the MD95-2042 SST record of the Iberian Margin (Martrat et al., 2007). Color code: black: Ba concentration, pink: Sr concentration.

5.4.3 GIS 23 and indicators for heavy rain events

The $\delta^{18}O$ records of RBH stalagmites displayed in Fig. 5.43, demonstrate that the pattern B type is predominant during GIS 23. The reconstruction of GIS 23 climate variability reflected in RBH stalagmites is difficult because none of the RBH stalagmites grew during the complete time duration of GIS 23. However, based on an unpublished stable isotope record of an RBH stalagmite one can conclude that climate conditions were wet and warm enough for stalagmite growth. However, for its entire growth duration, which reflects the end of the GIS 23, this stalagmite shows only little variation in the $\delta^{18}O$ signal. Thus, it was not chosen to represent the climate variability of GIS 23 as reflected in RBH stalagmites. Nonetheless, here, the proxies stalagmite RBH 39 reveal largest similarities with the $\delta^{18}O$ record of the NGRIP ice core for the beginning of GIS 23. Thus, this stalagmite is used to show the climate variability of the cave site for the beginning of GIS 23 as demonstrated in Fig. 5.43. Therefore, it is suggested that the peak, which can be found in Sr and U concentrations might indicate the precursor event as postulated by Capron et al. (2010a) for the NGRIP ice core. Even if possible within the 95% confidence limit, this assumption remains highly speculative and, thus, a quantitative comparison between the RBH proxies with other proxies cannot be performed. However, the sharp decrease reflected in both elements could reflect a temperature dropdown before temperature finally starts to increase again. Still this scenario implies high growth rates, which could have been triggered by heavy rain events. There are indicators for such heavy rain events during GIS 23, which can be seen in stalagmite RBH 47.

Fig. 5.44 displays the disturbed section of stalagmite RBH 47 from 110-150mm dft shown with the P concentration measured along the x-axis at 500µm resolution. Based on the stratigraphic sequences, it is possible to draw the conclusion that this section represents GIS 23 prior to diagenetic perturbation via post-depositional diagenesis. The layered section from 110 to 135mm dft might represent heavy rain events at the beginning or during GIS 23. Frisa et al. (2000) state that the conduction of such layers is possible during pronounced heavy rain events. The authors state that in this case, the layers should be associated with relatively large amounts of organic material transported by coarse particles and demonstrate an enrichment of P that is indicated by dark layers. Both can be observed in the pronounced section of stalagmite RBH 47 shown in Fig. 5.44. Thus, it is concluded that this section represents heavy rain events indicated

by the permanent switch between darker and lighter layers in association with rapid increasing and decreasing P concentrations.

None of the observed stalagmites show similar layers. Nonetheless, one has to take into account that stalagmite RBH 47 was retrieved from another part of the cave system and that the drip rate feeding the stalagmite could have been much more enhanced in this part of the cave in comparison to the others. Thus, if observed in just one single stalagmite these layers are an indicator of strong rain events during GIS 23.

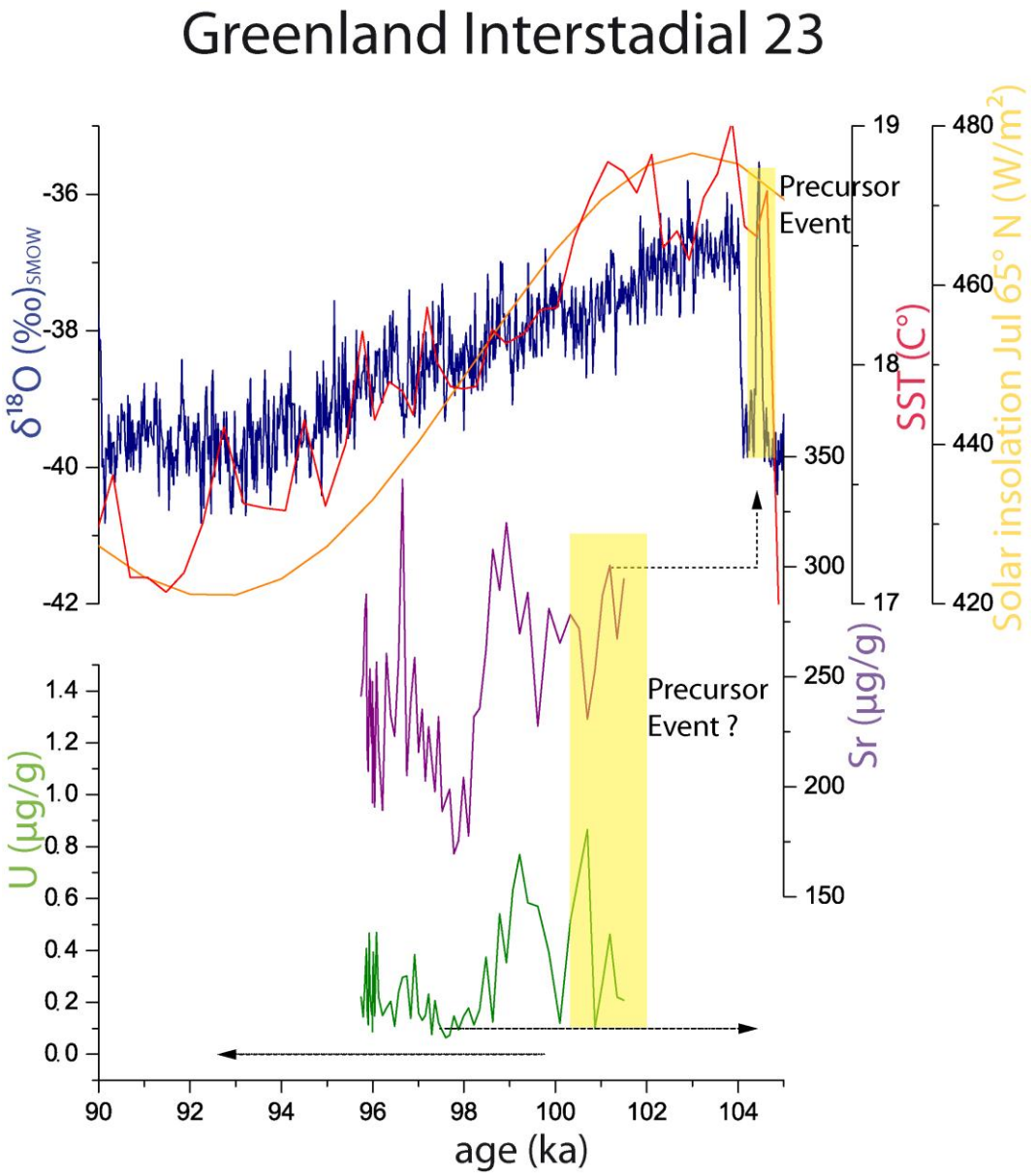

Figure 5.43: Climate variability of GIS 23 represented by stalagmite RBH 39 compared to the $\delta^{18}O$ record of NGRIP (Wolff et al., 2010), the July solar insolation curve at 65°N (Berger and Loutre. 1991) and the MD95-2042 SST record of the Iberian Margin (Martrat et al., 2007). Color code: olive: U concentration, pink: Sr concentration.

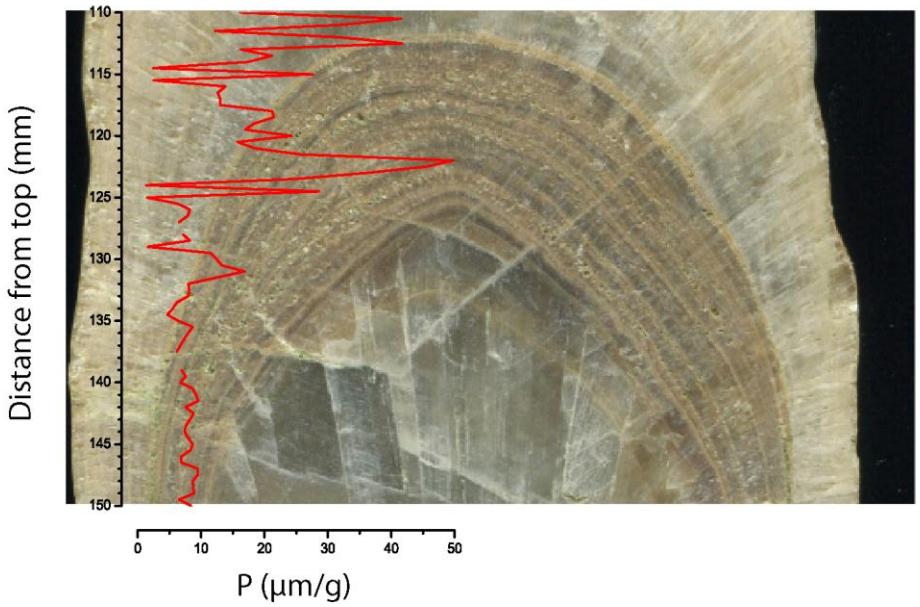

Figure 5.44: Disturbed section of stalagmite RBH 47 plotted again P displayed in dft (mm). P sample measurements have been taken along the growth axis. A compliance between P peaks and dark layers can be observed.

5.4.4 Past climate variability during GIS 21

As can be observed in Fig. 5.38, the pattern type A is the predominant driver of $\delta^{18}O$ variation during GIS 21. GIS 21 is associated with a solar insolation maximum (Berger and Loutre, 1991) a sea level maximum (Martinson et al., 1987) and rising SST (Martrat et al. 2007) (compare Fig. 5.40). However, the solar July solar insolation curve at 65° N displays, in comparison to the Eemian and GIS 21, lower values. This in turn, may be the reason why the pattern B type is not the predominant driver for $\delta^{18}O$ variations in RBH stalagmites. A comparison between the structures of GIS 21 as reflected in NGRIP and stalagmite RBH 32 is given in Fig. 5.45.

In the NGRIP ice core, it is striking that GIS 21 is preceded by a so-called "precursor-type event" and proceeded by a so-called "rebound-type event". Both types are discussed in detail by Capron et al. (2010a, 2012). Boch et al. (2011) identifies both types of events also in the NALPS record and provides accurate and precise Th/U-ages for the onset and cessation of both types (precursor-type: 85.07-84.97ka; rebound-type: 77.73-77.58ka). However due to the large Th/U-age uncertainties, comparable

statements about the onset and cessation of both events in the RBH stalagmites is not possible. Still, the similar characteristics of the U and Sr concentrations in stalagmite RBH 32 with the $\delta^{18}O$ record in NGRIP can be observed in Fig. 5.45. This finding suggests, that the characteristics in U and Sr concentrations at the beginning and the end of GIS 21 reflected in stalagmite RBH 32 represent both types of events. The Sr concentrations are characterized by a rapid shift from 275 to 475µg/g before they experience a sharp drop to the default value to increase then rapidly again to reach a Sr value of about 600µg/g. Contemporaneously, the U concentration describes a prominent increase from 0.6µg/g to 1.2µg/g, to decrease then again to reach a U concentration of about 0.6µg/g again before an increase up of to 1.5µg/g. These rapid transitions shown in the U and Sr concentrations are considered to reflect the precursor type event in RBH 32, which may be is equivalent to the designated precursor event documented in NGRIP (Capron et al., 2010a) and the NALPS record (Boch et al., 2011) for GIS 21.

In the proceeding sequence, the U and Sr concentrations observed in RBH 32 display a gradual concentration decrease, which is also observed in NGRIP for gradual is decreasing $\delta^{18}O$ values. In the age model conducted by StalAge, a rapid flip back to relatively high U and Sr concentrations are observed at 80.8 ka. An equivalent shift back to higher $\delta^{18}O$ values observed in the NGRIP record can be observed 79.2ka. Thus the rebound event displayed at the end of GIS 21 reflects an age difference of 1.6ka.

Nonetheless, within the 95% confidence interval, it is possible to spread the age model for stalagmite RBH in both directions to synchronize the NGRIP isotope record with the U and Sr record of stalagmite RBH 32. A similar $\delta^{18}O$ trend for the end of GIS 21 is also displayed by stalagmite RBH 39 revealing the same rebound-type event as displayed in the NGRIP ice core (Wolff et al., 2010) and NALPS (Boch et al., 2011).

Moreover, it can also be observed that the general trend of Sr and U concentrations in stalagmite RBH 32 as well the stable isotope record of stalagmite RBH 39 and to a less degree also in stalagmite RBH 32 show the typical pattern of GIS 21 observed in NGRIP. In comparison to NGRIP and selected RBH stalagmites, a similar $\delta^{18}O$ trend cannot be observed in the NALPS record for GIS 21.

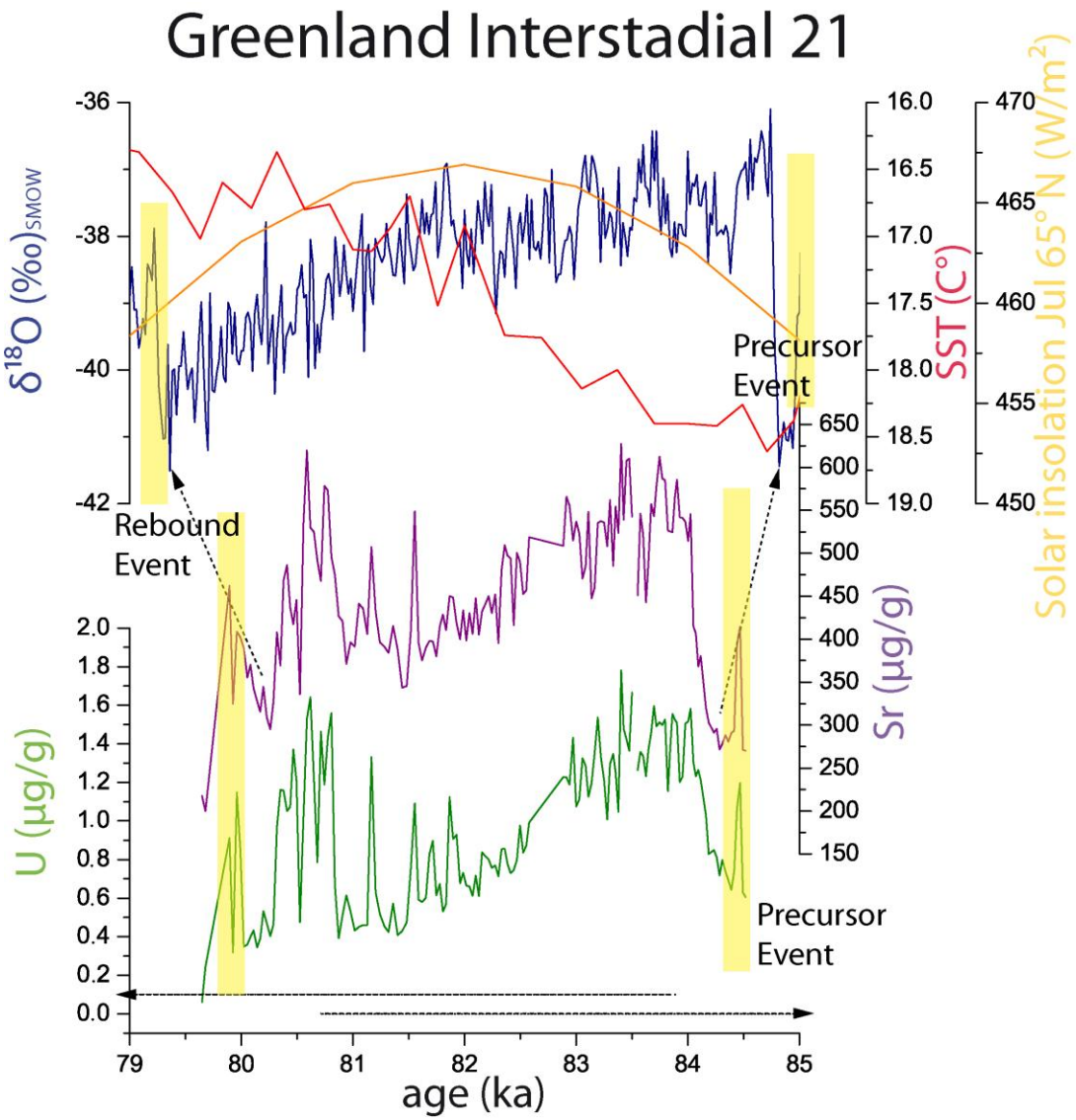

Figure 5.45: Climate variability of GIS 21 represented by stalagmite RBH 32 compared to the $\delta^{18}O$ record of NGRIP (Wolff et al., 2010), the July solar insolation curve at 65°N (Berger and Loutre, 1991) and the MD95-2042 SST record of the Iberian Margin (Martrat et al., 2007). Color code: olive: U concentration, pink: Sr concentration.

5.4.5 Past climate variability during GIS 20

As shown in Fig. 5.38, the pattern type A is the predominant driver of the $\delta^{18}O$ variation during GIS 20. Based on the age model and the variations of the U and Ba concentrations in stalagmite RBH 47, it is difficult to compare the general patterns of this record with the pattern of the $\delta^{18}O$ record displayed in NGRIP (compare Fig. 5.46). However within the 95% confidence interval it is possible to do so. In this case, the age model has to be widened in both age directions as displayed in Fig. 5.46. This potential scenario suggests one major growth phase, which can be subdivided into three distinct subphases displaying different growth rates.

1. The growth inception of stalagmite RBH 47 during this phase still represents the rebound-type event detected at the end of GIS 21 in stalagmite RBH 39 and displays a rather fast growth phase. This first phase is characterized by two pronounced Ba peaks of 28 and 27µg/g respectively and a rapid transition of Ba concentrations around 0.25 and 0.17µg/g.

2. Then, for the first time observed in RBH stalagmites, a phase of very slow growth is displayed separating GIS 21 and GIS 20. This is a unique feature observed in RBH stalagmites but could be explained. After the rebound-type event described for GIS 21 (Capron et al., 2010a), the AMOC is still in an exciting state and, thus, still supplies just enough moisture to generate some precipitation above the cave location. In this scenario the occurrence of precipitation would be very much restricted to the local area and could be additionally triggered by local topographic conditions. This second phase is coherent with low precipitation rate and a sharp decrease of the Ba and the U concentration (11.5 and 0.13µg/g).

3. At the third subphase displays a stronger AMOC. This is reflected in a major $\delta^{18}O$ increase of -38‰ in NGRIP and a rapid increase Ba (25µg/g) and U (0.23µg/g). In the subsequent sequence a gradual decrease of Ba in stalagmite RBH 47 and $\delta^{18}O$ in NGRIP can be observed, whereas the U concentration shows stronger variability but show overall all a gradual decreasing structure.

At the same time, the SST record (Martrat et al., 2007) reveals an earlier temperature increase than displayed for the NGRIP record. Additionally, the nature of GIS 20 remains to a certain degree unclear regarding that solar insolation is seen to be one potential key trigger of the AMOC reorganization. However, the solar insolation curve for July at 65°N is strongly decreasing during the onset of GIS 20 as displayed in Fig. 5.46.

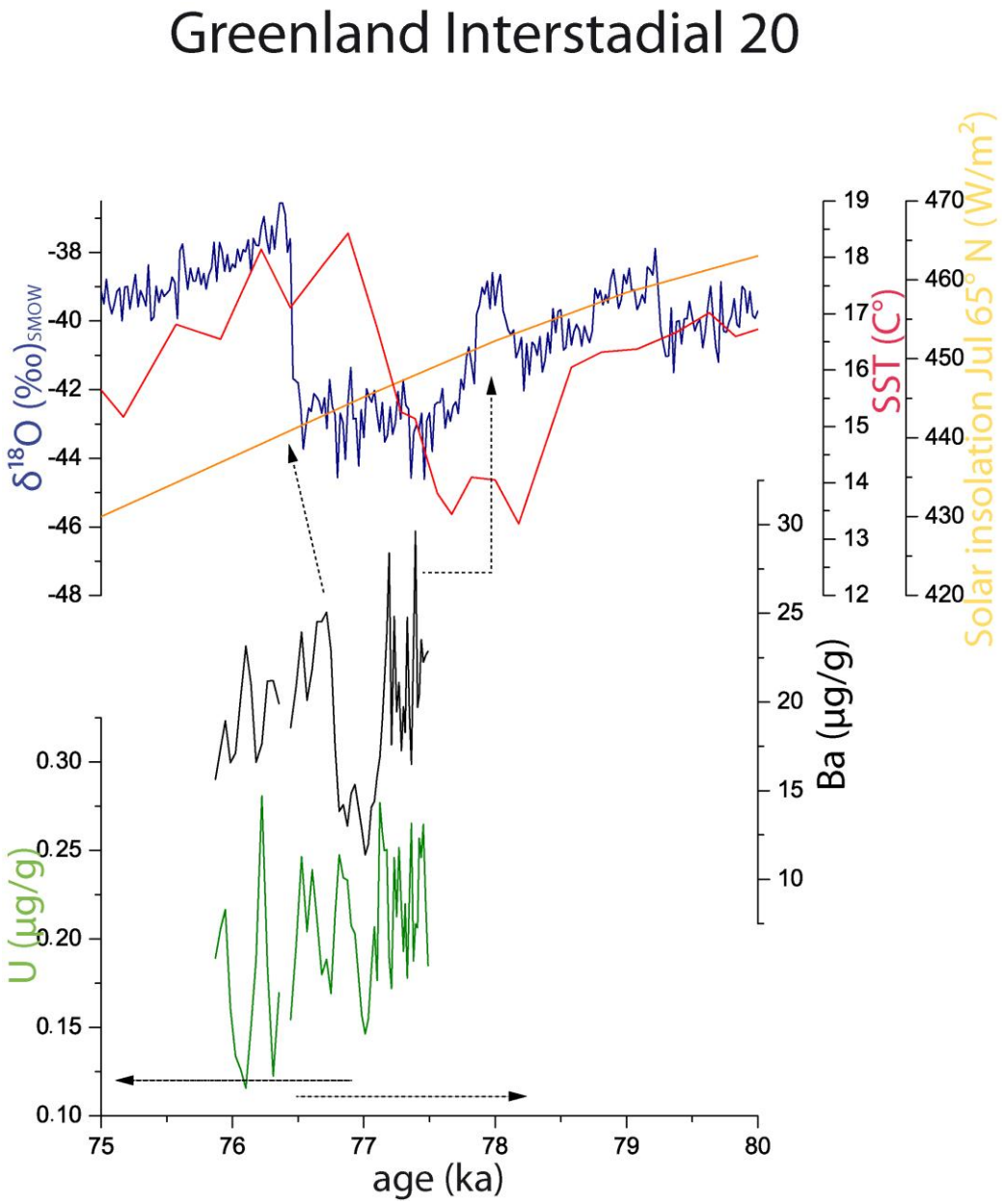

Figure 5.46: Climate variability of GIS 20 represented by stalagmite RBH 47 compared to the $\delta^{18}O$ record of NGRIP (Wolff et al., 2010), the July solar insolation curve at 65°N (Berger and Loutre, 1991) and the MD95-2042 SST record of the Iberian Margin (Martrat et al., 2007). Color code: olive: U concentration, black: Ba concentration.

5.4.6 Past climate variability during GIS 19

Figure 5.38 shows, that the pattern type A is the predominant driver of $\delta^{18}O$ variation during GIS 19. Stalagmite RBH 47 is the only RBH stalagmite that represents GIS 19 (compare Fig. 5.47). However, the reconstruction for GIS 19 is limited due to a very limited data set. Thus, a direct comparison to the $\delta^{18}O$ record of NGRIP (Wolff et al., 2010), the SST record of the Iberian margin (Martrat et al., 2007) and the July solar insolation curve at 65° N is not possible.

Nonetheless, the patterns of U and Sr concentrations show a short gradual. This gradual decrease is most likely caused by a reduction of microbial soil activity and, hence, indicates reduced conditions in which UO^{2+} cannot be mobilized and is interpreted as gradual shift from wetter and warmer to cooler and drier climate conditions. Therefore, the gradual decrease in both U an Sr represents a temperature cooing in stalagmite RBH 47. It is noteworthy that a similar decrease is observed in the $\delta^{18}O$ record of NGRIP. However, to what degree both records can be compared with each other remains unclear.

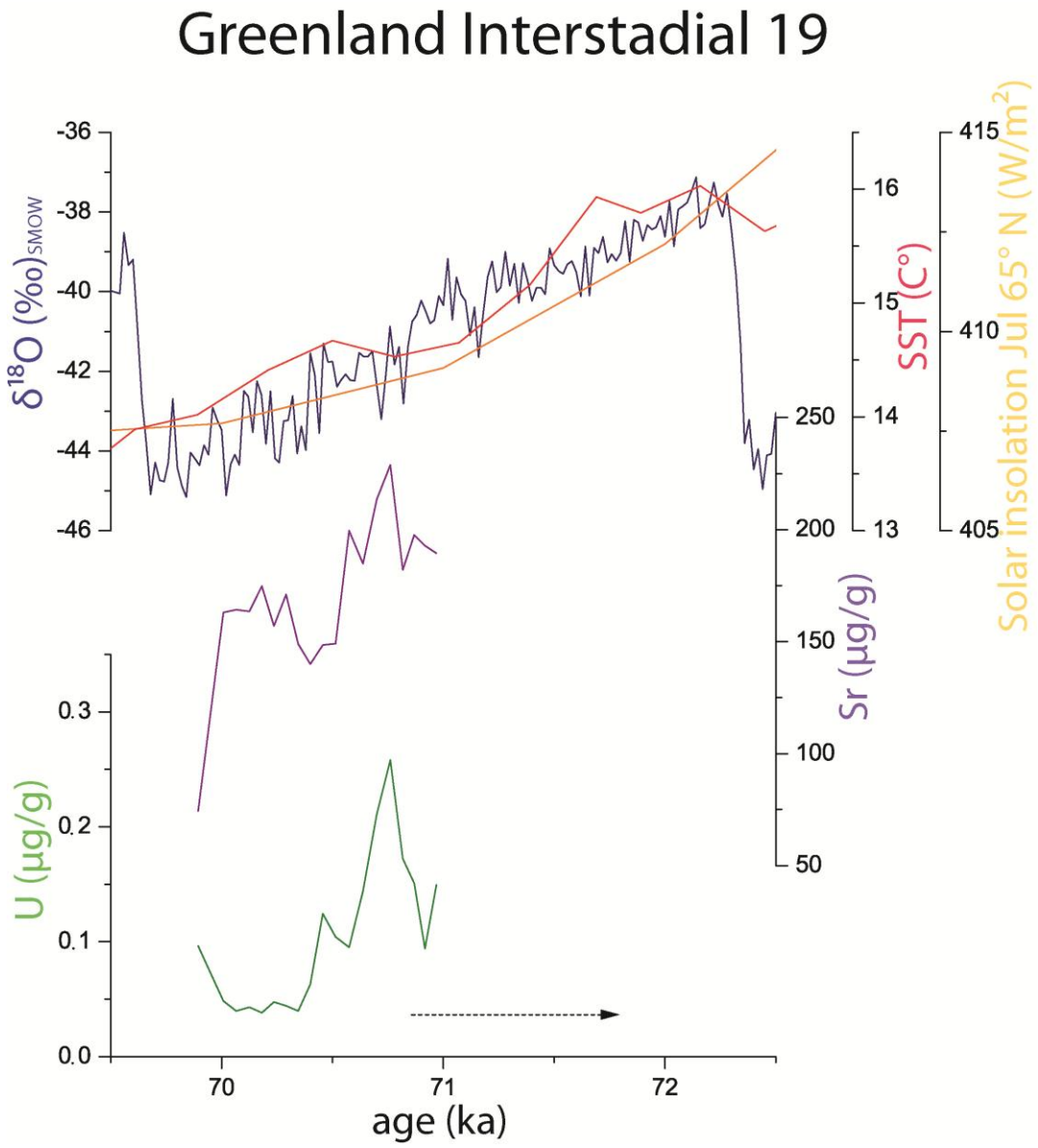

Figure 5.47: Climate variability of GIS 19 represented by stalagmite RBH 47 compared to the $\delta^{18}O$ record of NGRIP (Wolff et al., 2010), the July solar insolation curve at 65°N (Berger and Loutre, 1991) and the MD95-2042 SST record of the Iberian Margin (Martrat et al., 2007). Color code: olive: U concentration, pink: Sr concentration.

5.5. Summarizing remarks

RBH stalagmites only grow during the GIS. During GIS 25 and 22 no growth is observed. This might be related to the fact that GIS 25 and GIS 22 are not "real" GIS, but most likely appear to be rebound type events triggered by sea ice formation, which appear at the

end of the late Eemian and the very long GIS 23, which reveal very stable AMOC conditions (Capron et al. 2010a, 2012).
It is also noteworthy that the duration of the RBH stalagmite growth phases decreases with time, which might be related to the duration of the GIS itself (compare GIS 20 and 19) and to the fact that a general global cooling can be observed.

6. Conclusions and outlook

It has been also shown with thin section analysis that post-depositional diagenesis (PDD) can cause significant age inversions, which are generated when the Th/U system is reopened. This in turn may be caused by undersaturated drip waters, which react corrosively on the stalagmite surfaces. This process may be related to rapid climate change at the onset of the GIS and was modeled by Tolzmann et al. (submitted). The understanding of the processes that lead to PDD is essential for a better understanding of the U-system.

The reconstruction of past climate variability based on three selected RBH stalagmites in Northern Germany is difficult, due to the relatively large age uncertainties and to some extent short growth phases of RBH stalagmites.
Still, in the $\delta^{13}C$ records of RBH stalagmites a long-term cooling trend can be observed.
For the MIS 5, no continuous growth can be observed in RBH stalagmites. Instead, during MIS 5 the RBH stalagmites are characterized by several growth phases during. These growth phases seem to be associated with the late Eemian and the pronounced Greenland Interstadials (GIS) 24, 23, 21, 20 and 19. Thus, RBH stalagmites are also influenced by millennial climate change and, thus, sensitive to the reorganization of the AMOC (Atlantic Meridional Overturning Circulation).
The designated GIS are represented by rapid temperature shifts that range from 8-16°C +/-2.5°C (Capron et al. 2010a). However, no RBH stalagmite growth can be observed during GIS 25 and 22. Both GIS may be considered as rebound events, which are a function of sea ice formation, salinity and density in the high North Atlantic (Capron et al. 2012). This indicates that the impact of sea ice formation, which finally triggered the reorganization of the AMOC was too weak to establish an atmospheric–oceanic

circulation regime that provided enough precipitation to establish RBH stalagmite growth.

Temperature and precipitation variability reflected in the RBH stalagmites can be best identified in variations of U, Ba and Sr, which are following the structure of the $\delta^{18}O$ record of NGRIP (NGRIP members, 2004) on the GICC05modelext timescale (Wolff et al. 2010). In stalagmite RBH 32, the trend in Sr and U concentrations during GIS 21 can be compared best to the equivalent GIS observed in the $\delta^{18}O$ record of NGRIP (NGRIP members 2004) on the GICC05modelext time scale (Wolff et al. 2010).

Based on the identified section in stalagmite RBH 47 as well as in the trends observed in trace element variability, it can be assumed those growth periods of the RBH stalagmites were most likely associated with strong rain events during or at the beginning of these GIS.

Moreover, the $\delta^{18}O$ records of RBH stalagmites reveal two different pattern types (A and B), which are related to orbital configurations combined with relatively stable modes of the AMOC. Consequently, it is hypothesized that the higher evapotranspiration could possibly be reflected in very stable AMOC situations combined with pronounced peaks of orbital insolation as observed during the Eemian and GIS 23.

Future attempts to reconstruct paleoclimate variability stalagmites from the Rienberghöhle (RBH) might remain difficult. This has several reasons:

1. It has been shown that RBH stalagmites do show clear signs of PDD. This provides chances to receive a better understanding of cave internal processes that might lead to PDD (Tolzmann et al. 2012, submitted), which is important.
2. RBH stalagmites, which are not effected by PDD, react ultra-sensitive to changes of the AMOC and thus to the North Atlantic. These changes can be observed in trace elements as well as in changes of stable isotope signals. However due to cave internal processes, which are not fully understood, the trace element and stable isotopes are to some degree superimposed. Hence, a better understanding is required, which requires more future work.
3. The DASC (Deutsche Archiv für Sinterchronologie) is a unique archive of stalagmites, not only from the Riesenberghöhle, which are available for scientific investigation in order to receive a better understanding of paleoclimate and cave internal processes. However, due to insufficient storage it is

questionable if these stalagmites can still be used for paleoclimate investigations. Thus a close collaboration with scientists from universities is strongly recommended concerning the questions of storage and maintenance of these stalagmites for future research projects.

7. Bibliography

Badertscher, S., Fleitmann, D., Cheng, H., Edwards, R.L., Göktürk, O.M., Zumbühl, A., Leuenberger, M., Tüysüz, O., 2011. Pleistocene water intrusions from the Mediterranean and Caspian seas into the Black Sea. Nature Geoscience, 4 (4): 236-239.

Baldini, J.U.L., McDermott, F., Fairchild, I.J. (2002). Structure of the 8200-Year Cold Event Revealed by a Speleothem Trace Element Record, pp. 2203-2206,.

Baldini, J.U.L., McDermott, F., Baker, A., Baldini, L.M., Mattey, D.P., Railsback, L.B., 2005. Biomass effects on stalagmite growth and isotope ratios: A 20th century analogue from Wiltshire, England. Earth and Planetary Science Letters, 240: 486-494.

Bauch, H.A., Kandiano, E.S., Helmke, J., Andersen, N., Rosell-Mele, A., Erlenkeuser, H., 2011. Climatic bisection of the last interglacial warm period in the Polar North Atlantic. Quaternary Science Reviews, 30 (15-16): 1813-1818.

Berger, A., Loutre, M.F., 1991. Insolation values for the climate of the last 10 million years. Quaternary Science Reviews, 10: 297-317.

Bintanja, R., van de Wal, R.S.W., Oerlemans, J., 2005. Modelled atmospheric temperatures and global sea levels over the past million years. Nature, 437 (7055): 125-128.

Blume, H.P., Brümmer, G.W., Horn, R., Kögle-Knaber, I., Kretzschmar, R., Wilke, B.-M., Tiele-Bruhn, S., Welp, G., 2010. Scheffer/Schachtschabel Lehrbuch der Bodenkunde. Spektrum,

Boch, R., Cheng, H., Spötl, C., Edwards, R.L., Wang, X., Häuselmann, P., 2011. NALPS: a precisely dated European climate record 120-60 ka. Climate of the Past, 7 (4): 1247-1259.

Bögli, A., 1978. Karsthydrographie und physische Speläologie. Springer Verlag, Berlin.

Borsato, A., Quinif, Y., Bini, A., Dublyansky, Y., 2003. Open-system alpine speleothems: implications for U-series dating and paleoclimate reconstructions. Acta Geologica, 80: 71-83.

Bourdon, B., Turner, S.P., Henderson, G.M., Lundstrom, C.C., 2003. Introduction to U-series geochemistry. In: B. Bourdon, G.M. Henderson, C.C. Lundstrom, S.P. Turner (Eds.), Uranium-series Geochemistry. Mineralogical Society of America, Washington, DC, 656.

Brauer, A., Allen, J.R.M., Mingram, J., Dulski, P., Wulf, S., Huntley, B. (2007). Evidence for last interglacial chronology and environmental change from Southern Europe, pp. 450-455.

Braun, H., Ditlevsen, P., Chialvo, D.R., 2008. Solar forced Dansgaard-Oeschger events and their phase relation with solar proxies. Geophysical Research Letters, 35 (6)

Braun, H., Christl, M., Rahmstorf, S., Ganopolski, A., Mangini, A., Kubatzki, C., Roth, K., Kromer, B., 2005. Possible solar origin of the 1,470-year glacial climate cycle demonstrated in a coupled model. Nature, 438: 208-211.

Broecker, W.S., 2003. Does the trigger for abrupt climate change reside in the ocean or in the atmosphere. Science, 300: 1519-1522.

Burns, S.J., Fleitmann, D., Matter, A., Kramers, J., Al-Subbary, A.A., 2003. Indian Ocean climate and an absolute chronology over Dansgaard/Oeschger events 9 to 13. Science, 301: 1365-1367.

Capron, E., Laindais, A., Chappellaz, D., Buiron, D., Fischer, H., Johnson, S.J., Jouzel, J., Leuenberger, M., Masson-Delmotte, V., Stocker, T.F., 2012. A global pictures of the first abrupt climatic event occurring during the last glacial inception. Geophysical research letters, 39: 1-8.

Capron, E., Landais, A., Lemieux-Dudon, B., Schilt, A., Masson-Delmotte, V., Buiron, D., Chappellaz, J., Dahl-Jensen, D., Johnsen, S., Leuenberger, M., Loulergue, L., Oerter, H., 2010b. Synchronising EDML and NorthGRIP ice cores using $\delta^{18}O$ of atmospheric oxygen ($\delta^{18}Oatm$) and CH4 measurements over MIS5 (80-123 kyr). Quaternary Science Reviews, 29 (1-2): 222-234.

Capron, E., Landais, A., Chappellaz, J., Schilt, A., Buiron, D., Dahl-Jensen, D., Johnsen, S.J., Jouzel, J., Lemieux-Dudon, B., Loulergue, L., Leuenberger, M., Masson-Delmotte, V., Mayer, H., Oerter, H., Stenni, B., 2010a. Millennial and sub-millennial scale climatic variations recorded in polar ice cores over the last glacial period. Clim. Past Discuss., 6 (1): 135-183.

Chapman, M.R., Shakleton, N.J., 1999. Global ice-volume fluctuations, North Atlantic ice-rafting events, and deep-ocean circulation changes between 130 and 70 ka. Geology, 27, No. 9: 795-798.

Chen, J.H., Curran, H.A., White, B., Wasserburg, G.J., 1991. Precise chronology of the last interglacial period: ^{234}U-^{230}Th data from fossil coral reefs in the Bahamas. GSA Bulletin, 103: 82-97.

Cheng, H., Adkins, J., Edwards, R.L., Boyle, E.A., 2000a. U-Th dating of deep-sea corals. Geochimica et Cosmochimica Acta, 64: 2401-2416.

Cheng, H., Edwards, R.L., Hoff, J., Gallup, C.D., Richards, D.A., Asmerom, Y., 2000. The half-lives of uranium-234 and thorium-230. Chemical Geology, 169: 17-33.

Cheng, H., Edwards, R.L., Broecker, W.S., Denton, G.H., Kong, X., Wang, Y., Zhang, R., Wang, X., 2009. Ice age terminations. Science, 326: 248-252.

Cheng, H., Zhang, P.Z., Spötl, C., Edwards, R.L., Cai, Y.J., Zhang, D.Z., Sang, W.C., Tan, M., An, Z.S., 2012. The climatic cyclicity in semiarid-arid central Asia over the past 500,000 years. Geophys. Res. Lett., 39 (1): L01705.

Cherubini, P., Schweingruber, F.H., Piussi, P., 1996. Spatiotenraporal growth dynamics and disturbances in a subalpine spruce forest in the Alps: a dendroecological reconstruction. Canadian Journal of Forest Research, 26 (6): 991-1001.

Clark, P.U., Pisias, N.G., Stocker, T.F., Weaver, A.J., 2002. The role of the thermohaline circulation in abrupt climate change. Nature, 415: 863-869.

Claussen, M., Fohlmeister, J., Ganopolski, A., Brovkin, V., 2006. Vegetation dynamics amplifies precessional forcing. Geophysical Research Letters, 33: L09709.

Cliff, R.A., Spötl, C., Mangini, A., 2010. U/Pb dating of speleothems from Spannagel Cave, Austrian Alps: A high resolution comparison with U-series ages. Quaternary Geochronology, 5 (4): 452-458.

Colleoni, F., Masina, S., Cherchi, A., Navarra, A., Ritz, C., Peyaud, V., Otto-Bliesner, B., 2012. Modelling Northern Hemisphere ice sheets distribution during MIS5 and MIS7 glacial inceptions. Clim. Past Discuss., 8 (6): 6221-6267.

Couchoud, I., Genty, D., Hoffmann, D.L., Drysdale, R.N., Blamart, D., 2009. Millenial-scale climate variability during the Last Interglacial recorded in a speleothem from south-western France. Quaternary Science Reviews, 28: 3263-3274.

Crucifix, M., Loutre, F.M., 2002. Transient simulations over the last interglacial period (126-115 kyr BP): feedback and forcing analysis. Climate Dynamics, 19 (5-6): 417-433.

Cruz Jr, F.W., Burns, S.J., Karmann, I., Sharp, W.D., Vuille, M., Ferrari, J.A., 2006. A stalagmite record of changes in atmospheric circulation and soil processes in the Brazilian subtropics during the Late Pleistocene. Quaternary Science Reviews, 25 (21-22): 2749-2761.

Cruz Jr, F.W., Burns, S.J., Jercinovic, M., Karmann, I., Sharp, W.D., Vuille, M., 2007. Evidence of rainfall variations in Southern Brazil from trace element ratios (Mg/Ca and Sr/Ca) in a Late Pleistocene stalagmite. Geochimica et Cosmochimica Acta, 71 (9): 2250-2263.

Cruz Jr, F.W., Karmann, I., Viana Jr, O., Burns, S.J., Ferrari, J.A., Vuille, M., Sial, A.N., Moreira, M.Z., 2005a. Stable isotope study of cave percolation waters in subtropical Brazil: Implications for paleoclimate inferences from speleothems. Chemical Geology, 220: 245-262.

Cruz Jr, F.W., Burns, S.J., Karmann, I., Sharp, W.D., Vuille, M., Cardoso, A.O., Ferrari, J.A., Silva Dias, P.L., Viana Jr, O., 2005b. Insolation-driven changes in atmospheric circulation over the past 116,000 years in subtropical Brazil. Nature, 434: 63-66.

Dansgaard, W., 1964. Stable isotopes in precipitation. Tellus, 16: 436-468.

Dansgaard, W., Johnsen, S.J., Clausen, H.B., Dahl-Jensen, D., Gundestrup, N.S., Hammer, C.U., Hvidberg, C.S., Steffensen, J.P., Sveinbjornsdottir, A.E., Jouzel, J., Bond, G., 1993. Evidence for general instability of past climate from a 250-kyr ice-core record. Nature, 364 (6434): 218-220.

Dorale, J.A., Liu, Z., 2009. Limitations of Hendy test criteria in judging the paleoclimatic suitability of speleothems and the need for replication. Journal of Cave and Karst Studies, 71 (1): 73-80.

Dreybrodt, W., 2008. Evolution of the isotopic composition of carbon and oxygen in a calcite precipitating H_2O-CO_2-$CaCO_3$ solution and the related isotopic composition of calcite in stalagmites. Geochimica et Cosmochimica Acta, 72 (19): 4712-4724.

Dreybrodt, W., Scholz, D., 2011. Climatic dependence of stable carbon and oxygen isotope signals recorded in speleothems: From soil water to speleothem calcite. Geochimica et Cosmochimica Acta, 75 (3): 734-752.

Drysdale, R.N., Hellstrom, J., Zanchetta, G., Fallick, A.E., Sánchez Goni, M.F., Couchoud, I., McDonald, J., Maas, R., Lohmann, G., Isola, I., 2009. Evidence for obliquity forcing of Glacial Termination II. Science, 325: 1527-1531.

Edwards, R.L., Gallup, C.D., Cheng, H., 2003. Uranium-series dating of marine and lacustrine carbonates. In: B. Bourdon, G.M. Henderson, C.C. Lundstrom, S.P. Turner (Eds.), Uranium-series Geochemistry. Mineralogical Society of America, Washington, DC, 656.

Eisenman, I., Bitz, C.M., Tziperman, E., 2009. Rain driven by receding ice sheets as a cause of past climate change. Paleoceanography, 24 (4).

EPICA community members, 2004. Eight glacial cycles from an Antarctic ice core. Nature, 429: 623-628.

Esper, J., Frank, D.C., Battipaglia, G., Büntgen, U., Holert, C., Treydte, K., Siegwolf, R., Saurer, M., 2010. Low-frequency noise in $\delta^{13}C$ and $\delta^{18}O$ tree ring data: A case study of Pinus uncinata in the Spanish Pyrenees. Global Biogeochemical Cycles, 24 (4)

Fairchild, I.J., Treble, P.C., 2009. Trace elements in speleothems as recorders of environmental change. Quaternary Science Reviews, 28: 449-468.

Fairchild, I.J., Baker, A., 2012. Speleothem Science: Fom Process to Past Environments. Wilry-Blackwell,

Fairchild, I.J., Borsato, A., Tooth, A.F., Frisia, S., Hawkesworth, C.J., Huang, Y., McDermott, F., Spiro, B., 2000. Controls on trace element (Sr and Mg) compositions of carbonate cave waters: implications for speleothem climatic records. Chemical Geology, 166 (3-4): 255-269.

Fairchild, I.J., Smith, C.L., Baker, A., Fuller, L., Spötl, C., Mattey, D., McDermott, F., , E.I.M.F., 2006. Modification a preservation of environmental signals in speleothems. Earth-Science Reviews, 75 (1-4): 105-153.

Felis, T., Lohmann, G., Kuhnert, H., Lorenz, S.J., Scholz, D., Pätzold, J., Al-Rousan, S.A., Al-Moghrabi, S.M., 2004. Increased seasonality in Middle East temperatures during the last interglacial period. Nature, 429: 164-168.

Fensterer, C., Scholz, D., Hoffmann, D.L., Spötl, C., Pajón, J.M., Mangini, A., 2012. Cuban stalagmite documents relationship between Caribbean precipitation and the Atlantic Multidecadal Oscillation during the past 1.3 ka. The Holocene:

Fensterer, C., Scholz, D., Hoffmann, D.L., Spötl, C., Schröder-Ritzrau, A., Horn, C., Pajón, J.M., Mangini, A., 2013. Millennial-scale climate variability during the last 12.5 ka recorded in a Caribbean speleothem. Earth and Planetary Science Letters:

Fleitmann, D., Burns, S.J., Pekala, M., Mangini, A., Al-Subbary, A., Al-Aowah, M., Kramers, J., Matter, A., 2011. Holocene and Pleistocene pluvial periods in Yemen, southern Arabia. Quaternary Science Reviews, 30 (7-8): 783-787.

Fleitmann, D., Cheng, H., Badertscher, S., Edwards, R.L., Mudelsee, M., Göktürk, O.M., Fankhauser, A., Pickering, R., Raible, C.C., Matter, A., Kramers, J., Tüysüz, O., 2009. Timing and climatic impact of Greenland interstadials recorded in stalagmites from northern Turkey. Geophysical Research Letters, 36: L19707.

Fohlmeister, J., Schröder-Ritzrau, A., Scholz, D., Spötl, C., Riechelmann, D.F.C., Mudelsee, M., Wackerbarth, A.K., Gerdes, A., Riechelmann, S., Immenhauser, A., Richter, D.K., Mangini, A., 2012. Bunker Cave stalagmites: An archive for central European Holocene climate variability. Climate of the Past:

Frisia, S., 1996. Petrographic evidence for diagenesis in speleothems. Speleochronus, 7: 21-30.

Frisia, S., Borsato, A., 2010. Chapter 6 Karst. In: Developments in Sedimentology. Elsevier, 269-318.

Frisia, S., Bini, A., Quinif, Y., 1993. Morphologic, crystallographic and isotopic study of an acient flowstone (Grotta di Cunturines, Dolomiti): Implications for paleoenvironmental reconstructions. Speleochronus, 5: 3-18.

Frisia, S., Borsato, A., Fairchild, I.J., McDermott, F. (2000). Calcite Fabrics, Growth Mechanisms, and Environments of Formation in Speleothems from the Italian Alps and Southwestern Ireland, pp. 1183-1196

Frisia, S., Borsato, A., Fairchild, I.J., McDermott, F. (2000). Calcite Fabrics, Growth Mechanisms, and Environments of Formation in Speleothems from the Italian Alps and Southwestern Ireland, pp. 1183-1196

Gabrovsek, F., Dreybrodt, W., 2000. Role of mixing corrosion in calcite-aggressive H2O-CO2-CaCO3 solutions in the early evolution of Karst Aquifers in limestone. Water Resour. Res., 36 (5): 1179-1188.

Ganopolski, A., Rahmstorf, S., 2001. Rapid changes of glacial climate simulated in a coupled climate model. Nature, 409 (6817): 153-158.

Gascoyne, M., 1992. Palaeoclimate determination from cave calcite deposits. Quaternary Science Reviews, 11 (6): 609-632.

Genty, D., Blamart, D., Ouahdi, R., Gilmour, M., Baker, A., Jouzel, J., Van-Exter, S., 2003. Precise dating of Dansgaard-Oeschger climate oscillations in western Europe from stalagmite data. Nature, 421: 833-837.

Goldstein, S.J., Stirling, C.H., 2003. Techniques for measuring Uranium-series nuclides: 1992-2002. In: B. Bourdon, G.M. Henderson, C.C. Lundstrom, S.P. Turner (Eds.), Uranium-series Geochemistry. Mineralogical Society of America, Washington, DC, 656.

Grupe, O., 1933. Blatt Nr.2018 Kathrinhagen. Erläuterung zur geologischen Karte von Preußen und benachbarten Bundesstatten 1:25000. Preußische Geologische Landesanstalt., Berlin.

Hallmann, N., Burchell, M., Brewster, N., Martindale, A., Schöne, B.R., 2012. Holocene climate and seasonality of shell collection at the Dundas Islands Group, northern British Columbia, Canada. A bivalve sclerochronological approach. Palaeogeography, Palaeoclimatology, Palaeoecology.

Hellstrom, J., 2003. Rapid and accurate U/Th dating using parallel ion-counting multi-collector ICP-MS. Journal of Analytical Atomic Spectrometry, 18: 1346-1351.

Hellstrom, J., McCulloch, M., Stone, J., 1998. A Detailed 31,000-Year Record of Climate and Vegetation Change, from the Isotope Geochemistry of Two New Zealand Speleothems. Quaternary Research, 50 (2): 167-178.

Hellstrom, J.C., McCulloch, M.T., 2000. Multi-proxy constraints on the climatic significance of trace element records from a New Zealand speleothem. Earth and Planetary Science Letters, 179: 287-297.

Hellstrom, J.C., 2006. U-Th dating of speleothems with high initial ^{230}Th using stratigraphical constraint. Quaternary Geochronology, 1: 289-295.

Henderson, G.M., 2006. Caving in to new chronologies. Science, 313: 620-622.

Hendy, C.H., 1971. The isotopic geochemistry of speleothems - I. The calculation of the effects of different modes of formation on the isotopic composition of speleothems and their applicability as paleoclimatic indicators. Geochimica et Cosmochimica Acta, 35: 801-824.

Hercman, H., Pawlak, J., 2012. MOD-AGE: An age-depth model construction algorithm. Quaternary Geochronology.

Hill, C.A., Forti, P., 1993. Cave Minerals of the World. National Speleological Society, Huntsville, Alabama, USA.

Hoffmann, D.L., Prytulak, J., Richards, D.A., Elliott, T., Coath, C.D., Smart, P.L., Scholz, D., 2007. Procedures for accurate U and Th isotope measurements by high precision MC-ICPMS. International Journal of Mass Spectrometry, 264 (2-3): 97-109.

Holzkämper, S., Spötl, C., Mangini, A., 2005. High-precision constraints on timing of Alpine warm periods during the middle to late Pleistocene using speleothem growth periods. Earth and Planetary Science Letters, 236: 751-764.

Holzkämper, S., Mangini, A., Spötl, C., Mudelsee, M., 2004. Timing and progression of the Last Interglacial derived from a high alpine stalagmite. Geophysical Research Letters, 31: L07201.

Holzkämper, S., Holmgren, K., Lee-Thorp, J., Talma, S., Mangini, A., Partridge, T., 2009. Late Pleistocene stalagmite growth in Wolkberg Cave, South Africa. Earth and Planetary Science Letters, 282: 212-221.

Ivanovich, M., Harmon, R.S., 1992. Uranium-series Disequilibrium: Applications to Earth, Marine, and Environmental Sciences. Oxford University Press, Oxford.

Jaffey, A.H., Flynn, K.F., Glendenin, L.E., Bentley, W.C., Essling, A.M., 1971. Precision Measurement of Half-Lives and Specific Activities of ^{235}U and ^{238}U. Physical Review C, 4 (5): 1889-1906.

Jochum, K.P., Stoll, B., Herwig, K., Willbold, M., 2007. Validation of LA-ICP-MS trace element analysis of geological glasses using a new solid-state 193 nm Nd:YAG laser and matrix-matched calibration. Journal of Analytical Atomic Spectrometry, 22 (2): 112-121.

Jochum, K.P., Scholz, D., Stoll, B., Weis, U., Wilson, S.A., Yang, Q., Schwalb, A., Boerner, N., Jacob, D.E., Andreae, M.O., 2012. Accurate trace element analysis of speleothems and biogenic calcium carbonates by LA-ICP-MS. Chemical Geology, 318-319 (0): 31-44.

Jouzel, J., Masson-Delmotte, V., Cattani, O., Dreyfus, G., Falourd, S., Hoffmann, G., Minster, B., Nouet, J., Barnola, J.M., Chappellaz, J., Fischer, H., Gallet, J.C., Johnsen, S., Leuenberger, M., Loulergue, L., Luethi, D., Oerter, H., Parrenin, F., Raisbeck, G., Raynaud, D., Schilt, A., Schwander, J., Selmo, E., Souchez, R., Spahni, R., Stauffer, B., Steffensen, J.P., Stenni, B., Stocker, T.F., Tison, J.L., Werner, M., Wolff, E.W. (2007). Orbital and Millennial Antarctic Climate Variability over the Past 800,000 Years, pp. 793-796

Kaufmann, G., 2003. Stalagmite growth and palaeo-climate: the numerical perspective. Earth and Planetary Science Letters, 214: 251-266.

Kelly, S.D., Newville, M.G., Cheng, L., Kemner, K.M., Sutton, S.R., Fenter, P., Sturchio, N.C., Spötl, C., 2003. Uranyl Incorporation in Natural Calcite. Environmental Science & Technology, 37 (7): 1284-1287.

Kendall, A.C., Broughton, P.L., 1978. Origin of fabrics in Speleothems composed of columnar calcite crystals. Journal of Sedimentary Petrology, 48 (2): 519-538.

Kim, S.-T., O'Neil, J.R., 1997. Equilibrium and nonequilibrium oxygen isotope effects in synthetic carbonates. Geochimica et Cosmochimica Acta, 61 (16): 3461-3475.

Kobashi, T., Severinghaus, J.P., Brook, E.J., Barnola, J.-M., Grachev, A.M., 2007. Precise timing and characterization of abrupt climate change 8200 years ago from air trapped in polar ice. Quaternary Science Reviews, 26: 1212-1222.

Kühl, N., Litt, T., Schölzel, C., Hense, A., 2007. Eemian and Early Weichselian temperature and precipitation variability in northern Germany. Quaternary Science Reviews, 26 (25-28): 3311-3317.

Lachniet, M.S., Johnson, L., Asmerom, Y., Burns, S.J., Polyak, V., Patterson, W.P., Burt, L., Azouz, A., 2009. Late Quaternary moisture export across Central America and to Greenland: evidence for tropical rainfall variability from Costa Rican stalagmites. Quaternary Science Reviews, 28: 3348-3360.

Langmuir, D., 1978. Uranium solution-mineral equilibria at low temperatures with applications to sedimentary ore deposits. Geochimica et Cosmochimica Acta, 42 (6, Part A): 547-569.

Landais, A., Caillon, N., Goujon, C., Grachev, A.M., Barnola, J.-M., Chappellaz, J., Jouzel, J., Masson-Delmotte, V., Leuenberger, M., 2004. Quantification of rapid temperature change during DO event 12 and phasing with methane inferred from air isotopic measurements. Earth and Planetary Science Letters, 225: 221-232.

Landais, A., Masson-Delmotte, V.r., Jouzel, J., Raynaud, D., Johnsen, S., Huber, C., Leuenberger, M., Schwander, J., Minster, B.n.d., 2006. The glacial inception as recorded in the NorthGRIP Greenland ice core: timing, structure and associated abrupt temperature changes. Climate Dynamics, 26 (2-3): 273-284.

Landais, A., Dreyfus, G., Capron, E., Masson-Delmotte, V., Sanchez-Goani, M.F., Desprat, S., Hoffmann, G., Jouzel, J., Leuenberger, M., Johnsen, S., 2010. What drives the millennial and orbital variations of Delta18Oatm? Quaternary Science Reviews, 29 (1-2): 235-246.

Lauritzen, S.-E., Lundberg, J., 1999. Calibration of the speleothem delta function: an absolute temperature record for the Holocene in northern Norway. The Holocene, 9 (6): 659-669.

Lea, D.W., Pak, D.K., Spero, H.J., 2000. Climate impact of late quaternary equatorial pacific sea surface temperature variations. Science, 289: 1719-1724.

Li, W.-X., Lundberg, J., Dickin, A.P., Ford, D.C., Schwarcz, H.P., McNutt, R., Williams, D., 1989. High-precision mass-spectrometric uranium-series dating of cave deposits and implications for paleoclimate studies. Nature, 339: 534-536.

Lisiecki, L.E., Raymo, M.E., 2005. A Pliocene-Pleistocene stack of 57 globally distributed benthic $\delta^{18}O$ records. Paleoceanography, 20 (1): PA1003.

Lohmann, G., Lorenz, S.J., 2007. Orbital forcing on atmospheric dynamics during the last interglacial and glacial inception. In: Sirocko. F., T. Litt, M. Claussen, M.F. Sanchez-Goni (Eds.), The climate of past interglacials. 727-743.

Ludwig, K.R., Titterington, D.M., 1994. Calculation of $^{230}Th/U$ isochrons, ages, and errors. Geochimica et Cosmochimica Acta, 58 (22): 5031-5042.

Lunt, D., 2007. The key to the future is in the past. Weather, 62 (3): 79-80.

Lüthi, D., Le Floch, M., Bereiter, B., Blunier, T., Barnola, J.-M., Siegenthaler, U., Raynaud, D., Jouzel, J., Fischer, H., Kawamura, K., Stocker, T.F., 2008. High-resolution carbon dioxide concentration record 650,000-800,000[thinsp]years before present. Nature, 453 (7193): 379-382.

MacAyeal, D.R., 1993. Binge/purge oscillations of the Laurentide Ice Sheet as a cause of the North Atlantic's Heinrich events. Paleoceanography, 8 (6): 775-784.

Maier-Reimer, E., Mikolajewicz, U., Crowley, T., 1990. Ocean General Circulation Model Sensitivity Experiment with an open Central American Isthmus. Paleoceanography, 5 (3): 349-366.

Mangini, A., Spötl, C., Verdes, P., 2005. Reconstruction of temperature in the Central Alps during the past 2000 yr from a $\delta^{18}O$ stalagmite record. Earth and Planetary Science Letters, 235: 741-751.

Mangini, A., Verdes, P., Spötl, C., Scholz, D., Vollweiler, N., Kromer, B., 2007. Persistent influence of the North Atlantic hydrography on central European winter temperature during the last 9000 years. Geophysical Research Letters, 34 (2): L02704.

Martrat, B., Grimalt, J.O., Lopez-Martinez, C., Cacho, I., Sierro, F.J., Flores, J.A., Zahn, R., Canals, M., Curtis, J.H., Hodell, D.A., 2004. Abrupt temperature changes in the Western Mediterranean over the past 250,000 years. Science, 306: 1762-1765.

Martrat, B., Grimalt, J.O., Shackleton, N.J., de Abreu, L., Hutterli, M.A., Stocker, T.F., 2007. Four climate cycles of recurring deep and surface water destabilizations on the Iberian Margin. Science, 317: 502-507.

Maurer, A.-F., Galer, S.J.G., Knipper, C., Beierlein, L., Nunn, E.V., Peters, D., Toetken, T., Alt, K.W., Schöne, B.R., 2012. Bioavailable 87Sr/86Sr in different environmental samples. Effects of anthropogenic contamination and implications for isoscapes in past migration studies. Science of The Total Environment, 433 (0): 216-229.

McDermott, F., 2004. Palaeo-climate reconstruction from stable isotope variations in speleothems: a review. Quaternary Science Reviews, 23: 901-918.

McDonald, J., Drysdale, R., Hill, D., 2004. The 2002-2003 El Nino recorded in Australian cave drip waters: Implications for reconstructing rainfall histories using stalagmites. Geophysical Research Letters, 31: L22202.

McMillan, E.A., Fairchild, I.J., Frisia, S., Borsato, A., McDermott, F., 2005. Annual trace element cycles in calcite–aragonite speleothems: evidence of drought in the western Mediterranean 1200–1100 yr BP. Journal of Quaternary Science, 20 (5): 423-433.

Meyer, M.C., Spötl, C., Mangini, A., Tessadri, R., 2012. Speleothem deposition at the glaciation threshold. An attempt to constrain the age and paleoenvironmental significance of a detrital-rich flowstone sequence from Entrische Kirche Cave (Austria). Palaeogeography, Palaeoclimatology, Palaeoecology, 319-320 (0): 93-106.

Meyer, M.C., Cliff, R.A., Spötl, C., 2011. Speleothems and mountain uplift. Geology, 39 (5): 447-450.

Meyer, M.C., Cliff, R.A., Spötl, C., Knipping, M., Mangini, A., 2009. Speleothems from the earliest Quaternary: Snapshots of paleoclimate and landscape evolution at the northern rim of the Alps. Quaternary Science Reviews, 28 (15-16): 1374-1391.

Mickler, P.J., Stern, L.A., Banner, J.L., 2006. Large kinetic isotope effects in modern speleothems. GSA Bulletin, 118 (1/2): 65-81.

Mickler, P.J., Banner, J.L., Stern, L., Asmerom, Y., Edwards, R.L., Ito, E., 2004. Stable isotope variations in modern tropical speleothems: Evaluating equilibrium vs. kinetic isotope effects. Geochimica et Cosmochimica Acta, 68 (21): 4381-4393.

Milankovitch, M.M., 1941. Canon of Insolation and the Ice Age Problem (English Translations, Washington, D.C.). Königlich Serbische Akademie, Beograd.

Mook, W.G., 2000. Environmental isotopes in the hydrological cycle.

Morse, J.W., Mackenzie, F.T., 1990. Geochemistry of Sedimentary Carbonates.

Mühlinghaus, C., Scholz, D., Mangini, A., 2009. Modelling fractionation of stable isotopes in stalagmites. Geochimica et Cosmochimica Acta, 73: 7275-7289.

Neff, U., 2001. Massenspektrometrische Th/U-Datierung von Höhlensintern aus dem Oman: Klimaarchive des asiatischen Monsuns. PhD thesis. Heidelberg Academy of Science, Heidelberg.

NGRIP-members, 2004. High-resolution record of Northern Hemisphere climate extending into the last interglacial period. Nature, 431 (7005): 147-151.

O'Neil, J.R., Clayton, R.N., Mayeda, T.K., 1969. Oxygen Isotope Fractionation in Divalen Metal Carbonates. Journal of Chemical Physics, 51 (12): 12.

Peek, S., Clementz, M.T., 2012. Sr/Ca and Ba/Ca variations in environmental and biological sources: A survey of marine and terrestrial systems. Geochimica et Cosmochimica Acta, 95 (0): 36-52.

Rahmstorf, S., 2002. Ocean circulation and climate during the past 120,000 years. Nature, 419: 207-214.

Rahmstorf, S., Crucifix, M., Ganopolski, A., Goose, H., Kamenkovich, I., Knutti, R., Lohmann, G., Marsh, R., Mysak, L.A., Wang, Z., Weaver, A.J., 2005. Thermohaline circulation hysteresis: A model intercomparison. Geophysical research letters, 32:

Railsback, L.B., Dabous, A., Osmond J., K., Fleisher, C.J., 2002. Petrographic and Geochemical Screening of Speleothems for U-series Dating: An example from Recrystallized Speleothem from Wadi Sannur Cavern, Egypt Journal of Cave and Karst Studies, 64 (2): 108-116.

Raymo, M.E., Oppo, D.W., Curry, W., 1997. The Mid-Pleistocene climate transition: A deep sea carbon isotopic perspective. Paleoceanography, 12 (4): 546-559.

Richards, D.A., Dorale, J.A., 2003. Uranium-series chronology and environmental applications of speleothems. In: B. Bourdon, G.M. Henderson, C.C. Lundstrom, S.P. Turner (Eds.), Uranium-series Geochemistry. Mineralogical Society of America, Washington, DC, 656.

Richter, D.K., Meyer, S., Scholz, D., Immenhauser, A., submitted. Multiphase formation of Weichselian cryogenic calcites, Riesenberg Cave, NW Germany. Zeitschrift der Deutschen Gesellschaft für Geowissenschaften:

Riechelmann, D.F.C., Schröder-Ritzrau, A., Scholz, D., Fohlmeister, J., Spötl, C., Richter, D.K., Mangini, A., 2011. Monitoring Bunker Cave (NW Germany): A prerequisite to interpret geochemical proxy data of speleothems from this site. Journal of Hydrology, 409 (3-4): 682-695.

Rozanski, K., Aragas-Araguas, L., Gonfiantini, R., 1993. Isotopic patterns in modern global precipitation. In: Climate Change in Continental Isotope Records. 1-36.

Scholz, D., Hoffmann, D.L., 2008. ^{230}Th/U-dating of fossil reef corals and speleothems. Quaternary Science Journal (Eiszeitalter und Gegenwart), 57 (1-2): 52-77.

Scholz, D., Hoffmann, D.L., 2011. StalAge – an algorithm designed for construction of speleothem age models. Quaternary Geochronology, 6: 369-382.

Scholz, D., Mühlinghaus, C., Mangini, A., 2009. Modelling δ^{13}C and δ^{18}O in the solution layer on stalagmite surfaces. Geochimica et Cosmochimica Acta, 73 (9): 2592-2602.

Scholz, D., Mangini, A., 2007. How precise are U-series coral ages? Geochimica et Cosmochimica Acta, 71 (8): 1935-1948.

Scholz, D., Mangini, A., Meischner, D., 2007. U-redistribution in fossil reef corals from Barbados, West Indies, and sea level reconstruction for MIS 6.5. In: F. Sirocko, M. Claussen, T. Litt, M.F. Sanchez-Goni (Eds.), The climate of past Interglacials. Elsevier, Amsterdam, 119-140.

Scholz, D., Mangini, A., Felis, T., 2004. U-series dating of diagenetically altered fossil reef corals. Earth and Planetary Science Letters, 218 (1-2): 163-178.

Scholz, D., Hoffmann, D.L., Hellstrom, J., Bronk Ramsey, C., 2012. A comparison of different methods for speleothem age modelling. Quaternary Geochronology: 14: 94-104

Schülke, I., 1993. Die Oxford Schichtfolge im Steibruch Riesenberg (NW-Hameln). Hannover.

Sirocko, F., Seelos, K., Schaber, K., Rein, B., Dreher, F., Diehl, M., Lehne, R., Jäger, K., Krbetschek, M., Degering, D., 2005. A late Eemian aridity pulse in central Europe during the last glacial inception. Nature, 436: 833-836.

Spötl, C., Mangini, A., Richards, D.A., 2006. Chronology and paleoenvironment of Marine Isotope Stage 3 from two high-elevation speleothems, Austrian Alps. Quaternary Science Reviews, 25: 1127-1136.

Spötl, C., Vennemann, T.W., 2003. Continuous-flow isotope ratio mass spectrometric analysis of carbonate minerals. Rapid Communications in Mass Spectrometry, 17 (9): 1004-1006.

Spötl, C., Mangini, A., Frank, N., Eichstädter, R., Burns, S.J., 2002. Start of the last interglacial period at 135 ka: Evidence from a high Alpine speleothem. Geology, 30 (9): 815-818.

Stenni, B., Masson-Delmotte, V., Johnsen, S., Jouzel, J., Longinelli, A., Monnin, E., Raethlisberger, R., Selmo, E. (2001). An Oceanic Cold Reversal During the Last Deglaciation, pp. 2074-2077.

Terakado, Y., Masuda, A., 1988. The coprecipitation of rare-earth elements with calcite and aragonite. Chemical Geology, 69 (1â€ “2): 103-110.

Tolzmann, J., Scholz, D., Jochum, K.P., Hoffmann, D.L., Riechelmann, D.F.C., submitted. Post-depositional diagenesis in speleothems and its effect on the accuracy of 230Th/U-ages. Quaternary Geochronology: (in review).

Tooth, A.F., Fairchild, I.J., 2003. Soil and karst aquifer hydrological controls on the geochemical evolution of speleothem-forming drip waters, Crag Cave, southwest Ireland. Journal of Hydrology, 273: 51-68.

Trouet, V., Esper, J., Graham, N.E., Baker, A., Scourse, J.D., Frank, D.C., 2009. Persistent positive North Atlantic Oscillation mode dominated the Medieval Climate Anomaly. Science, 324: 78-80.

Tucker, M., 1988. Techniques in Sedimentology. Blackwell Scientific Publications.

von Grafenstein, U., Erlenkeuser, H., Brauer, A., Jouzel, J., Johnsen, S.J., 1999. A Mid-European Decadal Isotope-Climate Record from 15,500 to 5000 Years B.P. Science, 284 (5420): 1654-1657.

Wackerbarth, A.K., Scholz, D., Fohlmeister, J., Mangini, A., 2010. Modelling the $\delta^{18}O$ value of cave drip water and speleothem calcite. Earth and Planetary Science Letters, 299: 387-397.

Wainer, K., Genty, D., Blamart, D., Daëron, M., Bar-Matthews, M., Vonhof, H., Dublyansky, Y., Pons-Branchu, E., Thomas, L., van Calsteren, P., Quinif, Y., Caillon, N., 2011. Speleothem record of the last 180ka in Villars cave (SW France): Investigation of a large $\delta^{18}O$ shift between MIS6 and MIS5. Quaternary Science Reviews, 30 (1-2): 130-146.

Wang, Y., Cheng, H., Edwards, R.L., Kong, X., Shao, X., Chen, S., Wu, J., Jiang, X., Wang, X., An, Z., 2008. Millennial- and orbital-scale changes in the East Asian monsoon over the past 224,000 years. Nature, 451 (7182): 1090-1093.

Wanner, H., Broennimann, S., Casty, C., Gyalistras, D., Luterbacher, J.r., Schmutz, C., Stephenson, D., Xoplaki, E., 2001. North Atlantic Oscillation. Concepts And Studies. Surveys in Geophysics, 22 (4): 321-381.

Wedepohl, H., 1995. The composition of the continental crust. Geochimica et Cosmochimica Acta, 59 (7): 1217-1232.

Wolff, E.W., Chappellaz, J., Blunier, T., Rasmussen, S.O., Svensson, A., 2010. Millennial-scale variability during the last glacial: The ice core record. Quaternary Science Reviews, 29 (21-22): 2828-2838.

Wu, J.Y., Wang, Y.J., Cheng, H., Kong, X.G., Liu, D.B., 2012. Stable isotope and trace element investigation of two contemporaneous annually-laminated stalagmites from northeastern China surrounding the "8.2 ka event". Clim. Past, 8 (5): 1497-1507.

Zachos, J., Pagani, M., Sloan, L., Thomas, E., Billups, K., 2001. Trends, rhythms, and aberrations in global climate 65 Ma to Present. Science, 292: 686-693.

8. Appendix A

Appendix A: U and Th characteristics of RBH stalagmites

Stalagmite RBH 32

Table 1A: U and Th characteristics of stalagmite RBH 32. Note that all sample values displayed in red were conducted at CENIEH, Spain.

Lab ID	sample ID	dft (mm)	^{238}U [µg/g]	2σ-error	^{232}Th [ng/g]	2σ-error	(^{234}U/^{238}U)	2σ-error	(^{230}Th/^{238}U)	2σ-error	age uncorr. [ka]	2σ-error	age corrected [ka]	2σ-error	(^{234}U/^{238}U)$_{initial}$	2σ-error
JT41	1	17	0.470	0.003	1.755	0.028	1.535	0.004	0.829	0.006	80.39	0.88	80.33	0.86	1.672	0.005
UTO120	2	20	1.171	0.005	2.825	0.020	1.484	0.002	0.770	0.003	76.23	0.50	76.17	0.44	1.600	0.003
JT 72	3	36	0.617	0.005	1.665	0.021	1.521	0.008	0.837	0.007	82.54	1.16	82.50	1.20	1.658	0.009
JT 73	4	64	1.286	0.010	2.350	0.035	1.520	0.003	0.842	0.008	83.40	1.11	83.37	1.08	1.658	0.004
JT43	5	72	1.360	0.009	1.126	0.014	1.520	0.003	0.846	0.006	83.94	0.83	83.93	0.81	1.659	0.004
JT93	6	80	1.735	0.011	1.558	0.017	1.526	0.002	0.852	0.005	84.21	0.73	84.20	0.72	1.668	0.003
JT 74	7	87	0.376	0.003	1.926	0.038	1.453	0.005	0.929	0.015	103.90	2.65	103.82	2.77	1.607	0.007
JT94	8	116	1.116	0.007	2.028	0.022	1.450	0.003	0.922	0.006	102.97	1.12	102.95	1.11	1.602	0.004
JT42	9	131	0.610	0.004	0.737	0.013	1.458	0.005	0.913	0.009	100.54	1.60	100.52	1.56	1.608	0.006
JT 75	10	145	0.569	0.004	0.610	0.007	1.445	0.005	0.921	0.007	103.25	1.35	103.24	1.33	1.596	0.006
JT57	11	168	0.346	0.002	0.783	0.009	1.400	0.003	0.950	0.007	114.97	1.54	114.94	1.57	1.554	0.005
JT58	12	178	0.554	0.004	1.050	0.013	1.419	0.003	0.973	0.006	116.73	1.26	116.70	1.27	1.583	0.004
JT44	13	186	0.333	0.002	0.348	0.004	1.411	0.004	0.967	0.007	116.63	1.46	116.62	1.45	1.572	0.005
JT 76	14	202	0.569	0.005	0.249	0.003	1.388	0.007	0.965	0.009	120.08	2.18	120.07	2.23	1.544	0.008
JT 78	15	212	0.480	0.004	0.517	0.013	1.386	0.005	0.964	0.018	119.96	3.96	119.95	3.87	1.542	0.008
JT 77	16	240	0.113	0.001	0.115	0.002	1.363	0.003	0.953	0.009	121.44	2.03	121.43	2.05	1.511	0.005
UTO121	17	254	0.675	0.005	0.777	0.008	1.350	0.002	0.939	0.004	120.62	0.98	120.60	1.00	1.492	0.003
JT45	18	269	0.725	0.004	0.912	0.012	1.384	0.002	0.962	0.005	119.92	1.22	119.91	1.23	1.539	0.003

Stalagmite RBH 34

Table 2A: U and Th characteristics of stalagmite RBH 34. Note that all sample values displayed in red were conducted at CENIEH, Spain.

Lab ID	sample ID	dft (mm)	^{238}U [µg/g]	2σ-error	^{232}Th [ng/g]	2σ-error	($^{234}U/^{238}U$)	2σ-error	($^{230}Th/^{238}U$)	2σ-error	age uncorr. [ka	2σ-error	age corrected [	2σ-error	($^{234}U/^{238}U)_{initial}$	2σ-error
JT15	1	3	0.837	0.005	1.53	0.02	1.496	0.002	0.766	0.003	74.7	0.5	74.7	0.5	1.613	0.003
UTO138	2	18	0.38	0.04	14.68	1.69	1.404	0.003	0.848	0.004	96.2	0.8	95.5	0.9	**1.530**	**0.004**
UTO-112	9	30	0.83	0.01	0.161	0.002	1.411	0.002	0.915	0.004	106.5	0.9	106.5	0.9	1.556	0.003
JT16	4	62	0.944	0.005	1.17	0.02	1.425	0.003	0.909	0.006	103.7	1.1	103.6	1.1	1.570	0.004
JT17	5	83	1.006	0.006	0.90	0.02	1.426	0.005	0.893	0.006	100.8	1.1	100.7	1.1	1.566	0.005
JT14	6	126	0.925	0.006	1.50	0.02	1.431	0.005	0.907	0.005	102.6	1.0	102.5	1.0	1.576	0.005
UTO136	7	137	0.95	0.09	0.26	0.03	1.403	0.003	0.896	0.010	104.1	1.9	104.1	1.9	1.540	0.004
JT13	8	168	0.813	0.005	1.10	0.01	1.442	0.002	0.891	0.004	98.6	0.7	98.6	0.7	1.584	0.003
UTO137	3	174	0.52	0.04	15.76	1.30	1.337	0.003	0.925	0.008	120.4	1.9	119.8	1.9	1.472	0.005
JT12	10	190	0.877	0.006	2.24	0.03	1.367	0.005	0.955	0.005	121.3	1.4	121.3	1.4	1.517	0.006
UTO-113	11	204	1.37	0.01	1.94	0.02	1.366	0.002	0.964	0.004	123.4	1.0	123.4	1.0	1.518	0.003
JT11	12	221	1.255	0.007	0.84	0.01	1.359	0.002	0.940	0.005	119.3	1.2	119.3	1.1	1.503	0.003

Stalagmite RBH 39

Table 3A: U and Th characteristics of stalagmite RBH 39. Note that all sample values displayed in red were conducted at CENIEH, Spain.

Lab ID	sample ID	dft (mm)	^{238}U [µg/g]	2σ-error	^{232}Th [ng/g]	2σ-error	($^{234}U/^{238}U$)	2σ-error	($^{230}Th/^{238}U$)	2σ-error	age uncorr. [ka]	2σ-error	age corrected	2σ-error	($^{234}U/^{238}U)_{initial}$	2σ-error
JT49	1	4	0.190	0.001	2.216	0.024	1.497	0.003	0.777	0.005	76.39	0.65	76.21	0.66	1.616	0.003
JT26	2	6	0.127	0.001	2.174	0.034	1.498	0.008	0.764	0.013	74.61	1.81	74.34	1.84	1.614	0.010
JT70	3	13	0.345	0.003	0.529	0.006	1.469	0.006	0.804	0.007	82.25	1.11	82.22	1.12	1.592	0.007
UTO114	4	18	0.537	0.003	0.231	0.003	1.473	0.003	0.806	0.003	82.05	0.54	82.04	0.54	1.597	0.003
JT24	5	28	0.498	0.006	1.561	0.017	1.465	0.014	0.792	0.008	80.77	1.62	80.72	1.65	1.584	0.016
JT22	6	45	0.503	0.003	4.056	0.049	1.464	0.003	0.805	0.004	82.93	0.65	82.80	0.64	1.586	0.003
JT68	7	54	0.399	0.003	0.535	0.007	1.469	0.005	0.807	0.008	82.57	1.25	82.55	1.21	1.593	0.006
JT21	8	64	0.249	0.002	0.763	0.009	1.471	0.003	0.820	0.005	84.39	0.77	84.35	0.75	1.598	0.004
JT50	9	68	0.178	0.002	1.214	0.017	1.437	0.008	0.840	0.010	90.66	1.77	90.56	1.77	1.565	0.010
JT69	10	73	0.160	0.001	0.771	0.011	1.408	0.007	0.874	0.012	99.64	2.33	99.56	2.30	1.541	0.008
JT23	11	77	0.249	0.002	3.926	0.047	1.401	0.003	0.864	0.004	98.81	0.82	98.57	0.88	1.530	0.004
UTO140	12	90	0.188	0.016	0.643	0.058	1.399	0.004	0.850	0.005	96.46	0.88	96.40	0.88	1.524	0.004
UTO139	13	107	0.234	0.019	0.581	0.050	1.370	0.003	0.834	0.007	97.06	1.26	97.01	1.26	1.486	0.004
JT51	14	116	0.183	0.002	1.690	0.018	1.403	0.008	0.869	0.007	99.49	1.47	99.35	1.46	1.533	0.009
JT52	15	124	0.118	0.001	1.889	0.020	1.392	0.006	0.871	0.009	101.17	1.79	100.93	1.80	1.522	0.007
UTO115	16	133	0.392	0.002	0.440	0.004	1.367	0.002	0.877	0.004	105.31	0.81	105.28	0.83	1.494	0.003
JT71	17	138	0.348	0.003	0.476	0.006	1.384	0.003	0.899	0.008	107.26	1.62	107.24	1.65	1.520	0.004
JT55	18	143	0.517	0.004	1.155	0.014	1.384	0.003	0.873	0.005	102.32	1.06	102.29	1.03	1.512	0.003
JT67	19	147	0.501	0.005	2.046	0.028	1.385	0.011	0.886	0.011	104.68	2.34	104.62	2.35	1.517	0.013
JT20	20	158	0.692	0.005	0.792	0.011	1.391	0.003	0.898	0.004	106.09	0.87	106.07	0.90	1.528	0.003
JT53	21	162	0.041	0.000	0.571	0.006	1.362	0.007	0.913	0.012	113.43	2.72	113.23	2.70	1.498	0.009
JT66	22	166	0.220	0.002	0.400	0.005	1.357	0.005	0.924	0.009	116.24	2.05	116.21	2.02	1.496	0.007
JT54	23	178	0.150	0.001	0.996	0.011	1.335	0.003	0.953	0.007	126.41	1.70	126.33	1.74	1.479	0.004
JT25	24	190	0.151	0.001	1.208	0.014	1.348	0.004	0.948	0.005	123.00	1.34	122.89	1.35	1.493	0.005
JT19	25	191	0.242	0.001	0.951	0.010	1.347	0.003	0.944	0.004	122.33	1.00	122.28	1.01	1.490	0.004

Stalagmite RBH 47

Table 4A: U and Th characteristics of stalagmite RBH 47. Note that all sample values displayed in red were conducted at CENIEH, Spain.

Lab ID	sample ID	dft (mm)	^{238}U [µg/g]	2σ-error	^{232}Th [ng/g]	2σ-error	($^{234}U/^{238}U$)	2σ-error	($^{230}Th/^{238}U$)	2σ-error	age uncorr. [ka]	2σ-error	age corrected [ka]	2σ-error	($^{234}U/^{238}U)_{initial}$	2σ-error
JT2	1	10	0.194	0.002	1.472	0.016	1.609	0.013	0.796	0.007	71.00	1.22	70.88	1.21	1.744	0.015
UTO116	2	24	0.169	0.001	9.784	0.061	1.552	0.005	0.815	0.004	78.07	0.55	77.08	0.66	1.687	0.006
JT88	3	35	0.413	0.005	3.444	0.038	1.548	0.017	0.820	0.011	78.26	1.93	78.13	1.95	1.684	0.019
JT83	4	68	0.401	0.003	1.470	0.023	1.543	0.005	0.869	0.012	85.25	1.74	85.19	1.77	1.691	0.006
JT82	5	82	0.399	0.003	0.962	0.014	1.559	0.006	0.868	0.009	83.68	1.32	83.65	1.34	1.709	0.007
JT81	6	106	0.948	0.007	0.377	0.006	1.558	0.004	0.878	0.010	85.14	1.45	85.14	1.40	1.709	0.005
JT89	7	112	0.931	0.008	212.525	2.207	1.422	0.019	0.923	0.008	109.89	1.75	106.60	2.87	1.571	0.022
JT4	8	120	0.441	0.003	138.174	1.522	1.399	0.024	0.902	0.006	110.50	1.02	105.84	3.40	1.538	0.028
JT80	9	130	0.226	0.001	15.669	0.229	1.451	0.007	0.981	0.012	114.35	2.39	113.44	2.53	1.622	0.008
JT90	10	136	0.130	0.001	1.640	0.019	1.473	0.015	0.927	0.014	101.18	2.75	101.00	2.88	1.630	0.017
JT84	11	138	0.127	0.001	0.474	0.009	1.456	0.008	0.823	0.019	86.25	2.96	86.20	2.96	1.581	0.011
JT85	12	174	0.237	0.002	0.505	0.015	1.430	0.005	0.936	0.034	108.08	6.37	108.05	6.41	1.583	0.012
JT91	13	198	0.262	0.002	0.375	0.005	1.387	0.005	0.976	0.009	122.56	2.08	122.54	2.12	1.547	0.006
JT86	14	223	0.888	0.006	3.508	0.078	1.437	0.005	1.032	0.017	125.98	3.72	125.93	3.69	1.624	0.008
JT92	15	238	0.581	0.004	0.403	0.005	1.448	0.003	1.016	0.008	120.93	1.72	120.93	1.74	1.631	0.005
JT6	16	253	0.352	0.002	1.330	0.017	1.442	0.002	1.013	0.006	121.29	1.19	121.24	1.18	1.622	0.003
UTO117	17	292	1.016	0.007	0.123	0.002	1.461	0.003	1.025	0.004	120.81	0.94	120.81	0.93	1.648	0.003
JT5	18	310	0.715	0.005	2.626	0.028	1.489	0.005	1.016	0.005	114.81	1.14	114.77	1.23	1.676	0.006

9. Appendix B

Appendix B: Correlation matrixes of stable isotopes and selected trace elements in RBH stalagmites

Stalagmite RBH 32

Table 1B: Correlation matrixes of stable isotopes and selected trace elements of stalagmite RBH 32 for the Eemian as well as for GIS 23 and 21. Note that all correlation coefficients displayed in colors are significant with the 95% confidence interval. Red colors: negative correlation coefficients. Blue colors: positive correlation coefficients.

Eemian	*Mg*	*Al*	*P*	*Sr*	*Ba*	*Th*	*U*	$\delta^{13}C$	$\delta^{18}O$
Mg	1								
Al	-0.03	1							
P	0.03	0.19	1						
Sr	**-0.45**	**-0.22**	-0.04	1					
Ba	-0.10	-0.18	0.06	**0.67**	1				
Th	**0.41**	**0.73**	-0.10	***-0.38***	***-0.25***	1			
U	**-0.70**	0.02	-0.07	**0.56**	-0.06	**-0.32**	1		
$\delta^{13}C$	-0.03	-0.10	0.00	-0.07	0.06	**-0.38**	-0.17	1	
$\delta^{18}O$	**0.64**	-0.05	-0.03	**-0.38**	-0.10	0.12	**-0.58**	0.19	1

GIS 23	*Mg*	*Al*	*P*	*Sr*	*Ba*	*Th*	*U*	$\delta^{13}C$	$\delta^{18}O$
Mg	1								
Al	-0.01	1							
P	-0.27	**0.43**	1						
Sr	-0.11	**-0.20**	**-0.38**	1					
Ba	-0.03	-0.23	**-0.45**	**0.84**	1				
Th	-0.09	**0.93**	0.21	-0.30	-0.25	1			
U	**-0.42**	-0.13	-0.03	**0.67**	0.32	-0.18	1		
$\delta^{13}C$	0.11	-0.12	-0.04	0.13	0.19	-0.11	0.06	1	
$\delta^{18}O$	0.39	-0.06	-0.14	-0.23	-0.07	0.05	-0.37	0.005	1

GIS 21	*Mg*	*Al*	*P*	*Sr*	*Ba*	*Th*	*U*	$\delta^{13}C$	$\delta^{18}O$
Mg	1								
Al	0.31	1							
P	-0.22	**0.45**	1						
Sr	-0.06	-0.14	-0.23	1					
Ba	0.13	**0.52**	**0.39**	**0.16**	1				
Th	0.05	**0.89**	**0.37**	-0.02	**0.43**	1			
U	**-0.58**	-0.32	-0.04	**0.76**	-0.04	-0.14	1		
$\delta^{13}C$	**-0.50**	-0.09	0.16	-0.03	0.02	0.06	0.28	1	
$\delta^{18}O$	-0.02	-0.24	-0.02	-0.32	-0.31	-0.22	-0.17	**0.44**	1

Stalagmite RBH 39

Table 2B: Correlation matrixes of stable isotopes and selected trace elements of stalagmite RBH 39 for GIS 24, 23, 21 and 20. Note that all correlation coefficients displayed in colors are significant with the 95% confidence interval. Red colors: negative correlation coefficients. Blue colors: positive correlation coefficients.

GIS 24	*Al*	*Mg*	*P*	*Sr*	*Ba*	*Th*	*U*	$\delta^{13}C$	$\delta^{18}O$
Al	1								
Mg	**0.68**	1							
P	**0.58**	0.44	1						
Sr	**-0.53**	-0.23	**-0.47**	1					
Ba	**-0.68**	**-0.49**	**-0.63**	**0.81**	1				
Th	**0.98**	**0.70**	**0.70**	**-0.61**	**-0.78**	1			
U	-0.27	**-0.63**	-0.31	0.18	0.28	-0.27	1		
$\delta^{13}C$	-0.15	-0.17	**-0.39**	**-0.34**	-0.04	-0.27	**0.33**	1	
$\delta^{18}O$	0.04	-0.25	-0.26	-0.17	0.20	0.02	**0.46**	**0.63**	1

GIS 23	*Al*	*Mg*	*P*	*Sr*	*Ba*	*Th*	*U*	$\delta^{13}C$	$\delta^{18}O$
Al	1								
Mg	0.05	1							
P	0.17	-0.11	1						
Sr	-0.29	-0.25	**-0.31**	1					
Ba	-0.19	**-0.51**	-0.28	**0.85**	1				
Th	**0.97**	0.08	0.21	**-0.33**	-0.21	1			
U	-0.32	**-0.55**	-0.04	**0.48**	**0.35**	**-0.34**	1		
$\delta^{13}C$	-0.15	0.25	-0.12	0.11	0.10	-0.15	-0.06	1	
$\delta^{18}O$	0.03	0.01	**0.44**	**-0.36**	**-0.29**	0.08	-0.12	-0.01	1

gis 21	*Al*	*Mg*	*P*	*Sr*	*Ba*	*Th*	*U*	$\delta^{13}C$	$\delta^{18}O$
Al	1								
Mg	0.03	1							
P	0.28	0.33	1						
Sr	-0.17	0.07	0.008	1					
Ba	-0.20	-0.21	-0.211	**0.85**	1				
Th	**0.93**	-0.06	**0.341**	-0.10	-0.13	1			
U	-0.01	-0.44	-0.036	**0.76**	**0.71**	0.09	1		
$\delta^{13}C$	0.15	0.00	-0.066	**0.33**	0.25	0.18	**0.36**	1	
$\delta^{18}O$	-0.17	**0.52**	0.259	0.03	-0.20	-0.20	-0.28	-0.08	1

GIS 20	*Al*	*Mg*	*P*	*Sr*	*Ba*	*Th*	*U*	$\delta^{13}C$	$\delta^{18}O$
Al	1								
Mg	**0.78**	1							
P	**0.97**	**0.82**	1						
Sr	**-0.69**	**-0.86**	**-0.70**	1					
Ba	**-0.60**	**-0.83**	**-0.61**	**0.99**	1				
Th	**1.00**	**0.75**	**0.96**	**-0.65**	**-0.56**	1			
U	**0.37**	-0.03	**0.45**	0.25	0.36	0.38	1		
$\delta^{13}C$	**0.88**	**0.51**	**0.90**	**-0.52**	**-0.41**	**0.87**	**0.64**	1	
$\delta^{18}O$	0.01	0.11	-0.17	**-0.33**	**-0.39**	0.01	**-0.84**	**-0.32**	1

Stalagmite RBH 47

Table 3B: Correlation matrixes of stable isotopes and selected trace elements of stalagmite RBH 47 for the Eemian, GIS 24, 21, 20 and 19. Note that all correlation coefficients displayed in colors are significant with the 95% confidence interval. Red colors: negative correlation coefficients. Blue colors: positive correlation coefficients.

EEMIAN	*Al27*	*Mg*	*P*	*Sr*	*Ba*	*Th*	*U*	$\delta^{13}C$	$\delta^{18}O$
Al	1								
Mg	0.23	1							
P	0.06	0.09	1						
Sr	0.13	**0.80**	0.04	1					
Ba	-0.09	-0.05	-0.22	**0.17**	1				
Th	0.02	-0.09	0.07	0.01	-0.06	1			
U	0.19	**0.68**	0.14	**0.83**	-0.14	0.03	1		
$\delta^{13}C$	0.05	**0.79**	0.17	**0.83**	-0.14	0.04	**0.75**	1	
$\delta^{18}O$	0.11	0.06	-0.14	-0.13	0.01	0.07	-0.18	-0.01	1

GIS 24	*Al*	*Mg*	*P*	*Sr*	*Ba*	*Th*	*U*	$\delta^{13}C$	$\delta^{18}O$
Al	1								
Mg	0.02	1							
P	0.14	-0.33	1						
Sr	**-0.21**	**0.69**	**-0.55**	1					
Ba	-0.32	0.21	**-0.44**	**0.71**	1				
Th	0.06	0.17	-0.22	0.22	0.15	1			
U	-0.14	0.21	-0.13	**0.53**	**0.47**	0.15	1		
$\delta^{13}C$	0.05	-0.16	**0.57**	**-0.44**	**-0.43**	-0.18	-0.34	1	
$\delta^{18}O$	-0.12	-0.01	-0.27	0.16	**0.34**	0.17	0.35	-0.30	1

GIS 21	*Al*	*Mg*	*P*	*Sr*	*Ba*	*Th*	*U*	$\delta^{13}C$	$\delta^{18}O$
Al	1								
Mg	0.37	1							
P	0.12	**-0.41**	1						
Sr	**-0.26**	**-0.48**	-0.06	1					
Ba	-0.21	-0.05	**-0.49**	**0.76**	1				
Th	**0.56**	0.17	0.23	0.14	0.10	1			
U	-0.18	**-0.79**	**0.60**	**0.60**	0.03	0.15	1		
$\delta^{13}C$	-0.16	-0.16	-0.06	0.12	-0.07	-0.26	0.16	1	
$\delta^{18}O$	-0.27	-0.02	-0.08	0.13	0.12	-0.20	0.06	0.16	1

GIS 20	*Al*	*Mg*	*P*	*Sr*	*Ba*	*Th*	*U*	$\delta^{13}C$	$\delta^{18}O$
Al	1								
Mg	**0.52**	1							
P	**0.53**	0.16	1						
Sr	**-0.55**	-0.31	**-0.61**	1					
Ba	-0.33	0.06	**-0.52**	**0.85**	1				
Th	**0.54**	0.33	**0.55**	-0.42	-0.36	1			
U	0.02	0.12	0.33	0.02	0.07	-0.07	1		
$\delta^{13}C$	-0.08	0.02	0.01	-0.16	-0.32	0.17	-0.26	1	
$\delta^{18}O$	-0.08	-0.11	0.02	-0.06	-0.13	0.11	0.21	0.02	1

GIS 19	*Al*	*Mg*	*P*	*Sr*	*Ba*	*Th*	*U*	$\delta^{13}C$	$\delta^{18}O$
Al	1								
Mg	-0.09	1							
P	0.39	-0.38	1						
Sr	**-0.51**	**0.74**	-0.37	1					
Ba	0.09	**0.57**	-0.26	**0.63**	1				
Th	**0.86**	-0.35	0.34	**-0.69**	0.08	1			
U	0.13	0.42	0.32	**0.55**	**0.60**	-0.01	1		
$\delta^{13}C$	0.12	-0.42	-0.10	**-0.69**	**-0.48**	0.32	**-0.78**	1	
$\delta^{18}O$	-0.01	**-0.69**	0.10	**-0.77**	**-0.65**	0.25	**-0.76**	**0.88**	1

Eidesstattliche Erklärung

Ich versichere hiermit, die Arbeit selbständig und nur unter Verwendung der angegebenen Hiflsmittel verfasst zu haben.

Ich habe oder hatte die hier als Dissertation vorgelegte Arbeit nicht also Prüfungsarbeit für eine staatliche oder andere wissenschaftliche Prüfung eingereicht.

Ich hatte weder die jetzt als Dissertation vorgelegte Arbeit noch Teile davon bei einer abderen Fakultät bzw. einem anderen Fachbereich als Dissertation eingereicht.

Mainz, Januar 2013